UNIVERSIDADE FEDERAL DE PERNAMBUCO

CENTRO DE TECNOLOGIA E GEOCIÊNCIAS

DEPARTAMENTO DE GEOLOGIA

PROGRAMA DE PÓS-GRADUAÇÃO EM GEOCIÊNCIAS

JEFFERSON VALDEMIRO DE LIMA

CARACTERIZAÇÃO MINERALÓGICA, GEOQUÍMICA E ISOTÓPICA DO MAGMATISMO GRANÍTICO AO LONGO DA ZONA DE CISALHAMENTO PATOS, LIMITE ENTRE AS SUBPROVÍNCIAS CENTRAL E NORTE DA PROVÍNCIA BORBOREMA

Recife

2021

JEFFERSON VALDEMIRO DE LIMA

CARACTERIZAÇÃO MINERALÓGICA, GEOQUÍMICA E ISOTÓPICA DO MAGMATISMO GRANÍTICO AO LONGO DA ZONA DE CISALHAMENTO PATOS, LIMITE ENTRE AS SUBPROVÍNCIAS CENTRAL E NORTE DA PROVÍNCIA BORBOREMA

Tese apresentada ao Programa de Pós-Graduação em Geociências da Universidade Federal de Pernambuco, Centro de Tecnologia e Geociências, como requisito parcial para a obtenção do título de Doutor em Geociências. Área de Concentração: Geoquímica, Geofísica e Evolução Crustal.

Orientadora: Profª Drª Ignez de Pinho Guimarães

Coorientador: Prof. Dr. Sergio Pacheco Neves

Recife

2021

Catalogação na fonte:
Bibliotecário Carlos Moura, CRB-4 / 1502

L732c Lima, Jefferson Valdemiro de.
Caracterização mineralógica, geoquímica e isotópica do magmatismo granítico ao longo da Zona de Cisalhamento Patos, limite entre Subprovíncias Central e Norte da Província Borborema. / Jefferson Valdemiro de Lima. – 2021.
238 f.: il.

Orientadora: Profa. Dra. Ignez de Pinho Guimarães.
Coorientador: Prof. Dr. Sérgio Pacheco Neves.
Tese (doutorado) – Universidade Federal de Pernambuco. CTG. Programa de Pós-Graduação em Geociências, 2021.
Inclui referências.

1. Geociências. 2. Magmatismo Ediacarano. 3. Granitos sin-transcorrentes. 4. Província Borborema. 5. Petrogênese. 6. Subprovíncia Central. I. Guimarães, Ignez de Pinho (orientadora). II. Neves, Sérgio Pacheco (coorientador). III. Título.

550 CDD (22. ed.)

UFPE
BCTG/2022-124

JEFFERSON VALDEMIRO DE LIMA

CARACTERIZAÇÃO MINERALÓGICA, GEOQUÍMICA E ISOTÓPICA DO MAGMATISMO GRANÍTICO AO LONGO DA ZONA DE CISALHAMENTO PATOS, LIMITE ENTRE AS SUBPROVÍNCIAS CENTRAL E NORTE DA PROVÍNCIA BORBOREMA

Tese apresentada ao Programa de Pós-Graduação em Geociências da Universidade Federal de Pernambuco, Centro de Tecnologia e Geociências, como requisito parcial para a obtenção do título de Doutor em Geociências. Área de Concentração: Geoquímica, Geofísica e Evolução Crustal.

Aprovada em: 02/08/2021

BANCA EXAMINADORA

Prof.ª Dr.ª Ignez de Pinho Guimarães (Orientadora)
Universidade Federal de Pernambuco

Prof. Dr. Adejardo Francisco da Silva Filho (Examinador Interno)
Universidade Federal de Pernambuco

Prof.ª Dr.ª Valderez Pinto Ferreira (Examinadora Interna)
Universidade Federal de Pernambuco

Prof. Dr. Herbet Conceição (Examinador Externo)
Universidade Federal de Sergipe

Prof. Dr. Valdecir de Assis Janasi (Examinador Externo)
Universidade de São Paulo

AGRADECIMENTOS

Gostaria de agradecer a todos que de alguma forma contribuíram orientando, apoiando ou me incentivando a concretizar este trabalho, em particular:

A Deus, por me dar forças para superar as dificuldades;

A minha professora e orientadora, Ignez de Pinho Guimarães, cujo incentivo, dedicação, paciência e orientação foram fundamentais para a concretização desta tese, e a meu coorientador Sérgio Pacheco Neves, que da mesma forma, me ajudou com suas precisas e incisivas considerações;

A todos os professores do DGEO e PPGEOC que contribuíram para minha formação como geólogo, mestre e agora como doutor em geociências;

Aos professores Carlos José Archanjo, Elson Paiva de Oliveira, Miguel Angelo Stipp Basei, Nilson Botelho, Elton Luiz Dantas e Cristiano Lana que contribuíram grandemente com discussões dos resultados e/ou disponibilização de laboratório/dados, e foram essenciais para o desenvolvimento deste trabalho;

Aos professores Alcides Nóbrega Sial e Valderez Pinto Ferreira por terem disponibilizado os laboratórios que fazem parte do NEG-LABISE, onde grande parte das amostras foram preparadas, e aos técnicos e amigos que fazem parte deste grupo e que também forneceram assistência, em especial, Maria Emilia, Gilsa Santana, Renan Siqueira e Charles Henrique;

Aos técnicos dos diferentes laboratórios que forneceram suporte durante a realização das análises, em especial Íris Dias Dantas (Laboratório de Microssonda Eletrônica-UNB), José Vinícius Martins (Laboratório de química-ICP / USP) e Solange Lucena de Souza (Laboratório LA-MC-ICPMS / USP);

A meus pais e irmãs pelo apoio em todos os momentos de minha vida e por sempre acreditarem na minha carreira profissional;

À Flávia Araújo pelo incentivo, paciência e amor, que me ajudaram bastante ao longo do desenvolvimento desta tese;

Aos amigos que me ajudaram em algumas etapas deste trabalho, entre eles José Victor, Caio Cezar e Douglas Farias;

Aos professores que aceitaram compor a banca examinadora desta tese, junto a minha orientadora, Profs (a). Drs (a). Adejardo Francisco da Silva Filho, Valderez Pinto Ferreira, Valdecir de Assis Janasi e Herbert Conceição, como titulares, e os Profs. Drs. Gorki Mariano e Carlos José Archanjo, como suplentes;

À CAPES (Coordenação de Aperfeiçoamento de Pessoal de Nível Superior), pela bolsa de doutorado;

Ao CNPq (Conselho Nacional de Desenvolvimento Científico e Tecnológico) pelo apoio financeiro (Proc. 421353/2018-0) durante o desenvolvimento desta tese;

RESUMO

Magmatismo granítico e zonas de cisalhamento transcorrentes constituem importantes feições associadas à orogênese Brasiliana na Província Borborema, e a petrogênese dos granitoides e sua relação com os processos tectônicos são essenciais para o entendimento da evolução crustal. Nesta tese, foram estudados o Batólito Teixeira e o Complexo Esperança, duas grandes intrusões graníticas localizadas, respectivamente, na porção central e leste da Zona de Cisalhamento Patos. Dados U-Pb em zircão (585 a 600 Ma) e trama mineral e magnética indicam um alojamento pré-transcorrente para os granitoides do Batólito Teixeira. Estes granitoides apresentam assinatura química e assembleia mineral semelhante aos granitos tipo I oxidados, metaluminosos e com afinidade cálcio-alcalina de alto-K a shoshonítica, com teores de elementos traços típicos de granitos de alto Ba-Sr. Os baixos valores para o εNd (-13,68 a -16,04) e εHf (-16,27 a -20,80) e idades modelo T_{DM} (Nd e Hf) Paleoproterozoicas, juntamente com características químicas e idade do batólito sugerem fontes infracrustais anfibolíticas. É sugerido que fusão parcial ocorreu em crosta tectonicamente espessada depois de um longo período de tectônica contracional. Os granitoides do Complexo Esperança, alojados entre as Zonas de Cisalhamento Patos e Campina Grande, também apresentam afinidade com rochas cálcio-alcalinas de alto-K a shoshonítica, mas são associados a uma expressiva variabilidade química e isotópica. Os granitoides dos Plutons Pocinhos, Serrote da Cobra e Puxinanã apresentam idades modelo T_{DM} (Nd e Hf) Estaterianas a Calimianas, variando de 1.4 a 1.7 Ga e 1.6 a 1.8, respectivamente, e baixos valores para εNd (-5,90 a -7,35) e εHf (-2.83 a -6,90), enquanto os granitoides dos Plutons Areial e Remígio são caracterizados por valores fortemente negativos para o εNd (-15,29 a -16,71) e εHf (-12,20 a -21,03), e apresentam idades modelo T_{DM} (Nd e Hf) Paleoproterozoicas a Neoarqueanas. Estes dados, juntamente com as distintas características químicas sugerem fontes metaígneas Paleoproterozoicas de composição anfibolítica para o Pluton Areial, fontes Tonianas (ortognaisses Cariris Velhos) para os plutons Puxinanã, Serrote da Cobra e Pocinhos, e fontes metassedimentares para os granitoides de Remígio. A integração dos dados com contexto regional é compatível com um longo período de construção para o Complexo Esperança, desde o fim do regime contracional e pico metamórfico, com fonte de calor por espessamento crustal (~600 Ma; Plutons Pocinhos e Serrote da Cobra), até regime transcorrente, onde interação com fundidos máficos provenientes de descompressão do manto explica a origem dos magmas mais hibridizados dos Plutons Areial e Puxinanã (585 a 575 Ma), cujo alojamento foi controlado pela Zona de Cisalhamento Campina Grande. O alto gradiente geotérmico conduzido pelos pulsos magmáticos anteriores

e as altas temperaturas durante metamorfismo dinâmico relacionado a Zona de Cisalhamento Patos conduziram a fusão parcial das fontes metassedimentares que produziram o magmatismo do Pluton Remígio (~565 Ma). As condições termobarométricas de ambas as intrusões estudadas sugerem cristalização em profundidades compatíveis com a crosta intermediária a superior.

Palavras-chave: magmatismo Ediacarano; granitos sin-transcorrentes; Província Borborema; petrogênese; Subprovíncia Central.

ABSTRACT

Granitic magmatism and transcurrent shear zones are important features associated with the Brasiliana orogeny in the Borborema Province, and the petrogenesis of the granitoids and its relationship with the tectonic processes are essential for understanding the crustal evolution. In this thesis, the Teixeira Batholith and Esperança Complex, two large granitic intrusions located, respectively, in the central and eastern portion of the Patos Shear Zone were studied. U–Pb zircon data (585 to 600 Ma) and mineral and magnetic fabric indicate a pre-transcurrent emplacement for the granitoids of the Batholith Teixeira. These granitoids have a chemical signature and mineral assemblage similar to oxidized, metaluminous I- type granites, with high-K calc-alkaline to shoshonitic affinity, and with trace element contents typical of high-Ba-Sr granites. The low values for εNd (-13.68 to -16.04) and εHf (-16.27 to -20.80), and Paleoproterozoic (Nd and Hf) T_{DM} model ages, together with chemical characteristics and batholith age suggest infracrustal sources of amphibolitic composition. It is suggested that partial melting occurred in tectonically thickened crust after a long period of contractional tectonics. The granitoids of the Esperança Complex, emplacement between the Patos and Campina Grande Shear Zones, also show high-K calc-alkaline to shoshonitic affinity, but they are associated with an expressive chemical and isotopic variability. The granitoids of the Pocinhos, Serrote da Cobra and Puxinanã Plutons have Statherian to Calymmian Nd and Hf T_{DM} model ages, ranging from 1.4 to 1.7 Ga and 1.6 to 1.8 Ga, respectively, and low values for εNd (-5.90 to -7.35) and εHf (-2.83 to -6.90), while the Areial and Remigio Plutons are characterized by strongly negative values for εNd (-15.29 to -16.71) and εHf (-12.20 to -21 .03), and present Paleoproterozoic to Neoarchaean Nd and Hf T_{DM} model ages. These data, associated to different chemical characteristics, suggest Paleoproterozoic metaigneous sources of amphibolitic composition for the Areial Pluton, Tonian sources (Cariris Velhos orthogneisses) for the Puxinanã, Serrote da Cobra and Pocinhos Plutons, and metasedimentary sources for the Remigio granitoids. The integration of data with regional context is compatible with a long period of building for the Esperança Complex, from the end of the contractional regime, with a heat source by crustal thickening (~600 Ma; Pocinhos and Serrote da Cobra Plutons), until the strike-slip regime, where interaction with mafic melts originated by mantle decompression explain the origin of the more hybridized magmas of the Areial and Puxinanã Plutons (585 to 575 Ma), whose accommodation was controlled by the Campina Grande Shear Zone. The high geothermal gradient due to previous magmatic pulses and the high temperatures during dynamic metamorphism related to the Patos Shear Zone led to the partial melting of the

metasedimentary sources generating the Remígio pluton magmatism (~565 Ma). The thermobarometric conditions of both studied intrusions suggest crystallization at depths compatible with the intermediate to upper crust.

Keywords: Ediacaran magmatism; syn-transcurrent granites; Borborema Province; petrogenesis; Central Subprovince.

LISTA DE ILUSTRAÇÕES

Introdução

Figura 1 – Diagrama QAP com os trends evolutivos de Lameyre & Bowden (1982). 25

Figura 2 – Diagrama TAS com sobreposição das principais séries magmáticas. 26

Figura 3 – Mapa geológico simplificado das áreas estudadas. 30

Figura 4 – Mapa gamespectométrico da região correspondente ao Batólito Teixeira. 32

Figura 5 – Mapa gamaespectométrico da área do Complexo Esperança. 33

Contexto Geológico Regional

Figura 6 – Reconstrução pré-drit da porção oeste de Gondwana. Modificado de Van Schmus, at al(2008). 39

Figura 7 – Subdivisão da Província Borborema em Maciços Medianos, Lineamentos e Sistemas de Dobramentos, segundo Brito Neves (1975). 40

Figura 8 – Esboço geológico/tectônico da Província Borborema (Jardim de Sá et al. 1992; Jardim de Sá, 1994). 41

Figura 9 – Mapa geológico/tectônico da Província Borborema segundo Santos & Medeiros (1999) e Santos (2000). 43

Figura 10 – Principais domínios e zonas de cisalhamento da Província Borborema. Fonte: Modificado de Van Schmus, (2011). 45

Figura 11 – Mapa geológico com os principais domínios da Subprovíncia Central. 46

Artigo 1 - Mineral chemistry constrains on crystallization conditions and petrological evolution of the Teixeira Batholith granitoids, Borborema Province, NE Brazil

Figure 1 – Geological maps illustrating regional contexto. 51

Figure 2 – Simplified geological map of Teixeira Batholith. Based on Ferreira & Santos (2000) and Archanjo et al. (2008). 54

Figure 3 – Field and microstructural aspects of granitoids from the Teixeira Batholith. 56

Figure 4 –	Microscopic aspects of mafic and accessories minerals of the Teixeira Batholith granites.	58
Figure 5 –	Classification diagram for amphiboles of the studied granitoids.	60
Figure 6 –	Types of the cationic substitutions for Teixeira Batholith amphiboles.	61
Figura 7 –	Chemical characteristics of the studied biotite crystals.	62
Figure 8 –	Chemical classification of the biotites from the Teixeira Batholith.	64
Figure 9 –	Binary diagrams illustrating cationic substitutions in the studied biotites.	64
Figure 10 –	Chemical classification of the pyroxenes from the São Sebastião Facies.	65
Figure 11 –	An-Ab-Or ternary diagram for the classification of the studied plagioclase and K-feldspar (modified from Deer et al., 1992).	66
Figure 12 –	Chemical characteristics of the studied oxides and sulfides.	68
Figure 13 –	Cathode Luminescence images of the zircon grains from the Tendó Facies granitoids.	69
Figure 14 –	Chondrite-normalized REE patterns (Taylor e McLennan, 1985) of the studied zircons. A) Tx-08 sample; B) JD-01 sample.	70
Figure 15 –	A) Alt x Fe# diagram for the studied biotites (Anderson, 2008); B) AlIV x Fe/(Fe+Mg) diagram for the studied amphiboles, with the fields according to Anderson & Smith (1995); C) Oxygen fugacity of the Teixeira Batholith granites from the Log fO2 versus 103/T (K) diagram (Wones, 1989).	74

Artigo 2 - Post-collisional, high-Ba-Sr Teixeira Batholith granites: evidence for recycling of paleoproterozoic crust in the Alto Pajeú Domain, Borborema Province - NE-Brazil

Figure 1 –	A) Pre-drit reconstruction of the western portion of Gondwana from Van Schmus et al. (2008). Legend: BR/PA, Brasiliano/Pan-African belts; PaleoPr, Paleoproterozoic crust; NS, North Subprovince; TS, Central Subprovince; SS, South Subprovince; PEAL, Pernambuco-Alagoas domain; MK, Mayo Kebi terrane; NWCD, NW Cameroon domain; AYD, Adamawa-Yadé domain; YD, Yaoundé domain; OU,	106

Oubanguides fold belt; PaSZ, Patos shear zone; PeSZ, Pernambuco shear zone; TBL, Transbrasiliano Lineament; TBF, Tcholliré-Banyo fault; AF, Adamawa Fault; SF, Sanaga fault. Cities: N, Natal; R, Recife; S, Salvador; D, Douala; G, Garoua; K, Kaduna area of Nigeria; B) Major domains and shear zones of the Borborema Province (modified from Van Schmus et al., 2011). C) Central Subprovince of the Borborema Province with Ediacaran plutons highlighted in red (modified from Guimarães et al., 2016.

Figure 2 – Simplified geological map of Teixeira Batholith. Based on Ferreira & Santos, (2000) and Archanjo et al. (2008). 109

Figure 3 – Field aspects of Teixeira Batholith. 112

Figure 4 – Microstructural aspects of granitoids from the Teixeira Batholith. 114

Figure 5 – Geochemical characteristics of granitoids from the Teixeira Batholith. 117

Figure 6 – A) – L) Variation diagrams for major and trace elements. 118

Figure 7 – A) Chondrite-normalized REE patterns (Nakamura, 1974) of the studied granitoids; B) Primitive mantle-normalized (Sun and McDonough, 1989) trace element diagrams (spidergrams). 119

Figure 8 – The studied granitoids plot in the tectonic discriminant diagrams: (A) and (B), fields after Pearce et al. (1984) and Pearce (1996), respectively. WPG: Within Plate granites; POG: Post-orogenic granites; ORG: Ocean Ridge Granites; VAG: Volcanic Arc Granite. 120

Figure 9 – Tectonic setting discrimination diagrams of Whalen et al. (1987) for granitoids of the Teixeira Batholith. FG: fractionated granite field; OTG: unfractionated granite field; A: A-type granites; I & S: I- and S-type granites. 120

Figure 10 – Zircon U–Pb concordia diagram and corresponding representative zircons CL images from (a) Pedra D'Água Facies; (b) São Sebastião Facies; (c) Tendó Facies and (d) Santo Antônio Facies 122

Figure 11 – Isotope evolution diagram for Teixeira Batholith granitoids. 124

Figure 12 – Granitoids of the Teixeira Batholith plotted on the Ba-Rb-Sr ternary diagram (Tarney and Jones, 1994). 126

Figure 13 – Discriminant diagrams for source of the studied granitoids. 129

Artigo 3 - Multiple sources and multi-stage emplacement of the Esperança granitic complex and its relationship with the Patos – Campina Grande shear zone system, Borborema Province - NE Brazil

Figure 1 – A) pre-drit reconstruction of the western portion of gondwana from van schmus et al. (2008). Legend: br/pa, brasiliano/pan-african belts; paleopr, paleoproterozoic crust; ns, north subprovince; ts, central subprovince; ss, south subprovince; peal, pernambuco-alagoas domain; mk, mayo kebi terrane; nwcd, nw cameroon domain; ayd, adamawa-yadé domain; yd, yaoundé domain; ou, oubanguides fold belt; pasz, patos shear zone; pesz, pernambuco shear zone; tbl, transbrasiliano lineament; tbf, tcholliré-banyo fault; af, adamawa fault; sf, sanaga fault. Cities: n, natal; r, recife; s, salvador; d, douala; g, garoua; k, kaduna area of nigeria; b) major domains and shear zones of the borborema province (modified from van schmus et al., 2011). C) central subprovince of the borborema province with ediacaran plutons highlighted in red (modified from guimarães et al., 2016). Legend: rc: rio capibaribe domain; am: alto moxotó domain; ap: alto pajeú domain; pabd: piancó-alto brigida domain; cosz: coxixola shear zone; csz: congo shear zone; aisz: afogados da ingazeira shear zone; scsz: serra do caboclo shear zone; egc: esperança complex. Simplified geological map of the esperança complex. Field and petrographic aspects of esperança complex. 154

Figure 2 – Simplified geological map of the Esperança Complex. 157

Figure 3 – Field and petrographic aspects of Esperança Complex. 159

Figure 4 – Chemical classification of the biotite from the Esperança Complex 164

Figure 5 – Classification diagram for amphiboles of the studied granitoids. 165

Figure 6 – Chemical characteristics of the studied feldspars and oxydes. 166

Figure 7 – Geochemical characteristics of granitoids of the Esperança Complex. 168

Figure 8 – A) – L) Variation diagrams for major and trace elements of the Esperança Complex granitoids. 169

Figure 9 – Trace elements geochemical characteristics for the studied granitoids. 170

Figure 10 –	Tectonic setting discrimination diagrams for granitoids of the Esperança Complex.	171
Figure 11 –	Geochronological characteristics of the studied granitoids.	172
Figure 12 –	A) – E) Chondrite-normalized REE patterns (Taylor e McLennan, 1985) for the zircon crystals of the studied plutons.	176
Figure 13 –	Chemical and isotopic diagrams for the studied granitoids.	178
Figure 14 –	Trace element variation binary diagrams indicative of mineral fractionation.	185

LISTA DE TABELAS

Artigo 1 - Mineral chemistry constrains on crystallization conditions and petrological evolution of the Teixeira Batholith granitoids, Borborema Province, NE Brazil.

Table 1 – Representative electron microprobe analyses of amphiboles of the Teixeira Batholith. 91

Table 1 – (continued). 92

Table 2 – Representative electron microprobe analyses of biotite of the Teixeira Batholith. 93

Table 3 – Representative electron microprobe analyses of clinopyroxene of the São Sebastião Facies. 94

Table 4 – Representative electron microprobe analyses of plagioclase of the Teixeira Batholith. 95

Table 5 – Representative electron microprobe analyses of K-feldspar of the Teixeira Batholith. 96

Table 6 – Representative electron microprobe analyses of titanite of the Teixeira Batholith. 97

Table 7 – Representative electron microprobe analyses of magnetite of the Teixeira Batholith. 98

Table 8 – Representative electron microprobe analyses of sulfides of the Tendó Facies. 99

Table 9 – Representative electron microprobe analyses of epidote of the Teixeira Batholith. 99

Table 10 – LA-ICPMS analyses of zircon compositions of the Tendó Facies. 100

Table 11 – Estimation of temperature and pressure for the different facies of the Teixeira Batholith. 101

Artigo 2 - Post-Collisional, High-Ba-Sr Teixeira Batholith granites: evidence for delamination predating strike-slip shearing in the Borborema Province, NE-Brazil.

Table 1 – Representative whole-rock compositions of the Teixeira Batholith granitoids. 147

Table 2 – LA-ICP-MS U–Pb zircon data from some high Ba-Sr granitoid of the Batholith Teixeira. * Used analyzes in calculating Concordia age. 148
Table 3 – Lu-Hf isotopic data of the granites from the Teixeira Batholith. 149
Table 4 – Sm-Nd isotopic data for the studied granitoids and a sample of orthogneiss from the host rocks. 149

Artigo 3 - Multiple sources and multi-stage emplacement of the Esperança Granitic Complex and its relationship with the Patos – Campina Grande shear zone system, Borborema Province - NE Brazil.

Table 1 – Representative whole-rock compositions of the Esperança Complex granitoids. 204
Table 2 – U–Pb zircon data from the Esperança Complex granitoids. 205
Table 2 – Continued. 206
Table 2 – Continued. 207
Table 3 – Lu-Hf isotopic data of the granites from the Esperança Complex. 208
Table 4 – Sm-Nd isotopic data for the studied granitoids and host rocks. 209
Table 5 – Estimation of temperature and pressure for the Esperança Complex granitoids. 209

SUMÁRIO

1 INTRODUÇÃO 19

1.1 ESTUDO DE GRANITOS 19

1.1.1 Considerações gerais 19

1.1.2 Classificação de granitos 21

1.1.2.1 Classificação Alfabética 21

1.1.2.2 Granitos das séries Magnetita e Ilmenita 23

1.1.2.3 Classificação Tectônica 23

1.1.2.4 Classificação geoquímica de rochas graníticas 23

1.1.3 Granitos no contexto das séries magmáticas 24

1.2 APRESENTAÇÃO E OBJETIVOS 29

1.3 LOCALIZAÇÃO 30

1.4 METODOLOGIA 31

1.4.1 Etapas de campo 31

1.4.2 Petrografia 31

1.4.3 Química Mineral 33

1.4.4 Química de Zircão (LA-Q-ICP-MS) 34

1.4.5 Química em Rocha Total 35

1.4.6 Geologia Isotópica 36

2 CONTEXO GEOLÓGICO REGIONAL 38

2.1 PROVÍNCIA BORBOREMA 38

2.1.1 Subprovíncia Central 45

2.1.2 Magmatismo granítico na província Borborema e na Subprovíncia Central 46

3	**ARTIGO 1 MINERAL CHEMISTRY CONSTRAINS ON CRYSTALLIZATION CONDITIONS AND PETROLOGICAL EVOLUTION OF THE TEIXEIRA BATHOLITH GRANITOIDS, BORBOREMA PROVINCE, NE BRAZIL**	**49**
4	**ARTIGO 2 POST-COLLISIONAL, HIGH-BA-SR TEIXEIRA BATHOLITH GRANITES: EVIDENCE FOR DELAMINATION PREDATING STRIKE-SLIP SHEARING IN THE BORBOREMA PROVINCE, NE-BRAZIL**	**102**
5	**ARTIGO 3 MULTIPLE SOURCES AND MULTI-STAGE EMPLACEMENT OF THE ESPERANÇA GRANITIC COMPLEX AND ITS RELATIONSHIP WITH THE PATOS – CAMPINA GRANDE SHEAR ZONE SYSTEM, BORBOREMA PROVINCE - NE BRAZIL**	**150**
6	**CONSIDERAÇÕES FINAIS**	**224**
	REFERÊNCIAS	**228**

1 INTRODUÇÃO

1.1 ESTUDO DE GRANITOS

1.1.1 Considerações gerais

O termo “granito” deriva do latim *granum*, que significa grão. Ele foi usado pela primeira vez em 1596 pelo italiano Andrea Cesalpino (1519-1603), sem muitas preocupações com uma definição mais apurada, nem com os processos e mecanismos envolvidos em sua gênese. Granitoide é o termo usado na literatura para designar de forma geral, uma rocha plutônica com feições graníticas (rochas ígneas faneríticas, equigranulares e hipidiomórfica), baixo índice de cor, apresentando conteúdos variáveis de quartzo, feldspato alcalino e plagioclásio. Neste contexto, granito sensu latu consiste em um granitoide com mais de 10% de quartzo modal, já o granito sensu stricto deve conter por definição (classificação IUGS - Streckeisen, 1967) mais de 20% de quartzo e apresentar, no mínimo, volume modal de feldspato alcalino duas vezes maior que o de plagioclásio.

Granitos (sensu lato) são as rochas mais abundantes da crosta continental superior (Wedepohl, 1991), sendo o magmatismo granítico o principal responsável por sua diferenciação geoquímica. O estudo dos mecanismos envolvidos na geração, diferenciação composicional, transporte e alojamento de magmas ainda não são totalmente compreendidos, no entanto, sabe-se que os processos tectônicos condicionam a geração deste magmatismo. O entendimento da relação entre processos magmáticos e tectônicos é essencial para a compreensão da evolução da crosta continental.

A origem dos magmas está diretamente associada a fusão parcial de materiais em profundidades. Em grande parte, o processo de fusão inicia na porção superior do manto. O calor emanado pela passagem de magmas quentes através da crosta pode provocar processos adicionais de fusão parcial, e assim aumentar a complexidade química e petrológica das rochas continentais (Gill, 2014).

Segundo Bowen (1928), magmas graníticos poderiam ser gerados a partir da diferenciação por cristalização fracionada de magmas basálticos. Entretanto, experimentos mostram que este é um processo mais importante em pequenos corpos graníticos. A quantidade de material inicial que seria necessário para formar plutons de grande dimensão, torna improvável a geração de grandes corpos graníticos, exclusivamente, a partir de cristalização fracionada (Barbarin, 1999; Neves, 2012). Alguns autores estimam que para produzir o grande

volume de granito existente na terra, através deste tipo de processo, seria necessário um volume inicial de basalto dez vezes maior que o volume de granito, fato não observado em nenhuma região já estudada.

Vários outros mecanismos foram propostos com finalidade de investigar à origem e diversidade de magmatismo granítico. Os granitoides já foram apontados, em especial nas décadas de 40 e 50, como produtos de metassomatismo a partir de rochas metamórficas. Inclusive, o termo granitização foi criado com sentido similar, envolvendo, o processo de anatexia (Bonin et al., 1997).

Outro tipo de processo associado a diferenciação magmática é a assimilação, que consiste em um mecanismo no qual a contaminação xenolítica do magma, geralmente por material desprendido das paredes das rochas encaixantes, tem a capacidade de modificar a composição do magma inicialmente basáltica. Como a assimilação é acompanhada pela diminuição de temperatura do sistema, e de cristalização, é provável que a cristalização fracionada e a assimilação ocorram simultaneamente, assim dá-se o nome de assimilação seguida de cristalização fracionada (ACF) (DePaolo, 1981). Há também o processo em que dois líquidos imiscíveis, de composições diferentes são gerados a partir da separação de um magma inicialmente homogêneo. Este é um processo que pode desempenhar papel importante na formação de plutons sieníticos ultrapotássicos (Ferreira e Sial, 1994). No entanto, Neves (2012) chama à atenção para o fato de nenhum destes dois mecanismos serem considerados efetivos na origem de plutons de composição essencialmente granítica.

A hipótese mais aceita para geração da grande variedade geoquímica dos magmas graníticos é a fusão parcial de litotipos de composição variada no manto superior e na crosta, que pode ocorrer associada a arco vulcânico, margens continentais ativas, zonas de colisão continentais ou intraplacas (Gill, 2014). Rochas do manto superior podem originar magma basáltico através do processo de fusão parcial, e os fundidos originados podem interagir em graus diferentes com materiais crustais, gerando deferentes tipos de magmas. Plutons graníticos ocorrem, em especial, como produtos resultantes de convergência e colisão tectônica, ou mesmo após um grande evento de espessamento crustal. Portanto, uma grande variedade de tipos litológicos (rochas crustais ígneas, sedimentares e metamórficas) pode produzir magmas graníticos de composição diversificada, quando submetidos a processos de fusão parcial. Desta forma, dentre os processos capazes de gerar magmas graníticos, fusão parcial de rochas preexistentes é, sem dúvida, o mais importante (Neves, 2012).

1.1.2 Classificação de granitos

1.1.2.1 Classificação alfabética

Há vários esquemas na literatura para a classificação de granitos. Um dos primeiros e mais populares é o esquema de classificação química de rochas graníticas de Chappell e White (1974), conhecido como a classificação alfabética. Este sistema de classificação apresenta um cunho mais interpretativo com relação à gênese de granitos, onde estas rochas podem ser classificadas com tipo I, S, A, M ou C. Inicialmente, o alfabeto genético dos granitos foi formado pelos termos I e S, quando Chappell and White (1974) reconheceram estes dois tipos de granitos contrastantes no Lachlan Fold Belt, Australia.

O tipo-S é fortemente peraluminoso, refletindo numa associação mineral que inclui termos máficos mais aluminosos (cordierita, granada, muscovita, entre outros), além de biotita com pleocroísmo vermelho/marrom (devido ao baixo teor de ferro), relativamente potássica e geralmente apresentam conteúdo de SiO2 restrito (65 – 77 %). Com relação a origem de granitos tipo-S, é sempre associada a fusão parcial de metapelitos, com ou sem a participação de magmas básicos. O tipo-I é caracterizado por rochas metaluminosas a fracamente peraluminosas, relativamente sódicas, e com conteúdo de SiO_2 bastante variado (56 – 77 %), originado comumente, por fusão parcial de rochas ígneas ou meta-ígneas máficas, em níveis crustais profundos. A associação mineral de granitos Tipo-I compreende biotita com pleocroísmo verde/marrom e hornblenda, mineral incomum nos granitos pertencentes ao tipo-S.

Loiselle & Wones (1979) acrescentaram a esse esquema o “tipo-A”, que foi caracterizado, incialmente, como sendo granitoides potássicos, com alto conteúdo de FeO/FeO+MgO (Fe#), e alto conteúdo de Zr e outros HFSE (elementos de alto potêncial iônico). O termo “tipo A” foi utilizado devido a esses granitos apresentarem afinidade química alcalina e serem posicionados em ambiente geotectônico anorogênico, além de apresentarem uma assembleia anidra. Posteriormente, vários autores demonstraram que granitos Tipo-A não são restritos a ambientes anorogênicos, podendo ser gerados em qualquer momento durante um episódio tectônico-magmático, associado à extensão continental (King et al., 1997; Barbarin, 1999; Wu et al., 2002; Kebede and Koeberl, 2003; Mushkin et al., 2003;Whalen et al., 1987; Eby, 1990; Frost & Frost, 1997).

Eby (1992) subdividiu os granitos Tipo-A, levando em consideração os teores de elementos menores, entre eles, Y, Nb, Zr, Ce e Ga, nos subgrupos A1 e A2, ambos em ambientes tectônicos extensionais. O subtipo-A_1 tipicamente anorogênico, associado a atividade de pluma mantélica ou *hotspots*, com assinatura de elementos traços típicos de magmas OIB (basaltos de ilha oceânica). O subtipo-A2 origem crustal originado em ambiente pós-colisional.

Bonin (2007) associa a variedade de granitos tipo-A a grande quantidade de contexto geodinâmico onde eles são gerados: i) em regiões continentais, podem estar relacionados a um estágio orogênico pós-colisional, associados a zonas de cisalhamento transcorrentes; em regiões cratônicas, podem envolver um contexto de reativação de zonas de cisalhamento transcorrentes; em regime extensional, zona de rifte; e em margens passivas e ativas; ii) em regiões oceânicas, eles podem estar associados a limites de placa divergentes em dorsais oceânicas; ou num contexto tectônico intraplaca associados a ilhas oceânicas ou platôs oceânicos.

Apesar da variedade na composição de granitos tipo-A, algumas feições podem ser apontadas como típicas: alto conteúdo de álcalis ($Na_2O + K_2O$ = 7 a 11 wt. %); baixo conteúdo de CaO (<1,8 wt. %) composição peralcalina a subaluminosa, em alguns casos levemente peraluminosos; elevados valores de FeOt/(FeOt+MgO); elevado teores de halogênios, quando comparados a outros tipos de granitos; mineralogia composta por silicatos máficos ricos em ferro (annita, siderofilita, ferrohedenbergita, ferrohastingsita, faialita); silicatos máficos ricos em álcalis (aegirina, arfvedsonita, e riberkita) em suítes peralcalinas; feldspatos pertíticos; e enriquecimento em HFSE e ETR (Collins et al., 1982; Whalen et al., 1987; Eby, 1990).

Os tipos M e C foram adicionados à classificação alfabética por White (1979) e Kilpatrick & Ellis (1992) respectivamente. O tipo M foi interpretado como rochas graníticas derivadas a partir de fusão do manto, e geralmente associado a ambientes de arco de ilhas, incluindo plagiogranitos, enquanto o tipo-C foi definido como granitoides charnockíticos, cuja origem é associada a fusão de fontes máficas a intermediárias de alto-K, nas quais a hornblenda constitui uma fase anteriormente desidratada. Portanto, magmas tipo-C (~62% de SiO_2) originam granitos de granulação grossa, com feldspatos escuro, e hiperstênio, além de hornblenda, em maior proporção que biotita, augita e magnetita.

O maior problema da classificação alfabética consiste no fato dela admitir que as rochas graníticas são em grande parte, derivadas de uma única fonte, entretanto, muitos granitos são gerados a partir da mistura de fundidos mantélicos e crustais.

1.1.2.2 Granitos das séries Magnetita e Ilmenita

Esta classificação foi proposta por Ishihara (1977) a partir da mineralogia de minerais opacos em rochas graníticas no Japão. Dois grupos distintos, designados séries, foram identificados: 1) granitos com magnetita coexistindo com ilmenita (serie magnetita) e 2) granitos apresentando ilmenita sem magnetita (série ilmenita). Além disso, Ishihara (1977) observou que as rochas graníticas pertencentes a série ilmenita são relativamente reduzidas e apresentam suscetibilidade magnética menor que $100x10^6$ emu/g (susceptibilidade magnética por unidade de massa), enquanto as pertencentes a série magnetita são oxidadas, apresentam titanita e mostram suscetibilidade magnética maior que $100x10^6$ emu/g. Ambas são associadas a depósitos minerais distintos.

Apesar desse esquema não ser estritamente geoquímico, ele é baseado em reações de remoção, ou inibição de formação de magnetita. Há três reações conhecidas que controlam a estabilidade da magnetita em rochas graníticas. As reações associadas à desestabilização de magnetita em rochas reduzidas envolvem reações com silicatos de Fe-Mg (Frost et al., 1988; Fuhrman et al., 1988; Frost & Lindsley, 1991), já em rochas peralcalina seu consumo vem seguido de produtos como anfibólios e piroxênios sódicos. Além destes, Ishihara (1977) reconhece a redução por combustão de carbono durante fusão de rochas metassedimentares.

1.1.2.3 Classificação tectônica

A partir de uma compilação de mais de 600 análises, utilizando a geoquímica de elementos traços (Nb, Y, Ta, Rb, etc), Pearce et al. (1984) propuseram um esquema de classificação capaz de discriminar o contexto tectônico associado a origem de rochas graníticas. Assim, reconheceram geoquimicamente quatro tipos de ambientes tectônicos principais: granitos de cadeia oceânica, de arco vulcânico, intraplaca e colisionais.

Entretanto, sabe-se que a assinatura de elementos traços em granitoides é associado mais fortemente à fonte e história do líquido, do que ao ambiente tectônico em si. Os granitos pós-colisionais retratam bem esse problema, já que podem se projetar em qualquer um dos campos traçados por Pearce et al. (1984) por serem derivados de inúmeras fontes, dependendo da composição da crosta espessada durante a orogênese, fato que fez Pearce (1996) acrescentar o campo *Post-colg* (granitos pós-colisionais) ao diagrama discriminante (Y+Nb) x Rb.

1.1.2.4 Classificação geoquímica de rochas graníticas

Frost et al. (2001) propuseram uma classificação geoquímica, sem conotação tectônica ou genética para as rochas graníticas. Esta classificação é baseada em três parâmetros: i) Número de ferro (Fe#) = FeOt/FeOt+MgO; ii) MALI (*modified alkali-lime index*) = (Na_2O + K_2O − CaO); iii) ASI (*aluminum saturation index*) = [Al/(Ca – 1·67P + Na + K)].

O número de ferro está associado aos processos envolvidos na história de diferenciação da rocha, e aplicado principalmente para distinguir os granitos que apresentam forte enriquecimento em ferro, granitos ferrosos, dos de baixo ferro, granitos magnesianos os quais compreendem os toleítico e cálcio-alcalinos (Miyashiro, 1970). O MALI, por sua vez, é relacionado a alcalinidade das rochas, podendo classificá-las em alcálicas, álcali-cálcicas, cálcio-alcálicas e cálcicas. Este parâmetro corresponde, de certa forma, ao esquema proposto por PEACOCK (1931), porém utilizando um intervalo maior de variação de sílica. Já o ASI, compreende uma variável que considera a relação entre os álcalis e o alumínio disponível no sistema magmático, isso significa que as rochas com ASI>1 correspondem àqueles onde a quantidade de Al presente é maior do que os feldspatos podem acomodar, as rochas geradas possuem conríndon na norma e alguma fase aluminosa presente, sendo chamadas de peraluminosas. Com relação às rochas fracamente peraluminosas, essa fase pode ser biotita, já naquelas fortemente peraluminosas, esta fase pode ser cordierita, granada ou polimorfos de Al_2SiO_5. Quando o ASI < 1 e Na + K < Al, há a formação de rochas graníticas metaluminosas, onde o excesso de Ca, após a entrada do Al nos feldspatos, é guiada para formação de minerais contendo este elemento como hornblenda ou augita. Naquelas onde há ASI < 1 e Na + K > Al, são chamadas de rochas peralcalinas, e nessas o Na em excesso entra nos minerais ferromagnesianos, gerando hornblenda nas levemente peralcalinas, e anfibólios/piroxênios sódicos nas fortemente.

1.1.3 Granitos no contexto das séries magmáticas

No geral, as séries magmáticas apresentam características químicas bem definidas, fazendo com que elas estejam associadas a determinados padrões de diferenciação característicos, quando representadas nos diversos diagramas químicos, entre eles o AFM, TAS e CaO/ (Na_2O + K_2O). Alem destes diagramas, Lameyre & Bowden (1982) utilizaram o do diagrama ternário de classificação de rochas ígneas (Streckeisen, 1967) para representar as séries magmáticas. (Fig. 1).

Figura 1 – Diagrama ternário com os trends evolutivos de Lameyre & Bowden (1982). 1- série toleítica oceânica; 2- série cálcio-alcalina baixo-K; 3- séries subalcalinas (toleítica e cálcio-alcalina) médio e alto-K; 4- série shoshonítica; 5- série alcalina saturada em sílica sódica; 6- série peralcalina e ultrapotássica; 7- associação leucocrática peraluminosa.

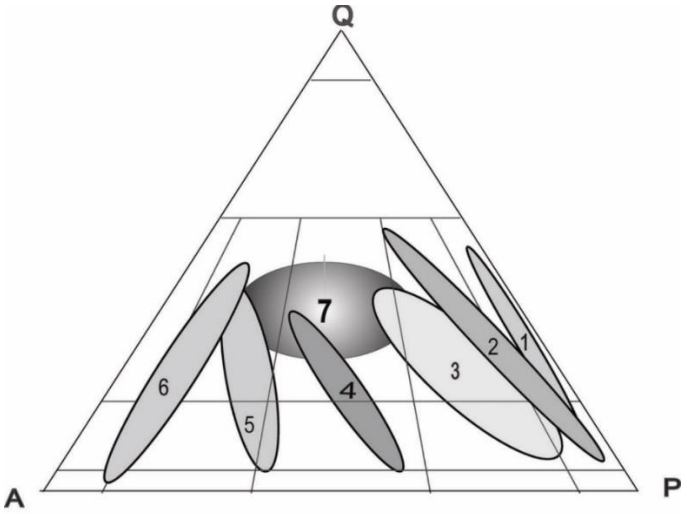

Fonte: Nardi (2016)

Nardi (2016) utilizando o diagrama TAS [SiO_2 x (Na_2O+K_2O)], redefiniu e subdividiu (Fig. 2) as séries alcalinas e subalcalinas propostas por Irvine e Baragar (1971): i) série subalcalina engloba as séries toleítica, komatiítica e cálcio-alcalina; e ii) série alcalina compreende as séries alcalina subsaturada em sílica, alcalina sódica saturada em sílica, shoshonítica ou alcalina potássica e alcalina ultrapotássica saturada em sílica (Fig. 2).

• Série toleítica – Esta série é associada, em grande parte, a um contexto de assoalho e cadeias mesoceânicas, e ambientes anorogênicos intraplacas continentais, embora também tenha sido evidenciado em granitoides pós-colisionais associados a transcorrência (Eby, 2006; Nardi & Bitencourt, 2007, Florisbal et al., 2012; Fontana et al., 2012). Compreende principalmente gabros, quartzo-gabros, tonalitos e trondhjemitos. No diagrama TAS, se distribuem na base (ambiente oceânico) ou no topo (série toleítica continental), do campo das rochas subalcalinas. As principais características químicas observadas em uma associação de rochas pertencente a série toleítica são o enriquecimento em ferro, que fica bastante evidente no diagrama AFM, e os baixos valores de Al_2O_3 dos basaltos toleíticos (12-14%) (Wilson, 1989), além dos baixos valores de água quando comparados as rochas da série cálcio-alcalinas. Outras características compreendem baixos teores de K, Rb, Ba, Sr e ETRL, principalmente nas rochas toleíticas oceânicas. A mineralogia compreende, nos termos máficos, dois piroxênios (piegeonita e augita), olivina, plagioclásio e óxidos de Fe e Ti. Os granitoides da série toleítica de baixo-K são correspondentes aos do tipo-M (White, 1979) ou de cadeias oceânicas (Pearce

et al., 1984), enquanto as rochas ácidas médio a alto-K ocorrem em associações de platôs continentais, e apresentam alta razão FeOT/MgO (> 0.9), baixos conteúdos de Al_2O_3 (< 14 %) e afinidade químicas com rochas tipo-A (Nardi & Bitencourt, 2009).

Figura 2 – Diagrama TAS com sobreposição das principais séries magmáticas.

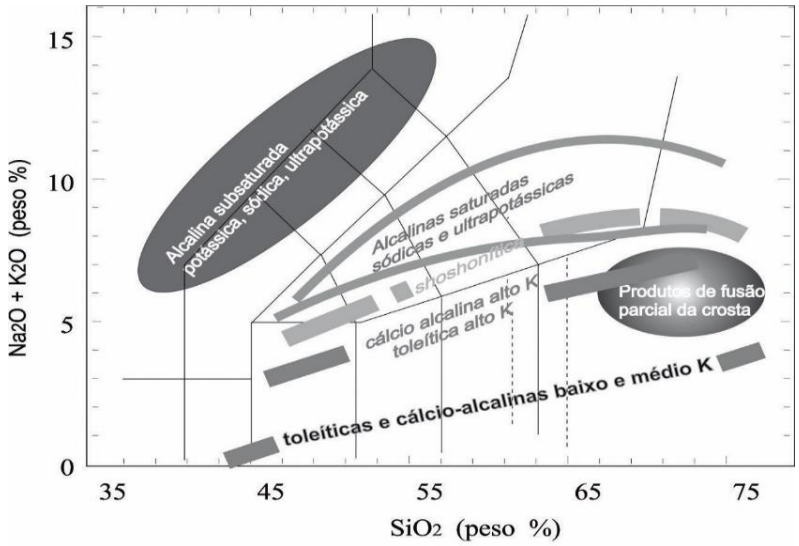

Fonte: Nardi (2016)

• Série komatiítica – Esta série compreende rochas que tem sua origem relacionada a fusão de material ultramáfico de manto empobrecido em ETRL, correspondendo a uma associação bastante característica das sequencias vulcano-sedimentares do Arqueano e Proterozoico inferior, muitas vezes nomeadas greenstone belts. Os típicos komatiitos, que caracterizam esta série, apresentam baixos valores (em peso de óxidos) de sílica (< 53%) e titânio (até 1%), e valores elevados de magnésio, geralmente maiores que 18%, mas que podem chegar até 30% (em base anidra), Ni (> 100ppm) e Cr (> 140ppm) (Le Maitre, 2002; Wernick, 2004). Enquanto os peridotitos komatiíticos caracterizam o membro mais primitivo desta série, os boninitos e dacitos são as rochas intermediária e ácida correspondentes, ou no caso de seus equivalentes intrusivos andesitos, tonalitos e trondjemitos. A mineralogia dessas rochas é caracterizada por fenocristais de olivina, geralmente com elevados teores de Cr_2O_3 (0,1-0,4%), e com a típica textura spinifex, quando a rocha apresenta valores maiores que 20% de MgO, e piroxênio com altos valores de Al_2O_3 (2 a 9%), além de uma matriz de Cr-espinélio, cromita, sulfetos, entre outros.

• Série Calcio-alcalina – O termo cálcio-alcalino já foi usado anteriormente com diversas conotações (Arculus, 2003; Middlemost, 1985; Nardi, 2016). Levando em consideração a visão mais atual e aceita pelos pesquisadores, a associação de rochas pertencentes a série cálcio-

alcalina compreende, no diagrama QAPF, os dioritos, quartzo-monzodioritos, granodioritos e granitos, além de seus correspondentes vulcânicos (andesitos, dacitos e riolitos) (Nardi, 2016). Nas associações tipo-TTG, tonalitos e trondhjemitos são os principais representantes (Condie, 2005; Castro, 2014) A mineralogia evidenciada em rochas da série cálcio-alcalina varia de acordo com o teor de potássio e de água (Nardi, 2016; Zimmer et al., 2010), podendo englobar desde plagioclásio, olivina, augita, ± óxido de Fe-Ti e piegeonita, até biotita e sanidina nos termos intermediários. Os elementos de alto potencial iônico como Ti, P, Zr, Nb e Terras Raras pesados, geralmente, se mantêm com valores abaixo dos encontrados em rochas de afinidade alcalina. Uma feição evidente é o enriquecimento de Sr, Ba, Rb e ETRL da série de baixo-K para a de alto-K. A associação cálcio-alcalina é bastante associada ao magmatismo originado em contexto de arco, onde sua origem pode ser vinculada ao manto afetado pela subducção, podendo predominar a fusão da própria placa subductada (em grande parte quando a placa subductada é relativamente jovem), da cunha mantélica metassomatizada pelos fluidos relacionados com a subducção ou mesmo, a fusão de fragmentos continentais carregados pela mesma, como sugerido por Castro (2014). Esse tipo de magmatismo também é característico em arco associado a orôgenos acrescionários, embora este tipo de configuração também possa incluir termos toleíticos baixo-K e shoshoníticos, e em ambientes pós-colisionais (Harris et al., 1986; Liégois et al., 1998; Roberts and Clemens, 1992), principalmente os granitoides de alto potássio.

- Série alcalina subsaturada em sílica - Esta série corresponde a porção inferior do diagrama QAPF, que é caracterizada pela presença de rochas com insuficiência em SiO_2 (ausência de quartzo) e presença modal e normativa de feldspatoides. Nas rochas altamente subsaturadas em sílica, haverá nefelina modal (estas rochas são raras), no entanto, há também aquelas que são consideradas levemente subsaturadas, essas, por outro lado, não apresentam nefelina modal, mas, têm nefelina normativa, o que torna difícil a identificação por meios ópticos. Apesar da ausência de nefelina, estas rochas basálticas apresentam, em geral, titano-augita e titano-magnetita na sua assembleia mineral. Estas rochas basálticas, que apresentam nefelina normativa, são bastante associadas a um contexto de ilhas vulcânicas, e são designadas álcali olivina basalto.

- Série alcalina sódica saturada em sílica – No diagrama QAPF, esta série compreende rochas que ocupam os campos dos gabros, sienitos, quartzo sienitos, álcali feldspato granito e granitos, enquanto no diagrama TAS ocupa o campo das rochas saturadas em sílica. No geral, estas rochas variam de metaluminosas a peralcalinas, com uma leve tendência de

enriquecimento dos HFSE (elementos de alto potencial iônico). Os granitoides metaluminosos constituem associações ígneas bimodais, caracterizados pela presença de rochas básicas, quartzo sienito e granito, que frequentemente apresenta uma assinatura química do tipo-A (Nardi e Bitencourt, 2009). A mineralogia máfica principal é composta por biotia e anfibólios sódicos-cálcicos. Já os granitoides peralcalinos compreendem anfibólio e piroxênio sódicos como máficos característicos. Em geral, os granitoides e correspondentes vulcânicos desta série são associados a ambiente pós-colisional, anorogênico ou a arco continental maduro.

• Série shoshonítica ou alcalina potássica – Apesar dos diferentes critérios utilizados para descrição do magmatismo de afinidade shoshonítica, a caracterização sugerida por Morrison (1980), é uma das mais utilizadas por petrólogos. Nesta, o termo shoshonítico fica diretamente relacionado às associações com sílica próximas aos basaltos saturados. Além disso, Le Maitre (1989) sugere a utilização dos valores dos álcalis para distinguir rochas ultrapotássicas das rochas shoshoníticas, estas últimas apresentam $K_2O > (Na_2O-2)$ e $K_2O/Na_2O < 2,0$, projetando-se no campo das rochas alcalinas saturadas em sílica no diagrama TAS (Le Maitre, 2002; MacDonald & Katsura, 1964; Irvine & Baragar, 1971; Le Bas et al., 1986). As rochas desta série definem o típico trend monzonítico de Lameyre & Bowden (1982), que compreende no diagrama QAPF, os campos referentes aos gabros, dioritos, monzodioritos, monzonitos, quartzo monzonitos e granitos, ou correspondentes vulcânicos e apresentam assinatura álcali-cálcicas e metaluminosas. Quando extrusivas, são designadas traquibasaltos potássicos, shoshonitos e latitos, além dos traquitos e riolitos (De Liz et al., 2009). As rochas graníticas desta série são representadas, em grande parte, por quartzo monzonitos e granitos, podendo ser diferenciadas das cálcio-alcalinas alto-K por se associarem com rochas monzoníticas e pela típica relação entre K_2O e Na_2O (Pagel & Leterrier, 1980; Tauson, 1983; Nardi, 1984). No geral, os granitoides em questão, apresentam regularidade nos padrões de ETR e elevados teores de Sr e Ba (Nardi, 1986), feição frequentemente associada a granitos tipo-I. Mineralogicamente, contém biotita e anfibólio cálcico como máficos predominantes e são frequentemente associados a ambientes de arco magmático continental maturo e pós-colisionais (Nardi, 2016).

• Série alcalina ultrapotássica saturada em sílica – Assim como as rochas shoshoníticas, as ultrapotássicas também são definidas com base no conteúdo de álcalis, no entanto, enquanto as primeiras precisam apenas apresentar valores de $K_2O > Na_2O$, os granitoides ultrapotássicos são assim denominados quando o teor de $K_2O > 2 \times Na_2O$. São principalmente pertita ou K-feldspato granitos associados com feldspato alcalino sienitos, quartzo sienitos, granitos metaluminosos sódicos, gabros, dioritos e lamprófiros (Nardi, 2016), e apresentam biotita e

anfibólio cálcico nos tipos metaluminosos e anfibólios alcalinos nos tipos peralcalinos. Este tipo de granitoide é frequentemente encontrado associado a ambientes anorogênicos ou pós-colisionais, onde constituem associações bimodais.

1.2 APRESENTAÇÃO E OBJETIVOS

Magmatismo granítico é apontado como o principal responsável pela diferenciação da crosta continental e, os processos tectônicos, por sua vez, são responsáveis pela geração destes magmas. Portanto, o estudo da relação entre processos magmáticos e tectônicos constitui a peça fundamental para o entendimento da evolução da crosta continental. Entretanto, os mecanismos envolvidos na geração, diferenciação, transporte e alojamento destes magmas, ainda precisam ser mais bem compreendidos.

Geologicamente, a região nordeste do Brasil compreende um cinturão Brasiliano caracterizado por longa e complexa evolução geológica, nomeado de Província Borborema, e dividida em três subprovíncias (Van Schmus et al., 2011): Norte, Central e Sul. Rochas graníticas e zonas de cisalhamentos transcorrentes constituem importantes feições da orogênese Brasiliana na Província Borborema. Nesta tese, será abordada a granitogênese ao longo da Zona de Cisalhamento Patos, importante estrutura que separa as Subprovíncias Central e Norte da Província Borborema.

Para tanto, serão apresentados os dados obtidos a partir da caracterização mineralógica/petrográfica, geoquímica (química mineral e química de rocha total), e isotópica (geocronológica e geoquímica isotópica) de duas grandes intrusões ígneas, localizadas imediatamente ao sul da Zona de Cisalhamento Patos: o Batólito Texeira e o Complexo Esperança (Fig. 3). O Batólito Teixeira ocorre na porção central da referida zona de cisalhamento e é composto por monzogranito, sienogranito e quartzo-sienitos agrupados em seis fácies: Pedra D'Agua, São Sebastião, Tendó, Jabre, Mãe D'Agua e Santo Antônio. O Complexo Esperança, por sua vez, compreende *sheets* de granitos enquadrados em cinco plutons: Puxinanã, Areial, Pocinhos, Remígio e Serrote da Cobra (Archanjo and Fetter, 2004; Sampaio, 2005) os quais mostram assinaturas geoquímicas e isotópicas distintas.

Figura 3 – Mapa geológico simplificado das áreas estudadas (Retângulo Amarelo). Legenda: 1) Coberturas Quaternárias; 2) Granitoides Brasilianos; 3) Gabros Brasilianos; 4) Complexos metassedimentares Brasilianos (a- Surubim e b- Seridó); 5) Complexo Sertânia; 6) Metassedimentos correlacionáveis ao Complexo São Caetano; 7) Ortognaisses Arqueanos / Paleoproterozóicos. ZCP– Zona de Cisalhamento Patos. Modificado do mapa geológico da Paraíba.

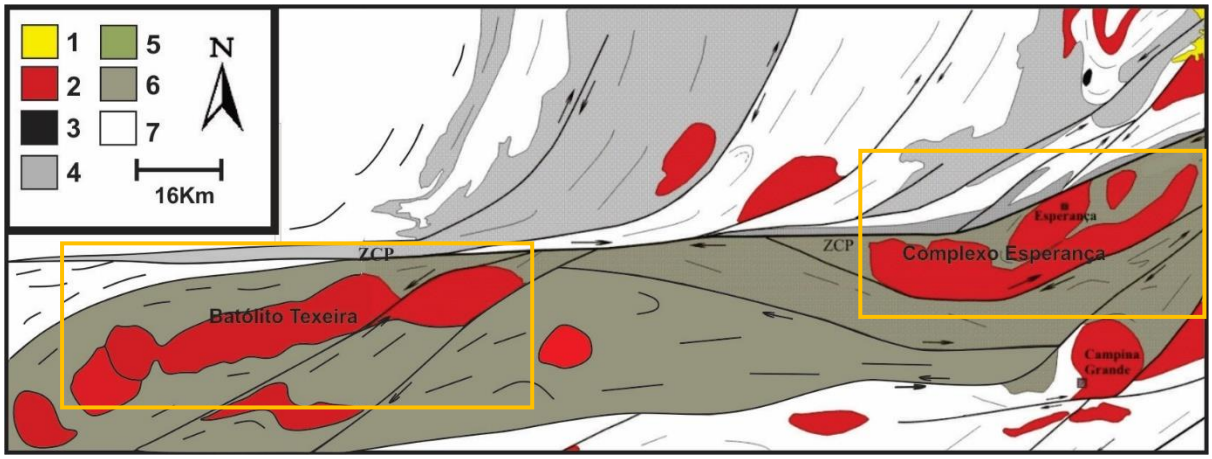

Fonte: O autor (2021)

Desta forma, pretendemos contribuir para o estudo da granitogênese na Subprovíncia Central, com foco na petrogênese dos granitoides, dentro de uma abordagem abrangente, no contexto da Orogênese Brasiliana, e as relações com as zonas de cisalhamentos de direção aproximada ENE-WSW. Vale salientar que ambas intrusões ígneas tratadas nesta tese já foram estudadas em trabalhos anteriores (Archanjo and Fetter, 2004; Sampaio, 2005), no entanto, a reavaliação destas intrusões, aplicando sobretudo novas sistemáticas, anteriormente não aplicadas, visando um melhor detalhamento petrológico também está entre o escopo desta tese, assim como analisar quimicamente as rochas e fases minerais que constituem os diversos plutons, principalmente naqueles sem dados anteriores, determinar o comportamento dos elementos traços em zircão dos granitoides dos plutons estudados, obter a idade de cristalização destes corpos (apenas três idades U-Pb em zircão, sendo duas no Complexo Esperança, e uma no Batólito Teixeira, estão disponíveis na literatura), analisar isotopicamente (Sm-Nd, Lu-Hf) as rochas estudadas, e por fim, combinar todos os dados obtidos a fim de estabelecer informações a respeito da rocha fonte e dos processos envolvidos durante a evolução das rochas graníticas estudadas, bem como seu enquadramento dentro do contexto geotectônico regional.

1.3 LOCALIZAÇÃO

Os dados obtidos para o desenvolvimento desta tese concentram-se em duas áreas próximas, ambas no estado da Paraíba (mesorregião do agreste paraibano). A área correspondente ao Complexo Esperança compreende parte dos municípios de Remígio,

Esperança, Areial, Montadas, Pocinhos e Puxinanã, enquanto a área do Batólito Teixeira, envolve parte dos municípios de Taperoá, Cacimbas, Teixeira, Matureia e Mãe D'Água.

1.4 METODOLOGIA

Para a confecção desta tese, foram utilizados métodos clássicos de um trabalho geológico, juntamente com a aplicação de novas sistemáticas aplicadas à petrologia (comportamento de elementos traços em zircão como traçador das fontes das rochas). No geral, esta metodologia envolveu uma revisão bibliográfica inicial dos principais aspectos geológicos das áreas estudadas, seguida por etapas de campo para a obtenção de dados e amostras, principalmente nos locais não abordados por trabalhos anteriores, e estudo de laboratório, onde as amostras foram trabalhadas e analisadas, fornecendo assim novos dados químicos e isotópicos necessários para a caracterização do magmatismo granítico ao longo da Zona de Cisalhamento Patos, limite entre as Subprovíncias Central e Norte da Província Borborema. A seguir, será apresentada uma breve revisão dos procedimentos utilizados em cada etapa.

1.4.1 Etapas de campo

No total, foram realizadas cinco etapas de campo, e nestas, foram utilizados instrumentos como lupa, imã, martelo, canivete, GPS, bússola, além de mapas geológicos e geofísicos base, construídos com os dados obtidos na etapa de revisão bibliográfica. Os mapas geológicos base do Batólito Teixeira e Complexo Esperança, foram confeccionados com o auxílio dos dados do Projeto Aerogeofísico Borda Leste do Planalto da Borborema (CPRM, 2008) em especial o mapa de composição ternária K-eTh-eU (RGB) (Figs. 4 e 5), além dos mapas geológicos das respectivas áreas estudadas com base em trabalhos anteriores (Archanjo et al., 2008; Sampaio, 2005; Guimarães et al. 2008; Rodrigues el al. 2011; Lages e Marinho, 2012; Cavalcante et al. 2018). Foi realizada a coleta de amostras nas áreas onde não se dispõe de amostras para análises, e foi verificado em campo as relações das rochas com dados disponíveis na literatura. Além disso, também foram obtidos dados estruturais como medições de foliação, lineação, entre outros que são importantes para o entendimento da relação entre os corpos ígneos estudados e a zona de cisalhamento Patos.

1.4.2 Petrografia

As amostras coletadas na etapa de campo foram descritas, macroscopicamente, e posterioremente selecionadas para a confecção de lâminas petrograficas, a serem estudadas no microscópio optico de luz transmitida no Laboratório de Microscopia Óptica do Departamento

de Geologia da Universidade Federal de Pernambuco (UFPE). Além disso, foi realizada a análise microscópica dos minerais opacos (óxidos e sulfetos), com o auxílio de um microscópio de luz refletida do Laboratório de Estudos Metalogenéticos Aplicados da UFPE. Neste mesmo laboratório, foram obtidas as fotomicrografias a partir do software analySIS instalado em computador acoplado ao microscópio. A confecção das seções delgadas e polidas ocorreu nos Laboratórios de Laminação da UFPE e USP.

A análise microscópica das amostras estudadas foi realizada com o objetivo de descrever e classificar a mineralogia e as microfeições presentes. Para isso, foi realizada uma análise modal das seções delgadas, a partir do método de visada, e assim, as proporções dos minerais presentes foram utilizadas para a classificação dos granitoides estudados, com base do diagrama QAPF de Streckeisen (1976). A partir das feições mineralógicas e estruturais observadas ao microscópio, algumas amostras foram selecionadas para a próxima etapa, que consistiu no estudo químico das fases minerais por Microssonda Eletrônica (química mineral).

Figura 4 – Mapa gamespectométrico da região correspondente ao Batólito Teixeira.

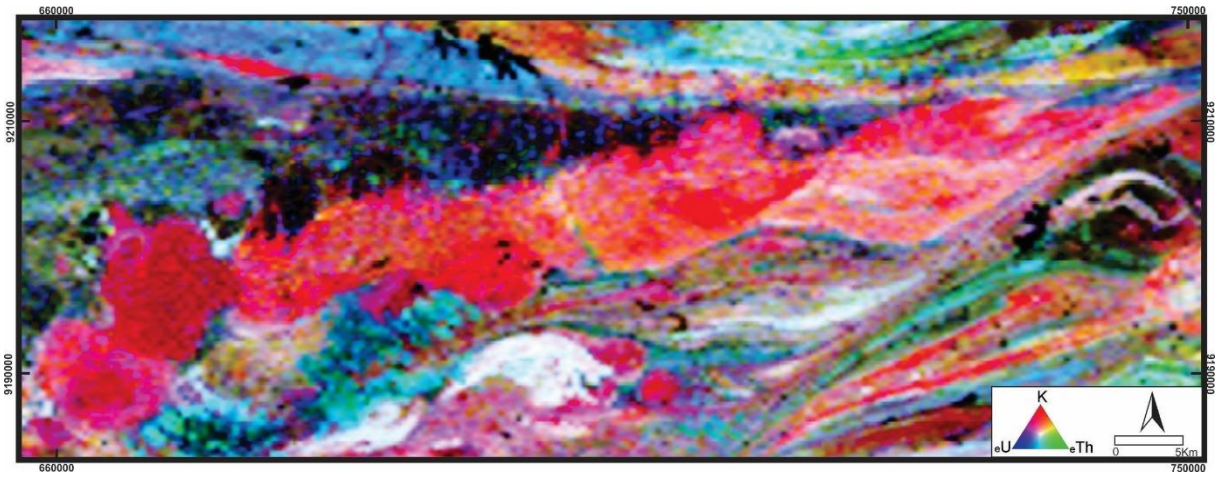

Figura 5 – Mapa gamaespectométrico da área do Complexo Esperança

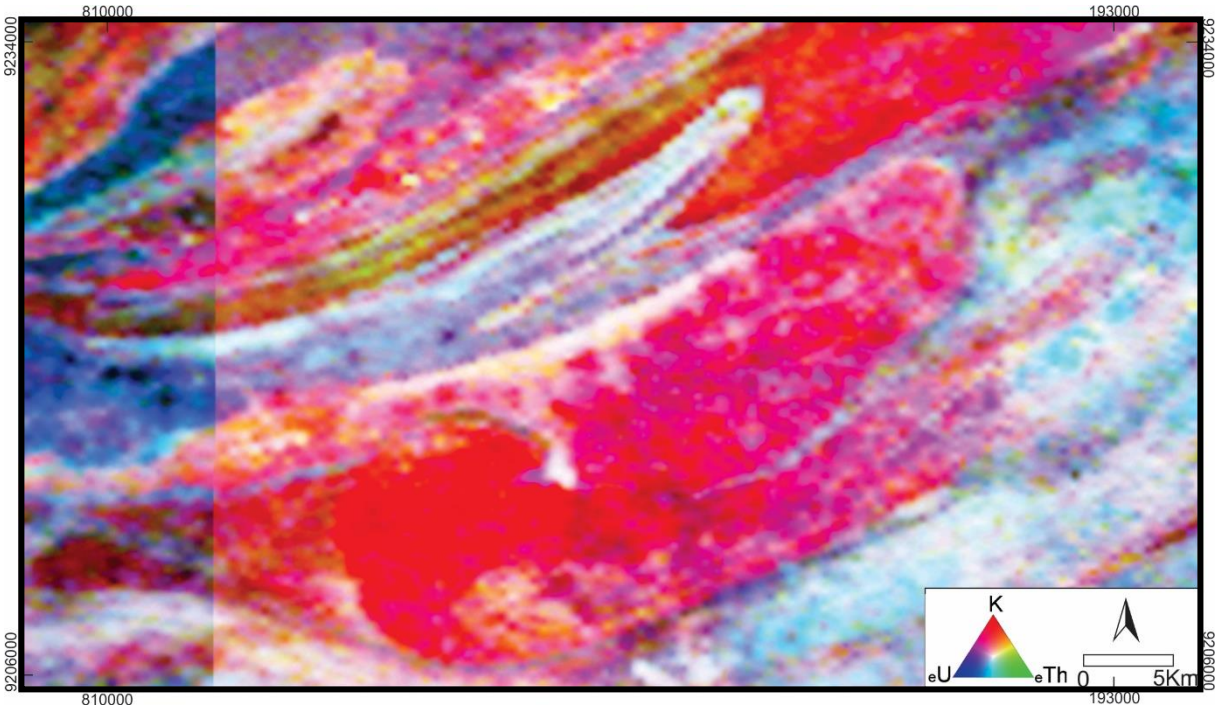

1.4.3 Química Mineral

Nesta etapa, foi realizada a caracterização química dos principais minerais presentes nas amostras selecionadas na etapa anterior (plagioclásio, feldspato alcalino, biotita, anfibólio, piroxênio, titanita, epidoto, sulfetos e minerais opacos). Para tanto, as seções polidas foram metalizadas com carbono em câmara de vácuo e em seguida analisadas através da Microssonda Eletrônica (JEOL modelo JXA-8230 com cinco espectrômetros WDS e um EDS) no Instituto de Geociências da Universidade da Universidade de Brasíllia, que opera em voltagem de aceleração de 15 kV, corrente de 10 nA, e um diâmetro do feixe eletrônico da ordem de μm para a análise de elementos maiores nos silicatos e óxidos.

Para a caracterização e classificação química das fases minerais analisadas foi realizado o recalculo de suas fórmulas estruturais a partir de planilhas do Microsoft® Office Excel 2010 (cedidas pelo Laboratório de Microssonda Eletrônica da UnB). Estes dados, inclusive, foram usados para inferir a condições termobarométricas (P e T) que operaram durante a cristalização do magma granítico. Para o cálculo da pressão de cristalização, foi utilizado o geobarômetro alumínio total em Hornblenda segundo a calibração de Schmidt (1992), e para o cálculo da temperatura utilizou-se o geotermômetro anfibólio – plagioclásio a partir da calibração de Blundy & Holland (1990), além do geotermômetro de saturação em zircão de Watson & Harrison (1983) e Watson(1987). Para as condições de fO^2 operantes durante a evolução e

cristalização dos magmas graníticos, foi utilizada a composição dos minerais máficos como estimativa e a equação proposta por Wones (1989) para a quantificação delas.

Além da caracterização química dos minerais por meio da Microssonda Eletrônica (plagioclásio, feldspato alcalino, biotita, anfibólio, piroxênio, titanita, epidoto, sulfetos e minerais opacos), também foi realizado o estudo de química em zircão, com ênfase na análise do comportamento de elementos traços presentes nesta fase mineral. Como este tipo de estudo envolve outros procedimentos, será discutido na próxima seção.

1.4.4 Química de Zircão (LA-Q-ICP-MS)

O zircão consiste em um dos mais importantes minerais usados como traçador petrogenético, porque incorpora um largo espectro de elementos traços na sua complexa estrutura cristalina. Isto proporciona uma abordagem ímpar das séries de mudanças nas condições de cristalização, permitindo-se inferir vários processos ao longo da origem e evolução magmática (Speer, 1982; Watson e Harrison, 2005).

O zircão é um mineral muito comum em rochas da crosta superior, podendo ser cristalizado a partir de fundidos ricos em sílica ou em graus metamórficos moderado a alto. Uma das principais características deste mineral, é sua capacidade de se manter quimicamente e isotopicamente íntegro, mesmo sendo exposto a múltiplos episódios de reciclagem sedimentar e ígnea, além disso, ele parece resistir a fases de residência no manto, via delaminação da crosta inferior e da subducção de sedimentos (Gao et al., 2014). Um dos fatores relacionados a sua robustez é apontado por Watson e Harrison, (1983), que associa a baixa solubilidade de zircões em fundidos silicáticos ao fato destes persistirem como relíquias refratárias em alguns magmas graníticos. Tudo isso torna o zircão o mineral mais confiável para se obter informações químicas-isotópicas usadas para descrever a origem, evolução e alojamento de magmas.

Apesar de múltiplos métodos analíticos serem disponíveis para o estudo de elementos traços em zircão, apenas os métodos in situ (LA-ICP-MS) são suficientemente sensíveis a ponto de determinar com confiabilidade os elementos que ocorrem em teores menores que ppm, e são capazes de evitar, sobretudo, inclusões na superfície, fraturas, danos causados por radiações e outras imperfeições capazes de afetar os resultados (Hoskin, 1998). Especialmente em área de ocorrência de orógeno colisional, métodos analíticos que não usem análises pontuais, não proporcionarão resultados confiáveis, pois em geral as rochas são portadoras de uma população heterogênea de zircões, e de zircões com núcleos herdados.

Para a obtenção dos grãos de zircão, as amostras de granitoides passaram por processos convencionais de separação. Inicialmente, foi realizada uma seleção de amostras, levando em consideração aspectos estruturais, petrográficos e geoquímicos determinados nas etapas anteriores. Em seguida, as amostras foram britadas, levemente moídas e depois passaram por peneiramento a úmido, com peneiras que contêm abertura de 0,500mm, 0,250mm e 0,125mm, onde as frações mais representativas obtidas do peneiramento seguiram para a secagem em estufa. Posteriormente, foi o feito o bateamento, onde houve a concentração dos materiais mais densos, e para a separação das frações magnéticas foi utilizado uma lupa binocular e o separador magnético isodinâmico de Frantz. Em seguida, a fração não magnética passou por mais uma etapa de separação por densidade, desta vez utilizando a técnica dos líquidos densos, onde foi feito o uso do bromofórmio. Por fim, os grãos de zircão menos afetados por processos de metamictização foram dispostos nos mounts e polidos até aproximadamente a metade de sua espessura para expor a morfologia interna. Além de imagens obtidas em Lupa, também foram usadas as imagens de Catodoluminescência (CL) para a caracterização de sua estrutura interna, muito importante para o controle do local escolhido nos zircões a serem analisados, prevenindo a análise de porções indesejadas.

As análises de elementos traços e terras raras dos grãos de zircão foram realizadas no Laboratório de Química (ICP-AES/MS) do Núcleo de Apoio à Pesquisa Geoanalítica do Instituto de Geociências - USP. Para isto, foi utilizado um espectrômetro de massa quadrupolar Thermo Scientific iCAP, com plasma indutivamente acoplado (ICP-QMS), e controlado pelo software Qtegra, associado a um sistema de ablação a laser modelo New Wave 213 A/F (para o Nd, YAG deep UV – 213 nm). A amostragem foi realizada em modo raster a 60 μm, com furos de 30 μm e passo de 1 μm/s. Como software de redução de dados foi utilizado o Glitter® (GEMOC Laser ICP-MS Total Trace Element Reduction).

1.4.5 Química em Rocha Total

O objetivo principal desta etapa é o estudo químico em rocha total dos granitoides estudados, buscando informações, a partir das composições das amostras analisadas, das séries magmáticas, ambiente geotectônicos, e possíveis processos de diferenciação (cristalização fracionada, fusão parcial, entre outras) predominantes durante a evolução dos magmas. Além disso, podem ser determinadas as possíveis fontes e processos associados à origem das rochas graníticas dos plutons estudados, a partir do estudo dos elementos terras raras e elementos traços.

Inicialmente, foi feita uma seleção de amostras representativas a serem analisadas, onde foram escolhidas apenas lascas frescas e livres de capa de alteração. Em seguida, houve a conversão das amostras de granitoides em pó. A preparação dos pós foi realizada nos Laboratórios de Preparação de Amostras do DGEO e do NEG-LABISE, ambos da UFPE. Esta preparação seguiu os seguintes procedimentos: remoção de pequenas partes alteradas, quando presente, britagem (britador de mandíbula), quarteamento, e pulverização no moinho de discos.

As análises das amostras pulverizadas foram realizadas pelo laboratório ALS no Canada, onde foram utilizadas as técnicas de ICP-ES (Inductively Coupled Plasma Emission Spectrometry) para elementos maiores (onze óxidos) e ICP-MS (Inductively Coupled Plasma Mass Spectrometry) para elementos menores, com fusão alcalina por $LiBO_2$. Os resultados das análises dos granitoides foram trabalhados no Microsoft® Office Excel 2010 e em softwares específicos para reprodução de gráficos (Golden Software-Grapher 8 e GCDkit 3.00).

1.4.6 Geologia Isotópica

Dados isotópicos são muito importantes para caracterização das fontes e idade dos processos antigos associados a origem de granitos. Nesse contexto, se destacam duas frentes principais: a geocronologia, que possibilita principalmente a determinação de idades de cristalização, e a geoquímica isotópica, que é muito importante para a caracterização dos protólitos dos granitóides estudados.

O estudo geocronológico buscou a determinação da idade de cristalização dos granitoides dos plútons/fácies pertencentes ao Complexo Esperança e Batólito Teixeira. Foram analisadas cinco amostras do Complexo Esperança, e quatro amostras do Batólito Teixeira, com uma média de 25 grãos de zircão analisados por amostra. A datação dos grãos de zircão foi realizada no Centro de Pesquisas em Geocronologia e Geoquímica Isotópica do Instituto de Geociências da USP e no Laboratório de Geologia Isotópico da Universidade Estadual de Campinas, utilizando a técnica LA-ICP-MS (Laser Ablation Inductively Coupled Plasma Mass Spectrometry). Os dados da análise de uma amostra (CG-7) do Complexo Esperança foram fornecidos pelo prof. Dr. Carlos José Archanjo. Diferente das demais amostras, esta foi analisada por SHRIMP (Sensitive High-Resolution Ion Microprobe) no Centro de SHRIMP de Pequim (Academia Chinesa de Ciências Geológicas). Detalhes das diferentes técnicas e amostras serão apresentados nos capítulos 3, 4 e 5.

A geoquímica isotópica dos granitoides estudados foi desenvolvida a partir do método Lu-Hf em zircão. Este sistema isotópico tem se tornado uma das ferramentas mais importantes em conjunto com o método U-Pb. A derivação mantélica pode ser definida pontualmente pela idade modelo (T_{DM}), com igual valor interpretativo propiciado originalmente pelo sistema Sm-Nd e a interpretação petrogenética pode ser definida pelo parâmetro εHf para cada zircão analisado, e quando comparado com a curva de evolução de Hf para o reservatório condrítico (CHUR), fornece a assinatura isotópica do possível ambiente de formação (manto ou crosta) do magma. Assim, a combinação do método geocronológico U-Pb associado à assinatura isotópica Lu-Hf permite inferir o magma dos quais os zircões derivaram e cristalizaram, permitindo caracterizar diferentes eventos magmáticos e/ou metamórficos e, a contribuição da crosta e do manto na fonte dos magmas (Gerdes & Zeh, 2006; Gerdes & Zeh, 2009).

As análises isotópicas in situ de Hf nos cristais de zircão estudados foram realizadas por LA-MC-ICP-MS (Laser Ablation Inductively Coupled Plasma Mass Spectrometry) no Laboratório de Geocronologia da Universidade de Ouro Preto. Parte das análises foram realizadas nos mesmos grãos datados, pelo método U-Pb, de modo que possam ser calculados os valores de εHf e T_{DM} no momento de sua cristalização. A configuração do laser seguiu os padrões de Gerdes and Zeh (2006, 2009) e a geometria da ablação é caracterizada com spots variando de 40 a 55 μm. Mais detalhes referentes as condições analíticas, padrões e confiabilidade das análises serão apresentadas no capítulo 3, 4 e 5.

2 CONTEXTO GEOLÓGICO REGIONAL

2.1 PROVÍNCIA BORBOREMA

A Província Borborema (Almeida et al., 1981; Brito Neves, 1983) compreende uma região de aproximadamente 450.000 km^2, situada a norte do Cráton São Francisco, sendo delimitada a leste e norte pelas bacias sedimentares da margem costeira, e a oeste pela Bacia do Parnaíba. Consiste em um sistema orogênico caracterizado por longa e complexa evolução, cujos eventos geológicos iniciaram no arqueano, mas que só no neoproterozoico, com a orogênese Brasiliana/Pan-Africana (Schmus et al., 2008; Schmus et al., 1995; Dantas et al., 1998 entre outros), houve a finalização de seu arcabouço geológico atual.

A Província Borborema, segundo as reconstruções pré-drift de De Wit et al. (1999) (Fig. 6), constitui a porção oeste de um importante cinturão Brasiliano que se estende do Brasil até a parte NW da África, resultante da colisão, a cerca de 600 Ma, dos crátons São Francisco-Congo e São Luís-Oeste Africano (Schmus et al., 2008; Schmus et al., 1995; Van Schmus et al., 2000; Dantas et al., 1998), apresentando-se adjacente a cinturões Pan-africanos e terrenos cratônicos do oeste da África (Jardim de Sá, 1984; Brito Neves & Cordani, 1991; Trompette, 1997; Brito Neves et al., 2002; Neves, 2003).

A Província Borborema compreende três unidades principais: embasamento paleoproterozoico composto por complexos gnáissicos migmatíticos, em grande parte de afinidade TTG (Hackspacher et al., 1990; Van Schmus et al., 1995; Van Schmus et al., 2008; Kozuch, 1997; Neves, 2011; Neves et al., 2006; Santos, 1995; Santos et al., 2015) contendo pequenos núcleos Arqueanos com idades U-Pb (zircão) na faixa de 3,4-3,1 Ga (Brito Neves, 1995; Brito Neves et al., 1995; Van Schmus et al., 1995; Dantas et al., 1998, 2004, 2013); faixas de dobramentos neoproterozoicas (toniana a ediacarana), constituídas de sequências supracrustais deformadas e metamorfizadas que circundam os complexos gnáissicos; e granitoides tonianos (Brito Neves et al., 2000; Santos et al., 2010; Oliveira et al., 2010; Guimarães et al., 2012; Van Schmus et al., 2011; Caxito et al., 2014; Guimarães et al., 2016; Neves et al., 2020) a ediacarano (Hollanda et al., 2003; Guimarães et al., 2009; da Silva Filho et al., 2010; da Silva Filho et al., 2014; Ferreira et al., 2015; Sial e Ferreira, 2016; da Silva Filho et al., 2016, entre vários outros trabalhos), que ocorrem intrudidos nas demais unidades. Extensas zonas de cisalhamento de caráter transcorrente, com direção dominantemente NE-SW e E-W delimitam a província Borborema em unidades menores (subprovíncia, domínios, subdomínios, etc). Algumas zonas de cisalhamento mostram conexão com zonas de

cisalhamento do continente Africano (Caby, 1989; Bertrand & Jardim de Sá, 1990; Trompette, 1994; Van Schmus et al., 2008).

Figura 6 - Reconstrução pré-drit da porção oeste de Gondwana. Legenda: Br/PA, Faixas Brasilianas/Pan-Africanas; PaleoPr, Crosta Paleoproterozoica. Subprovíncias e domínios: SN, Subprovíncia Norte; SC, Subprovíncia Central; SS, Subprovíncia Sul; PEAL, Domínio Pernambuco-Alagoas; DS, Domínio Sergipano; MK, Terreno Mayo Kebi; DCNW, Domínio Cameroon NW; DAY, Domínio Adamawa-Yadé; DY, Domínio Yaoundé; OU, Faixa Oubanguides. Zonas de cisalhamento e Falhas: ZCPa, Zona de cisalhamento Patos; ZCPe, Zona de Pisalhamento Pernambuco; LTB, Lineamento Transbrasiliano; FTB, Falha Tcholliré-Banyo; FA, Falha Adamawa. Cidades: N, Natal; R, Recife; S, Salvador; D, Douala; G, Garoua; K, Kaduna/Nigeria).

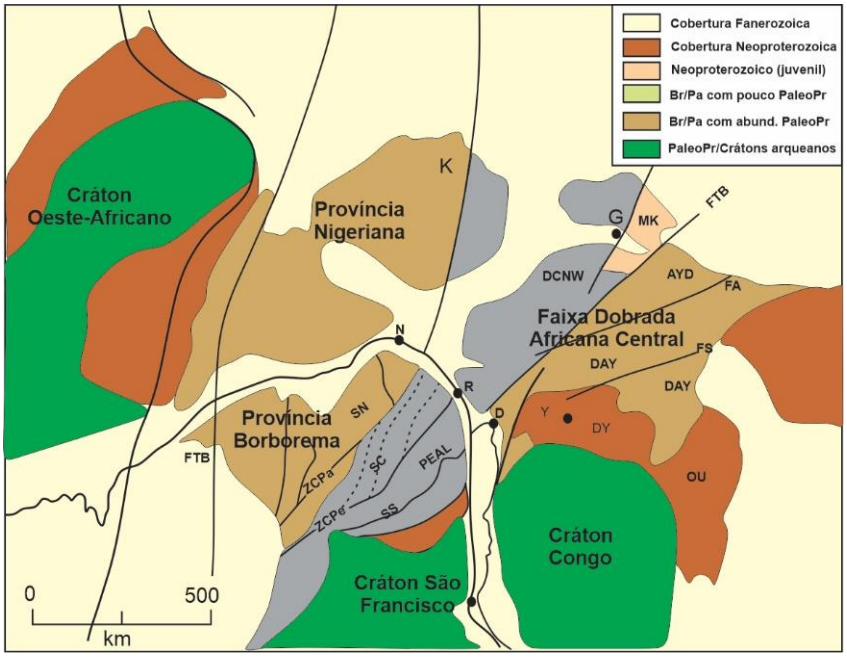

Fonte: Modificado de Van Schmus, at al (2008).

Há vários modelos propostos para a evolução e divisão da província Borborema em domínios tectônicos. Os trabalhos pioneiros (Brito Neves, 1975; Almeida et al. 1976; Brito Neves, 1983) (Fig. 7) reuniam, em grande parte, compilados de dados de campo (litológicos e estruturais), assim como dados de fotointerpretação. Nestes trabalhos, o arcabouço tectônico da Borborema era caracterizado por um conjunto de maciços (complexos gnáissicos migmatíticos Paleoproterozoicos e Arqueanos intrudidos por granitoides 1Brasilianos) e sistemas de dobramentos (supracrustais deformadas e metamorfizadas), originados a partir de processos orogênicos associados ao ciclo Brasiliano há aproximadamente 600 Ma (final do neoproterozoico), o que caracteriza o chamado modelo monocíclico.

Figura 7 - Subdivisão da Província Borborema em Maciços Medianos, Lineamentos e Sistemas de Dobramentos.. Maciços Medianos: (A) Pernambuco-Alagoas; (B) Caldas Brandão-São José do Campestre; (C) Rio Piranhas; (D) Tauá; (E) Santa Quitéria; (F) Granja; (G) Marginal do Cráton São Francisco. Lineamentos: (Lpa) Lineamento Patos; (Lpe) Lineamento Pernambuco. Sistemas de Dobramentos: (a) Sergipano; (b) Pajeú-Paraíba; (c) Riacho do Pontal; (d) Piancó-Alto Brígida; (e) Seridó; (f) Jaguaribeano; (g) Rio Curú-Independência.

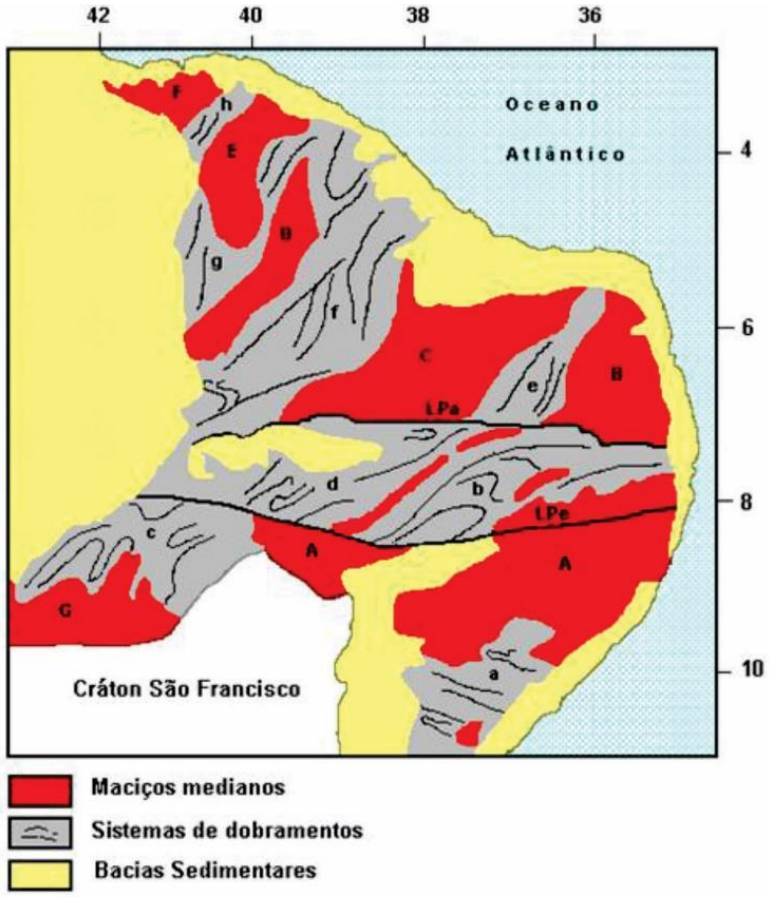

Fonte: Brito Neves (1975)

Posteriormente, Jardim de Sá e Hackspacher (1980), Macedo et al. (1984) e Jardim de Sá (1984) introduziram o modelo policíclico para explicar a origem e evolução da província Borborema. Neste modelo, foi proposto que a deposição e deformação das supracrustais seriam associadas ao Ciclo Transamazônico-Eburniano. Em seguida, no Brasiliano, haveria o retrabalhamento, assim como a formação do magmatismo granítico reconhecido em toda Borborema. A partir de dados de datação por Rb/Sr (método impreciso, porém importante para aquela época) foi definido que as supracrustais foram depositadas ainda no proterozoico e deformada no brasiliano (Santos e Brito Neves, 1984) apesar de ainda não haver, naquele momento, uma idade definida. Nesse contexto, estes autores propuseram a divisão da província Borborema nos seguintes domínios estruturais: Médio Coreaú, Cearense, Transnordestino ou Central, Extremo Nordeste e Sergipano.

Jardim de Sá et al. (1992) e Jardim de Sá (1994) observaram que as heterogeneidades existentes naquela província eram suficientes para sugerir a sua estruturação em terrenos de evolução distinta. Estes terrenos eram separados por zonas de cisalhamentos, e sobrepostos por deformação e magmatismo brasiliano (Fig. 8).

Figura 8 - Esboço geológico/tectônico da Província Borborema. FNC - Faixa Noroeste do Ceará, DCC - Domínio Ceará Central, FOJ - Faixa Orós - Jaguaribe, FSD - Faixa Seridó, FSC - Faixa Salgueiro-Cachoeirinha, FPO - Faixa Riacho do Pontal, FSE - Faixa Sergipana, TPA - Terreno Pernambuco-Alagoas, TCF - Terreno Canindé do São Francisco, TMA - Terreno Marancó.

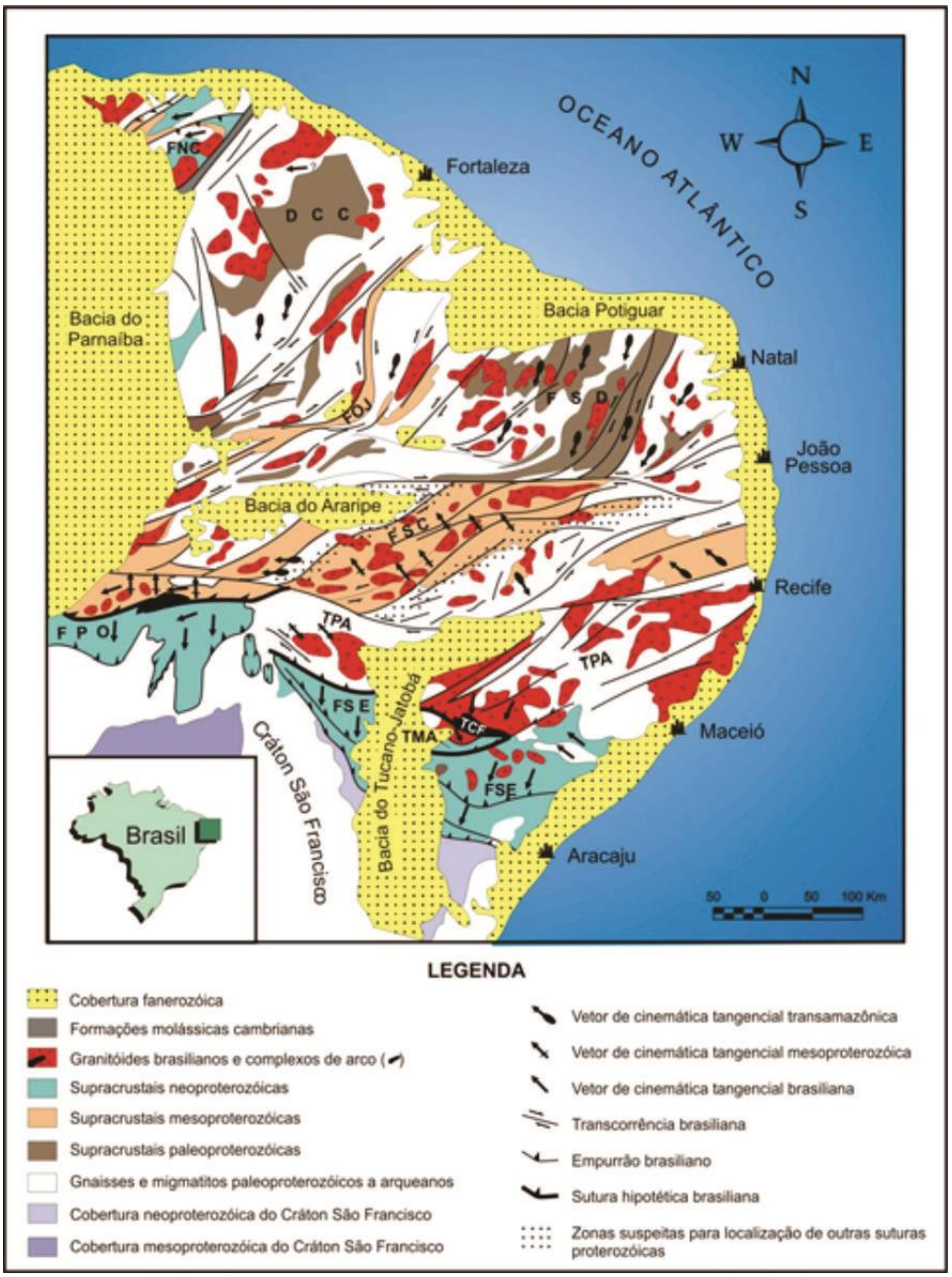

Fonte: Jardim de Sá et al. 1992

Com os avanços propiciados por novas metodologias baseadas na geoquímica isotópica e geocronologia, em especial a partir da análise em zircão, método mais robusto, novos dados a respeito desta província foram obtidos, contribuindo para o detalhamento da evolução dela, assim como a criação de novos esquemas de compartimentação. A partir desses novos dados de geocronologia U/Pb em zircão, foi reconhecido por Santos (1993), um novo evento tectono-metamórfico associado a evolução da província Borborema, chamado de Cariris Velho. Este evento é datado do início do Neoproterozoico (1,0 a 0,92 Ga). Mais tarde, a existência deste evento foi corroborada por outros trabalhos (Brito Neves et al., 1995; Van Schmus et al., 1997), nos quais eles associam a colagem dos terrenos alóctones a sul da Zona de Cisalhamento Patos ao Ciclo Cariris Velho. Este evento teria gerado um superterreno de margem continental desenvolvido ao longo da margem noroeste do Cráton São Francisco/Congo Kasai.

Contemporaneamente, os dados obtidos a partir dessas novas metodologias confirmam a existência de um importante evento orogênico do Paleoproterozoico inferior a médio, designado de ciclo Transamazônico. Este evento foi inicialmente documentado a partir da presença de material com assinatura de crosta oceânica a sul da Zona de Cisalhamento Patos, onde rochas máficas apresentam idade de cristalização de 2,1 Ga e idade modelo entre 2,1 e 2,5 Ga. Posteriormente, a orogênese Transamazônica, um dos importantes ciclos na formação da crosta continental da Plataforma Sul-Americana, foi reconhecida amplamente em toda a Província Borborema.

Santos (1995, 1996) associa a evolução da Borborema a um ciclo acrescionário com eventos de acreção, colisão e dispersão de terrenos, e propôs a existência de 12 terrenos tectonoestratigráficos, além de microterrenos e fragmentos antigos. Posteriormente, tudo isso foi agrupado em cinco domínios maiores (Médio Coreaú, Cearense, Rio Grande do Norte, Zona Transversal e Externo) (Santos, 1998). Neste modelo, a Zona de Cisalhamento Patos corresponde ao limite isotópico da Borborema, onde o segmento norte seria constituído por grande contribuição de embasamento arqueano e paleoproterozoico, enquanto no segmento sul predominavam terrenos meso e neoproterozoicos.

Subsequentemente, o modelo de terrenos foi aprimorado por novos dados geocronológicos e geofísicos (Oliveira & Santos,1993; Oliveira & Medeiros, 2000, Santos & Medeiros, 1999; Oliveira e Medeiros, 2018), e a partir disto, a província Borborema foi dividida nos domínios Medio Coreaú, Cearense, Rio Grande do Norte, Zona Transversal e Meridional (Fig. 9).

Figura 9 - Mapa geológico/tectônico da Província Borborema.

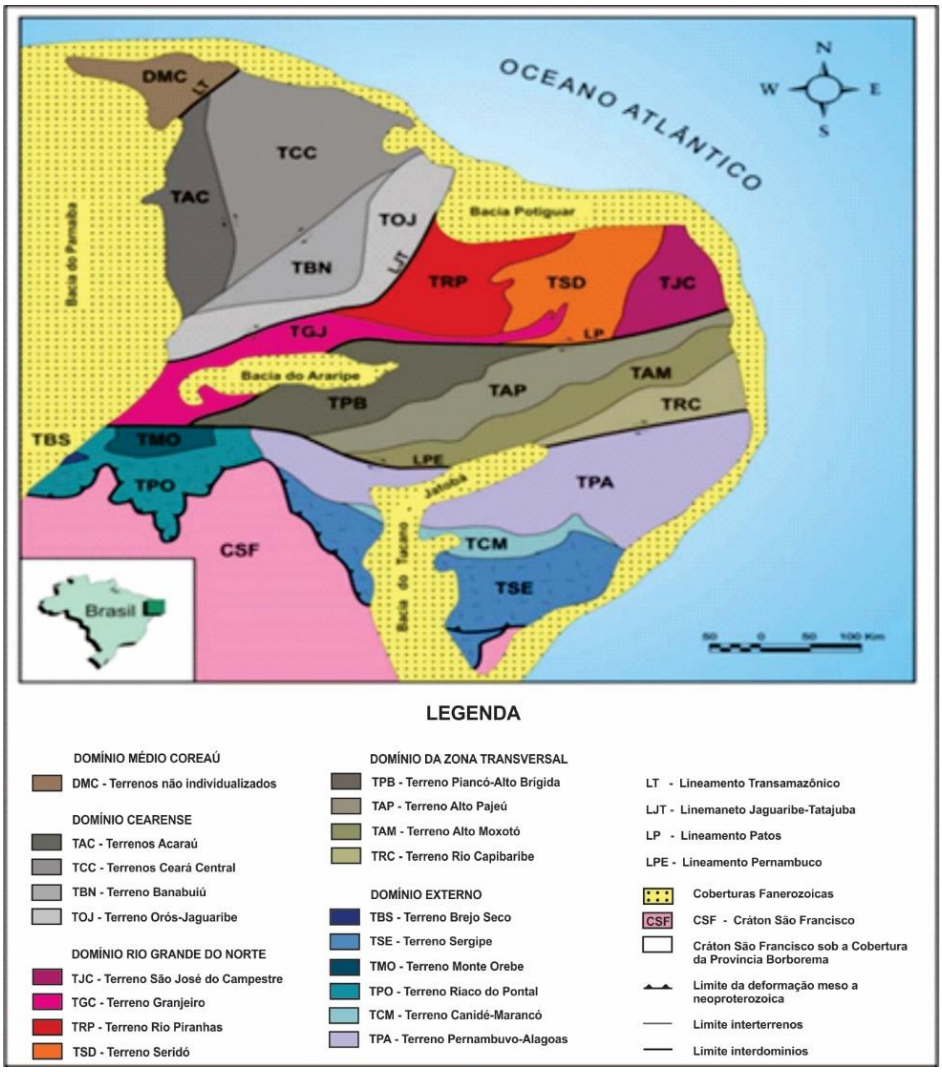

Fonte: Santos & Medeiros (1999).

O modelo de terrenos tectonoestratigráficos é contestado por outro grupo de pesquisadores que defendem uma evolução intracontinental para a Província Borborema (Neves & Mariano, 2001; Neves, 2003; Neves et al., 2006; Neves, et al., 2015). Enquanto o primeiro modelo defende que Província Borborema estaria segmentada em terrenos tectonoestratigráficos distintos, limitados pelas zonas de cisalhamento e amalgamados pela Orogênese Brasiliana, o segundo propõe que a Província Borborema faz parte de um único bloco crustal, antes da separação do Supercontinente Pangea, consolidado desde 2,0 Ga, neste modelo as zonas de cisalhamento são interpretadas como feições orogênicas tardias.

O modelo de orogênese intracontinental é baseada em várias evidências. Uma das maiores é a ausência de zonas de sutura associadas à orogênese Brasiliana no interior da Província Borborema. Vale salientar que Retroeclogitos Criogeniano/Ediacarano foram

identificados localmente em Bodocó no extremo oeste de Pernambuco (Beurlen et al., 1992), interpretadas por (Neves et al. 2000) como associados ao fechamento de pequenas bacias. Trabalhos recentes têm mostrados que alguns dos limites de terrenos proposto por Santos (1995), caracterizados por zonas de cisalhamento, não correspondem a zonas de sutura, como o caso da zona de cisalhamento Pernambuco, sugerindo que a Borborema seria constituída por uma larga massa continental durante o final do Neoproterozoico. Além disso, há bastante similaridade química e isotópica associada ao manto litosférico sob grande parte da província, inclusive em regiões correspondentes aos diferentes terrenos (Neves & Mariano, 1997; 2000; Mariano et al., 2001).

A assinatura química de elementos traços em rochas de diferentes graus de diferenciação (teores elevados de elementos incompatíveis), juntamente com a assinatura isotópica caracterizada por valores de épsilon Nd fortemente negativos sugerem ausência de material juvenil durante o Ediacarano. O mais provável é a derivação a partir de um manto litosférico enriquecido durante a orogênese Riaciana, assim como apontado por diversos trabalhos (Guimarães e Silva Filho, 1998; Guimarães e Silva Filho, 1992; Silva Filho e Guimarães, 1991; Almeida et al., 2002; Mariano et al., 2001; Neves et al., 2006; Neves e Mariano, 2004). Motivo de grande debate, o evento Cariris Velhos é largamente associado a rochas metavulcânicas e ortognáisses com assinatura geoquímica de magmas originados em contexto tectônico intraplaca (Guimarães et al., 2012; Guimarães et al., 2016). Metagranitoides de idade Toniana com assinatura química de granito tipo-A também foram evidenciados no Cinturão Sergipano, no domínio Pernambuco-Alagoas e na faixa Riacho do Pontal (Carvalho, 2005; Brito Neves et al., 2008; Cruz and Accioly, 2013; Caxito et al., 2014). Estes dados geoquímicos e geocronológicos sugerem que o evento Cariris Velho corresponde a um evento essencialmente extensional. Isto também pode ser corroborado pela presença de zircões herdados da crosta Cariris Velhos no Grupo Seridó (Van Schmus et al., 2003), sugerindo ausência de um grande oceano entre os domínios Norte e Central da Província Borborema (Neves, 2015).

Van Schmus et al. (1995, 2011), Brito Neves et al., (2000) e Neves, (2003) dividiram a Província Borborema em três subprovíncias, inicialmente denominadas dominios (Fig. 10): subprovínica Norte, que compreende a região a norte da zona de cisalhamento Patos e engloba os domínios Rio Grande do Norte, Ceará e Médio Coreaú; Subprovíncia Transversal ou Central, localizada entre as zonas de cisalhamento Patos e Pernambuco, e constituída pelos domínios Rio Capibaribe, Alto Moxotó, Alto Pajeú e Piancó-Alto Brígida; e subprovíncia Sul, que consiste na região a sul da zona de cisalhamento Pernambuco e inclui os domínios Pernambuco

– Alagoas, Sergipano e Riacho do Pontal. Trabalhos mais recentes têm mostrado continuidade entre o PEAL e a Subprovíncia Central (Neves et al., 2011; Silva Filho et al. 2013).

Figura 10 – Principais domínios e zonas de cisalhamento da Província Borborema. Subprovíncia Norte (CE: Domínio Ceará Central; MC: Domínios Médio Coreaú; RGN: Domínio Rio Grande do Norte); Subprovíncia Sul (PEAL: Domínio Pernambuco-Alagoas; RP: Domínio Riacho do Pontal; SE: Domínio Sergipano); Subprovíncia Central (AM: Domínio Alto Moxoto; AP: Domínio Alto Pajeú; PAB: Domínio Piancó-Alto Brígida; RC: Domínio Rio Capibaribe); ZCPa: Z.C. Patos; ZCPW e ZCPE: Z.C. Pernambuco Oeste e Leste, respectivamente; ZCS: Sobral; ZCSP: Zona de Cisalhamento Senador Pompeu; ZCJ: Zona de Cisalhamento Jaguarib; ZCJC: Zona de Cisalhamento João Câmara; ZCPA: Zona de Cisalhamento Portoalegre; ZCRS: Zona de Cisalhamento Riachão; TSZ: Zona de Cisalhamento Tauá; ZCAI: Zona de Cisalhamento Afogados da Ingazeira; ZCSC: Zona de Cisalhamento Serra do Caboclo; ZCC: Zona de Cisalhamento Congo; C: Cobertura Fanerozoica.

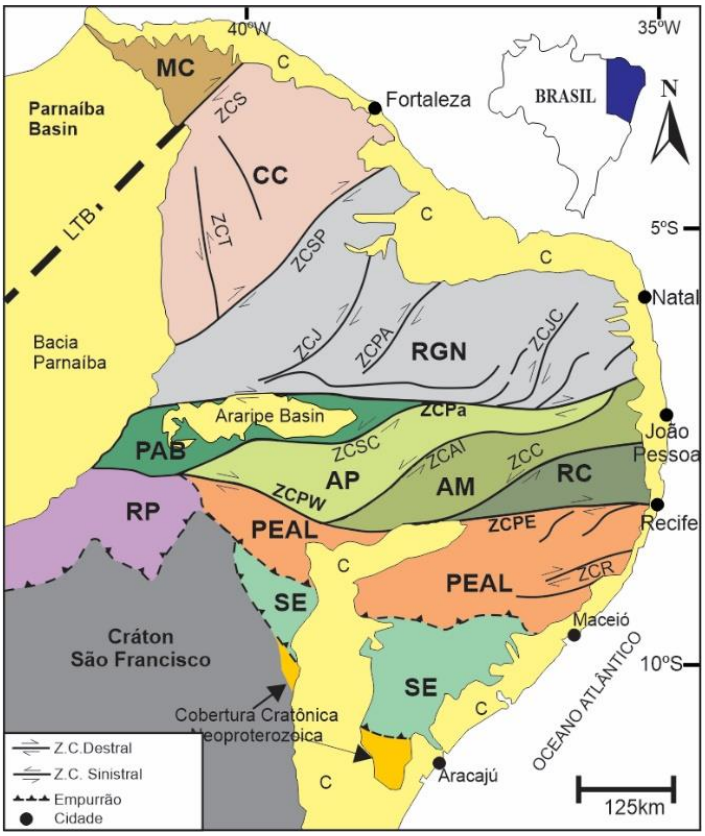

Fonte: Modificado de Van Schmus et al. (2011)

2.1.1 Subprovíncia Central

Esta subprovíncia compreende um segmento crustal situado entre as Zonas de Cisalhamentos Patos e Pernambuco, e é caracterizada por um embasamento gnáissico migmatítico de idade Paleoproterozoica e pequenos núcleos Arqueanos, além de supracrustais Neoproterozoicas e granitoides de idades Toniana e Ediacarana. A subprovincia Central foi dividida (Van Schmus et al. 2011), de oeste para leste (Fig. 11), em Domínio Piancó Alto Brígida, Domínio Alto Pajeú, composta por rochas supracrustais e ortognaisses, Domínio Alto Moxotó, onde predomina o embasamento Riaciano com pequenos núcleos arqueanos,

fortemente retrabalhado no Ediacarano e poucos plutões brasilianos, e Domínio Rio Capibaribe, constituído de seqüências supracrustais Ediacarana/Criogeniana e plutons dominantemente Ediacaranos.

Figura 11 – Mapa geológico simplificado da Subprovíncia Central com plutons Ediacaranos destacados em vermelho. Legenda: AM: Domínio Alto Moxoto; AP: Domínio Alto Pajeú; PAB: Domínio Piancó-Alto Brígida; RC: Domínio Rio Capibaribe); ZCPa: Z.C. Patos; ZCPW e ZCPE: Z.C. Pernambuco Oeste e Leste, respectivamente; ZCAI: Zona de Cisalhamento Afogados da Ingazeira; ZCSC: Zona de Cisalhamento Serra do Caboclo; ZCCo: Zona de Cisalhamento Coxixola; ZCC: Zona de Cisalhamento Congo; C: Cobertura Fanerozoica.

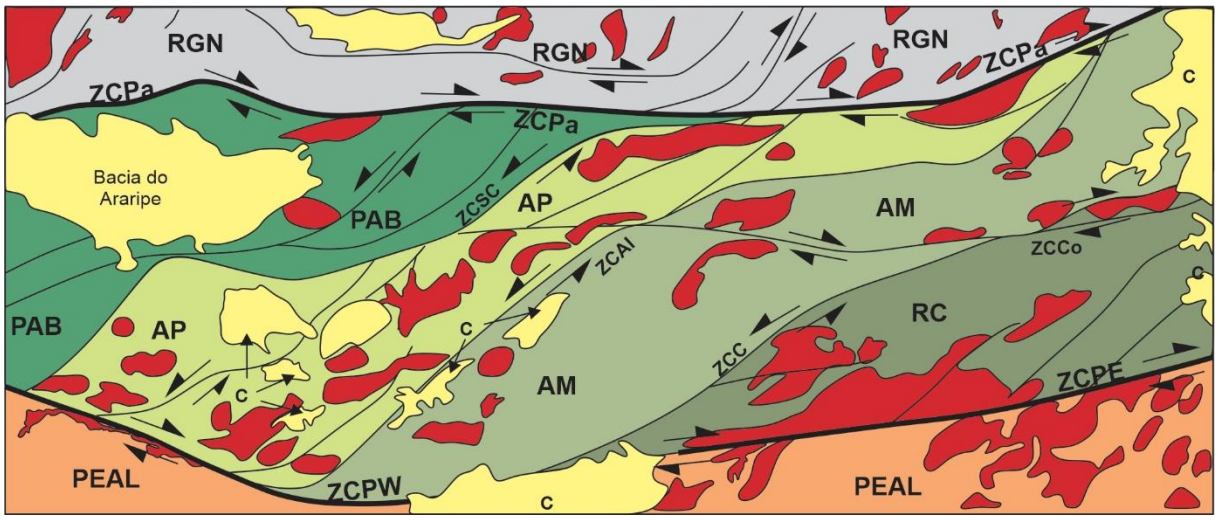

Fonte: Modificado de Guimarães et al. (2016)

Esta subprovíncia é caracterizado por um trend estrutural ENE-WSW a EW, devido ao movimento destral entre estas duas zonas de cisalhamento (Patos e Pernambuco). Este contexto estrutural foi descrito por Jardim de Sá (1994) como uma megaestrutura em dominó (Fig. 4B e C), sendo caracterizada por um sistema de zonas de cisalhamento transcorrentes dextrais, com direção EW a ENE-WSW, e sinistrais, com direção NNE-SSW a NE-SW. Estas zonas de cisalhamento representam limites de um mosaico de faixas ou terrenos tectono-estratigráficos e retrabalham uma foliação de baixo ângulo presente em ortognaisses e rochas supracrustais, sendo espacialmente associadas com plutons graníticos e sieníticos. (Vauchez e Egydio-Silva, 1992; Guimarães & Da Silva Filho, 1998; Ferreira et al., 1998; Neves & Mariano, 1999; Neves et al., 2000; Silva & Mariano, 2000).

2.1.2 Magmatismo granítico na província Borborema e na Subprovíncia Central

Rochas graníticas constituem importantes feições da orogênese Brasiliana na Província Borborema. Estas se apresentam através de inúmeras intrusões de dimensão e forma variadas, em grande parte associadas a zonas de cisalhamento. As determinações químico-isotópicas, em especial a idade destes plutons ediacaranos, são fundamentais para o

entendimento da duração da deformação brasiliana, e assim a evolução da Província Borborema, que por sua vez é essencial para o completo entendimento da ancestralidade e da amalgamação da parte norte de Gondwana Ocidental.

Há inúmeros trabalhos que visam a caracterização e tipologia dos granitoides da Província Borborema. Os trabalhos pioneiros (Almeida et al., 1967; Brito Neves & Pessoa, 1974; Santos & Melo, 1978) usaram dados petrográficos e estruturais, e posicionavam estas rochas com relação a orogênese Brasiliana. O esquema proposto por Almeida at al. (1967) dividiu os granitoides em 04 tipos: granitos sin-tectônicos, que compreendem o tipo Conceição – granodioritos e tonalitos de granulação média a fina, 2) tipo Itaporanga – granodioritos porfiríticos com megacristais de K-feldspatos; 3) granitoides tardi-tectônicos que contém os tipos Itapetim - biotita granitos finos associados com o tipo Itaporanga, e 4) Catingueira – granitos peralcalinos, sienitos e quartzo sienitos.

A partir de dados estruturais e relação inclusão-intrusão, Jardim de Sá et al. (1981) analisaram os granitoides brasilianos e pré-brasilianos na Faixa Seridó, e assim criaram as categorias G1, G2 e G3. Esta classificação foi aprimorada com dados geoquímicos no trabalho de Jardim de Sá (1994), onde foram caracterizadas diferentes suítes (suíte porfirítica subalcalina, granitoides alcalinos, associação diorítica, granitoides shoshoníticos, suíte leucogranítica e suíte cálcio-alcalina).

Sial (1986) estudou geoquimicamente os granitoides pertencentes à Faixa Cachoeirinha (Piancó Alto Brígida) na Subprovíncia Central e os correlacionou aos quatro tipos propostos por Almeida et al. (1967): 1) cálcio-alcalinos (Tipo Conceição); 2) cálcio-alcalinos potássicos (Tipo Itaporanga); 3) peralcalinos (Tipo Catingueira); e 4) trondhjemítico (Tipo Serrita). Posteriormente, Ferreira et al. (1998) estudaram os granitos e sienitos da porção ocidental da Subprovíncia Central, e a partir dos dados geoquímicos, isotópicos e de susceptibilidade magnética, os associaram a oito tipos principais: cálcio-alcalino com epídoto magmático (Conceição); cálcio alcalino de alto potássio sem epídoto magmático (Itaporanga); cálcio-alcalino de alto potássio com epídoto (São Rafael); cálcio-alcalinos peraluminosos (Ouro Branco); trondhjemitos (Serrita); peralcalinos (Catingueira) e shoshoníticos; sienitoides metaluminosos de alto potássio (Terra Nova); e sienitoides peralcalinos ultrapotássicos (Triunfo/Baixa Verde).

Guimarães et al. (1998), enquadraram os granitos do subprovíncia Central em cinco tipos principais a partir de dados químicos, isotópicos, e U-Pb em zircão: cálcio-alcalinos

normais; cálcio-alcalinos de alto potássio (com afinidades shoshoníticas); sienogranitos, quartzo sienitos e sienitos com afinidades shoshoníticas; biotita granitos (transicionais entre alcalinos e shoshoníticos); biotita sienogranitos leucocráticos; biotita sienogranitos co-magmáticos com basalto e dacitos (idades mais jovens). Estes granitoides foram reagrupados por Guimarães et al. (2004) em quatro tipos, levando em consideração a relação entre idade, quimismo e contexto tectônico atuante: 1) Granitos cálcio-alcalinos com idade de cristalização de 644 a 610 Ma, modificado posteriormente por Guimarães et al. (2011), para ~620 Ma; 2) Granitos cálcio-alcalinos de alto-K e shoshonítico com idade U-Pb, em zircão, variando de 590 a 581 Ma, associados a transição entre evento de baixo ângulo e evento de transcorrência; 3) Granitos alcalinos pós-colisionais com idade U-Pb de cerca de 570 Ma; e 4) Granitóides tipo-A pós-orogênicos associados a magmatismo bimodal subvulcânico com idade entre 540 e 512 Ma.

Van Schmus et al. (2011) relacionou os granitoides brasilianos com as fases de deformação, utilizando principalmente dados químicos e isotópicos, assim foram criados cinco estágios de magmatismo: I – entre 650 e 610 Ma, onde crosta oceânica teria sido subduzida sob litosfera crustal Paleoproterozoica, com significante material juvenil contribuiu para a origem do magma; II –caracterizado pela diminuição na colocação de plutons, cujo período corresponde, no geral, com o pico de metamorfismo termal, deformação contracional, e migmatização e precede a transição para a deformação transcorrente; III –corresponde aos plutons do grupo 2 de Guimarães et al. (2004) (590 – 580 Ma), que foram gerados durante a transição de deformação dominantemente contracional a transcorrente, e apresentam caracteristicamente idades modelo TDM (Sm-Nd) variando de 1,7 a 2,1 Ga, sendo derivados, em grande parte, da fusão de litosfera paleoproteozoica; IV – predomínio de plutons pós-tectônicos de cerca de 570 Ma (grupo 3 de Guimarães et al., 2004), intrudidos durante a transição deformação compressional/deformação transcorrente. Geoquimicamente, apresentam restrita variação de sílica, são aluminosos e caracterizados por anomalias de Eu, Sr e P. Além disso, tendem a se projetar no campo intraplaca no diagrama de Pearce. Apresentam assinatura química e isotópica indicativa de origem a partir do manto subcontinental superior ou da crosta inferior; V) Os granitóides que representam este estágio, apresentam idades entre 533 e 548 Ma, e são geoquimicamente similares ao grupo IV, com maior conteúdo de FeO/Feo+MgO e classificados como granitos tipo-A (Guimarães et al., 2004).

3 ARTIGO 1 - MINERAL CHEMISTRY CONSTRAINS ON CRYSTALLIZATION CONDITIONS AND PETROLOGICAL EVOLUTION OF THE TEIXEIRA BATHOLITH GRANITOIDS, BORBOREMA PROVINCE, NE BRAZIL

Jefferson Valdemiro de Lima [a, *], Ignez de Pinho Guimarães [a], Sérgio Pacheco Neves [a, b], Iris Dias Santos [c], Caio Cezar Garnier Brainer [a], Elton Luiz Dantas [d]

[a] Geosciences Post-graduation Program, Technologic and Geosciences Center, Pernambuco Federal University, Rua Acadêmico Hélio Ramos, s/n, 50740-530, Recife, Brazil. E-mails: *jefferson1901@hotmail.com; ignez@ufpe.br; caio.cgbrainer@ufpe.br

[b] CNPq (Brazilian Research Council) Researcher; Department of Geology, Technologic and Geosciences Center, Pernambuco Federal University, Rua Acadêmico Hélio Ramos, s/n, 50740-530, Recife, Brazil. E-mail: sergio.neves@ufpe.br

[c] Institute of Geoscience, University of Brasilia, ICC Central, Subsolo A, Sala ASS-360/13, 70910-900, Brasília-DF, Brazil. E-mail: irisdiassantos@gmail.com

[d] CNPq (Brazilian Research Council) Researcher; Institute of Geoscience, University of Brasilia, Geochronology Laboratory, 70910-900, Brasília-DF, Brazil. E-mail: elton@unb.br

* Corresponding Author

Abstract

The Ediacaran Teixeira Batholith comprises an EW - elongated intrusion of c. 800 km^2, emplaced in supracrustal rocks and orthogneisses immediately south of the central portion of the Patos Shear Zone, at the limit between the North and Central Subprovinces of the Borborema Province. It is composed of syenogranite, monzogranite and quartz syenite, whose petrographic and textural aspects allow subdivide the batholith into six facies. From petrographic data, mineral chemistry, and zircon trace element composition (LA-Q-ICPMS), the physical crystallization parameters (T, P and fO_2) were obtained, as well as important information for granitoids petrogenesis. The mafic mineral assemblage in these granitoids is

dominated by amphibole, with Fe/(Fe+Mg) ratio ranging from 0.57 to 0.72 (hastingsite, ferro-ferri-hornblende and ferro-pargasite), in addition to clinopyroxene, mainly of hedenbergite composition and biotite that shows Fe/(Fe+Mg) ratio ranging from 0.4 to 0.7 and are classified as siderophyllite and eastonite. Titanite, epidote, zircon, magnetite, and pyrite are the main accessory phases, and occur with petrographic and chemical features typical of primary origin, constituting a mineral association like that observed in magnetite-series granites. The paragenesis and chemical signature of the studied minerals suggest that the Teixeira Batholith is constituted by oxidized I-type granites. In particular, the Hf contents (9810 to 11143 ppm) of the studied zircon crystals, together with the biotite composition and the presence of magmatic epidote, suggest that these granitoids were generated from a magma with high-potassium affinity and crystallized at a temperature ranging from 995 to 701 °C and pressure ranging between 4.7 and 3.7 kbar; conditions corresponding to intermediate crustal levels.

Keywords: I-type granites; Borborema Province; Mineral chemistry; Geothermobarometry; Zircon REE patterns

1. Introduction

The Borborema Province (Fig. 1A) comprises most of the northeastern region of Brazil. According to pre-drift reconstructions it lies adjacent to the Pan-African belts and cratonic terrain of West Africa (Jardim de Sá, 1984; Brito Neves and Cordani, 1991; Trompette, 1997; Van Schmus et al., 2008, among others). Its actual framework resulted from the Brasiliano/Pan-African Orogeny (640-550 Ma), which involved the collision of the São Francisco-Congo and São Luís-West African cratons (Van Schmus et al., 2008; Van Schmus et al., 1995 and references therein).

Numerous late-Neoproterozoic granitic intrusions (ca. 650-550 Ma) are documented in the Borborema Province – NE-Brazil, providing an important marker for the evolution of the Brasiliano Orogeny (Van Schmus et al., 2008 and references therein). In addition to the granitic magmatism, the Brasiliano Orogeny was responsible for low- to medium-pressure and varied temperature metamorphism, and the development of continental-scale shear zones (Bittar, 1998; Leite et al., 2000; Vauchez et al., 1995; Guimarães et al., 2004; Neves et al., 2006; Neves, 2015; Archanjo et al., 2008, 2021; Van Schmus et al., 1995; Viegas et al., 2014; Caxito et al., 2020 and references therein).

Figure 1 – Geological maps illustrating regional context. A) Major domains and shear zones of the Borborema Province (modified from Van Schmus et al., 2011). Legend: Northern Subprovince (MC: Médio Coreaú Domain; CC: Ceará Central Domain; RGN: Rio Grande do Norte Domain); Southern Subprovince (RP: Riacho do Pontal Domain; SD: Sergipano Domain; PEAL: Pernambuco-Alagoas Domain); PaSZ: Patos Shear Zone; WPSZ and EPSZ: West and East Pernambuco Shear Zones; SSZ: Sobral Shear Zone; SPSZ: Senador Pompeu Shear Zone; JSZ: Jaguaribe Shear Zone; JCSZ: João Câmara Shear Zone; PASZ: Portoalegre Shear Zone; RSZ: Riachão Shear Zone; TSZ: Tauá Shear Zone; C: Phanerozoic cover; B) Transversal Subprovince of the Borborema Province with Ediacaran plutons highlighted in red (modified from Guimarães et al., 2016). Legend: RC: Rio Capibaribe Domain; AM: Alto Moxotó Domain; AP: Alto Pajeú Domain; PABD: Piancó-Alto Brigida Domain; TB: Teixeira Batholith; CoSZ: Coxixola Shear Zone; CSZ: Congo Shear Zone; AISZ: Afogados da Ingazeira Shear Zone; SCSZ: Serra do Caboclo Shear Zone.

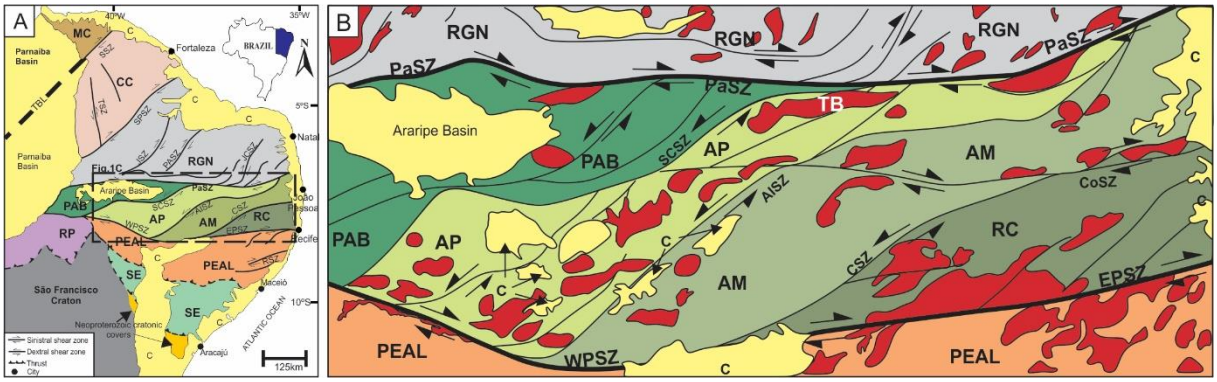

Granites are the most abundant rock type of the upper continental crust (Wedepohl, 1991), and despite presenting a simple felsic mineralogy (quartz + alkali feldspar + plagioclase), they are linked to the varied modal/chemical composition, genesis, and mode of occurrence (Bonin et al., 2020). Mineral chemistry is an important tool to estimate the crystallization pressure and temperature of granitic magmas (Hammarstrom and Zen, 1986; Hollister et al.,

1987; Wones, 1989; Blundy and Holland, 1990; Schmidt, 1992; Anderson and Smith, 1995; among) and for assessing the geochemical affinities of the granitoids (A-, I- or S-type signature), fundamental for understanding of sources. Biotite, amphibole, and pyroxene are common ferromagnesian minerals in granitoids, and their varied composition and textural aspects are strongly controlled by the chemistry and redox conditions of the magma from which they originated (Chappell and White, 1974; Nachit et al.,1985; Abdel-Rahman, 1994; Stussi and Cuney, 1996; Putirka 2016, among others). The chemical characterization of accessory minerals also contributes to the understanding of the petrogenetic evolution of granitic magmas. For example, Enami et al. (1993) used the titanite composition as a function for estimating pressure and temperature; Fe-Ti oxides also have compositions dependent of the redox conditions and magma nature, and can be used to frame granitic rocks in the classification of Ishihara (1977); epidote represents another important accessory phase, used to estimate the emplacement pressure, fO_2 and ascension rate of epidote-bearing magmas (Zen and Hammarstrom, 1984; Schmidt and Thompson 1996, Ferreira et al., 2003, Schmidt and Poli, 2004; Sial et al., 1999, 2008; Brasilino et al., 2011; Silva et al., 2020; Lima et al., 2021a); and zircon is an important isotopic tracer (U-Pb/Lu-Hf), and it has been used to infer physicochemical conditions of magma, and the components involved in the source (Pupin, 2000, Bruguier et al., 2020).

In this work, we present the mineralogy and mineral chemistry of the rock-forming (amphibole, biotite, pyroxene, feldspars) and accessory (titanite, epidote, Fe-Ti oxides, sulfides, and zircon) mineral phases for all facies of the Teixeira Batholith, located south of the Patos Shear Zone in the NW portion of the Central Subprovince - Borborema Province (Figs. 1A and B). The data are used to define the pressure, temperature and fO_2 during the magmatic evolution of the Teixeira Batholith, and in addition we highlight the relationships between the

composition of the minerals and the chemical signature of the magma, to contribute to the understanding of their petrogenesis.

2. Geological context

2.1. Field and microtextural aspects

The Teixeira Batholith is located in the northwestern portion of the Central subprovince of the Borborema Province (Fig. 1B). It comprises an ENE-trending large igneous body, ~ 800 km^2, composed of six facies, cropping out immediately south of the central part of the continental scale Patos Shear Zone (Fig. 2). It intrudes Neoproterozoic metasedimentary units to the south and southeast, and Tonian coarse grained, porphyroclastic metagranitoids of syenogranitic composition, to the southwest. The Teixeira Batholith is crosscut by three NE-SW trending sinistral shear zones (Taperoá, Itapetim and Tendó), which limited the different facies, and by several sets of fractures of NE-SW to NW-SE trending. Locally, the granitoids are crosscut by ENE-WSW sinistral shear bands, quartz veins and pegmatite dikes. Internally, the granitic rocks preserve magmatic features, but at the edges of the intrusion, the occurrence of sheared granitoids is compatible with the structural context associated to presence of the shear zones. This evidence corroborates the pre-transcurrent context defined by magnetic fabric reported by Archanjo et al. (2008).

The Teixeira Batholith is a ~600 to 585 Ma intrusion (Archanjo et al., 2008; Lima et al., 2021b) composed of syenogranites, monzogranites and syenites, divided into six main facies (Pedra D'Água, São Sebastião, Tendó, Jabre, Mãe D'Água and Santo Antônio) according to petrographic and textural aspects. The Pedra D'Água Facies occupies the easternmost portion of the Teixeira Batholith, between the Itapetim and Taperoá shear zones. It occurs mainly as ENE-trending subvertical sheets (Fig. 3A) constituted by equigranular, medium grained biotite-amphibole monzogranite to syenogranite, displaying ENE-WSW stretched biotite and quartz crystals, and locally, intercalated with the country rocks (Fig. 3B). There is a predominance of

features suggestive of dextral kinematics, although close to sinistral shear zones, sinistral criteria are also observed. They present typical fabric of sub magmatic to solid-state deformation with quartz crystals showing strong undulose extinction, subgrain rotation recrystallization (Fig. 3C) and discrete ribbons, and feldspars crystals with micro-kinks and deformation bands.

Figure 2 - Simplified geological map of Teixeira Batholith. Based on Ferreira & Santos (2000) and Archanjo et al. (2008).

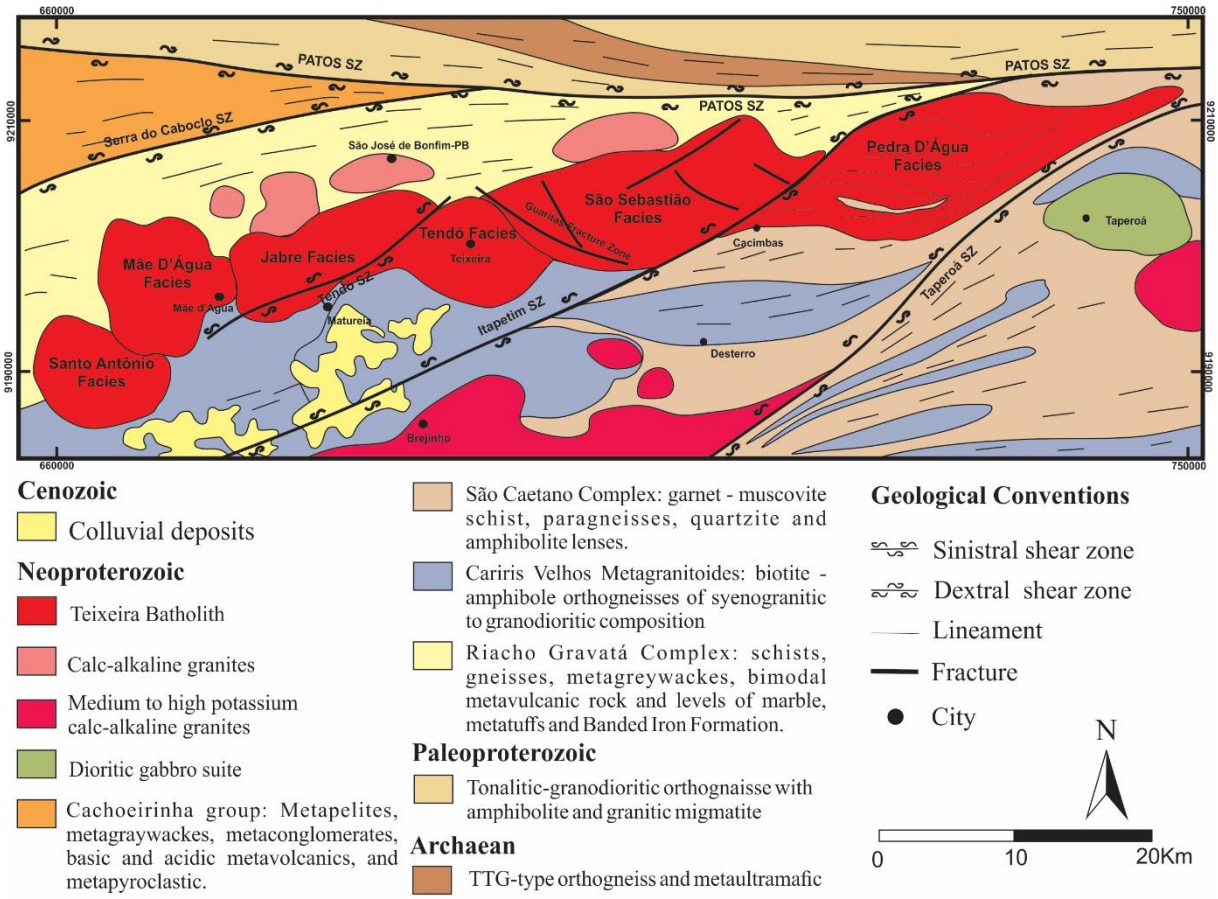

The other Teixeira Batholith facies are dominated by granites showing less intense solid-state deformation, except at the intrusion edges, where they are intensely affected by the shear zones. The São Sebastião Facies makes contact to the east, with the Pedra D'Água Facies and it is intruded between the Itapetim Shear Zone and the NW-trending fracture system (Guaritas Fracture Zone). It is characterized by medium-grained, equigranular to slightly porphyritic amphibole-pyroxene syenogranite to quartz syenite (Fig. 3D). The Tendó Facies outcrops in the central region of Teixeira Batholith. It is constituted by mesocratic, equigranular, medium-grained biotite-amphibole monzogranites, with several enclaves (Fig. 3E) composed of fine-grained amphibole diorite to monzonite and rounded to elongated shapes. The Jabre Facies crops out east of the Tendó Facies comprising equigranular, leucocratic, medium to fine grained amphibole monzogranite to syenogranite, enclosing rare mafic enclaves, and locally with preserved flow texture (Fig. 3F). The Mãe D'Água Facies occurs in the western region of the Teixeira Batholith and consists of mesocratic, porphyritic, coarse-grained biotite-amphibole monzogranites. Magmatic foliation defined by feldspar and mafic minerals orientation is crosscut by foliation related to solid-state deformation, showing S-C fabrics, indicating sinistral kinematics, and locally concentric structures are present (Fig. 3G). The Santo Antônio Facies comprises the westernmost portion of the Teixeira Batholith and consists of leucocratic, medium to coarse grained, equigranular to slightly porphyritic, amphibole-biotite monzogranite (Fig. 3H). They show discreet magmatic banding and enclose microgranular mafic enclaves and amphibolitic xenoliths (Fig. 3I).

The microtextural analyses of the São Sebastião, Tendó, Jabre, Mãe D'Água and Santo Antônio facies shows a predominance of typically magmatic fabric. Quartz occurs as well-developed anhedral crystals and/or as interstitial subgrain aggregates with grain boundary migration and locally, chessboard extinction (Fig. 3J), which are features commonly associated with deformation at magmatic to sub-magmatic conditions (Passchier and Trouw, 2005).

Plagioclase occurs as anhedral to subhedral zoned crystals (Fig. 3K), and often exhibits subgrain rotation, submagmatic fractures (Fig. 3L) and deformed lamellae. K-feldspar, perthitic orthoclase and microcline show rims replaced by myrmekite, possibly resulting from the percolation of hot fluids associated with high-T deformation.

Figure 3 – Field and microstructural aspects of granitoids from the Teixeira Batholith. A) Granitic sheets of the Pedra D'Água Facies; B) Schist lenses with C-S fabric indicating dextral kinematics; C) Photomicrograph showing subgrain rotation recrystallization in quartz crystals; D) Equigranular syenogranite with well-developed pyroxene crystals; E) Granitic rock from Tendó Facies with partially hybridized enclave; F) Flow texture in leucocratic granitic rock; G) Concentric structures in the Mãe D'Água monzogranite; H) White leucocratic granite from Santo Antônio Facies; I) Amphibolitic xenolith in the Santo Antonio Facies; J) Chessboard extinction pattern in quartz; K) Igneous zoning in plagioclase phenocryst (pl); L) Plagioclase crystal (Pl) with submagmatic fracture.

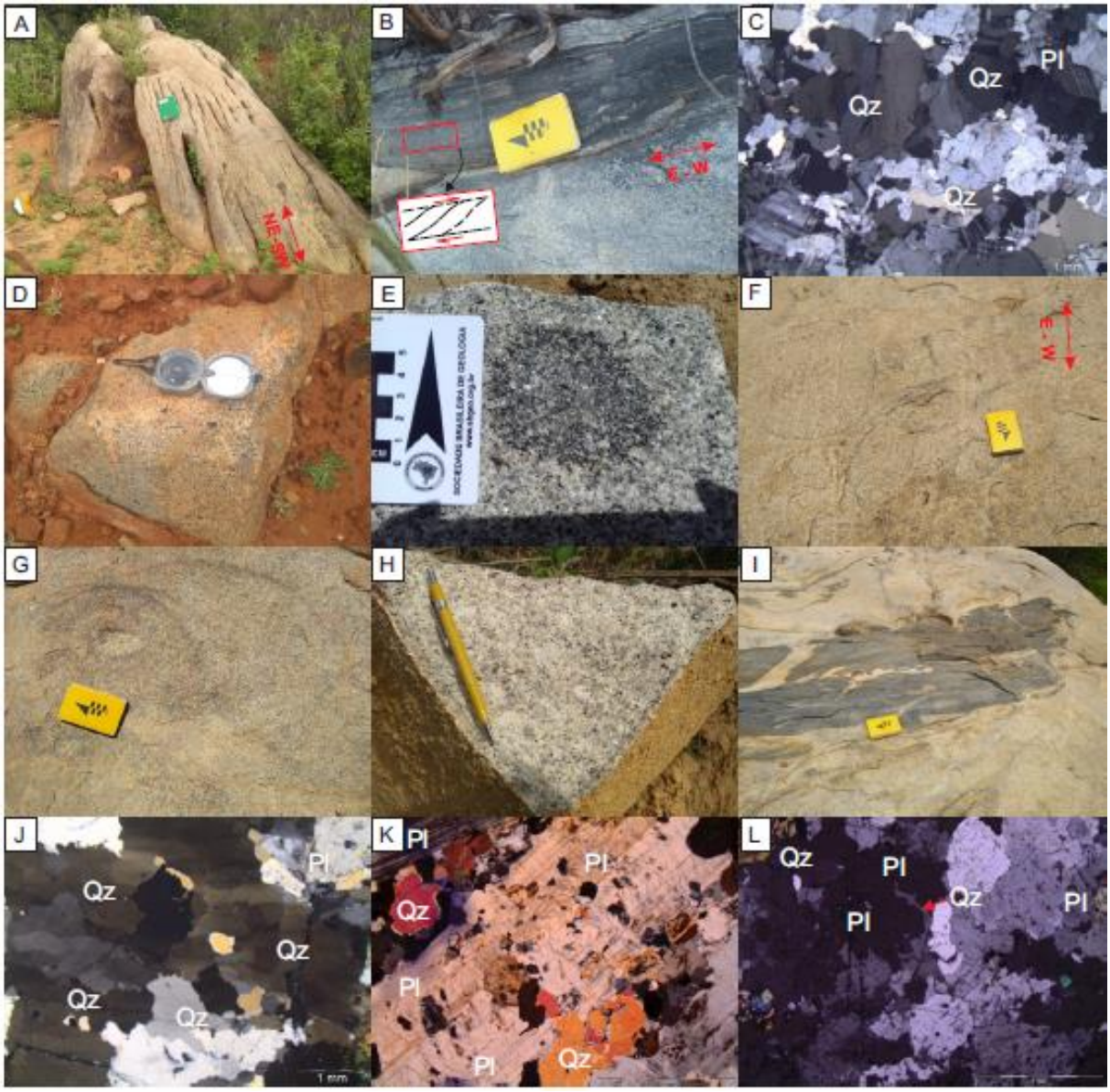

2.2. Petrography

In addition to quartz, K-feldspars, and plagioclase, the studied granitoids comprise biotite and amphibole as main mafic mineral phases, and titanite, epidote, opaque minerals, apatite, and zircon as accessory minerals. Pyroxene was identified only in two facies, the Pedra D'Água facies, where they occur as an accessory phase, and the São Sebastião Facies, where it is part of the main mineralogy.

Amphibole occurs as subhedral to anhedral crystals (Fig. 4A), locally poikilitic with inclusions of zircon, titanite, and opaque minerals. Biotite occurs as thin lamellae with pleochroism ranging from yellow to brown. In the Pedra D'Água facies, the biotite lamellae are oriented, chloritized and locally show kink-bands. Inclusions of epidote and zircon are common. Pyroxene was observed in the São Sebastião and Pedra D'Água facies as subhedral crystals of pale green color, with zircon and apatite inclusions, locally replaced by epidote and aggregates of Fe-Ti oxides (Fig. 4B). In the Pedra D'Água Facies, the pyroxenes are highly deformed and locally altered to actinolite (Fig. 4C).

Titanite is the most common accessory phase in all facies of the Teixeira Batholith. It occurs as two distinct textural types: I) euhedral to subhedral crystals of brown color, included within biotite and amphibole, being interpreted as primary titanite; and II) anhedral crystals, often forming granular aggregates, constituting a secondary phase. Epidote occurs mainly as euhedral crystals of yellow color (Fig. 4D), partially encompassed by biotite and amphibole, suggesting a magmatic origin. Opaque minerals, most of the Fe-Ti oxides class, comprise up to 2% of modal percentage in the Pedra D'Água, São Sebastião and Santo Antônio Facies. Fe-Ti oxides are represented essentially by magnetite (Fig. 4E), which occurs mainly as euhedral to subhedral crystals. They are often surrounded by larger crystals of amphibole, biotite and clinopyroxene and, under reflected light, show anisotropic gray color thin lamellae arranged according to the octahedral structural planes of the magnetite, mainly at the edges of the

crystals. This type of texture is generally associated with martitization processes, due to exposition of pre-existing magnetite crystals to late- and post-magmatic oxidation reactions, generating hematite/maghemite.

Sulfides were recorded in small modal percentage (~0.3%) in the granitoids of the Tendó Facies. They occur as subhedral crystals of high reflectivity, yellow color and without anisotropy, typical of pyrite (Fig. 4F). Locally, pyrite occurs as small anhedral crystals associated with isotropic, non-identified orange material, that percolates microfractures and cleavage plans in amphibole, mainly close to the contacts between granite and enclaves. Apatite and zircon occur as small crystals, usually included in mafic minerals phases.

Figure 4 – Microscopic aspects of mafic and accessories minerals of the Teixeira Batholith granites. A) Subhedral and anhedral crystals of amphibole (Amp), with partially encompassed titanite (Ttn) crystals; B) Clinopyroxene (Cpx) crystals replaced by aggregates formed by epidote (Ep) and magnetite (Mag); C) Fibrous actinolite (Act) crystals originated from the uralitization of pyroxenes; D) Epidote euhedral crystal (Ep) included in biotite (Bt); E) Euhedral magnetite crystal (Mag), affected by oxidation process at the edges; F) Pyrite (Py) crystal associated with late material throughout the cleavage in amphibole.

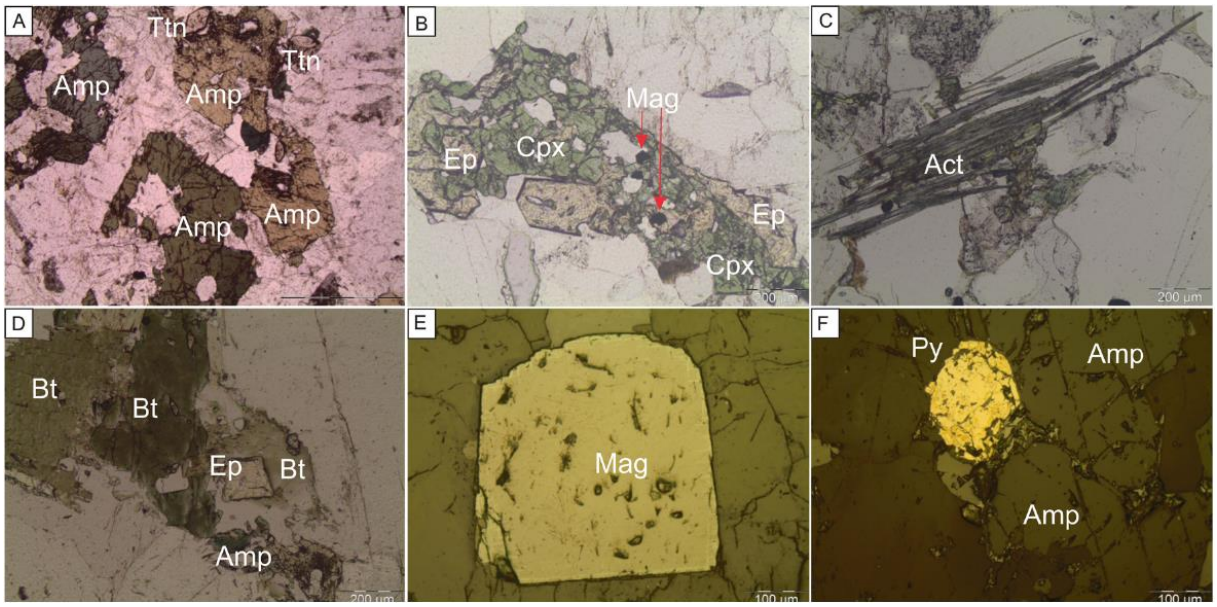

3. Analytical techniques

Mineral chemical analyses were obtained with an electron probe microanalyzer (EPMA) JEOL JXA-8230 at the Brasília University. The samples were carbon coated on vacuum

chamber. The analyses were carried out using a beam size of 5 μm for plagioclase and 1 μm for other minerals, an acceleration voltage of 15 kV and a probe current of 10 nA for silicates and oxides, while for the analysis of sulfides, a voltage of 20 kV and current of 20 nA were used. Amphibole, biotite, pyroxene, feldspars, titanite, oxides and epidote were analyzed. The analyzed crystals were TAP for Na, F, Mg, Si, Al, and P; PETJ for K, Ca and Cl; LIF for Ti, Cr, Mn, Ni, V and Fe; and LIFH for Fe. The analytical standards for instrument calibration were albite (Na), fluorite (F), forsterite (Mg), microcline (Si, Al and K), apatite (P), vanadinite (V and Cl), $MnTiO_3$ (Ti and Mn), Cr_2O_3 (Cr), NiO (Ni), andradite and Fe_2O_3 (Fe). The structural formulae calculation used the following oxygen bases: (23) amphibole, (24) biotite, (6) pyroxene, (24) plagioclase, (24) K-feldspar, (5) titanite, (12.5) epidote, (32) magnetite and (24) ilmenite. Representative analyses are shown in tables 1 to 9.

The zircon trace element abundances were quantified in-situ, in twenty-six zircon grains of two granitoids samples (TX-08, JD-01) of the Tendó Facies, using plasma quadrupole mass spectrometer (LA-Q-ICPMS; iCAP Q – Thermo Scientific) coupled to a New Wave 213 laser ablation system, at the Geosciences Institute - São Paulo University, Brazil. Ablation was done in raster mode, using a laser spot of 30 μm (1 μm/s scan speed). The NIST 610 standard glass was used as the external calibration standard, while Zr was used as the internal standard. The reference data for the NIST 610 calibration standard glass are given in Norman et al. (1996, 1998). The Glitter software (Van Achterbergh et al., 2001) was used for drift correction, data reduction and abundance determinations. The results are presented in Table 10.

4. Mineral chemistry

4.1. Amphibole

Amphibole analyses were performed in 134 amphibole crystals from all facies of the Teixeira Batholith. Representative analyses are shown in Table 1. The analyzed amphibole

crystals show (Na + K + Ca) values like those observed in magmatic amphiboles (Fig. 5A) (Czamanske and Wones, 1973). According to Locock (2014) the analyzed amphiboles display $^{B}(Ca+\Sigma M^{2+})/\Sigma B \geq 0.75$ and $^{B}Ca/\Sigma B \geq {}^{B}\Sigma M^{2+}/\Sigma B$ and belong to the calcium subgroup (Fig. 5B) according to the amphibole nomenclature of Hawthorne et al. (2012). The Jabre Facies has calcium amphiboles with composition ranging from hastingsite to ferro-ferri-hornblende, while in the other facies, the amphiboles are essentially hastingsite, with few crystals showing ferro-pargasite composition.

Figure 5 – Classification diagrams for amphiboles of the studied granitoids. A) Composition of amphibole crystals plotted in the Si^{IV} x (Na + K + Ca) diagram, with fields after Czamanske e Wones (1973); B) Classification of the studied amphiboles according to Hawthorne et al. (2012).

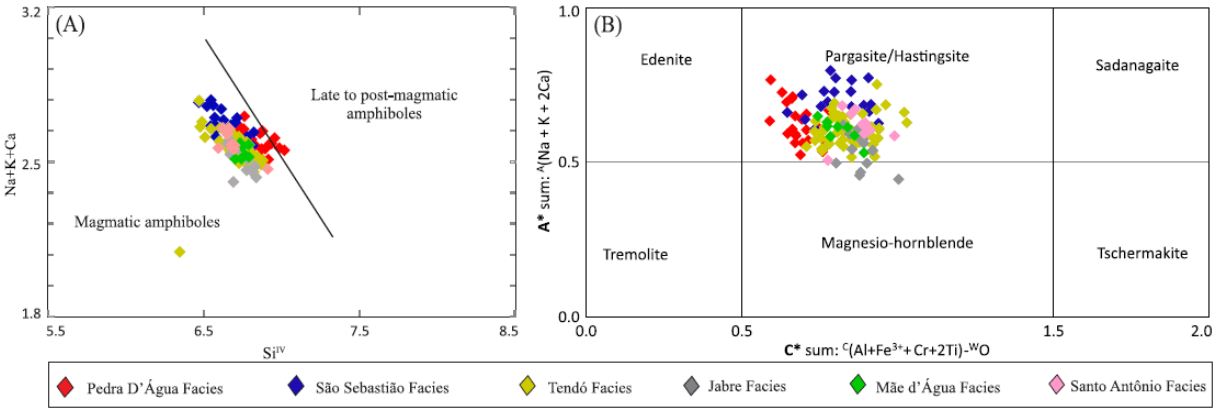

Amphibole allows a variety of substitutions on the crystallographic sites, which can be characterized by a simple exchange, involving one or more anion, to keep the crystallochemical balance (Spear, 1983). The analyzed amphibole crystals plotted in the $(Na + K)_A$ versus Al^{IV} diagram (Fig. 6A), show slight positive trends, except for the Pedra D'Água Facies, which are dispersed. The positive trends are related to the edenitic exchange vector ($\square_A + Si = Na_A + Al^{IV}$). According to Blundy and Holland (1990), this exchange is favored by an increase of temperature. However, the amphibole trends of all studied facies are similar, suggesting crystallization under similar temperatures. The edenitic substitution is clearly depicted by the strong negative correlation between $Al^{IV} + (Na+K)_A$ versus Si (Fig. 6B). Nevertheless, the

tschermakitic substitution $R^2_{M1\text{-}M3}$= (Al^{IV}+Al^{VI}) also played an important role (Fig. 6C). In general, this type of substitution involves the entrance of Al^{VI} to replace divalent cations in the M_1-M_3 sites (Czamanske and Wones, 1973; Vyhnal et al., 1991). Strong negative correlations between (Ti + Al^{IV}) and (Al^{VI} + Si) suggest substitutions between Al and Ti in the octahedral site (Fig. 6D).

Figure 6 – Types of the cationic substitutions for Teixeira Batholith amphiboles. A and B) Diagrams illustrating the edenitic type substitution; C) Diagram showing tschermackitic substitution; D) Diagram showing the importance of Ti in substitutions.

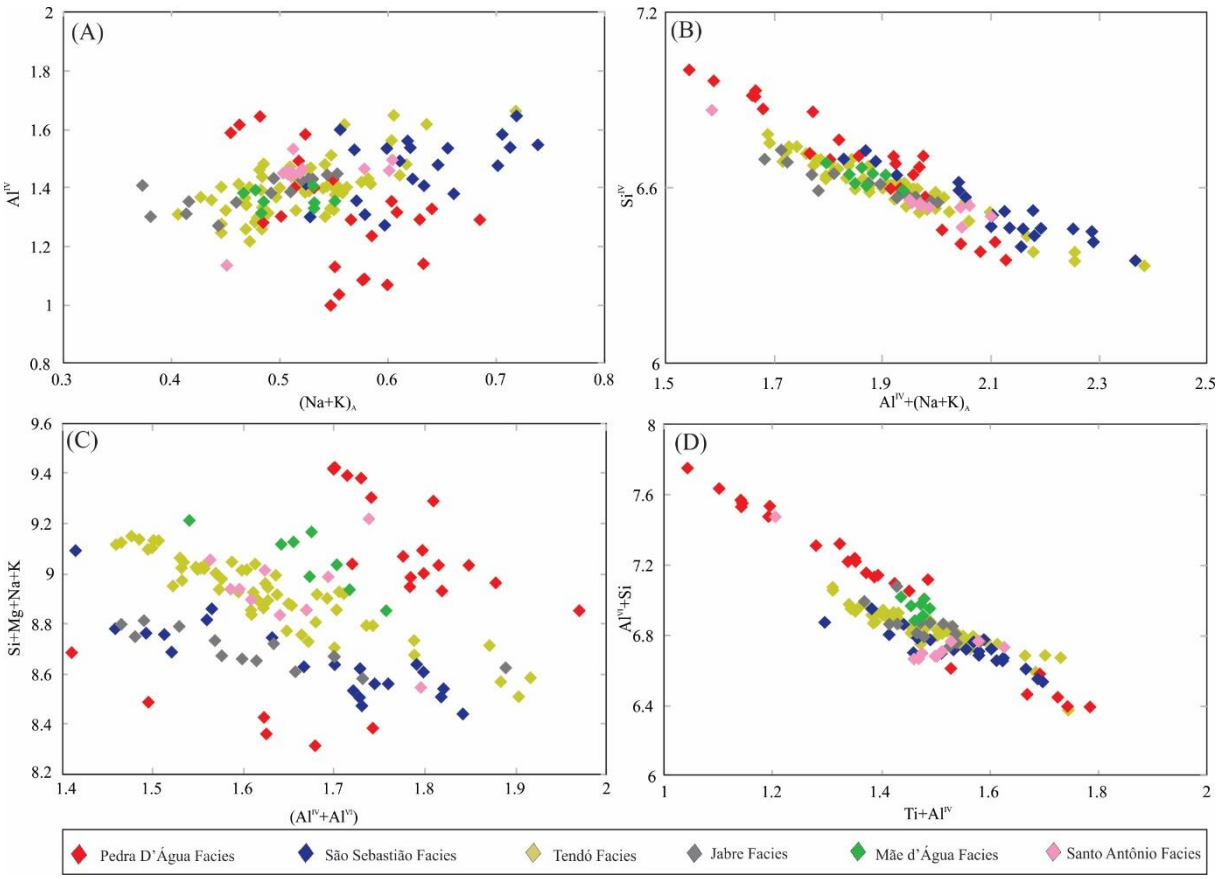

4.2. Biotite

Biotite is found in smaller modal proportion than amphibole, and thus analyses were performed only for 50 crystals. Representative results are shown in Table 2. Because biotite develops in more open geochemical systems, its characterization through chemical classification schemes, must be done cautiously. The analyzed biotite crystals projected in the Nachit et al. (2005) diagram fall mainly between the field of rebalanced primary and primary

biotite (Fig. 7A), which is corroborated by its microtextural aspect. The rebalanced primary biotite flakes may have originated through late magmatic rebalancing. Analyses that fall in the secondary biotite field are excluded from the next classification diagrams.

Figure 7 - Chemical characteristics of the studied biotite crystals. A) MgO x $10TiO_2$ x MnO + FeO ternary diagram (Nachit et al., 1985) for the studied biotites; B) Compositional variation of biotites in the Fe x Ti x Mg ternary diagram.

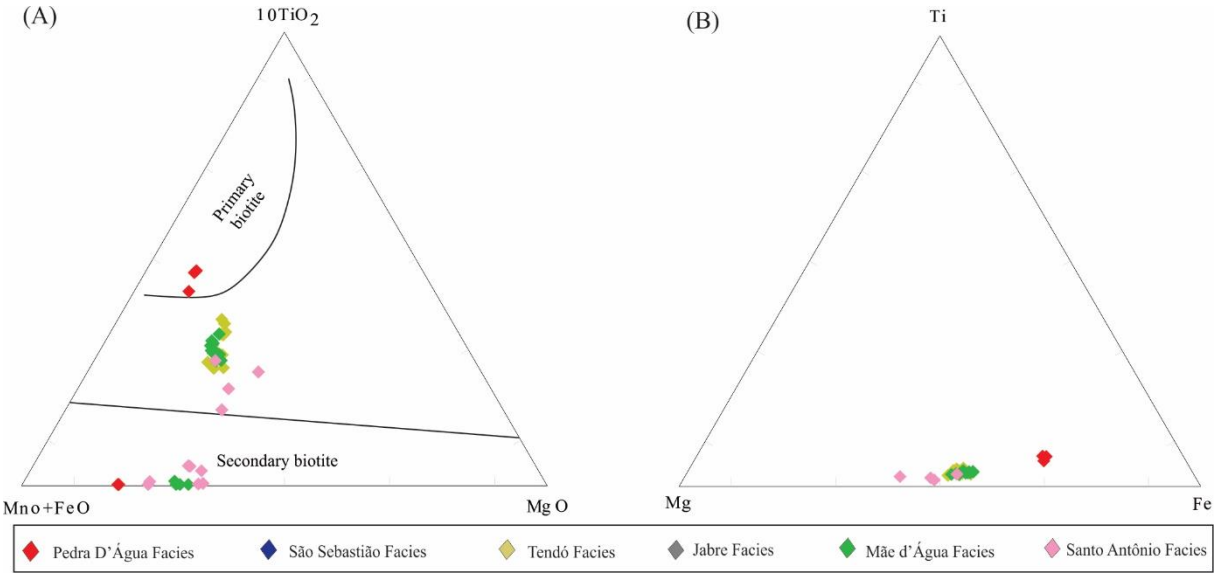

Biotite crystals of the Pedra D'Água Facies are Fe-rich compared to those from the Santo Antônio Facies, which are Mg-richer, and those from the Tendó Facies and Mãe D'Água Facies have intermediate Fe and Mg contents (Fig. 7B). The analyses show similar behavior in the Fe# [Fe/(Fe + Mg)] versus SI (solidification index) diagram (Fig. 8A), which has been efficient in the study of different plutons of batholitic bodies, since the biotite chemical trend is directly associated with the evolutionary character of the host granitoids. Biotite crystals of the Pedra D'Água Facies show higher Fe# values (0.711 to 0.718) and lower SI values (14.12 - 14.85), while those of the Santo Antônio Facies have lower Fe# values (0.421 to 0.533) and higher SI values (25.21 to 32.86), suggesting that among the facies containing biotite, the granites of Pedra D'Água Facies are the most evolved, while those of Santo Antônio Facies are the least evolved (Fig. 8A). The analyzed biotite of the Tendó and Mãe D'Água Facies project

in intermediate position in this diagram. In the classification scheme proposed by Speer (1984), based on the content of Al^{IV} versus Fe#, biotite crystals of Pedra D'Água Facies are enriched in the siderophyllite molecule, those of the Santo Antônio Facies plot in the eastonite field, and those of the other facies fall close to the limit between the siderophyllite and eastonite fields (Fig. 8B).

The Al^{T} contents of biotite crystals from the different facies of the Teixeira Batholith ranges from 2.31 to 2.75, and the analyses plot in the field of the sub-alkaline series (Fig. 8C). In the discriminant diagrams of Abdel Rahman (1994) (Fig. 8 D, E and F), biotite analyses from the Tendó, Jabre and Santo Antônio facies plot in the field of calc-alkaline granites, those from the Pedra D'Água Facies also plot mainly in this field, and those from the other facies plot in the limit between the alkaline and peraluminous fields.

Cationic substitutions are associated with changes in the crystalline structure of biotite, driven by changes in the physical and chemical conditions to which this mineral was subjected. Stussi and Cuney (1996) suggested a direct relationship between certain types of substitution and the chemical signature of the magma. Four types of substitutions were used for this principle: A (Mg ←→ Fe) (Fig. 9A); B (M^{2+VI}, Si ←→Al^{VI}, Al^{IV}) (Fig. 9B); C (M^{2+VI}, $2Al^{IV}$←→□^{VI}, 2Si) (Fig. 9C); and D ($3M^{2+VI}$←→$2Al^{VI}$, □^{VI}) (Fig. 9D). The biotite crystals of the Teixeira Batholith form, in general, discrete negative trends for all substitution schemes proposed by Stussi and Cuney (1996) in Figure 9, suggesting similarity with biotites of calc-alkaline granites, as observed in the classification proposed by Abdel Rahman (1994).

Figure 8 – Chemical classification of the biotites from the Teixeira Batholith. A) S.I. [100MgO/(MgO+FeO+Fe2O3+Na2O+K2O)] versus Fe/(Fe + Mg) diagram; B) Fe# x Al^{IV} diagram; C) Mg x Al_T diagram after Nachit et al. (1985); D), E), F) Discriminant diagrams after Abdel-Rahman (1994). Legend: A: alkaline anorogenic; C: calc-alkaline; P: peraluminous.

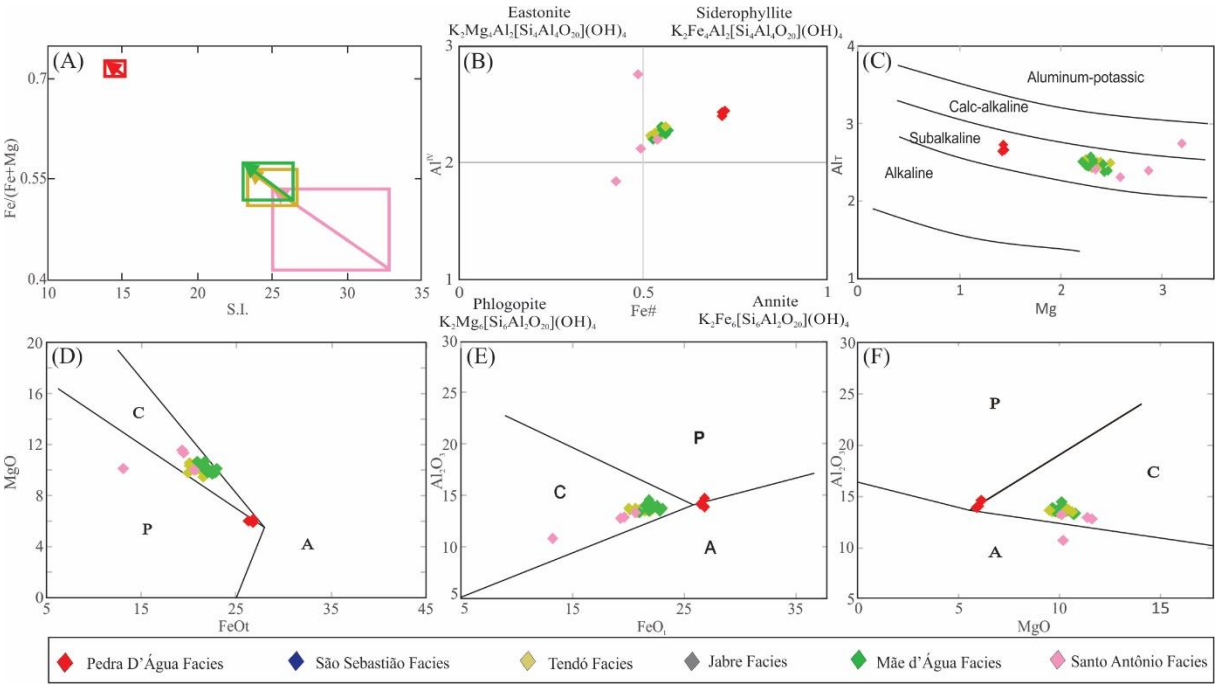

Figure 9 – Binary diagrams illustrating cationic substitutions in the studied biotites. A), B), C) and D) Trends indicative of cationic substitutions proposed by Stussi & Cuney (1996).

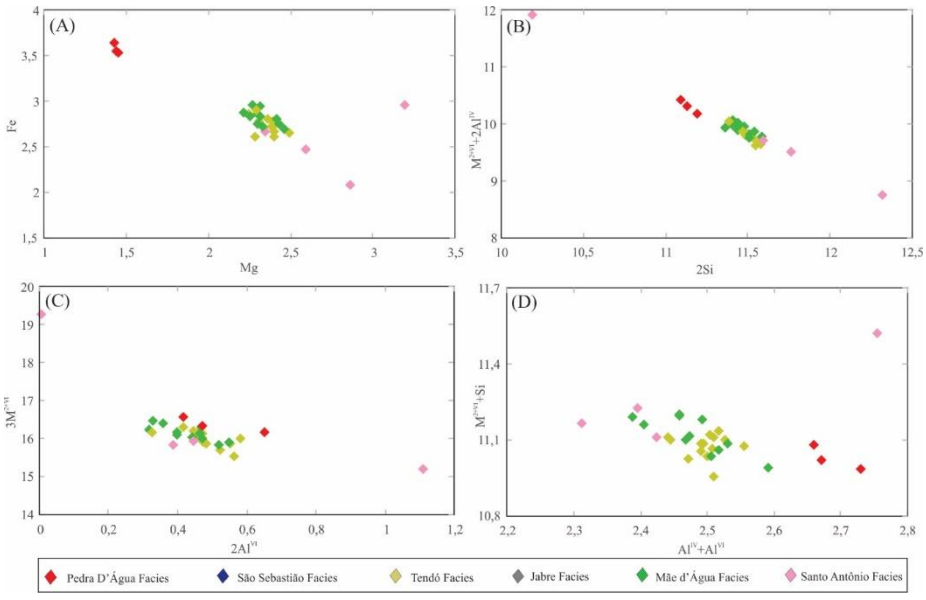

4.3. Clinopyroxene

Clinopyroxene is abundant in the granites of São Sebastião Facies and occurs as an accessory phase in the Pedra D'Água Facies. Thirteen clinopyroxene crystals of the São Sebastião Facies were analyzed (Table 3). Due to the degree of alteration, no analyzes were performed in clinopyroxene crystals of the Pedra D'Água Facies.

The clinopyroxenes from the São Sebastião Facies are characterized by contents of SiO_2 ranging from 50.11 to 51.83 wt.% of CaO from 17.89 to 21.46 wt.%, and FeO between 15.85 and 21.31 wt.%. The analyzed crystals plotted in the binary J (2Na) versus (Ca + Mg + Fe^{2+}) diagram of Morimoto (1988) fall mainly in the Ca-Mg-Fe pyroxene field (Quad) (Fig. 10A) and some in the field of sodium-calcium pyroxenes (Na-Ca). For a more detailed classification, the analyzed Ca-Fe-Mg pyroxene were projected in the Fs ($Fe_2Si_2O_6$) - Wo ($Ca_2Si_2O_6$) - En ($Mg_2Si_2O_6$) ternary diagram where they classify as hedenbergite (Fig. 10B), while the sodium-calcium pyroxenes projected in the Ae ($NaFe^{3+}Si_2O_6$) - Q (Wo, Em, Fs) - Jd ($NaAlSi_2O_6$) ternary diagram, are classified as aegirine-augite (Fig. 10C).

Figure 10 – Chemical classification of the pyroxenes from the São Sebastião Facies. A) Composition of the analyzed pyroxenes in J (2Na) versus Q (Ca + Mg + Fe2+) diagram according to Marimoto (1988); B) Classification of Ca-Mg-Fe pyroxenes in the Fs - Wo – En diagram; C) Classification of sodium-calcium pyroxenes, plotted on the Ae-Q-Jd ternary diagram.

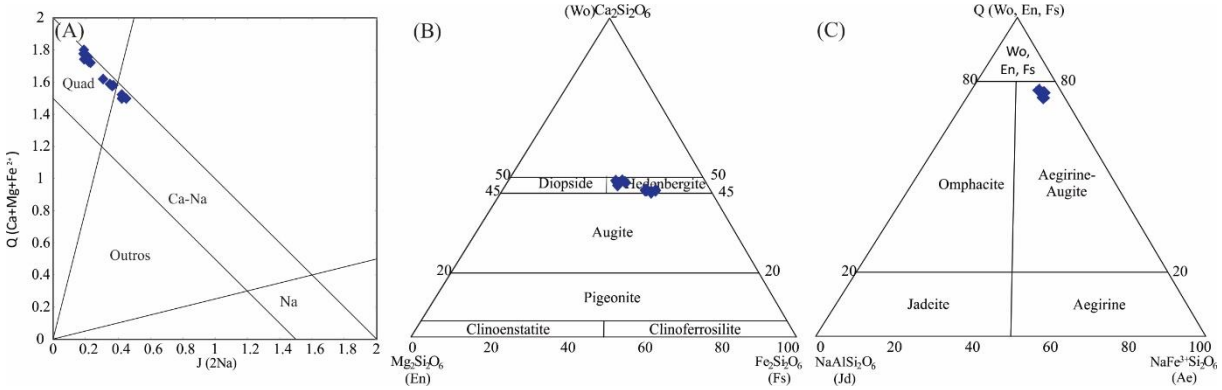

4.4. Feldspars

Analyzed plagioclase crystals (115) from the Texeira Batholith (Table 4) are sodic with albite molecule contents ranging $Ab_{83\ -\ 90}$ (Pedra D'Água Facies), $Ab_{84\ –\ 98}$ (São Sebastião Facies), $Ab_{83\ –\ 88}$ (Tendó Facies), $Ab_{86\ –\ 96}$ (Jabre Facies), $Ab_{81\ –\ 84}$ (Mãe D'Água Facies) and

Ab_{85-93} (Santo Antônio Facies), ranging in composition from oligoclase to albite (Fig. 11). The uniform albite contents may be associated with similar temperature during the crystallization of the different facies. Profiles (core/rim) in plagioclase crystals with compositional zoning are characterized mainly by enrichment in sodium and depletion in calcium from core to rim, typical of normal zoning, feature commonly associated with fractionation processes.

Eleven crystals of K-feldspar were analyzed (Table 5). They are mainly orthoclase (Fig. 11), with compositions $Or_{92-96\%}$ (São Sebastião Facies), $Or_{89-95\%}$ (Tendó Facies), $Or_{89-92\%}$ (Mãe D'Água Facies) and $Or_{92\%}$ (Santo Antônio Facies). One analyzed crystal of the Tendó Facies revealed a potassium core ($An_{0.1}Ab_{7.9}Or_{92}$) surrounded by an albite/oligoclase rim ($An_{10.5}Ab_{88.5}Or_1$) characterizing a rapakivi-like texture. The K-feldspars have a high barium content, reaching up to 2 wt.% BaO in Tendó Facies.

Figure 11 - An-Ab-Or ternary diagram for the classification of the studied plagioclase and K-feldspar (modified from Deer et al., 1992).

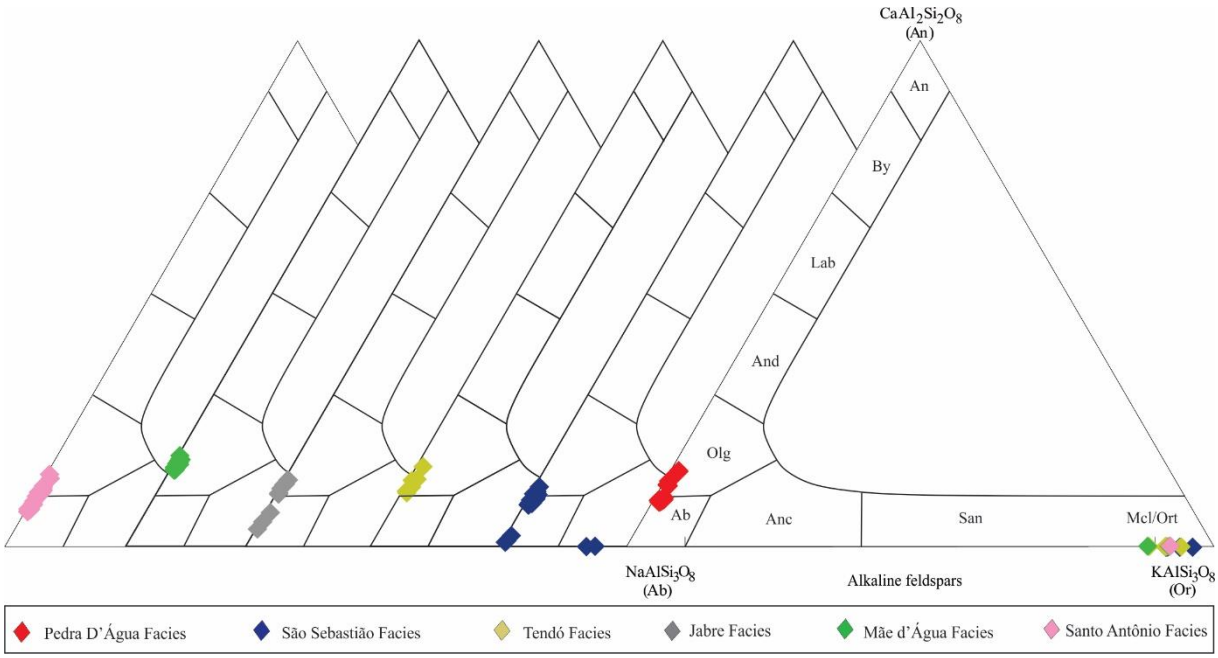

4.5. Titanite

26 crystals of titanite identified as an early magmatic phase were selected for analysis (Table 6). The analyzed crystals are characterized by contents of TiO_2 ranging from 31.6 to 37.0 wt.%, of FeO between 0.8 and 2.7 wt.%, and of CaO ranging from 26.64 to 29.1 wt.%,

and show homogeneous and relatively depleted aluminum contents, ranging between 2.9 and 3.7 wt.% (Pedra D'Água Facies), 1.0 and 2.4 wt.% (São Sebastião Facies), 0.8 and 2.1 wt.% (Tendó Facies), 1.0 and 1.2 wt.% (Jabre Facies), 1.7 and 1.9 wt.% (Mãe D'Água Facies) and 1.9 and 2.9 wt.% (Santo Antônio Facies), typical of primary titanite (Tulloch, 1979; Enami et al., 1993).

4.6. Magnetite

Iron titanium oxides are relatively common in granitoids of the Teixeira Batholith. Twenty-five euhedral to subhedral crystals from the Pedra D'Água, São Sebastião and Santo Antônio facies were analyzed (Table 7). They show similar compositions, characterized by contents of Fe_2O_3 ranging from 60.28 to 69.52 wt.%, of FeO between 29.6 and 31.42 wt.%, and of TiO_2 ranging from 0 to 0.25 wt.%, in addition to magnetite molecule ranging from $Mag_{97-99\%}$ (Pedra D'Água Facies), $Mag_{98-99\%}$ (São Sebastião Facies) and $Mag_{97-99\%}$ (Santo Antônio Facies). In the ternary diagram of Buddington and Lindsley (1964), the analyzed magnetites fall between Fe_3O_4 (pure magnetite) and Fe_2O_3 (pure hematite) (Fig. 12A), which associated to the presence of martitization along the structural planes of the magnetite, suggest that they are oxidized magnetites. Several geological processes can generate oxidation of titanomagnetite to titanohematite/titanomaghemite (Buddington and Lindsley, 1964). Magnetite with Fe_2O_3 contents higher than 6 or 7 wt.%, show lamellae of martite, mainly in the edges, with planar shape and well-defined angles, suggesting penetration of late fluids along the octahedral planes of the magnetite, leading to the oxidation process, and partially transforming magnetite into maghemites. Locally, magnetite crystals are almost completely altered.

4.7. Sulfides

Sulfides occur in greater modal percentage in granitoids of the Tendó Facies. Six crystals were analyzed and show a typical pyrite composition (Fe = 43.19 – 46.32%; S = 50.5 – 53.6%; Cu = 0 – 0.061%) (Table 8). The sulfides crystallized as euhedral to subhedral crystals,

locally fractured, and as a late phase associated with barite (Fig. 12B and C), filling venules or along the cleavage of amphiboles, mainly in the enclaves. The unusual presence of barite in this type of rock is probably associated with the destabilization of minerals with high barium content such as K-feldspar and mica.

Figure 12 – Chemical characteristics of the studied oxides and sulfides. A) Fe_2O_3 x TiO_2 x FeO ternary diagram for the studied oxides according to the classification by Buddington and Lindsley, (1964); B) SEM image of crystal where the darkest parts are associated with pyrite and the lightest with barite; C) EDS spectrum with peaks of counts obtained in points made in the crystal of Fig. 12B (Location indicated by the circles).

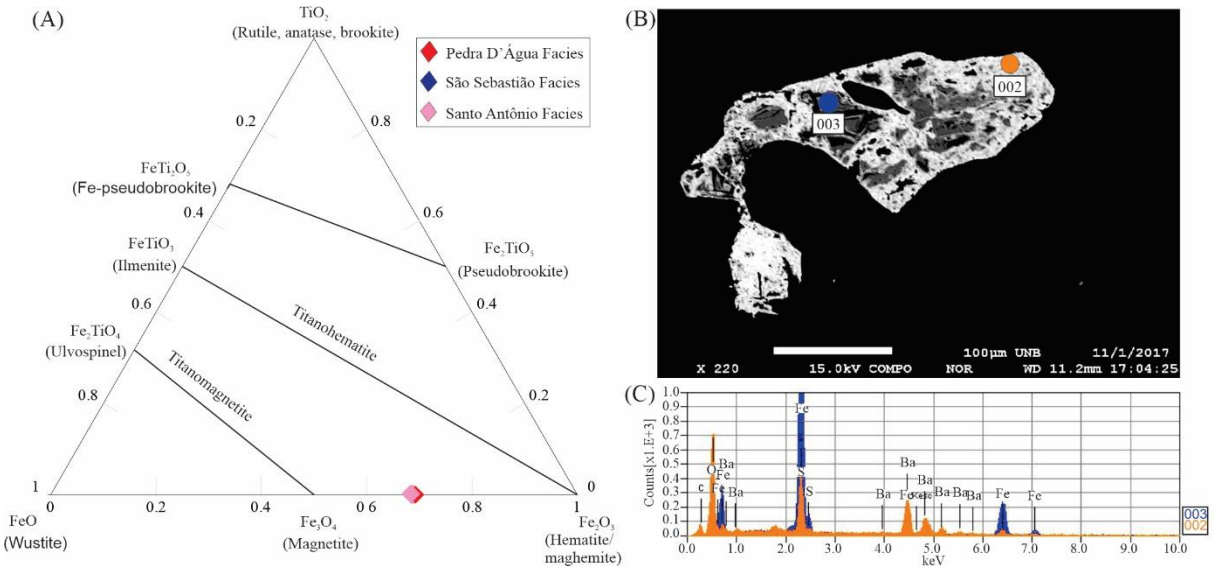

4.8. Epidote

Epidote is one of the main accessory minerals in the granitoids of the Teixeira Batholith and occurs as primary crystals included in biotite, amphibole and pyroxene. Fourteen epidote crystals from the Mãe D'Água and Santo Antônio facies were analyzed (Table 9). The crystals present FeO contents ranging from 10.6 to 14.0 wt.%, CaO from 18.0 to 23.2 wt.% and Al_2O_3 from 17.8 to 22.8 wt.%.

According to the value for the pistacite molecule (Ps), calculated as Ps = [Fe^{3+}/(Fe^{3+}+ Al)], epidote crystals of magmatic origin i.e., those with Ps ranging from 25 to 29% can be differentiated from those crystals of secondary origin (Tulloch, 1979; Johnston and Wyllie, 1988 and Vyhnal et al., 1991). Magmatic epidote with Ps up to 33% have been described in several studies in Borborema Province (Sial et al., 1999, 2008, Ferreira et al., 2003, 2011, 2015;

among others). Hence, Ps between 27 and 31% in the Mãe D'Água Facies and between 30 and 32% in the Santo Antônio Facies, suggest that the analyzed epidote crystals from both facies have a magmatic origin, which is corroborated by low TiO_2 values (< 0.3 wt.%) (Evans and Vance 1987). The presence of magmatic epidote suggests that crystallization occurred under relatively high fO_2 conditions (Schmidt and Thompson, 1996).

4.9. Zircon trace elements composition

Zircon trace element composition constitutes an important tool for the reconstruction of magmatic histories and identification of magma sources (Grimes et al., 2007; Burnham and Berry, 2012). In this study, the trace elements in zircon prove to be a useful tool in identifying the physical conditions during the magmatic evolution and post-magmatic processes.

Most of the analyzed zircon grains (Table 10) show oscillatory zoning and xenocryst cores (Fig. 13). In general, the cores are sub-rounded, unzoned, or more rarely show chaotic zoning. Systematic U-Pb zircon dating performed on the Teixeira granitoids (Lima et al., 2021b) provided Concordia ages ranging from 585 to 600 Ma, and mainly Paleoproterozoic $^{207}Pb/^{206}Pb$ ages for the xenocryst cores. Micro-inclusions of apatite occur in some analyzed crystals.

Figure 13 – Cathodoluminescence images of the zircon grains from the Tendó Facies granitoids.

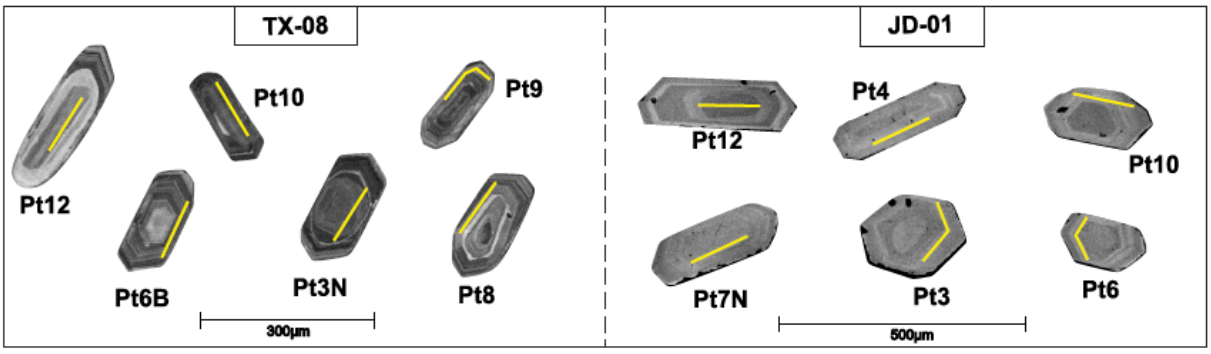

The studied zircon grains from the monzogranite samples (TX-08 and JD-01) have chondrite (Taylor and McLennan, 1985) normalized Rare Earth Element (REE) patterns (Figs. 14A and B) characterized by enrichment in high REE (HREE), and slight positive Ce and negative Eu anomalies. The analyzed rims of the zircon grains have Th/U ratios ranging from

0.01 to 0.80, absence of significant Ce anomalies (Ce/Ce*mean = 3.0 – 3.5) and slight negative Eu anomalies, with Eu/Eu*mean ratios ranging from 0.76 to 0.89. The absence of significant Ce and Eu anomalies, and flat light REE (LREE) patterns displayed by most analyzed zircon grains (Fig. 14), are common features of zircon grains affected by post-magmatic processes (Hoskin, 2005; Hoskin and Schaltegger, 2003). Unaltered cores or slightly altered magmatic zircon crystals, display REE patterns characterized by expressive positive Ce anomalies (Ce/Ce*mean = 12.0 – 15.4), modest negative Eu anomalies (Eu/Eu*mean = 0.46 – 0.64) and mean values for the Th/U ratio ranging from 0.19 to 0.39.

Figure 14 – Chondrite-normalized REE patterns (Taylor e McLennan, 1985) of the studied zircons. A) Tx-08 sample; B) JD-01 sample.

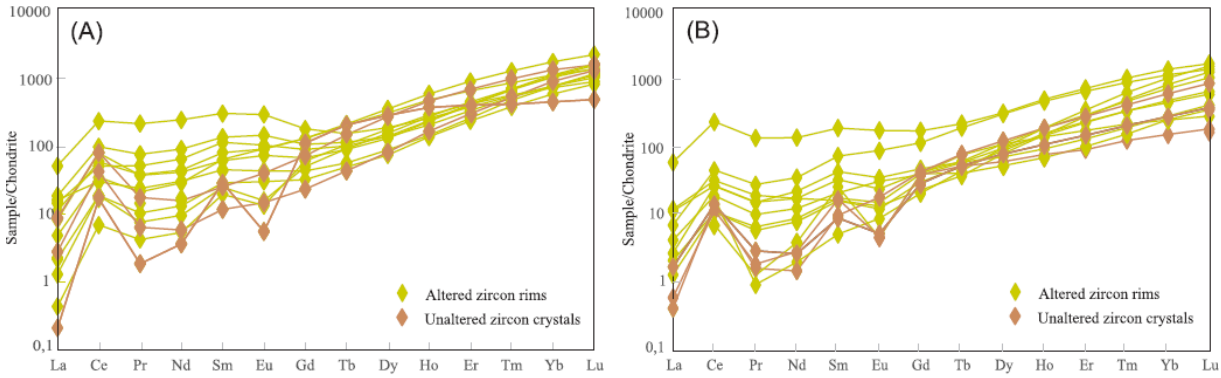

5. Discussions

5.1. Mineralogical characterization, chemical affinity and petrogenetic implications

In the lack of contamination processes, the mineralogical composition of igneous rock is directly associated with the chemical composition of the parental magma, which in turn depends on the source and the processes related to its evolution. The mafic mineral phases of the granitoids from Teixeira Batholith (monzogranites, syenogranites and quartz-syenites) comprise amphibole, dominantly calcium-rich (hastingsite, ferro-ferri-hornblende and ferro-pargasite; Hawthorne et al., 2012) and biotite rich in the molecules of siderophyllite and eastonite (Speer, 1984). Clinopyroxene is restricted to the Pedra D'Água and São Sebastião

Facies, most showing hedenbergite composition, although aegirine-augite occurs locally (Morimoto, 1988).

Titanite is the most common accessory phase in all granitic facies of the Teixeira Batholith. Its euhedral shape associated to occurrence as inclusions in ferro-magnesian minerals, suggests that titanite is an early crystallized phase. The mafic mineral phases composition associated to magnetite and titanite in the studied granitoids are characteristics of I-type granites (Chappell and White, 1992), corroborating the whole-rock chemistry data reported by Lima et al., (2021b), which suggest that the Teixeira Batholith comprises I-type granitoids of the magnetite series.

The composition of the studied primary biotite from the Teixeira granitoids is compatible with biotite crystallized from magmas with a transitional calc-alkaline to subalkaline composition (Nachit et al., 1985; Abdel-Rahman, 1994), which is corroborated by the presence of magmatic epidote. In the Central Subprovince, magmatic epidote is reported in many shoshonitic and high-K calc-alkaline granitoids (Sial, 1990; Guimarães et al., 2011; Sial and Ferreira, 2016 and references therein).

According to Vilalva et al. (2019) the Hf content in zircon may be an effective tool to distinguish alkaline affinity rocks (<10,000ppm) from those of subalkaline affinity (> 10,000ppm). The analyzed zircon grains are characterized by Hf contents ranging from 9810 to 11143 ppm, intermediate between the contents of Hf expected for zircon crystals of subalkaline and alkaline rocks. The Hf contents in the analyzed zircon grains, the biotite chemical data, and the presence of magmatic epidote, are characteristics compatible with a high-potassium calc-alkaline to shoshonitic affinity for the studied granitoids, as well as suggested by Lima et al., (2021b) from whole-rock chemical data**.** Granitoids with shoshonitic to high-K calc-alkaline affinity constitute important post-collisional granitic suites associated with the Brasiliano/Pan-African orogeny and occur widely distributed in the Borborema Province (Guimarães et al.,

2004; Sial and Ferreira, 2016; Van Schmus et al., 2011 among others) and in several sectors of the Central African Orogen and the Tuareg Shield (Litvinovsky et al., 2021 and references therein). In general, post-collisional magmatism encompasses high-K rocks in the early stages that evolves into an alkaline magmatism in the late post-collisional phase. The mineral assemblage and chemical data of the mafic and accessory phases of the Teixeira granitoids are similar to other granitic rocks of high-K signature and ages within the 610 - 570 Ma interval (Guimarães et al., 2004; Lima et al., 2021b,c; Sial and Ferreira, 2016; Van Schmus et al., 2011) in the Alto Pajeú Domain. Thus, the mineral chemistry together with the age and the whole-rock chemistry (Lima et al., 2021b) of the Teixeira granitoids, suggest that the Teixeira Batholith represent an early post-collisional Brasiliano magmatism in the Borborema Province.

5.2. Estimation of crystallization parameters

5.2.1 Temperature

Calcic amphibole composition is sensitive to pressure, temperature, and bulk composition, making it a potentially useful phase to estimate the conditions under which evolved magmas crystallized. To quantify the solidification temperatures of the studied magmas, a geothermometer based on the plagioclase-amphibole equilibrium was used (Blundy and Holland, 1990). This geothermometer provided temperatures ranging from 662 to 735 ºC (Table 11). Some temperatures data obtained for the different facies is slightly lower than the solidus temperature of the granitic systems. It suggests high H_2O content in the magma, which is corroborated by the presence of magmatic epidote (Naney, 1983; Johannes and Holtz, 1996).

We also apply our data in the empirical equation proposed by Putirka (2016), which is based on the element partitioning between amphibole and silicate melt, without recognizing equilibrium between amphibole and other phases. The amphibole - liquid thermometer of Putirka (2016), was built up using natural and experimental calcic amphibole data from Ridolfi

and Renzulli, (2012), but with better precision (± 30ºC). The obtained temperatures (701 to 778 °C) are slightly higher than those obtained using the Blundy and Holland (1990) geothermometer and are more consistent with the mafic mineral assembly including amphibole, small amount of biotite, and clinopyroxene, present in the Pedra D'Água and São Sebastião facies. It is worth noting that we used alteration-free euhedral amphibole crystals to ensure a condition closer to equilibrium with the melt.

The system liquidus is commonly estimated from accessory mineral saturation geothermometers, such as apatite and zircon (Harrison and Watson, 1984; Watson and Harrison, 1983). Several experiments demonstrate that zircon solubility in crustal melts is associated with melt composition and temperature (Watson 1979; Watson and Harrison 1983; Harrison and Watson, 1984; Boehnke et al., 2013), so the concentration of Zr in the rock, can be used to estimate the crystallization temperature of zircon in liquids saturated in Zr (Watson, 1987). Considering the calibration proposed by Watson and Harrison (1983), the temperature calculated for the Teixeira Batholith granitoids magmas varies from 737.4 to 810.8 ºC (Table 11). In addition, we used the equation proposed by Boehnke et al. (2013), that revised and refined the original zircon saturation solubility model of Watson and Harrison (1983), using a modern electron and high-resolution ion microprobe. The obtained temperatures range from 680 to 761 °C (Table 11), which are values considered low for the peak temperature associated with the magma that originated the Teixeira Batholith. In the Santo Antonio facies, the obtained temperature based on the calibration of Boehnke et al. (2013) are lower than those obtained by the amphibole-liquid and amphibole-plagioclase geothermometer. However, according to Harrison et al. (2007) and Moecher et al. (2014) zircon saturation temperature does not always correspond to the temperature at the start of zircon crystallization, and in granitic magmas, zircon can crystallize in a wide temperature range, as suggested by the temperature range (684

- 988 °C; Table 11) obtained in the studied granitoids using Ti-zircon geothermometer (Watson et al., 2006).

The presence of apatite micro-inclusions in the studied zircon crystals suggests that apatite was an early crystallized phase and the temperatures calculated using the apatite saturation geothermometer should be close to the liquidus conditions. The geothermometers Mg-in-liquid (Molina et al., 2015) and apatite saturation (Harrison and Watson, 1984) yielded temperatures between 772 and 995°C, with uniform maximum temperatures (Table 11) for individual facies of the Teixeira Batholith and are interpreted as the liquidus.

The high crystallization temperatures obtained for the Teixeira granitoids are like those observed for high temperature granites (Chappell and White, 2001). However, the studied granitoids are predominantly of infracrustal origin and do not have an important contribution of mantle material (Lima et al., 2021b). Thus, the high temperature values must reflect significant heat input in the crust during the genesis of the Teixeira magmatism.

Figure 15- A) Alt x Fe# diagram for the studied biotites (Anderson, 2008); B) Al^{IV} x Fe/(Fe+Mg) diagram for the studied amphiboles, with the fields according to Anderson & Smith (1995); C) Oxygen fugacity of the Teixeira Batholith granites from the Log fO2 versus 10^3/T (K) diagram (Wones, 1989).

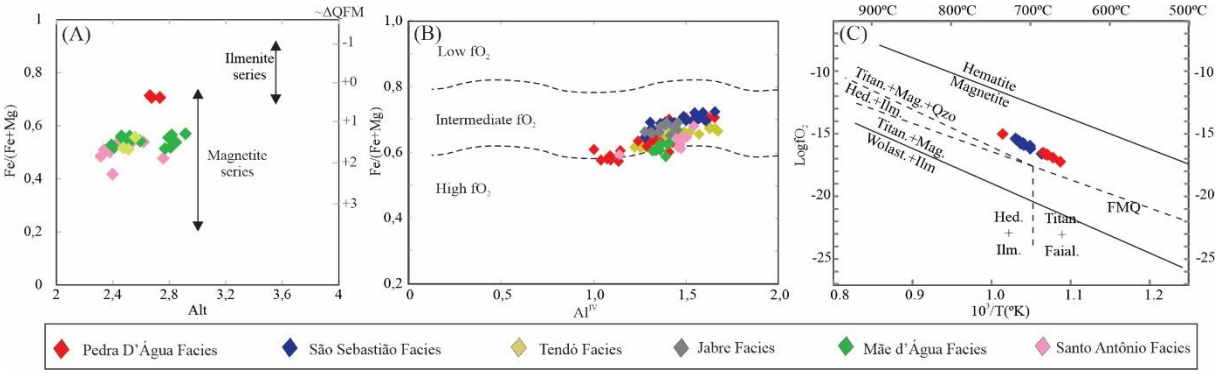

5.2.2. Pressure and depth of emplacement

The calculation of the pressure during crystallization of the magma which originated the Teixeira Batholith was performed using the classic Al-in-amphibole geobarometer. Pioneering work (Hammarstrom and Zen, 1986; Hollister et al., 1987; Schmidt, 1992) demonstrated that the Al_t content in hornblende of calc-alkaline granites is directly proportional to pressure, when

buffered for the quartz + hornblende + plagioclase + K-feldspar + biotite + titanite + magnetite or ilmenite assemblage (Hammarstrom and Zen, 1986; Hollister et al., 1987; Anderson and Smith, 1995). Among the various calibrations (Hollister et al., 1987; Blundy and Holland, 1990; Schmidt, 1992), the proposal by Schmidt (1992) admits a wider pressure range (2.5 to 13.0 kbar) and lower error (0.6 kbar). The pressure calculated using the Schmidt (1992) calibration for the studied granitoids, varies from 3.93 to 5.99 kbar (Table 11).

However, Anderson and Smith (1995) showed that the geobarometer of Schmidt (1992) is not suitable for rocks with high Fe/(Fe+Mg) and for amphiboles with Fe# > 0.65 and proposed a new calibration. The values for the crystallization pressure obtained from the calibration of Anderson and Smith (1995) for each facies of the Teixeira Batholith are presented in Table 11. The granitoids of the different facies of Teixeira Batholith present varied values for Fe# in mafic minerals. The amphiboles of the São Sebastião and Jabre facies have high Fe# values, 0.65 to 0.72 and 0.65 to 0.69, respectively. Therefore, in these two facies, the pressures calculated by the Anderson and Smith (1995) calibration are more consistent.

The pressures obtained from the Al-in-amphibole geobarometer are quite heterogeneous, considering both the Teixeira Batholith and the individual facies, and indicate an emplacement depth around 12.3 to 19.7 km. Since there is no evidence of tectonic displacement, the obtained pressure variation is unrealistic. It is more likely that amphibole crystallized at depths, and it was transported by the magma to shallower levels in the magma chamber. Convection within the magma chamber was probably an efficient process, as indicated by field features (Fig. 3G). Thus, the lower limit of the estimated pressures, i.e., 3.75 to 4.71 kbar (Table 11) is more coherent, and point to emplacement depths of 11.7 to 14.7 km.

5.2.3. Oxygen fugacity

The composition of biotite, amphibole and Fe-Ti oxides are used to estimate the oxygen fugacity, because their compositions are strongly fO_2 dependent (Wones, 1989; Frost, 1991;

Clark, 1999; Dall'Agnol et al., 2005; Dall'Agnol and Oliveira 2007). In general, the biotite of the Teixeira Batholith granitoids show slight Fe# [Fe/(Fe+Mg)] variations. Biotite analyzed from Jabre, Mãe D'Água and Santo Antônio facies have Fe# ranging from 0.4 to 0.6, like those reported by Anderson (2008) for biotite of granites originated from magmas crystallized under high fO_2, the so-called granites of the magnetite series (Fig. 15A). Biotite crystals of the Pedra D'Água Facies show Fe# values close to 0.7, reflecting slightly lower fO_2 conditions. The Fe/(Fe+Mg) values of the studied amphiboles follow the same patterns observed in the biotite compositions (Fig. 15B), reflecting amphiboles crystallized under intermediate to high fO_2 conditions.

The analyzed epidote grains display pistacite molecule values typical of magmatic epidote (Ps= 0.26 – 0.31), making it a good indicator of the conditions acting during the magmatic evolution (Naney, 1983; Zen and Hammarstrom, 1984; Brandon et al., 1996; Sial et al., 1999). The stability field of the magmatic epidote fits mainly between the QFM and HM buffers (Liou, 1973). Epidote crystallization under high fO_2 conditions occurs under relatively lower pressure (Schmidt and Thompson, 1996). Thus, the presence of magmatic epidote in the studied granitoids suggests crystallization under relatively oxidizing conditions.

The composition of the mafic minerals of the Teixeira Batholith granitoids, and the presence of primary crystals of magnetite, titanite, epidote and pyrite constituting a mineral assemblage like that suggested by Ishihara (1977) for the granites of the magnetite series, are compatible with their classification as oxidized I-type granites (Ishihara, 1977; Chappell and White, 1992). The REE patterns of analyzed unaltered zircon grains, with pronounced positive Ce anomalies and slight negative Eu anomalies corroborates with crystallization from oxidized magmas (Burnham and Berry, 2012; Trail et al., 2012), in which Eu^{2+} was extremely limited in abundance, and Ce^{3+} is oxidized to Ce^{4+}, reflecting the stabilization of Ce^{4+} at high fO_2.

To quantify the fO_2 of magmatic rocks, Wones (1989) proposed an equation based on the relationship between fO_2 with the P and T during the evolution of the magma, based on the following relationship: hedenbergite + ilmenite + oxygen = titanite + magnetite + quartz. It is worth noting that the equation formulated by Wones (1989) was initially applied only to mineral assemblies containing hedenbergite. Therefore, the fO_2 values were only estimated for the granites of Pedra Água and São Sebastião facies. The fO_2 values obtained for the studied granites vary from 10^{-15} to 10^{-17}(Fig. 15C), compatible with fO_2 conditions above the FMQ buffer, corroborating crystallization under oxidizing conditions.

5.3. Post-magmatic process

In the studied granitoids solid-state deformation is most concentrated along the edges of the intrusion, except in the Pedra D'Água Facies which comprises sheets of sheared granite emplaced between the Patos, Itapetim and Taperoá shear zones. Pegmatite dykes and quartz veins are locally observed and reflect late hydrothermal processes. The chemical characteristics of the studied zircon crystals like hydrothermal zircon grains reported in the literature (Hoskin, 2005; Hoskin and Schaltegger, 2003), also support a context involving post-magmatic hydrothermalism. Chlorite associated with destabilization of primary ferromagnesian minerals, barite associated to destabilization of feldspars and rebalanced biotite grains (Nachit et al., 1985) suggest interaction with late-stage fluids in the subsolidus stage. Myrmekitic intergrowths is a microscopic feature frequently recorded in the studied granitoids and may also be associated with volatiles-rich late magmatic fluids (Hibbard, 1979). The presence of hematite/maghemite at the edges of magnetite crystals, typical of martitization process, corroborates high fO_2 conditions at late stage. According to Lima et al. (2000), late fluids associated with reactivation of the shearing system (Itapetim Shear Zone), were responsible for the gold and sulfides precipitation/oxidation in the SW of the Teixeira Batholith. These features

indicative of late magmatic processes observed in the studied granitoids may be associated with the reactivation of the shear zones present in the region, including the Itapetim Shear Zone.

6. Conclusions

The granitoids of the Teixeira Batholith, mainly represented by syenogranites, monzogranites and quartz syenites, have calcium amphibole (hastingsite, ferro-ferri-hornblende and ferro-pargasite) as the main mafic mineral, with Fe# ranging from 0.57 to 0.72, small amounts of clinopyroxene (hedenbergite and aegirine-augite) and biotite (Fe# = 0.4 - 0.7), which varies in composition from eastonite to siderophyllite. The mafic mineral phases composition associated to the presence of primary crystals of titanite, magnetite, epidote and pyrite, similar to the mineral assembly of magnetite-series granites, suggest the classification of the studied granitoids as oxidized I-type granites.

The chemical composition of the studied biotites, transitional between the calc-alkaline to subalkaline series, the presence of magmatic epidote and the Hf content of the studied zircon crystals (9810 to 11143 ppm) suggests that these minerals were crystallized from a magma with high-potassium signature.

The thermobarometric parameters associated with the crystallization conditions of the magma that originated the Teixeira Batholith granitoids are characterized by temperatures within the 995 - 701 °C interval (amphibole-liquid and Mg-in-liquid geothermometer, and apatite saturation temperature), pressure varying from 4.71 to 3.75 kbar (aluminum-in hornblende geobarometer), and intermediate to high fO_2 conditions (above the FMQ buffer). These physical parameters suggest the emplacement of the Teixeira Batholith at intermediate crustal levels (~14.7 to 11.7 km).

Post-magmatic processes associated with the action of fluids are indicated by the presence of several petrographic and chemical features, in addition to field aspects (pegmatite

dykes and quartz veins), such as: hydrothermal zircon, rebalanced biotite grains, saussuritization of plagioclase, large-scale myrmekitic intergrowths, and generation of chlorite from the destabilization of primary ferromagnesian minerals and barite associated to destabilization of feldspars. Moreover, magnetite crystals are often affected by martitization process, which corroborates the action of high fO_2 fluids in the subsolidus stage, that we interpreted as associated with the reactivation of the shear zones system present in the studied area.

Acknowledgements

We acknowledge Vinícius Martin and Dr. Valdecir Janasi (University of São Paulo), and Dr. Nilson Botelho (University of Brasilia) for the chemical analysis. This work was supported by the Brazilian National Research Council (CNPq), Proc. 421353/2018-0. JVL thanks CAPES for the doctoral scholarship.

References

Abdel-Rahman, A.F.M, 1994. Nature of biotites from alkaline, calc-alkaline and peraluminous magmas. Journal of Petrology, 35, 525-541.

Anderson, J.L., Barth, A.P., Wooden, J.L., Mazdab, F., 2008. Thermometry and Thermobarometers in Granitic Systems. Reviews in Mineralogy and Geochemistry, 69(1), 121-142.

Anderson, J.L., Smith, D.R., 1995. The Effects of temperature and fO_2 on the Al-in-hornblende barometer. American Mineralogist, 80, 549-559.

Archanjo, C.J., Hollanda, M.H.B.M., Rodrigues, S.W.O, Brito Neves, B.B., Armstong, R., 2008. Fabrics of pre- and syntectonic granite plutons and chronology of shear zones in the Eastern Borborema Province, NE Brazil. Journal of Structural Geology, 30, 310-336.

Archanjo, C.J., Hollanda, M.H.B.M., Viegas, L.G.F., 2021. Late Ediacaran lateral-escape tectonics as recorded by the Patos shear zone, NE Brazil. Brazilian Journal of Geology, 51(2), 1-15.

Bittar, S.M.B., 1998. Faixa Piancó – Alto Brígida: Terrenos tectonoestratigráficos sob regimes metamórficos e deformacionais contrastantes. Ph.D. thesis, Instituto de Geociências-Universidade de São Paulo.

Blundy, J., Holland, T., 1990. Calcic amphibole equilibria and a new amphibole-plagioclase geothermometer. Contributions to Mineralogy and Petrology, 104, 208-224.

Boehnke, P., Watson, E.B., Trail, D., Harrison, T.M., Schmitt, A.K., 2013. Zircon saturation re-revisited. Chemical Geology, 351, 324-334.

Bonin, B., Janoušek, V., Moyen, J.F., 2020. Chemical variation, modal composition and classification of granitoids. Geol. Soc. Lond. Spec., 491, 9–51.

Brandon, A.D., Creaser R.A., Chacko T., 1996. Constraints on Rates of Granitic Magma Transport from Epidote Dissolution Kinetics. Science, 271(5257), 1845-1848.

Brasilino, R.G., Sial, A.N., Ferreira, V.P., Pimentel, M.M., 2011. Bulk rock and mineral chemistries and ascent rates of high-K calc-alkalic epidote-bearing magmas, Northeastern Brazil. Lithos, 127(3-4), 441-454.

Brito Neves, B.B., Cordani, U.G., 1991. Tectonic evolution of South América during the Late Proterozoic. Precambrian Research, 53, 23–40.

Bruguier, O., Caby, R., Bosch, D.C., Ouzegane, K., Deloule, E., Dhuime, B., Bendaoud, A., Kienast, J.R., 2020. A case study of in situ analyses (major and trace elements, U-Pb geochronology and Hf-O isotopes) of a zircon megacryst: Implication for the evolution of the Egéré terrane (Central Hoggar, Tuareg Shield, Algeria). Precambrian Research, 351, 105966.

Buddington, A.F., Lindsley, H.D., 1964. Iron-Titanium oxides minerals and synthetic equivalents. Journal of Petrology, 5(2), 310-357.

Burnham, A. D., Berry A. J., 2012. An experimental study of trace element partitioning between zircon and melt as a function of oxygen fugacity. Geochim. Cosmochim. Acta, 95, 196-212.

Caxito, F.A., Santos, L.C.M.L., Ganade, C.E., Bendaoud, A., Fettous, E.H., Bouyo, M.H., 2020. Toward an integrated model of geological evolution for NE Brazil–NW Africa: The Borborema Province and its connections to the Trans-Saharan (Benino-Nigerian and Tuareg shields) and Central African orogens. Braz. J. Geol., 50, e20190122.

Chappell, B. W., White, A. J. R., 2001. Two contrasting granite types: 25 years later. Australian Journal of Earth Science, 48(4), 489-499.

Chappell, B.W., White, A.J.R., 1974. Two contrasting granite types. Pacific Geology, 8, 173-174.

Chappell, B.W., White, A.J.R., 1992. I- and S- type granites in Lachlan Fold Belt. Transactions Royal Society Edinburgh, 83, 1–26.

Clark D.A., 1999. Magnetic Petrology of igneous intrusion: implications for exploration and magnetic interpretation. Exploration Geophysics, 30, 5-26.

Czamanske, G. K., Wones, D. R., 1973. Oxidation during magmatic differentiation, Finnmarka Complex, Oslo area, Norway; part 2, the mafic silicates. Journal of Petrology, 14(3), 349-380.

Dall'Agnol R., Teixeira N.P., Rämö O.T., Moura C.A.V., Macambira M.J.B., Oliveira D.C., 2005. Petrogenesis of the Paleoproterozoic, rapakivi, A-type granites of the Archean Carajás Metallogenic Province, Brazil. Lithos, 80, 101-129.

Dall'agnol, R., Oliveira, D.C., 2007. Oxidized, magnetite-series, rapakivi-type granites of Carajás, Brazil: Implications for classification and petrogenesis of A-type granites. Lithos, 93, 215-233.

Deer, W.A., Howie, R.A., Zussman, J., 1992. An introduction to the rock-forming minerals. 2. ed., Longman, Harlow.

Enami, M., Suzuki, K., Liou, J.G., Bird, D.K., 1993. Al-Fe^{3+} anf F-OH substitution in titanite and constraints on their P-T dependence. Eur. J. Mineral., 5, 219-231.

Evans, B.W., Vance, J.A., 1987. Epidote phenocrysts in dacitic dikes, Boulder County, Colorado. Contributions to Mineralogy and Petrology, 96, 178-185.

Ferreira V.P., Sial A.N., Pimentel M.M., Armstrong R., Spicuzza M.J., Guimarães I.P., Silva Filho A.F., 2011. Contrasting sources and P-T crystallization conditions of epidote-bearing granitic rocks, northeastern Brazil: O, Sr, and Nd Isotopes. Lithos, 121(1-4), 189-201.

Ferreira V.P., Valley J.W., Sial A.N, Spicuzza M.J., 2003. Oxygen isotope compositions and magmatic epidote from two contrasting metaluminous granitoids, NE Brazil. Contributions to Mineralogy and Petrology, 145, 205-216.

Ferreira, C.A., Santos, E.J., 2000. Jaguaribe SE - Folha SB. 24-Z, Estados do Ceará, Rio Grande do Norte, Paraíba e Pernambuco, single ed. Programa Levantamentos Geológicos Básicos do Brasil-CPRM, 1:500.000.

Ferreira, V.P., Sial, A.N., Pimentel, M.M., Armstrong, R., Guimarães, I.P., Silva Filho, A.F., Lima, M.M.C., Silva, T.R., 2015. Reworked old crust-derived shoshonitic magma: The Guarany pluton, Northeastern Brazil. Lithos, 232, 150-161.

Frost, B.R., 1991. Introduction to oxygen fugacity and its petrologic importance. In: Lindsley D.H. (Ed.), Oxide Minerals: Petrologic and Magnetic Significance. Mineralogical Society of America, Reviews in Mineralogy, 25, 1-9.

Grimes, C.B., John, B.E., Kelemen, P.B., Mazdab, F.K., Wooden, J.L., Cheadle, M.J., Hanghøj, K., Schwartz, J.J., 2007. Trace element chemistry of zircons from oceanic crust: a method for distinguishing detrital zircon provenance. Geology, 35, 643-646.

Guimarães, I. P., Brito, M. F. L., Lages, G. A., Da Silva Filho, A. F., Santos, L., Brasilino, R. G., 2016. Tonian granitic magmatism of the Borborema Province, NE Brazil: A review. Journal of South American Earth Sciences, 68, 97-112.

Guimaraes, I.P., Da Silva Filho, A.F., Almeida, C.N., Van Schmus, W.R., Araujo, J.M.M., Melo, S.C., Melo, E.B., 2004. Brasiliano (Pan-African) granitic magmatism in the Pajeú-Paraíba belt, northeast Brazil: an isotopic and geochronological approach. Precambrian Res., 135, 23-53.

Guimarães, I.P., Silva Filho, A.F., Almeida, C.N., Macambira, M., and Armstrong, R.A., 2011. U-Pb SHRIMP data constraints on calc-alkaline granitoids with 1.3-1.6 Ga Nd TDM model ages from the central domain of the Borborema province, NE Brazil: Journal of South America Earth Sciences, 31, 383–396.

Hammarstron, J.M., Zen, E.A., 1986. Aluminum in hornblende: An empirical igneous geobarometer. American Mineralogist, 71(11-12), 1297-1313.

Harrison T.M., Watson E.B., 1984. The behavior of apatite during crustal anatexis: Equilibrium and kinetic considerations. Geochimica et Cosmochimica Acta, 48(7), 1467-1477.

Harrison, T. M., Watson, E. B., Aikman, A. B., 2007. Temperature spectra of zircon crystallization in plutonic rocks. Geology, 35(7), 635-638.

Hawthorne, F.C., Oberti, R., Harlow, G.E., Maresch, W.V., Martin, R.F., Schumacher, J.C., Welch, M.D., 2012. Nomenclature of the amphibole supergroup. American Mineralogist, 97(11-12), 2031-2048.

Hibbard, M.J., 1979. Myrmekite as a marker between preaqueous and postaqueous phase saturation in granitic systems. GSA Bulletin, 90 (11), 1047–1062.

Hollister, L.S., Grisson, G.C., Peters, E.K., Stowell, H.H., Sisson, V.B., 1987. Confirmation of the empirical correlation of Al in hornblende with pressure of solidification of calc-alkaline plutons. American Mineralogist, 72, 231-239.

Hoskin, P.W., Schaltegger, U., 2003. The composition of zircon and igneous and metamorphic petrogenesis. Reviews in Mineralogy and Geochemistry, 53(1), 27-62.

Hoskin, P.W.O., 2005. Trace-element composition of hydrothermal zircon and the alteration of Hadean zircon from the Jack Hills, Australia. Geochimica et Cosmochimica Acta, 69(3), 637-648.

Ishihara, S., 1977. Magnetite-series and ilmenite-series granitic rocks. Mining Geology, 27, 293–305.

Jardim De Sá, E.F., 1984. A evolução proterozóica da Província Borborema. In: Proceedings of the XI Geological Symposium of Northeast Brazil. Extended Abstract, 297–316.

Johannes, W., Holtz, F., 1996. Petrogenesis and Experimental Petrology of Granitic Rocks, first ed. Springer, Berlim.

Johnston A.D., Wyllie P.J., 1988. Interaction of granitic and basic magmas: experimental observations on contamination processes at 10 kbar with H_2O. Contributions to Mineralogy and Petrology, 98, 352-362.

Leite, P.R.L.B., Bertrand, J.M., Lima, E.S., Leterrier, J., 2000. Timing of granitic magmatismin the northern Borborema Province, Brazil: A U-BP study of granitoids from the Alto Pajeu Terrain. Journal of South American Earth Sciences, 13, 549–559.

Lima, B.T.A., Ferreira, V.P., Ardila, D.H., Neves, C.H.F.S., Sial, A.N., 2021a. Crystallization conditions of the Carmo stock, NE Brazil: Implications for magmatic epidote-bearing granitoids petrogenesis. Journal of South American Earth Sciences, 110(5-6), 103427.

Lima, J.V., Guimarães, I.P., Neves, S.P., Archanjo, C.J., Amorim, J.V.A., Farias, D.J.S., Martins, J.V., 2021c. Multiple sources and multi-stage emplacement of the Esperança Granitic complex and its relationship with the Patos – Campina Grande shear zone system, Borborema Province - NE Brazil. Lithos, 404-405, 106477.

Lima, J.V., Guimaraes, I.P., Neves, S.P., Baseis, M.A.S., da Silva Filho, A.F., Brainer, C.C.G., 2021b. Post-collisional, high-Ba-Sr Teixeira Batholith granites: Evidence for recycling of Paleoproterozoic crust in the Alto Pajeú domain, Borborema Province – NE-Brazil, 405-406, 106469.

Lima, R.G., Archanjo, C.J., Macedo, J.W.P., Melo Jr., G., 2000. Anomalias de suscetibilidade magnética no batólito granıtico de Teixeira (Província da Borborema, Nordeste do Brasil) e sua relação com a zona de cisalhamento de Itapetim. Revista Brasileira de Geociências, 30 (4), 685–692.

Liou, J.G., 1973. Synthesis and stability relations of epidote, $Ca_2AI_2FeSi_30_{12}$ (OH). Jour. Petrol., 14, 381-413.

Litvinovsky, B.A., Vapnik, Y., Eyal, M., Eyal, Y., 2021. The role of mantle and the ancient continental crust in the generation of post-collisional high-K calc-alkaline and alkaline granites, with main reference to the Arabian-Nubian Shield. Lithos, 388-389, 106049.

Locock, A.J., 2014. An Excel spreadsheet to classify chemical analyses of amphiboles following the IMA 2012 recommendations. Comput. Geosci., 62, 1–11.

Moecher, D.P., McDowell, S.M., Samson, S.D., Miller, C.F., 2014. Ti-in-zircon thermometry and crystallization modeling support hot Grenville granite hypothesis. Geology, 42(3), 267-270.

Molina, J.F., Moreno, J.A., Castro, A., Rodríguez, C., Fershtater, G.B., 2015. Calcic amphibole thermobarometry in metamorphic and igneous rocks: New calibrations based on plagioclase/amphibole Al-Si partitioning and amphibole/liquid Mg partitioning. Lithos, 232, 286-305.

Morimoto, N. 1988. Nomenclature of pyroxenes. Mineralogy and Petrology, 39, 55–76.

Nachit, H., IbhI, A., Abia, E.H., Ohoud, M.B., 2005. Discrimination between primary magmatic biotites, reequilibrated and neoformed biotites. Comptes Rendus Geoscience, 337, 1415-1420.

Nachit, H., Razafimahefa, N., Stussi, J.M. and Carron, J.P., 1985. Composition chimique des biotites et typologie magmatique des granitos. Comptes Rendus de l'Académie des sciences Paris, 301(11), 813–818.

Naney, M.T. 1983. Phase equilibria of rock-forming ferromagnesian silicates in granitic systems. American Journal of Science, 283, 993-1033.

Neves, S. P., Bruguier, O., Vauchez, A., Bosch, D., Silva, J. M. R. And Mariano, G., 2006. Timing of crust formation, deposition of supracrustal sequences, and Transamazonian and Brasiliano metamorphism in the East Pernambuco belt (Borborema Province, NE Brazil): implications for western Gondwana assembly. Precambrian Research, 149, 197-216.

Neves, S.P., 2015. Constrains from zircon geochronology on the tectonic evolution of the Borborema Province: widespread intracontinental Neoproterozoic reworking of a Paleoproterozoic accretionary orogen. J. S. Am. Earth Sci., 58, 150–164.

Norman, M.D., Griffin, W.L., Pearson, N.J., Garcia, M.O., O'Reilly, S.Y., 1998. Quantitative analysis of trace element abundances in glasses and minerals: a comparison of laser ablation inductively coupled plasma mass spectrometry, solution inductively coupled plasma mass spectrometry, proton microprobe and electron microprobe data. J. Anal. At. Spectr., 13, 477–482.

Norman, M.D., Pearson, N.J., Sharmon, A., Griffin, W.L., 1996. Quantitative analysis of trace elements in geological materials by laser ablation ICP-MS: Instrumental operating conditions and calibration of NIST glasses. Geostandards Newsletter, 20, 247-261.

Passchier, C.W., Trouw, R.A.J., 2005. Microtectonics. Springer-Verlag, Berlin/ Heidelberg.

Pupin, J. P., 2000. Granite genesis related to geodynamics from Hf-Y in zircon. Transaction of the Royal Society of Edinburg: Earth Sciences, 91, 254-256.

Putirka, K., 2016. Amphibole thermometers and barometers for igneous systems and some implications for eruption mechanisms of felsic magmas at arc volcanoes. American Mineralogist, 101 (4), 841–858.

Ridolfi, F., Renzulli, A., 2012. Calcic amphiboles in calc-alkaline and alkaline magmas: thermobarometric and chemometric empirical equations valid up to 1,130 °C and 22 GPa. Contribution to Mineralogy and Petrology, 163, 877–895.

Schmidt, M.W., 1992. Amphibole composition in tonalite as a function of pressure: an experimental calibration of the Al-in-hornblende barometer. Contributions to Mineralogy and Petrology, 110, 304-310.

Schmidt, M.W., Poli, S., 2004. Magmatic Epidote. Reviews in Mineralogy and Geochemistry, 56(1), 399-430.

Schmidt, M.W., Thompson, A.B., 1996. Epidote in calc-alkaline magmas: an experimental study of stability, phase relationships, and the role of epidote in Magmatic evolution. American Mineralogist, 81, 424-474.

Sial, A.N., 1990. Epidote-bearing calc-alkalic granitoids in Northeast Brazil. Brazilian Journal of Geology, 20(1-4), 88-100.

Sial, A.N., Ferreira V.P., 2016. Magma associations in Ediacaran granitoids of the Cachoeirinha–Salgueiro and Alto Pajeú terranes, northeastern Brazil: Forty years of studies. Journal of South American Earth Sciences, 68, 113-133.

Sial, A.N., Toselli, A.J., Saavedra, J., Parada, M.A., Ferreira, V.P., 1999. Emplacement, petrological and magnetic susceptibility characteristics of diverse magmatic epidote-bearing granitoid rocks in Brazil, Argentina, and Chile. Lithos, 46, 367-392.

Sial, A.N., Vasconcelos, P.M., Ferreira, V.P., Pessoa, R.R., Brasilino, R.G., Morais Neto, J.M., 2008. Geochronological and mineralogical constraints on depth of emplacement and ascension rates of epidote-bearing magmas from northeastern Brazil. Lithos, 105(3-4), 225-238.

Silva, T.R., Ferreira, V.P., Lima, M.M.C., Sial, A.N., 2020. Rapid magma ascent and formation of the Águas Belas-Canindé granitic batholith, NE Brazil: evidence of epidote dissolution and thermobarometry. Brazilian Journal of Geology, 50(2), 01-10.

Speer, J. A., 1984. Micas in igneous rocks. Reviews in Mineralogy and Geochemistry, 13, 299-356.

Stussi, J.M., Cuney, M., 1996. Nature of biotite from alkaline, calc-alkaline and peraluminous magmas by Abdel-Fatthan M. Abdel-Rahman: a comment. Journal of Petrology, 37, 1025-1029.

Taylor, S.R., McLennan, S.H., 1985. The Continental Crust: Its Composition and Evolution, Blackwell Scientific, Oxford.

Trail, D., Watson, E.B., Tailby, N.D., 2012. Ce and Eu anomalies in zircon as proxies for the oxidation state of magmas. Geochimica et Cosmochimica Acta, 97 (2012), 70–87.

Trompette, R., 1997. Geology of Western Gondwana (200–500 Ma) Pan-African Aggregation of South America and Africa, first ed. Bakelma, Rotterdam/Broofield.

Tulloch, A.J., 1979. Secondary Ca-Al silicates as low-grade alteration products of granitoid biotite. Contrib. Mineral. Petrol., 69, 105-117.

Van Achterbergh, E., Ryan, C.G., Jackson, S.E., Griffin, W.L., 2001. Data Reduction Software for LA-ICP-MS: Appendix. Assocication Canada (MAC), Canada, 239p.

Van Schmus, W. R., Kozuch, M., Brito Neves, B. B., 2011. Precambrian history of the Zona Transversal of the Borborema Province, NE Brazil: Insights from SmeNd and UePb geochronology. Journal of South American Earth Sciences 31, 227-252.

Van Schmus, W.R., Brito Neves, B.B, Harckspacher, P., Babinsky, M., 1995. U/BP and Sm/Nd geochronologic studies of the eastern Borborema Province, northeastern Brazil: initial conclusions. Journal of South American Earth Science, 8, 267-288.

Van Schmus, W.R., Oliveira, E.P., Silva Filho, A.F., Toteu, S.F., Penaye, J., Guimarães, I.P., 2008. Proterozoic links between the Borborema province, NE Brazil, and the Central African Fold Belt. Geological Society of London, Special Publication, 294, 69–99.

Vauchez, A., Neves, S.P., Caby, R., Corsini, M., Egydio-Silva, M., Arthaud, M.H., Amaro, V., 1995. The Borborema shear zone system, NE Brazil. Journal of South American Earth Science, 8, 247-266.

Viegas, L.G.F., Archanjo, C.J., Hollanda, M.H.B.M., Vauchea, A., 2014. Microfabrics and zircon UePb (SHRIMP) chronology of mylonites fromthe Patos shear zone (Borborema Province, NE Brazil). Precambrian Research, 243, 1-17.

Vilalva, F.C.J., Simonetti, A., Vlach, S.R.F., 2019. Insights on the origin of the Graciosa A-type granites and syenites (Southern Brazil) from zircon U-Pb geochronology, chemistry, and Hf and O isotope compositions. Lithos, 340–341, 20– 33.

Vyhnal, C.R., McSween, H.Y., Speer, J.A., 1991. Hornblende chemistry in southern Appalachian granitoids: Implication for aluminum hornblende thermobarometry and magmatic epidote stability. American Mineralogist, 76(1-2), 176-188.

Watson, E.B., 1979. Zircon saturation in felsic liquids: experimental data and applications to trace element geochemistry, Contrib. Mineral. Petrol., 70, 407-419.

Watson, E.B., 1987. The hole of accessory minerals in granitoids geochemistry. In: Hutton Conference of The Origin of Granites, 4, Edinburgh, 209-211.

Watson, E.B., Harrison, T.M., 1983. Zircon saturation revisited: temperature and composition effects in a variety of crustal magma types. Earth and Planetary Science Letters, 64, 295 – 304.

Watson, E.B., Wark, D.A., Thomas, J.B., 2006. Crystallization thermometers for zircon and rutile. Contrib. Mineral. Petrol., 151, 413–433.

Wedepohl, K. H., 1991. Chemical composition and fractionation of the continental crust. Geologische Rundschau, 80, 207-223.

Wones, D.R., 1989. Significance of the assemblage titanite + magnetite + quartz in granitic rocks. American Mineralogist, 74 (7-8), 744–749.

Zen, E., Hammarstron, J.M., 1984. Magmatic epidote and its petrologic significance. Geology, 12, 515-518.

Table 1 Representative electron microprobe analyses of amphiboles of the Teixeira Batholith

Facies	Pedra D'Água Facies						São Sebastião Facies						Tendó Facies					
Sample	JD11	JD11	JD11	JD28	JD28	JD28	JD40	JD40	JD40	JD30	JD30	JD30	JD01A	JD01A	JD01B	JD01B	JD01AB	JD01B
Spot	C2af2	C2af3	C3af1	C4af1	C6af1	C7af2	C2af1	C2af2	C6af2	C1af1	C2af1	C3af2	C3af1	C6af1	C3af1	C3af2	C8af2	C4af2
wt.%																		
SiO_2	42.44	43.24	41.71	45.11	43.88	43.06	43.13	40.59	39.97	41.75	42.79	43.08	40.69	43.28	43.76	43.08	42.57	37.11
TiO_2	bdl	0.20	bdl	0.54	0.36	0.50	0.19	0.25	0.32	0.92	0.61	1.19	0.94	0.76	0.75	0.82	0.61	0.61
Al_2O_3	7.44	7.18	7.75	9.64	10.42	9.77	7.69	9.61	9.84	9.40	8.49	7.95	10.31	8.78	8.18	8.52	8.82	8.46
Cr_2O_3	0.06	bdl	bdl	0.02	0.13	0.03	0.19	0.01	0.04	0.04	0.06	0.02	0.03	bdl	bdl	0.03	0.06	0.01
MnO	0.85	1.27	1.22	1.02	0.92	1.11	0.84	0.84	0.85	0.86	0.77	0.86	0.56	0.73	0.82	0.66	0.90	0.69
FeO	25.84	26.05	25.47	19.00	20.52	21.96	23.43	24.81	25.40	24.67	23.63	24.50	23.45	22.70	22.15	22.52	23.26	22.41
NiO	bdl	0.10	0.03	0.04	0.01	0.01	0.02	0.01	0.04	0.03	bdl	0.04	0.11	0.08	bdl	bdl	bdl	0.01
MgO	5.13	5.18	5.18	7.84	7.00	6.46	7.07	5.52	5.35	5.59	6.33	6.03	6.15	7.08	7.89	7.35	6.87	6.25
CaO	11.29	11.27	11.31	11.16	11.21	11.18	11.24	11.10	11.15	11.03	11.26	11.08	11.13	11.21	11.19	10.87	10.88	10.59
Na_2O	1.33	1.15	1.25	1.55	1.31	1.68	1.49	1.58	1.55	1.65	1.46	1.46	1.23	1.28	1.38	1.42	1.57	1.35
K_2O	1.24	1.09	1.19	1.40	1.32	1.42	1.35	1.79	1.70	1.51	1.26	1.22	1.59	1.28	1.24	1.23	1.38	1.53
F	0.61	0.24	0.38	bdl	0.20	0.38	0.69	0.92	0.23	0.56	0.56	0.58	0.54	0.64	0.53	0.50	0.45	0.53
Cl	bdl	bdl	0.00	0.01	0.21	0.01	bdl	0.01	0.00	0.03	0.02	0.01	0.02	0.01	0.02	bdl	0.01	0.02
O=F,Cl	-0.26	-0.10	-0.16	0.00	-0.13	-0.16	-0.29	-0.39	-0.10	-0.24	-0.24	-0.25	-0.23	-0.27	-0.23	-0.21	-0.19	-0.23
Total	95.97	96.85	95.32	97.31	97.35	97.40	97.04	96.63	96.34	97.78	96.98	97.78	96.52	97.56	97.66	96.80	97.17	89.32
Structural formulae based on 23 oxygens																		
Si	6.86	6.91	6.79	6.89	6.77	6.73	6.82	6.55	6.47	6.63	6.78	6.81	6.51	6.77	6.82	6.79	6.72	6.47
Ti	0.00	0.02	0.00	0.06	0.04	0.06	0.02	0.03	0.04	0.11	0.07	0.14	0.11	0.09	0.09	0.10	0.07	0.08
Al	1.42	1.35	1.49	1.74	1.89	1.80	1.43	1.83	1.88	1.76	1.58	1.48	1.94	1.62	1.50	1.58	1.64	1.74
Cr	0.01	0.00	0.00	0.00	0.02	0.00	0.02	0.00	0.00	0.00	0.01	0.00	0.00	0.00	0.00	0.00	0.01	0.00
Mn^{2+}	0.12	0.17	0.17	0.13	0.12	0.15	0.11	0.11	0.12	0.12	0.10	0.12	0.08	0.10	0.11	0.09	0.12	0.10
Fe^{2+}	3.49	3.48	3.47	2.43	2.65	2.87	3.10	3.35	3.44	3.27	3.13	3.24	3.14	2.97	2.89	2.97	3.07	3.27
Ni	0.00	0.01	0.00	0.00	0.00	0.00	0.00	0.00	0.01	0.00	0.00	0.01	0.01	0.01	0.00	0.00	0.00	0.00
Mg	1.24	1.23	1.26	1.79	1.61	1.50	1.67	1.33	1.29	1.32	1.49	1.42	1.47	1.65	1.83	1.73	1.62	1.62
Ca	1.96	1.93	1.97	1.83	1.85	1.87	1.90	1.92	1.93	1.88	1.91	1.88	1.91	1.88	1.87	1.83	1.84	1.98
Na	0.42	0.36	0.39	0.46	0.39	0.51	0.46	0.49	0.49	0.51	0.45	0.45	0.38	0.39	0.42	0.43	0.48	0.46
K	0.26	0.22	0.25	0.27	0.26	0.28	0.27	0.37	0.35	0.30	0.25	0.25	0.32	0.26	0.25	0.25	0.28	0.34
Sum	15.76	15.70	15.79	15.61	15.60	15.77	15.82	15.97	16.01	15.90	15.78	15.80	15.87	15.74	15.76	15.77	15.84	16.06

(continued on next page)

Table 1 (continued)

Facies	Jabre Facies						Mãe D'Água Facies						Santo Antonio Facies					
Sample	JD70	JD70	JD70	JD70	JD70	JD70	JD63	JD63	JD63	JD63	JD63	JD63	IM02	IM02	JD54B	JD54B	JD54B	JD54B
Spot	C2af1	C2af2	C3af1	C5af1	C5af2	C7af1	C4af1	C6af1	C6af2	C7af1	C8af1	C9af2	C11af2	C13af1	C7af1	C3af1	C6af2	C6af1
wt.%																		
SiO_2	42.56	42.57	41.70	41.84	41.71	42.96	43.86	44.08	43.98	44.14	43.49	42.75	40.99	41.89	42.30	42.43	42.11	42.05
TiO_2	0.16	0.48	1.11	0.79	0.90	0.88	1.12	1.19	0.81	1.06	0.85	0.58	0.77	0.95	0.06	0.20	0.05	0.01
Al_2O_3	10.36	9.53	8.95	8.64	8.70	8.06	9.53	9.32	9.45	9.20	9.29	9.45	9.67	9.22	8.57	8.77	8.66	9.16
Cr_2O_3	0.05	0.01	bdl	bdl	bdl	0.05	bdl	0.03	0.03	0.02	0.05	0.01	0.06	0.03	0.07	0.16	0.08	0.07
MnO	0.81	0.76	0.70	0.86	0.75	0.83	0.63	0.66	0.69	0.60	0.64	0.77	0.97	1.36	1.40	1.42	1.42	1.48
FeO	22.16	23.98	24.10	23.85	23.85	23.45	21.84	21.65	21.21	21.46	22.16	22.24	23.33	21.12	22.42	22.97	22.86	23.24
NiO	bdl	0.14	0.03	bdl	bdl	0.02	0.04	bdl	0.05	bdl	bdl	bdl	0.05	bdl	bdl	0.01	bdl	0.01
MgO	6.58	6.24	5.98	6.40	6.27	6.72	7.37	7.78	8.26	7.77	7.32	7.20	6.07	7.41	7.75	7.24	7.38	7.03
CaO	11.21	11.59	11.27	11.50	11.37	11.47	11.16	10.85	10.99	11.14	11.45	11.16	11.00	11.07	10.86	10.76	10.93	11.30
Na_2O	0.96	1.14	1.25	1.14	1.15	0.95	1.53	1.65	1.53	1.54	1.38	1.41	1.19	1.50	1.51	1.56	1.42	1.50
K_2O	1.13	1.21	1.38	1.23	1.30	1.07	1.39	1.31	1.31	1.16	1.37	1.36	1.44	1.38	1.33	1.30	1.34	1.43
F	0.00	0.75	0.88	0.56	0.34	0.71	0.30	0.24	0.41	0.05	0.05	0.65	0.61	0.91	0.49	0.56	0.79	0.70
Cl	bdl	0.02	bdl	0.01	0.01	0.02	0.02	0.02	0.01	0.01	bdl	0.01	bdl	bdl	bdl	bdl	bdl	bdl
O=F,Cl	0.00	-0.32	-0.37	-0.24	-0.14	-0.30	-0.13	-0.10	-0.18	-0.02	-0.02	-0.28	-0.26	-0.38	-0.21	-0.24	-0.33	-0.29
Total	95.99	98.09	96.99	96.58	96.20	96.88	98.67	98.66	98.55	98.11	98.04	97.29	95.88	96.47	96.55	97.12	96.70	97.67
Structural formulae based on 23 oxygens																		
Si	6.69	6.67	6.67	6.68	6.68	6.81	6.75	6.77	6.74	6.79	6.73	6.70	6.59	6.65	6.70	6.69	6.68	6.62
Ti	0.02	0.06	0.13	0.09	0.11	0.10	0.13	0.14	0.09	0.12	0.10	0.07	0.09	0.11	0.01	0.02	0.01	0.00
Al	1.92	1.76	1.69	1.63	1.64	1.51	1.73	1.69	1.71	1.67	1.70	1.75	1.83	1.72	1.60	1.63	1.62	1.70
Cr	0.01	0.00	0.00	0.00	0.00	0.01	0.00	0.00	0.00	0.00	0.01	0.00	0.01	0.00	0.01	0.02	0.01	0.01
Mn^{2+}	0.11	0.10	0.09	0.12	0.10	0.11	0.08	0.09	0.09	0.08	0.08	0.10	0.13	0.18	0.19	0.19	0.19	0.20
Fe^{2+}	2.91	3.14	3.22	3.19	3.20	3.11	2.81	2.78	2.72	2.76	2.87	2.91	3.14	2.80	2.97	3.03	3.03	3.06
Ni	0.00	0.02	0.00	0.00	0.00	0.00	0.00	0.00	0.01	0.00	0.00	0.00	0.01	0.00	0.00	0.00	0.00	0.00
Mg	1.54	1.46	1.43	1.53	1.50	1.59	1.69	1.78	1.89	1.78	1.69	1.68	1.46	1.75	1.83	1.70	1.75	1.65
Ca	1.89	1.95	1.93	1.97	1.95	1.95	1.84	1.78	1.80	1.84	1.90	1.87	1.90	1.88	1.84	1.82	1.86	1.91
Na	0.29	0.35	0.39	0.35	0.36	0.29	0.46	0.49	0.45	0.46	0.41	0.43	0.37	0.46	0.46	0.48	0.44	0.46
K	0.23	0.24	0.28	0.25	0.26	0.22	0.27	0.26	0.26	0.23	0.27	0.27	0.30	0.28	0.27	0.26	0.27	0.29
Sum	15.61	15.74	15.83	15.81	15.81	15.69	15.76	15.77	15.76	15.72	15.76	15.78	15.82	15.86	15.87	15.85	15.86	15.90

Table 2 Representative electron microprobe analyses of biotite of the Teixeira Batholith.

Facies	Pedra D'Água Facies			Tendó Facies			Mãe D'Água Facies			Santo Antônio Facies		
Sample	JD11	JD11	JD11	JD01AB	JD01B	JD01B	JD63	JD63	JD73	IM02	IM02	IM02
Spot	C3bt01	C3bt02	C4bt01	C1bt1	C1bt2	C10bt2	C3bt1	C10bt1	C4bt1	C4bt1	C1bt1	C13bt1
wt.%												
SiO_2	34.08	35.27	34.57	37.15	36.58	36.16	36.88	36.79	36.95	38.58	32.59	37.22
TiO_2	2.95	2.51	2.98	1.31	1.09	1.19	1.23	1.48	1.53	0.64	0.78	1.21
Al_2O_3	13.87	14.61	14.09	13.71	13.50	13.68	13.59	13.42	15.51	12.87	10.76	13.21
FeO	26.77	26.78	26.41	21.21	20.13	21.59	21.62	22.80	20.24	19.45	13.21	20.58
MnO	0.63	0.62	0.65	0.41	0.15	0.60	0.46	0.43	0.36	1.08	0.03	1.00
MgO	5.89	6.10	6.02	10.42	10.61	9.49	10.40	9.80	10.55	11.40	10.16	10.09
CaO	0.01	0.03	0.01	0.01	0.13	0.00	0.03	0.05	0.00	0.01	0.00	0.07
Na_2O	0.05	0.11	0.02	0.04	0.07	0.08	0.03	0.04	0.09	0.02	0.02	0.06
K_2O	8.97	8.10	8.98	9.37	9.26	9.12	8.67	8.95	10.15	9.61	7.52	9.29
BaO	-	-	-	0.13	0.18	0.23	-	-	-	0.09	0.00	0.11
F	0.88	0.58	0.68	1.65	1.66	1.31	0.40	0.84	0.56	2.45	2.72	2.17
Cl	0.01	0.00	0.02	0.00	0.03	0.00	0.00	0.00	0.01	0.00	0.01	0.01
Cr_2O_3	0.08	0.02	0.00	0.00	0.01	0.03	0.06	0.06	0.01	0.00	0.00	0.14
NiO	0.00	0.08	0.05	0.08	0.02	0.06	0.00	0.03	0.01	0.01	0.02	0.00
Li_2O*	0.23	0.57	0.37	1.11	0.95	0.83	1.03	1.01	1.05	1.52	0.00	1.13
H_2O*	3.26	3.51	3.40	3.10	3.01	3.16	3.66	3.46	3.69	2.77	1.88	2.82
Subtotal	97.68	98.88	98.27	99.70	97.36	97.51	98.06	99.15	100.70	100.50	79.71	99.08
O=F,Cl	0.37	0.24	0.29	0.70	0.70	0.55	0.17	0.35	0.24	1.03	1.15	0.92
Total	97.30	98.64	97.98	99.00	96.66	96.96	97.89	98.79	100.47	99.47	78.56	98.17
Structural formulae based on 24 oxygens												
Si	5.55	5.59	5.56	5.74	5.77	5.73	5.74	5.72	5.60	5.88	6.16	5.80
Al^{iv}	2.45	2.41	2.44	2.26	2.23	2.27	2.26	2.28	2.40	2.12	1.84	2.20
Al^{vi}	0.21	0.33	0.24	0.23	0.28	0.29	0.23	0.18	0.36	0.19	0.55	0.22
Ti	0.36	0.30	0.36	0.15	0.13	0.14	0.14	0.17	0.17	0.07	0.11	0.14
Cr	0.01	0.00	0.00	0.00	0.00	0.00	0.01	0.01	0.00	0.00	0.00	0.02
Fe	3.64	3.55	3.55	2.74	2.65	2.86	2.81	2.96	2.56	2.48	2.09	2.68
Mn	0.09	0.08	0.09	0.05	0.02	0.08	0.06	0.06	0.05	0.14	0.01	0.13
Mg	1.43	1.44	1.44	2.40	2.49	2.24	2.41	2.27	2.38	2.59	2.86	2.34
Ni	0.00	0.01	0.01	0.01	0.00	0.01	0.00	0.00	0.00	0.00	0.00	0.00
Li*	0.15	0.36	0.24	0.69	0.60	0.53	0.65	0.63	0.64	0.93	0.00	0.71
Ca	0.00	0.01	0.00	0.00	0.02	0.00	0.00	0.01	0.00	0.00	0.00	0.01
Na	0.02	0.03	0.01	0.01	0.02	0.03	0.01	0.01	0.02	0.01	0.01	0.02
K	1.86	1.64	1.84	1.85	1.86	1.84	1.72	1.78	1.96	1.87	1.81	1.85
Ba	0.00	0.00	0.00	0.01	0.01	0.01	0.00	0.00	0.00	0.01	0.00	0.01
OH*	3.55	3.71	3.65	3.19	3.17	3.34	3.80	3.59	3.73	2.82	2.37	2.93
F	0.45	0.29	0.35	0.81	0.83	0.66	0.20	0.41	0.27	1.18	1.62	1.07
Cl	0.00	0.00	0.00	0.00	0.01	0.00	0.00	0.00	0.00	0.00	0.00	0.00
Fe/Fe+Mg	0.72	0.71	0.71	0.53	0.52	0.56	0.54	0.57	0.52	0.49	0.42	0.53

Li_2O and H_2O calculations after Tindle and Webb (1990)

Table 3 Representative electron microprobe analyses of clinopyroxene of the Santo Antônio Facies.

Sample	JD39	JD39	JD39	JD40	JD40	JD40
Spot	C6px1	C9px1	C10px2	C1px1	C4px01	C8px01
wt.%						
SiO_2	50.32	50.78	50.11	51.27	51.13	51.83
TiO_2	0.057	0.062	0.055	0	0.028	0.024
Al_2O_3	0.78	1.017	1.15	0.021	1.023	0.78
FeO	20.62	20.97	21.31	17.22	16.54	15.85
MnO	1.07	1.11	1.17	0.017	0.01	1.11
MgO	4.90	4.49	4.29	7.67	7.43	7.35
CaO	18.58	18.77	18.19	21.38	21.46	21.19
Na_2O	2.33	2.43	2.69	1.31	1.48	1.30
Cr_2O_3	0	0.02	0	0.04	0	0
V_2O_3	0.04	0.06	0.06	0.02	0	0.05
NiO	0.07	0.02	0.01	0.01	0	0.01
Total	98.80	99.75	99.05	98.96	99.09	99.50
Structural formulae based on 6 oxygens						
Si	1.987	1.989	1.975	1.998	1.983	2.009
Al	0.013	0.011	0.025	0.001	0.017	0.000
Fe^{3+}	0.000	0.000	0.000	0.001	0.000	0.000
ΣT	2	2	2	2	2	2
Al	0.024	0.036	0.029	0.000	0.030	0.036
Fe^{3+}	0.162	0.154	0.197	0.099	0.096	0.041
Ti	0.002	0.002	0.002	0.000	0.001	0.001
Cr	0.000	0.001	0.000	0.001	0.000	0.000
V	0.001	0.002	0.002	0.000	0.000	0.002
Ni	0.002	0.001	0.000	0.000	0.000	0.000
Mg	0.289	0.262	0.252	0.446	0.430	0.425
Fe^{2+}	0.519	0.533	0.505	0.453	0.440	0.472
Mn	0.000	0.010	0.013	0.000	0.000	0.023
ΣM1	1	1	1	1	1	1
Fe^{2+}	0.000	0.000	0.000	0.008	0.000	0.000
Mn	0.035	0.027	0.026	0.001	0.000	0.013
Li	0.000	0.000	0.000	0.000	0.000	0.000
Ca	0.786	0.788	0.768	0.893	0.892	0.880
Na	0.178	0.185	0.206	0.099	0.111	0.098
ΣM2	1	1	1	1	1	1
J	0.357	0.370	0.412	0.198	0.222	0.196
Q	1.594	1.584	1.525	1.799	1.762	1.777
%Wo	44.768	45.349	44.596	46.997	47.998	48.395
%En	16.445	15.105	14.628	23.454	23.128	23.349
%Fs	38.787	39.546	40.776	29.548	28.874	28.257
Total	100	100	100	100	100	100
%Q	79.985	79.788	75.272	89.853	86.052	92.009
%Jd	3.735	4.730	5.293	0.096	4.568	3.708
%Ae	16.280	15.482	19.436	10.051	9.380	4.283
Total	100	100	100	100	100	100

Table 4 Representative electron microprobe analyses of plagioclase of the Teixeira Batholith.

Facies	Pedra D'Água Facies			São Sebastião Facies			Tendó Facies			Jabre Facies			Mãe D'Água Facies			Santo Antônio Facies		
Sample	JD28	JD28	JD11	JD30	JD39	JD39	JD01A	JD01A	JD01AB	JD70	JD70	JD70	JD63	JD63	JD73	JM02	JM02	JD54B
Spot	C7pl1	C10pl1	C2pl1	C5pl1	C7pl2	C10pl1	C2pl1.B	C6pl1	C12 pl1	C3pl1	C5pl2	C8pl2	C8pl01	C10pl1.c	C2pl2	C2pl1.c	C8pl1	C3pl1
wt.%																		
SiO_2	64.67	63.97	65.40	65.48	67.24	65.59	65.58	65.34	66.57	64.69	64.34	67.51	64.13	64.34	63.98	64.76	67.07	66.19
TiO_2	0.04	0.00	0.00	0.00	0.04	0.03	0.04	0.00	0.03	0.03	0.00	0.00	0.03	0.05	0.06	0.06	0.00	0.00
Al_2O_3	22.50	23.35	20.41	21.17	19.85	21.74	21.12	21.32	21.63	21.69	21.74	19.93	21.27	22.00	22.41	21.54	19.94	21.19
FeO	0.05	0.03	0.07	0.04	0.15	0.06	0.04	0.07	0.25	0.07	0.00	0.00	0.00	0.04	0.00	0.04	0.03	0.06
MgO	0.00	0.00	0.03	0.02	0.00	0.00	0.01	0.00	0.06	0.00	0.02	0.00	0.01	0.00	0.00	0.00	0.00	0.00
CaO	2.44	2.84	1.89	2.04	0.19	0.03	2.25	2.70	3.12	2.36	2.71	0.73	3.60	3.25	3.77	2.79	1.41	2.19
BaO	0.00	0.00	0.00	0.00	0.00	0.00	0.03	0.06	0.15	0.00	0.00	0.00	0.00	0.00	0.00	0.07	0.01	0.00
Na_2O	9.53	8.73	10.68	10.51	11.16	9.09	10.39	9.59	9.08	10.06	9.80	11.22	9.91	10.07	9.54	9.20	10.44	10.78
K_2O	0.14	0.22	0.21	0.15	0.07	2.66	0.16	0.23	0.18	0.07	0.14	0.07	0.14	0.13	0.06	0.08	0.08	0.12
Total	99.35	99.14	98.67	99.41	98.69	99.19	99.61	99.29	101.07	98.96	98.75	99.45	99.10	99.88	99.82	98.53	98.98	100.53
Structural formulae based on 24 oxygens																		
Si	2.40	2.38	2.45	2.43	2.50	2.45	2.44	2.43	2.44	2.41	2.41	2.50	2.40	2.39	2.38	2.42	2.49	2.44
Ti	0.00	0.00	0.00	0.00	0.00	0.00	0.00	0.00	0.00	0.00	0.00	0.00	0.00	0.00	0.00	0.00	0.00	0.00
Al	0.98	1.02	0.90	0.93	0.87	0.96	0.92	0.93	0.93	0.95	0.96	0.87	0.94	0.96	0.98	0.95	0.87	0.92
Mg	0.00	0.00	0.00	0.00	0.00	0.00	0.00	0.00	0.00	0.00	0.00	0.00	0.00	0.00	0.00	0.00	0.00	0.00
Ca	0.10	0.11	0.08	0.08	0.01	0.00	0.09	0.11	0.12	0.09	0.11	0.03	0.14	0.13	0.15	0.11	0.06	0.09
Ba	0.00	0.00	0.00	0.00	0.00	0.00	0.00	0.00	0.00	0.00	0.00	0.00	0.00	0.00	0.00	0.00	0.00	0.00
Na	0.69	0.63	0.77	0.76	0.80	0.66	0.75	0.69	0.65	0.73	0.71	0.81	0.72	0.73	0.69	0.67	0.75	0.77
K	0.01	0.01	0.01	0.01	0.00	0.13	0.01	0.01	0.01	0.00	0.01	0.00	0.01	0.01	0.00	0.00	0.00	0.01
Or	0.84	1.39	1.14	0.84	0.42	16.11	0.91	1.33	1.10	0.37	0.81	0.38	0.78	0.74	0.34	0.51	0.45	0.65
An	12.30	15.03	8.79	9.60	0.95	0.15	10.57	13.26	15.78	11.45	13.15	3.44	16.59	15.04	17.87	14.29	6.93	10.04
Ab	86.86	83.57	90.07	89.57	98.63	83.75	88.52	85.41	83.13	88.18	86.04	96.17	82.63	84.22	81.79	85.20	92.62	89.30

Table 5 Representative electron microprobe analyses of K-feldspar of the Teixeira Batholith.

Facies	São Sebastião Facies				Tendó Facies				Mãe D'Água Facies		SAF
Sample	JD40	JD40	JD39	JD39	JD01A	JD01AB	JD01AB	JD01AB	JD63	JD63	JM02
Spot	C1pl1	C9pl02	C3pl1	C4pl1	C2pl1.c	C6kf1	C6kf2	C8kf1	C4pl01	C6pl01	C3kf1
wt.%											
SiO_2	63.84	63.58	63.10	61.11	64.32	63.37	63.71	64.21	63.97	61.65	64.19
TiO_2	0.02	0.02	0.02	0.00	0.10	0.00	0.00	0.00	0.00	0.03	0.11
Al_2O_3	19.47	19.45	19.67	18.29	18.62	18.16	18.62	18.56	19.70	16.04	17.95
FeO	0.06	0.09	0.03	0.04	0.08	0.00	0.02	0.09	0.10	0.06	0.03
MgO	0.00	0.01	0.03	0.00	0.00	0.00	0.00	0.00	0.00	0.00	0.00
CaO	0.00	0.01	0.00	0.00	0.01	0.00	0.01	0.00	0.01	0.04	0.02
BaO	0.00	0.00	0.00	0.00	1.58	1.96	1.60	1.37	0.00	0.00	0.46
Na_2O	0.88	0.86	0.40	0.60	0.83	0.57	1.15	0.88	0.82	1.19	0.80
K_2O	14.96	15.12	15.85	14.67	14.78	15.02	14.20	14.98	15.13	14.20	15.25
Total	99.23	99.13	99.08	94.71	100.31	99.07	99.30	100.09	99.73	93.21	98.82
Structural formulae based on 24 oxygens											
Si	2.47	2.46	2.45	2.46	2.49	2.49	2.48	2.49	2.47	2.51	2.50
Ti	0.00	0.00	0.00	0.00	0.00	0.00	0.00	0.00	0.00	0.00	0.00
Al	0.89	0.89	0.90	0.87	0.85	0.84	0.85	0.85	0.89	0.77	0.82
Mg	0.00	0.00	0.00	0.00	0.00	0.00	0.00	0.00	0.00	0.00	0.00
Ca	0.00	0.00	0.00	0.00	0.00	0.00	0.00	0.00	0.00	0.00	0.00
Ba	0.00	0.00	0.00	0.00	0.02	0.03	0.02	0.02	0.00	0.00	0.01
Na	0.07	0.06	0.03	0.05	0.06	0.04	0.09	0.07	0.06	0.09	0.06
K	0.74	0.75	0.79	0.75	0.73	0.75	0.71	0.74	0.74	0.74	0.76
Or	91.77	92.04	96.33	94.17	92.06	94.57	89.04	91.81	92.35	88.57	92.51
An	0.02	0.03	0.00	0.00	0.06	0.00	0.04	0.00	0.07	0.18	0.09
Ab	8.21	7.93	3.67	5.83	7.88	5.43	10.92	8.19	7.59	11.25	7.40

SAF: Santo Antônio Facies

Table 6 Representative electron microprobe analyses of titanite of the Teixeira Batholith.

Facies	Pedra D'Água Facies			São Sebastião Facies			Tendó Facies			Jabre Facies		Mãe D'Água Facies			Santo Antônio Facies		
Sample	JD28	JD28	JD28	JD40	JD30	JD30	JD01A	JD01AB	JD01AB	JD70	JD70	JD63	JD73	JD73	IM02	IM02	IM02
Spot	C6t1	C9t1	C14t1	C7t01	C4t1	C5t1	C8t1	C7t1	C10t2	C3t1	C3t2	C6t01	C2t1	C3t1	C3t1	C11t1	C12t1
wt.%																	
SiO_2	31.27	30.11	30.45	30.34	29.51	29.87	30.51	30.72	30.85	30.33	30.25	32.13	31.02	31.39	30.83	30.87	30.27
TiO_2	32.67	32.46	33.67	34.97	33.98	33.63	36.59	35.49	33.83	35.99	35.64	35.99	37.00	33.88	31.61	34.12	33.94
Al_2O_3	3.68	3.78	2.91	1.74	2.44	1.87	1.89	1.45	1.66	1.08	1.22	1.91	2.79	3.89	3.00	2.39	2.75
FeO	1.83	1.92	1.96	1.92	1.53	2.29	1.13	1.47	1.83	1.72	2.03	1.09	0.89	1.49	2.75	1.09	1.22
MnO	0.17	0.11	0.21	0.17	0.22	0.20	0.02	0.20	0.14	0.07	0.12	0.17	0.03	0.07	0.27	0.08	0.09
MgO	0.01	0.02	0.01	0.01	0.00	0.03	0.02	0.01	0.01	0.02	0.02	0.00	0.03	0.00	0.10	0.00	0.04
CaO	27.61	27.66	27.42	27.58	26.72	27.26	28.21	27.84	27.54	27.50	27.69	27.27	28.54	29.11	27.83	27.76	27.71
F	0.52	1.34	0.36	0.72	0.11	1.43	0.69	0.62	0.64	0.77	0.77	0.68	0.32	0.60	1.51	0.71	0.56
Cr_2O_3	0.05	0.03	0.00	0.02	0.00	0.02	0.00	0.07	0.09	0.06	0.00	0.06	0.00	0.08	0.12	0.09	0.00
NiO	0.00	0.03	0.01	0.07	0.00	0.00	0.00	0.02	0.00	0.00	0.00	0.00	0.00	0.02	0.01	0.02	0.08
Total	97.74	97.37	96.97	97.45	94.50	96.54	99.04	97.79	96.48	97.47	97.73	99.24	100.58	100.42	97.79	97.03	96.53
Structural formulae based on 5 oxygens																	
Si	1.04	1.02	1.02	1.02	1.02	1.02	1.01	1.03	1.05	1.02	1.02	1.05	1.00	1.02	1.04	1.04	1.02
Al^{iv}	0.14	0.15	0.12	0.07	0.10	0.08	0.07	0.06	0.07	0.04	0.05	0.07	0.11	0.15	0.12	0.09	0.11
Ti	0.82	0.83	0.85	0.89	0.88	0.87	0.91	0.89	0.86	0.91	0.90	0.89	0.90	0.83	0.80	0.86	0.86
Cr	0.00	0.00	0.00	0.00	0.00	0.00	0.00	0.00	0.00	0.00	0.00	0.00	0.00	0.00	0.00	0.00	0.00
Fe^{3+}	0.05	0.05	0.06	0.05	0.04	0.07	0.03	0.04	0.05	0.05	0.06	0.03	0.02	0.04	0.08	0.03	0.03
Mn	0.00	0.00	0.01	0.00	0.01	0.01	0.00	0.01	0.00	0.00	0.00	0.00	0.00	0.00	0.01	0.00	0.00
Mg	0.00	0.00	0.00	0.00	0.00	0.00	0.00	0.00	0.00	0.00	0.00	0.00	0.00	0.00	0.01	0.00	0.00
Ni	0.00	0.00	0.00	0.00	0.00	0.00	0.00	0.00	0.00	0.00	0.00	0.00	0.00	0.00	0.00	0.00	0.00
Ca	0.98	1.00	0.99	0.99	0.99	1.00	1.00	1.00	1.00	0.99	1.00	0.96	0.99	1.01	1.01	1.00	1.00

Table 7 Representative electron microprobe analyses of magnetite of the Teixeira Batholith.

Facies	Pedra D'Água Facies				São Sebastião Facies				Santo Antônio Facies			
Sample	JD28	JD28	JD28	JD28	JD39	JD40	JD39	JD39	IM02	IM02	IM02	JD54B
Spot	C1ox	C4ox2	C10ox1	C13ox1	C3ox1	C5ox01	C5ox1	C7ox1	C6ox2	C15ox1	C15ox2	C4ox1
wt.%												
SiO_2	-	-	-	-	0.03	0.08	0.05	0.11	0.03	0.02	0.03	0.06
TiO_2	0.14	0.16	0.06	0.02	0.00	0.01	0.12	0.12	0.00	0.25	0.00	0.20
Al_2O_3	0.13	0.33	0.03	0.10	0.53	0.04	0.03	0.04	0.04	0.48	0.17	0.08
Fe_2O_3	66.66	66.33	68.31	67.44	65.12	67.35	66.77	69.17	67.53	66.36	67.66	68.98
FeO	29.87	29.87	30.78	29.85	29.61	30.07	30.24	30.86	30.17	30.07	30.51	31.07
MnO	0.59	0.34	0.11	0.66	0.00	0.22	0.00	0.16	0.34	0.61	0.23	0.32
MgO	0.00	0.02	0.04	0.02	0.01	0.02	0.00	0.02	0.00	0.00	0.00	0.03
CaO	0.00	0.01	0.00	0.00	0.00	0.00	0.04	0.06	0.00	0.03	0.00	0.03
Na_2O	-	-	-	-	0.02	0.03	0.00	0.04	0.00	0.00	0.00	0.00
K_2O	0.01	0.05	0.00	0.00	0.00	0.01	0.02	0.03	0.00	0.00	0.00	0.00
Cr_2O_3	0.11	0.08	0.04	0.00	0.00	0.01	0.03	0.00	0.05	0.04	0.09	0.01
V_2O_3	0.22	0.16	0.20	0.23	0.02	0.12	0.07	0.00	0.11	0.14	0.15	0.10
NiO	0.00	0.00	0.02	0.00	0.00	0.04	0.08	0.14	0.03	0.04	0.00	0.13
Total	97.73	97.36	99.58	98.32	95.35	98.00	97.44	100.77	98.30	98.02	98.83	101.01
Structural formulae based on 32 oxygens												
Ni	0.000	0.000	0.001	0.000	0.000	0.001	0.003	0.004	0.001	0.001	0.000	0.004
Si	0.000	0.000	0.000	0.000	0.001	0.003	0.002	0.004	0.001	0.001	0.001	0.002
Ti	0.004	0.005	0.002	0.001	0.000	0.000	0.004	0.004	0.000	0.007	0.000	0.006
Cr	0.003	0.002	0.001	0.000	0.000	0.000	0.001	0.000	0.001	0.001	0.003	0.000
V	0.007	0.005	0.006	0.007	0.001	0.004	0.002	0.000	0.004	0.004	0.005	0.003
Al	0.006	0.015	0.001	0.005	0.025	0.002	0.001	0.002	0.002	0.022	0.008	0.003
Fe^{3+}	1.975	1.970	1.988	1.987	1.973	1.989	1.985	1.986	1.991	1.956	1.983	1.978
Mg	0.000	0.001	0.001	0.001	0.000	0.000	0.000	0.000	0.000	0.000	0.000	0.002
Fe^{2+}	0.004	0.001	0.000	0.000	0.000	0.000	0.002	0.000	0.000	0.007	0.001	0.002
ΣM	2.000	2.000	2.000	2.000	2.000	2.000	2.000	2.000	2.000	2.000	2.000	2.000
Fe^{3+}	0.000	0.000	0.000	0.000	0.001	0.001	0.000	0.001	0.000	0.000	0.000	0.000
Mg	0.000	0.000	0.001	0.000	0.000	0.001	0.000	0.001	0.000	0.000	0.000	0.000
Fe^{2+}	0.980	0.985	0.995	0.978	0.997	0.988	0.997	0.985	0.989	0.979	0.992	0.988
Mn	0.020	0.012	0.004	0.022	0.000	0.007	0.000	0.005	0.011	0.020	0.007	0.010
Ca	0.000	0.001	0.000	0.000	0.000	0.000	0.002	0.003	0.000	0.001	0.000	0.001
Na	0.000	0.000	0.000	0.000	0.002	0.002	0.000	0.003	0.000	0.000	0.000	0.000
K	0.000	0.003	0.000	0.000	0.000	0.000	0.001	0.001	0.000	0.000	0.000	0.000
ΣT	1.000	1.000	1.000	1.000	1.000	1.000	1.000	1.000	1.000	1.000	1.000	1.000
% Mag	97.10	97.98	98.88	97.30	98.69	98.79	99.16	98.57	98.53	96.85	98.88	97.65

Table 8 Representative electron microprobe analyses of sulfides of the Tendó Facies.

Sample	JD01B	JD01B	JD01AB	JD01AB	JD01AB	JD01AB
Spot	C7s1	C8s1	C4s1	C5s1	C6s1	C2s1
wt.%						
Zn	0.00	0.02	0.02	0.01	0.03	0.04
Se	0.00	0.00	0.00	0.00	0.00	0.03
S	53.33	53.66	50.49	52.92	53.29	53.24
Pb	0.13	0.19	0.16	0.18	0.16	0.19
Cd	0.02	0.00	0.04	0.00	0.00	0.00
Fe	44.65	46.32	43.19	45.82	45.00	45.78
Co	0.01	0.02	0.57	0.04	0.03	0.09
Cu	0.00	0.01	0.06	0.02	0.01	0.00
Ni	1.79	0.00	0.52	0.34	1.05	0.03
Mo	0.13	0.08	0.09	0.11	0.09	0.11
Ag	0.00	0.02	0.00	0.01	0.00	0.00
Total	100.06	100.32	95.13	99.44	99.67	99.48

Table 9 Representative electron microprobe analyses of epidote of the Teixeira Batholith.

Facies	Mãe D'Água Facies						Santo Antônio Facies	
Sample	JD63	JD63	JD63	JD73	JD73	JD73	JD54B	JD54B
Spot	C3ep01	C1ep01	C5ep01	C4ep1	C7ep1	C3ep2	C7ep1	C9ep1
wt.%								
SiO_2	38.33	37.37	37.46	37.83	37.98	38.56	37.31	37.08
TiO_2	0.07	0.12	0.03	0.00	0.27	0.11	0.00	0.00
Al_2O_3	21.51	22.19	21.66	21.46	22.52	22.69	21.60	22.03
FeO	13.05	13.00	12.28	13.86	11.51	12.71	14.04	13.62
MnO	0.18	0.20	0.20	0.04	0.25	0.09	0.41	0.52
CaO	22.43	22.31	22.54	22.23	23.24	22.87	22.63	22.70
Total	95.58	95.18	94.17	95.42	95.77	97.02	95.98	95.94
Structural formulae based on 12.5 oxygens								
Si	3.08	3.02	3.06	3.05	3.05	3.05	3.01	2.99
Ti	0.00	0.01	0.00	0.00	0.02	0.01	0.00	0.00
Al	2.04	2.12	2.09	2.04	2.13	2.11	2.05	2.09
Fe^{+3}	0.88	0.88	0.84	0.94	0.77	0.84	0.95	0.92
Mn	0.01	0.01	0.01	0.00	0.02	0.01	0.03	0.04
Ca	1.93	1.93	1.97	1.92	2.00	1.94	1.95	1.96
Ps	0.30	0.29	0.29	0.31	0.27	0.28	0.32	0.30

Table 10 LA-ICPMS analyses of zircon compositions of the Tendó Facies.

Sample	TX08														
Analyses	Pt1	Pt2	Pt3B	Pt3N*	Pt4	Pt5	Pt6N	Pt6B	Pt7	Pt8	Pt9	Pt10	Pt11	Pt12	Pt13
Si	160240.47	165481.38	160617.28	166377.27	162593.55	163992.63	161189.84	161905.98	162574.30	162116.48	165837.27	163889.38	162770.80	168511.20	168422.25
Ti	9.83	13.47	50.72	10.36	17.00	27.88	14.88	4.85	16.78	95.90	36.72	16.59	8.60	6.18	29.37
Zr	496007.16	496007.13	496007.13	496007.16	496007.16	496007.16	496007.16	496007.13	496007.13	496007.13	496007.13	496007.13	496007.16	496007.16	496007.13
Hf	10496.42	10524.59	12330.96	12974.54	11588.25	9531.36	11346.41	11988.27	9508.29	9726.11	11306.36	8357.52	12219.69	14066.36	11185.51
La	0.869	4.61	7.78	<0.092	0.913	0.516	0.170	1124	1.97	22.08	3.42	3.60	6.79	0.079	6.04
Ce	20.44	66.47	111.25	0.609	20.45	20.58	7.39	46.94	38.53	271.49	89.94	91.94	33.21	18.39	57.17
Pr	1.61	6.11	12.21	<0.077	2.24	1166	0.641	0.980	3.33	35.57	5.94	2.76	3.78	0.279	8.25
Nd	10.67	37.00	76.14	<0.63	13.95	7.67	4.27	4.63	23.54	209.89	34.48	12.83	24.91	2.87	54.36
Sm	7.71	22.00	37.30	2.40	11.47	6.59	5.17	3.07	17.29	84.93	16.55	6.70	12.19	7.66	31.06
Eu	3.03	9.27	15.04	0.197	3.30	1.57	1.32	1.47	9.38	30.80	7.51	4.05	4.39	0.54	10.62
Gd	11.40	47.78	38.58	18.43	27.68	17.92	21.82	8.22	47.29	65.63	24.07	25.88	15.36	40.02	32.53
Tb	3.33	14.84	7.87	7.50	8.21	6.34	7.24	2.90	14.09	10.64	6.09	10.24	3.87	14.45	6.96
Dy	33.32	164.18	62.64	63.41	84.27	70.28	81.06	36.35	143.38	85.16	59.33	125.49	39.60	131.72	63.73
Ho	13.93	61.72	21.07	13.34	29.70	28.01	29.75	16.95	49.71	26.71	23.92	47.76	14.68	38.53	24.54
Er	71.04	278.38	100.49	37.38	127.66	137.55	126.87	90.18	200.55	113.97	121.69	210.92	78.06	122.00	126.74
Tm	16.50	57.04	22.90	4.85	27.28	30.49	24.59	22.62	38.02	24.18	29.38	43.52	20.52	18.02	30.82
Yb	178.14	543.59	237.31	37.41	272.87	318.11	223.80	276.63	344.25	235.86	326.12	413.30	232.93	136.27	344.89
Lu	38.73	107.73	52.21	5.82	58.33	66.56	42.31	62.08	64.26	48.48	74.12	75.35	55.16	22.82	77.31
Th	100.46	178.21	313.75	12.25	136.72	97.09	96.57	185.54	110.83	301.08	367.31	111.27	160.96	151.08	156.76
U	339.28	906.85	1087.29	628.1	354.4	231.72	433.07	617.44	619.18	601.9	698.91	729.66	444.82	209.13	655.34
Eu/Eu*	0.99	0.87	1.21	0.09	0.57	0.44	0.38	0.89	1.00	1.26	1.15	0.94	0.98	0.09	1.02
Ce/Ce*	4.05	2.94	2.67	-	3.35	6.21	5.26	10.49	3.52	2.27	4.67	6.84	1.54	28.76	1.89
Sample	JD01														
Analyses	Pt1	Pt2	Pt3	Pt4	Pt5	Pt6	Pt7n	Pt7b	Pt8	Pt9	Pt10	Pt11*	Pt12	Pt13b	Pt13n*
Si	102576.27	92965.38	96262.06	105811.02	140639.39	133784.44	161930.73	160045.56	163301.58	161722.83	167512.03	163140.98	172689.47	169648.53	166380.05
Ti	6.10	12.49	5.09	6.15	76.04	6.99	5.44	723.49	14.30	5.87	15.70	<4.89	<5.14	5.54	4.74
Zr	496007.09	496007.09	496007.13	496007.09	496007.09	496007.09	496007.09	496007.09	496007.06	496007.09	496007.06	496007.09	496007.09	496007.09	496007.06
Hf	7832.28	5233.01	6050.25	8324.91	9273.58	8169.74	11426.07	11436.42	12850.40	12436.17	9067.72	12129.06	12461.10	11579.13	8884.84
La	0.515	4.55	0.838	0.669	24.27	1.68	0.235	4.82	<0.080	1076	2.80	0.078	0.163	<0.074	<0.072
Ce	11.39	28.16	11.49	14.81	252.94	19.99	12.05	33.88	7.40	27.84	48.31	4.67	15.26	18.59	3.84
Pr	0.984	2.32	0.870	0.434	20.79	1.51	0.272	2.89	0.188	2.28	4.19	<0.072	0.234	0.136	<0.054
Nd	6.81	13.59	6.09	2.03	109.56	9.61	2.18	13.60	3.01	17.25	27.70	<0.52	1.13	1.53	0.59
Sm	4.48	8.36	4.02	2.24	49.45	5.35	4.28	4.09	6.57	11.00	18.95	<0.44	2.46	1.29	0.85
Eu	1.45	2.29	1.16	0.498	17.16	3.00	0.442	1.27	0.431	3.36	8.56	0.391	1.73	0.83	0.58
Gd	13.56	14.14	10.20	9.66	59.75	13.14	13.03	7.76	13.63	16.17	39.47	3.22	14.37	6.96	2.75
Tb	4.92	3.94	3.31	3.41	14.44	3.79	3.34	2.41	2.63	3.88	12.64	1.19	5.07	2.85	1.11
Dy	46.68	47.91	36.96	33.20	137.93	40.89	25.58	33.70	22.31	30.45	131.66	16.69	52.69	41.31	9.74
Ho	13.35	18.06	15.18	10.36	48.58	13.94	7.32	14.36	6.55	8.87	45.49	7.02	18.09	18.16	3.30
Er	48.90	83.82	66.07	41.79	207.72	64.36	25.35	79.58	28.11	36.70	187.32	37.30	78.93	98.90	15.35
Tm	8.75	18.97	13.81	8.26	42.58	13.71	4.97	20.15	6.22	7.68	36.51	9.27	16.76	25.73	3.21
Yb	69.90	207.35	128.42	78.67	396.30	137.17	42.29	237.53	70.64	79.48	331.25	109.85	172.25	293.93	31.84
Lu	12.27	46.09	25.99	16.35	74.29	28.64	7.90	56.04	15.30	17.97	61.63	27.74	38.08	68.19	7.00
Th	22.65	41.84	53.12	20.28	371.91	65.94	40.86	135.06	103.68	27.41	228.76	21.8	111.57	118.41	7.61
U	433.15	99.6	128.43	190.67	462.32	220.86	184.06	477.26	394.53	93.35	462.45	432.77	444.39	379.61	49.43
Eu/Eu*	0.57	0.64	0.55	0.33	0.96	1.09	0.18	0.69	0.14	0.77	0.96	-	0.89	0.84	1.15
Ce/Ce*	3.75	2.03	3.15	6.44	2.64	2.94	11.16	2.12	-	4.16	3.30	-	18.38	-	-

Pt* Analyzes with LREE content below detection limit (not plotted in Figure 14).

Table 11 - Estimation of temperature and pressure for the different facies of the Teixeira Batholith

Facies	PAF		SSF		TF		JF		MAF		SAF	
Temperature (°C)	Min	Max	Min	Max	Min	Max	Min	Max	Min	Max	Min	Max
Blund and Holland (1990)	662	735	686	719	696	709	677	713	692	707	707	716
Putirka (2016)	701	758	722	753	727	778	717	747	742	768	725	770
Watson and Harrison (1983)	759	811	766	798	743	787	768	798	763	776	737	767
Boehnke et al. (2013)	703	761	711	746	716	731	709	744	706	722	680	715
Watson et al. (2006)	-	-	-	-	684	988	-	-	-	-	-	-
Molina et al. (2015)	851	996	845	899	891	995	900	919	901	920	827	924
Harrison and Watson (1984)	795	954	772	875	842	922	849	893	880	915	776	869
Pressure (kbar)	Min	Max	Min	Max	Min	Max	Min	Max	Min	Max	Min	Max
Schmidt et al. (1992)	4.71	5.94	3.93	5.76	4.01	5.97	3.96	5.99	4.32	5.36	4.43	4.94
Anderson and Smith (1995)	3.88	5.61	3.75	5.23	3.90	4.34	3.85	5.97	3.96	5.01	4.05	4.51

PAF: Pedra D'Água Facies; SSF: São Sebastião Facies; TF: Tendó Facies; JF: Jabre Facies; MAF: Mãe D'Água Facies; SAF: Santo Antônio Facies.

4 ARTIGO 2 - POST-COLLISIONAL, HIGH-BA-SR TEIXEIRA BATHOLITH GRANITES: EVIDENCE FOR RECYCLING OF PALEOPROTEROZOIC CRUST IN THE ALTO PAJEÚ DOMAIN, BORBOREMA PROVINCE - NE-BRAZIL

Jefferson Valdemiro de Lima [a, *], Ignez de Pinho Guimarães [a], Sérgio Pacheco Neves [a, b], Miguel Angelo Stipp Basei [c], Adejardo Francisco da Silva Filho [a]; Caio Cezar Garnier Brainer[a]

[a] Geosciences Post-graduation Program, Technologic and Geosciences Center, Pernambuco Federal University, Rua Acadêmico Hélio Ramos, s/n, 50740-530, Recife, Brazil. E-mails: *jefferson1901@hotmail.com; ignez@ufpe.br; caio.cgbrainer@ufpe.br; afsf56@gmail.com.

[b] CNPq (Brazilian Research Council) Researcher; Department of Geology, Technologic and Geosciences Center, Pernambuco Federal University, Rua Acadêmico Hélio Ramos, s/n, 50740-530, Recife, Brazil. E-mail: sergio.neves@ufpe.br

[c] Institute of Geoscience, São Paulo University, Rua do Lago 562, 05508-080, São Paulo, SP, Brazil. E-mail: baseimas@usp.br

Abstract

Late-Neoproterozoic granitoids of diversified nature and ages (640 – 525 Ma) are widely distributed in the Borborema Province and their petrogenesis can provide important insights about the Brasiliano/Pan-African Orogeny (ca. 650-550 Ma). The Neoproterozoic Teixeira Batholith comprises an ENE – elongated intrusion of c. 800 km^2 emplaced in metasedimentary rocks and orthogneisses in central Borborema Province immediately south of the Patos Shear Zone. Textures and modal mineral percentage allow to divide the batholith into six petrographic facies, ranging in composition from monzogranite to quartz syenite, containing less than 10% of modal mafic mineral phases (amphibole ± clinopyroxene and biotite). Titanite, epidote, apatite, zircon and Fe-Ti oxide are the main accessory phases. LA-ICP-MS U-Pb zircon

data from four facies yield ages ranging from 585 to 600 Ma, like other Neoproterozoic pre- to early-transcurrent intrusions related to the Brasiliano orogeny. The granitoids belong to the magnetite series, are metaluminous and have high-K calk-alkaline to shoshonitic affinities. Major and trace elements data are typical of granites originating from high barium-strontium (HiBaSr) magmas, i.e., high Ba (1825 – 7370 ppm), Sr (1110 – 2530 ppm), low Rb (56 – 137 ppm), Th (1.6 – 15.8 ppm), Nb (6.2 – 34.7 ppm), Y (3.7 – 33.2 ppm) and HREE contents (Gd-Lu: 3.64 – 24.36 ppm). The granitoids have negative $\varepsilon Nd_{(590Ma)}$ (-13.68 to -16.04) and $\varepsilon Hf_{(t)}$ (-16.27 to -20.80) values, and Paleoproterozoic Nd and Hf T_{DM} model ages ranging from 2.08 to 2.23 and 2.3 to 2.6, respectively, similar to the ages of basement rocks of the Central subprovince. The isotopic data and trace elements signature suggest magma generation by partial melting of Paleoproterozoic mafic/intermediate lower crust, leaving a plagioclase-free and garnet and/or amphibole-bearing residue. Partial melting occurred after a long period of contractional tectonics, and predated development of the Patos shear zone by ca. 20 Ma.

Keywords: High-Ba-Sr granitoids; Borborema Province; Post-collisional magmatism; Crustal reworking; Petrogenesis; Alto Pajeú domain

1. Introduction

Granites are primary components of the continental crust and the main agents of the continental crust differentiation. Granites can be generated by heat increase during mass transfer from mantle to crust, which may involve crustal reworking, by partial melting of the intermediate to deep crust due to radioactive heating during orogenesis, and/or by fractionation of mantle-derived magmas (Barbarin, 1999; Chappell and White, 1992). The variety of processes involved in the granitic magma source, evolution and emplacement are responsible for a great diversity of mineralogical and chemical-isotopic features, constituting an important key to the understanding of continental crustal growth and evolution.

Many classifications have been proposed to granitic rocks. Chappell and White (1974) and White (1979), based on the magma sources, identified three main groups of granites: i) I-type (metaigneous source); ii) S-type (metasedimentary source) and iii) M-type, produced from sources with strong mantle signature and generally associated with island arch environments, including plagiogranites. Loiselle and Wones (1979) add a new letter to the "alphabet soup" classification: A-type granites, which are usually linked to extensional settings and can originate from partial melting of crustal sources (e.g. tonalite, granulitic residue or charnockite) or from differentiation of alkaline basaltic magmas. Based on geochemical data, Tarney and Jones (1994) proposed a new group of granites: high-Ba–Sr granitoids (HiBaSr), characterized by trace element compositions distinct from typical I-, S- and A-type granitoids, including high Ba (>500 ppm), Sr (>300 ppm) and light REEs, and low Nb, Ta and heavy REEs. Granites with such geochemical signature have been described in arc settings (Fowler et al., 2001, 2008; Tarney and Jones, 1994) or associated with post-collisional settings (Atherton and Ghani, 2002; Choi et al., 2009; Lara et al., 2017).

Granitoids and strike-slip shear zones are common features in the post-collisional stage of the Neoproterozoic Brasiliano (Pan-African) Orogeny in the Borborema Province of northeastern Brazil (Fig. 1) (Neves, 2015; Santos et al., 2008; Vauchez et al., 1995). The duration of these events and crustal evolution of the Borborema Province during the late Neoproterozoic are better understood from the age and petrogenesis of Brasiliano plutons (Guimarães et al., 2004, 2011; Van Schmus et al., 2011).

The Teixeira Batholith, in the north part of the Alto Pajeú domain, constitutes one of the largest intrusions in central Borborema Province (Fig. 1). Its occurrence just south of the Patos Shear Zone suggests intrusion related to strike-slip shearing in a post-collisional setting. This inference is consistent with the zircon U-Pb SHRIMP crystallization age of 590 Ma reported by Archanjo et al. (2008), which post-dates the regional metamorphic peak by c. 30 Ma

(Guimarães et al., 2004, 2011; Medeiros, 2004; Neves et al., 2006, 2017; Sial and Ferreira, 2016; Silva and Neves, 2021). Although the Teixeira Batholith has already been the subject of a detailed study by means of Anisotropy of Magnetic Susceptibility technique (Archanjo et al., 2008), there are few chemical and isotopic data available in the literature (Ferreira et al., 1998; Santos and Medeiros, 1999), which makes it difficult to provide further details about its petrogenesis.

In this work, we present a petrographic and geochemical study for all facies that constitute the Teixeira Batholith, as well as zircon U–Pb ages and Lu-Hf isotope data, and whole-rock Nd isotopes. The systematic geochemical and isotopic dataset provide constraints on the sources of the magma and on the mechanisms of magmatic evolution and were used to discuss the petrogenetic and tectonic implications of post-collisional high Ba-Sr granitoids in the context of the evolution of the Borborema Province

2. Regional geological setting

The Borborema Province comprises a region ~ 450,000 km^2 that, according to pre-drift reconstructions, constitutes the western portion of an important Brasiliano/Pan-African belt that extends from Brazil to the northwestern and central portions of Africa (Caxito et al., 2020; Neves, 2003; Trompette, 1997; Van Schmus et al., 2008) (Fig. 1 A and 1B). The Borborema Province comprises a Paleoproterozoic basement composed of migmatitic orthogneisses with TTG and calc-alkaline affinity (Neves et al., 2006; Santos et al., 2015) containing small Archean nuclei (Dantas et al., 2004, among others). The Transamazonian Cycle (2.2 Ga to 2.0 Ga) corresponds to the main period of crust formation in the Borborema Province and includes a series of accretionary and collisional events that formed most of its migmatitic gneiss basement (Neves, 2021 and references therein), that are part of a Paleoproterozoic collage which led to the assembly of the Columbia Supercontinent.

Figure 1 – A) Pre-drit reconstruction of the western portion of Gondwana from Van Schmus et al. (2008). Legend: BR/PA, Brasiliano/Pan-African belts; PaleoPr, Paleoproterozoic crust; NS, North Subprovince; TS, Transversal Subprovince; SS, South Subprovince; PEAL, Pernambuco-Alagoas domain; MK, Mayo Kebi terrane; NWCD, NW Cameroon domain; AYD, Adamawa-Yadé domain; YD, Yaoundé domain; OU, Oubanguides fold belt; PaSZ, Patos shear zone; PeSZ, Pernambuco shear zone; TBL, Transbrasiliano Lineament; TBF, Tcholliré-Banyo fault; AF, Adamawa Fault; SF, Sanaga fault. Cities: N, Natal; R, Recife; S, Salvador; D, Douala; G, Garoua; K, Kaduna area of Nigeria; B) Major domains and shear zones of the Borborema Province (modified from Van Schmus et al., 2011). Legend: Northern Subprovince (MC: Médio Coreaú Domain; CC: Ceará Central Domain; RGN: Rio Grande do Norte Domain); Southern Subprovince (RP: Riacho do Pontal Domain; SD: Sergipano Domain; PEAL: Pernambuco-Alagoas Domain); PaSZ: Patos Shear Zone; WPSZ and EPSZ: West and East Pernambuco Shear Zones; SSZ: Sobral Shear Zone; SPSZ: Senador Pompeu Shear Zone; JSZ: Jaguaribe Shear Zone; JCSZ: João Câmara Shear Zone; PASZ: Portoalegre Shear Zone; RSZ: Riachão Shear Zone; TSZ: Tauá Shear Zone; C: Phanerozoic cover; Line A-B is the location of cross-section in Fig. 15. C) Transversal Subprovince of the Borborema Province with Ediacaran plutons highlighted in red (modified from Guimarães et al., 2016). Legend: RC: Rio Capibaribe Domain; AM: Alto Moxotó Domain; AP: Alto Pajeú Domain; PABD: Piancó-Alto Brigida Domain; TB: Teixeira Batholith; CoSZ: Coxixola Shear Zone; CSZ: Congo Shear Zone; AISZ: Afogados da Ingazeira Shear Zone; SCSZ: Serra do Caboclo Shear Zone.

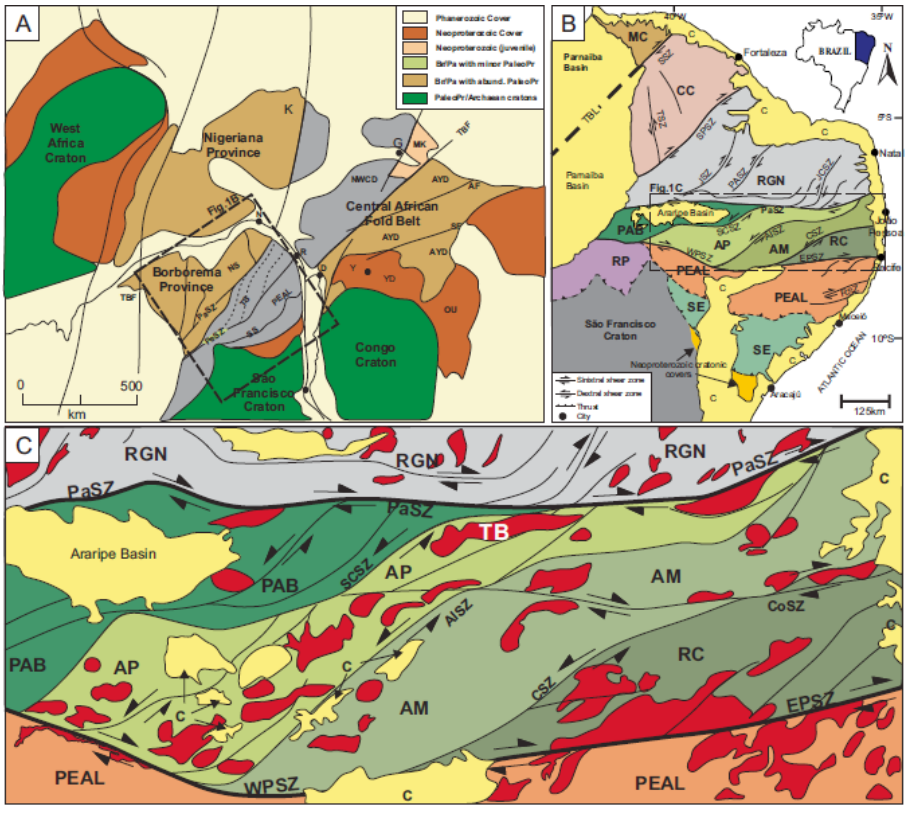

In the early Neoproterozoic, the Borborema Province was affected by the Cariris Velhos (ca. 1000-940 Ma) event. This event is mainly characterized by granitic intrusions (now orthogneisses) and bimodal metavolcanic suites, including pyroclastic rocks, intercalated with metapelites, marbles and banded iron formations of restricted occurrence (Guimarães et al., 2012, 2016; Kozuch, 2003; Santos et al., 2010; Van Schmus et al., 2008, 2011).

The Brasiliano Orogeny was responsible for the actual architecture of the Borborema Province. It is associated with low- to medium-pressure and varied temperature metamorphism, in addition of an expressive granitic magmatism and the development of continental-scale shear zones (Archanjo et al., 2008; Bittar, 1998; Caxito et al., 2020; Guimarães et al., 2004; Neves et al., 2006, 2017; Sial and Ferreira, 2016; Van Schmus et al., 2011; Vauchez et al., 1995; Viegas et al., 2014). The E-trending Patos and Pernambuco shear zones divide the Borborema Province into three subprovinces (Van Schmus et al., 2011) (Fig. 1C): i) Northern, north of the Patos shear zone; ii) Southern, south of the Pernambuco shear zone and iii) Central, between the Patos and Pernambuco shear zones. The Central subprovince has ENE-WSW strike and comprises four domains, from west to east: Piancó Alto Brígida, Alto Pajeú, Alto Moxotó, and Rio Capibaribe. The study area is located in the Alto Pajeú domain, which is the type-area of the Cariris Velhos event.

Based on mineralogical e geochemical data, Guimarães et al. (2004) divided the plutons of the Central subprovince into four types: (1) Calc-alkaline granites with U-Pb zircon TIMS ages ranging from 610 to 644 Ma, later refined to from 600 to 620 Ma based on new U-Pb zircon dating by SHRIMP (Guimarães et al., 2011); (2) high-K calc-alkaline and shoshonitic granitoids with U-Pb zircon (TIMS) ages of 590 –581 Ma, intruded during the transition between a flat-lying foliation-forming event and a transcurrent event; (3) post-collisional alkaline granites with U-Pb zircon TIMS crystallization age of about 570 Ma, which corresponds to the final stage of the Brasiliano/Pan-African orogeny and the beginning of

uplift, synchronous with a series of ultrapotassic intrusions, mainly in the western sector of the Central subprovince; and (4) post-orogenic granitoids with extensional character (A-type signature), associated with subvolcanic bimodal magmatism and crystallization ages between 540 and 512 Ma.

Another scheme classifies the granitic plutons according to their structural characteristics and ages (Neves et al., 2020 and references therein): (1) pre-transcurrent plutons (usually older than 610 Ma), associated with thrusting and crustal thickening; (2) early-transcurrent plutons (590-580 Ma-old), emplaced during the transition from a contractional to a transcurrent regime; (3) syn- to late transcurrent plutons (580-550 Ma-old), associated with the advanced stages of development of transcurrent shear zones. The last two groups characterize the post-collisional stage and there is a decrease in the volume of granitic magmatism in the time interval 610-590 Ma (Neves, 2015).

3. Geological context of Teixeira Batholith

3.1. Field aspects

The Teixeira Batholith (Fig. 2) comprises an EW - elongated intrusion of ~ 800 km^2, composed of granites and quartz syenites, intruded into metasedimentary rocks (paragneiss and quartzite) and orthogneisses from the Alto Pajeú domain, immediately south of the central portion of the Patos Shear Zone. The contacts between the Teixeira Batholith and its host rocks are generally sharp, featuring a strong contrast that is remarkable in geomorphological patterns, where the granitoids crop out as steep ridges and hills of different sizes, including the Jabre Peak, which reaches 1197 m in height.

To the north, the host rocks correspond to the Riacho Gravatá Complex, which comprises a metavolcano-sedimentary sequence which includes schists, gneisses, metagreywackes, with intercalations of marble, metatuffs and Banded Iron Formation (BIF)

and bimodal metavolcanic rock (mainly felsic) (Guimarães et al., 2012; Santos et al., 2010). To the south, the granitoids intrude metasedimentary rocks (garnet – muscovite schist, paragneisses, quartzite and amphibolite lenses) mapped as São Caetano Complex (Ferreira and Santos, 2000), and Tonian orthogneisses. Ultramafic rocks, greenschists and BIF are rare in the São Caetano Complex, while in the Riacho Gravatá Complex they occur more frequently. Guimarães et al (2012) suggest that the Riacho Gravatá and São Caetano Complexes are associated with extensional events, with the sedimentary input to the precursor basins occurring, respectively, from 1091 to 920 Ma, and after 806 Ma. The Brasiliano Orogeny promoted the development of a planar fabric in the supracrustal rocks, with greenschist facies metamorphism (Bittar, 1998), and reworking of basement rocks. The orthogneisses occur mainly in the SSW portion of the studied area, comprising medium- to coarse-grained, porphyroclastic biotite - amphibole orthogneisses of syenogranitic to granodioritic composition, which were interpreted by Ferreira and Santos (2000) as representing Cariris Velhos metagranitoids.

Figure 2 - Simplified geological map of Teixeira Batholith. Based on Ferreira and Santos (2000) and Archanjo et al. (2008).

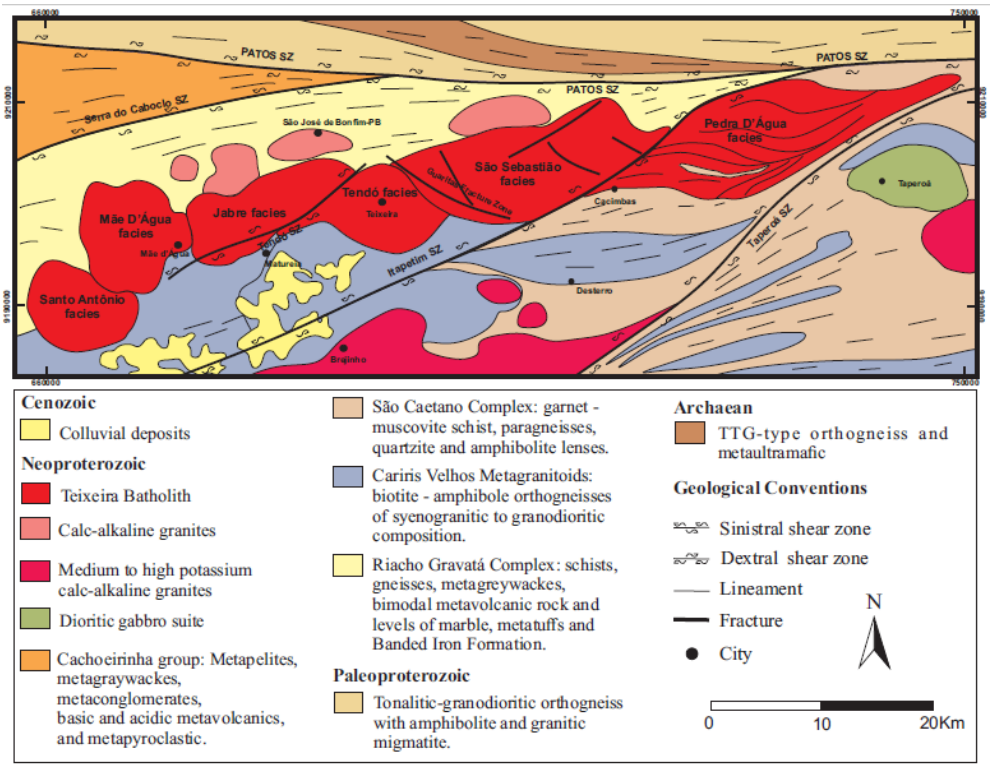

The granitoids from the eastern portion of the batholith occur between the E-W dextral Patos Shear Zone and the NE-SW sinistral Taperoá Shear Zone. In the central and western regions, the granitoids are cut by conjugate fractures and NE-SW sinistral shear zones (Itapetim and Tendó) responsible for the pinch-and-swell shape of the batholith (Archanjo et al., 2008). In general, there is no strong evidence of internal deformation, except for the presence of fracture planes and sheared rocks that define small, outcrop-scale shear zones at the edge of the body.

In general, the granitoids from the Teixeira Batholith are petrographically monotonous, comprising leucocratic to mesocratic monzogranites, syenogranites, and, locally, quartz syenites. There is no evidence suggesting an origin from different magmatic pulses, i.e., no dikes, no truncating contacts of rocks with different facies, or presence of angular enclaves associated with previous magmatic pulses. However, petrographic and textural aspects allow subdivision of the batholith into six facies, which are named, from east to west (Fig. 2), Pedra D'Água, São Sebastião, Tendó (Tendó domain of Archanjo et al., 2008), Jabre, Mãe D'Água and Santo Antônio.

The Pedra D'Água facies comprises sheets of equigranular, medium-grained biotite-amphibole monzogranite to syenogranite in the easternmost portion of the Teixeira Batholith, between the Itapetim and Taperoá NE-trending sinistral shear zones. The sheets are parallel and ENE-trending (Fig. 3A), being especially evident in the southern portion, where the outcrops consist entirely of subvertical sheets of sheared granite, locally intercalated with metric wide lenses of country rocks (Fig. 3B). Unlike the rocks that constitute the other facies, the granitoids of the Pedra D'Água facies show strong evidence of solid-state deformation, with ENE-WSW stretched biotite and quartz crystals.

The São Sebastião facies occurs between the Itapetim Shear Zone and a NW-trending fracture system (Guaritas Fracture Zone). This facies comprises medium-grained, equigranular

to slightly porphyritic amphibole-clinopyroxene syenogranite to quartz syenite. It is distinct from the other facies by the presence of pyroxene among the essential mafic minerals. Enclaves of mesocratic syenogranites, rich in pyroxene clots (Fig. 3C and D), showing crenulated to lobate contacts with the host leucogranites, suggest interactions between magmas of distinct compositions. Close to the Itapetim shear zone, in the eastern portion of the body, the granitoids are sheared, showing a NE-SW preferential orientation, parallel to the main trace of the shear zone.

The Tendó and Mãe D'Água facies, in the central and western portion of the Teixeira Batholith, respectively, are comprised mainly by biotite-amphibole monzogranites. In the Tendó facies, the granites are mesocratic, equigranular, medium-grained and contain a small number of mafic enclaves and xenoliths. The Mãe D'Água facies comprises mesocratic, porphyritic, coarse grained monzogranites (Fig. 3E), with rare enclaves. Locally, the granitoids of the Mãe D'Água facies have circular and concentric magmatic structures and inconspicuous foliation, defined mainly by orientation of mafic minerals that occurs in the N, NW, and E portions, parallel to the edges of the intrusion. Locally, the granitoids of Tendó and Mãe D'Água facies are cut by ENE-WSW sinistral shear bands (Fig. 3F).

The Jabre facies is in contact to the east with the Tendó facies through the Tendó Shear Zone. It consists of leucocratic, equigranular, medium to fine grained amphibole monzogranite to syenogranite. Microgranular mafic enclaves are locally present and evidence for strong solid-state deformation was not found.

The Santo Antônio facies constitutes the westernmost portion of the Teixeira Batholith. It comprises leucocratic, medium- to coarse-grained, equigranular to slightly porphyritic, amphibole-biotite monzogranite, enclosing microgranular enclaves and country rocks xenoliths. It shows E-trending foliation, defined by the orientation of mafic minerals, without strong evidence of solid-state deformation, and locally discreet magmatic banding (Fig 3G).

Figure 3 – Field aspects of the Teixeira Batholith. A) Granitic sheets of the Pedra D'Água Facies, with elongated parallel enclaves; B) Schist lenses in granitoid of the Pedra D'Água Facies with sheared leucocratic bands indicating dextral kinematics; C) Lobate contacts between syenogranites rich in pyroxene clots (right) and leucocratic granite (left) typical of the São Sebastião Facies; D) Detail of pyroxene-rich syenogranite that occurs locally in contact with São Sebastião Facies granitoids; E) Porphyritic, coarse-grained, slightly oriented syenogranite of the Mãe D'Água Facies; F) Monzogranite of the Tendó Facies cut by sinistral shear band; G) Magmatic banding in granitic rock of the Santo Antônio Facies; H) Mafic microgranular enclave hosted by leucocratic granite of the Santo Antônio Facies.

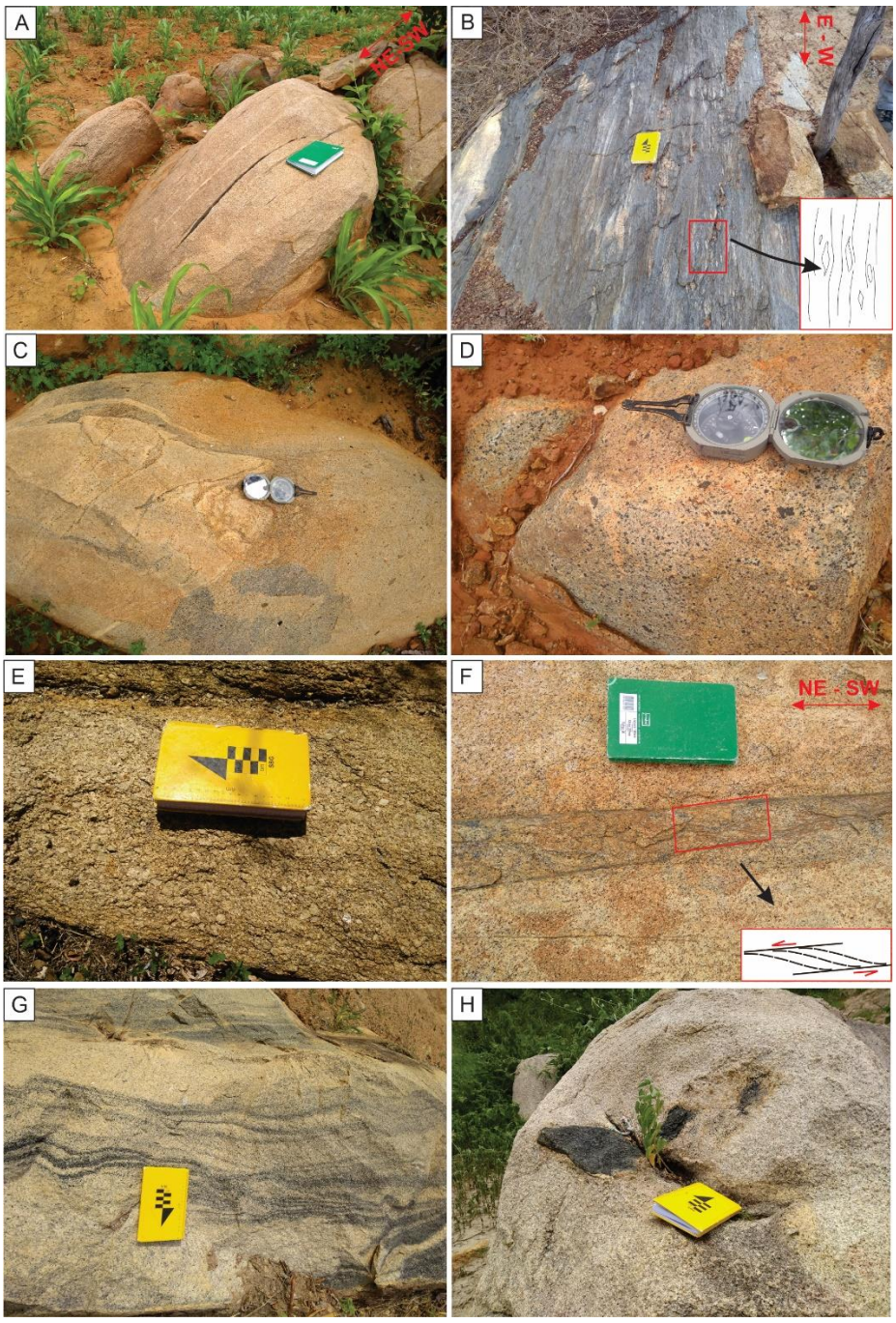

Enclaves in the Tendó and Santo Antônio facies, where they occur more frequently, are classified as mafic microgranular enclaves (MME) (Fig. 3H). They consist of fine-grained amphibole diorite to monzonite, showing rounded to elongated shapes and evidence for interaction between magmas of different compositions i.e., the most primitive are homogeneous and melanocratic and those affected by hybridization processes are mesocratic, showing sinuous and crenulated contacts with the host granitoids. In addition to the MME, xenoliths and ENE-WSW elongate decametric to centimetric rich-biotite surmicaceous enclaves are locally present.

3.2. Petrography

In facies dominated by magmatic textures (São Sebastião, Tendó, Jabre, Mãe D'Água and Santo Antônio facies), quartz occurs as well-developed anhedral crystals exhibiting undulose extinction, or as interstitial subgrain aggregates showing grain boundary migration suggestive of recrystallization processes at relatively high temperature. Locally, it shows chessboard extinction (Fig. 4A), a feature commonly associated with deformation at near solidus conditions. Plagioclase occurs as anhedral to subhedral zoned crystals (Fig. 4B), commonly showing features suggestive of high-temperature deformation (> 550 °C), such as subgrain rotation (Fig. 4C) and submagmatic fractures (Fig. 4D). K-feldspar occurs as subhedral to anhedral crystals of perthitic orthoclase, exhibiting lamellae ranging from films to irregular stains, and as microcline with the typical tartan twinning. They often show rims replaced by myrmekite.

The sheared granitoids of Pedra D'Água facies comprise quartz crystals with typical features of solid-state deformation, such as strong undulose extinction, subgrain rotation recrystallization (Fig. 4E) and discrete ribbons (Fig. 4F). Perthitic orthoclase often shows micro-kinks. Deformation bands occur usually in plagioclase phenocrysts. In most samples,

kinematic criteria indicate dextral shear, but sinistral shear criteria are developed locally, especially close to the NE-SW shear zones.

Figure 4 – Microstructural aspects of granitoids from the Teixeira Batholith. A) Chessboard extinction pattern in quartz associated with high-temperature deformation; B) Plagioclase phenocryst (pl) with preserved igneous zoning; C) Plagioclase grain showing recrystallization by subgrain rotation; D) Submagmatic fracture (arrow) in plagioclase crystal (Pl) indicating high-temperature deformation; E) Anhedral quartz (Qz) showing subgrain rotation recrystallization associated a solid-state deformation; F) Quartz forming discrete ribbons; G) Well-developed subhedral amphibole (Amp) with accessory mineral inclusions; H) Clinopyroxene (Cpx) replaced by aggregates of epidote (Ep) and magnetite (Mag); I) Euhedral magnetite crystal (Mag), affected by oxidation process at the edges.

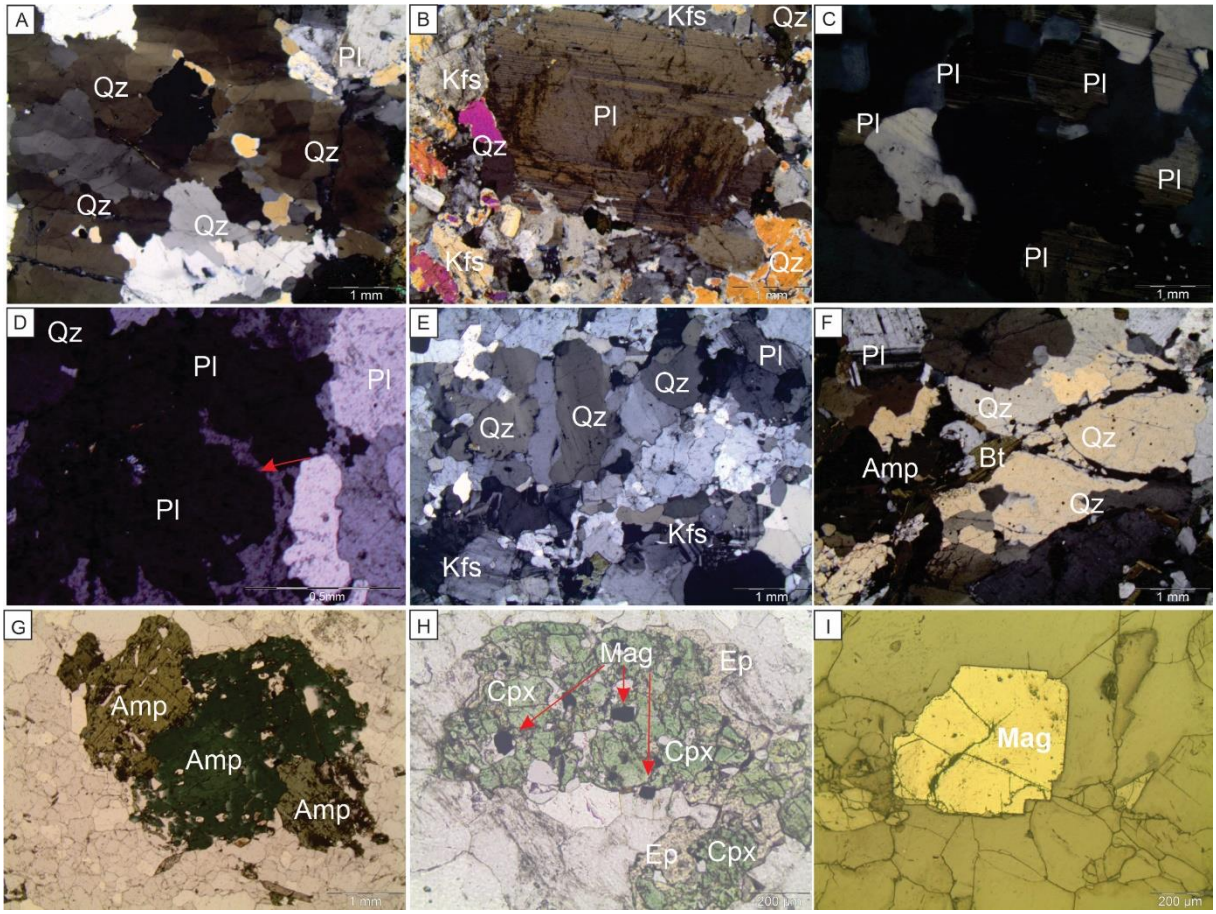

The main mafic minerals are amphibole and biotite. Amphibole (Fig. 4G) is present in all facies in modal percentages ranging from 1 to 10 %. Biotite occurs in low amounts (0 to 1%) in the Pedra d'Água, São Sebastião and Jabre facies, and reach up to 5% in the Mãe D'Água, Tendó and Santo Antônio facies. Clinopyroxene is mainly restricted to the São Sebastião facies, where it constitutes the main ferro-magnesian mineral, and occur as accessory

phase in the northern portion of the Pedra D´Água facies. In the São Sebastião facies, the clinopyroxene is represented by green anhedral or subhedral crystals of aegirine-augite, with deep to pale green pleochroism, locally replaced by epidote and aggregates of Fe-Ti oxides (Fig. 4H), while in the Pedra D'Água facies are highly deformed and altered by uralitization processes, resulting in fibrous actinolite.

Amphibole occurs as subhedral to anhedral crystals and locally, as elongated and deformed prismatic crystals, commonly showing titanite, apatite, epidote and opaque minerals inclusions. Biotite occurs as subhedral to anhedral thin flakes, intensely deformed, and slightly oriented, especially in the Pedra D'Água facies.

The accessory phases are titanite, epidote, opaque minerals, apatite, and zircon. Titanite is the main accessory mineral and occurs as small euhedral crystals included or partially encompassed by biotite and amphibole, being interpreted as primary titanite. Locally, titanite occurs as granular aggregates, constituting a late phase. Epidote occurs as euhedral to subhedral crystals, partially encompassed by the main ferromagnesian minerals, suggesting a magmatic origin. Opaque minerals, that occur in greater modal percentage in the Pedra D'Água, São Sebastião and Santo Antônio facies, are represented essentially by euhedral crystals of magnetite (Fig. 4I), that under reflected light are isotropic and show pinkish gray color. In the Tendó facies, opaque minerals are made up of sulfides, which occurs as small crystals of high reflectivity, yellow color and without anisotropy, common features of pyrite. Apatite and zircon occur as small crystals included in the other mafic minerals.

4. Analytical techniques

The analytical procedures used include: 1) ICP-AES (Inductively Coupled Plasma Emission Spectrometry) and ICP-MS (Inductively Coupled Plasma Mass Spectrometry) for major-and trace-element analyses; 2) LA-ICP-MS (Laser Ablation Inductively Coupled Plasma

Mass Spectrometry) for zircon dating; 3) LA-MC-ICPMS (Laser Ablation Multi-collector Inductively Coupled Plasma Mass Spectrometer) for zircon Hf isotope analysis; 4) Thermal Ionization Mass Spectrometry for Nd whole-rock isotope analysis. Detailed analytical procedures are available in Electronic Appendix 1A.

5. Whole-rock geochemistry

The different facies of the Teixeira Batholith show similar SiO_2 contents (Table 1). The granites of the Santo Antônio facies are the most acidic, with SiO_2 contents ranging from 68.8 to 72.0 wt%, and those of the Tendó facies have the lowest values of silica (53.5 – 67.4 wt.%). The granitoids are metaluminous to slightly peraluminous (Fig. 5A), showing Aluminum Saturation Index (ASI) values ranging from 0.79 to 1.02 (Pedra D'Água facies), 0.90 to 0.98 (São Sebastião facies), 0.68 to 0.95 (Tendó facies), 0.93 to 0.95 (Jabre facies), 0.97 to 0.99 (Mãe D'Água facies) and 0.95 to 1.03 (Santo Antônio facies). The analysis of the São Sebastião facies plot close to the limit between the metaluminous and peralkaline fields, reflecting the presence of Na-rich pyroxene, such as aegirine-augite.

According to the geochemical classification of Frost et al. (2001), the granitoids range from the ferroan to the magnesian series (Fig. 5B) and plot mainly in the alkali-calcic and alkalic fields of the MALI (Modified Alkali-Lime index) versus SiO_2 diagram of Frost et al. (2001) (Fig. 5C). They show high total alkalis ($K_2O + Na_2O$) contents, ranging from ~ 7 to 11 wt.% and K_2O/Na_2O ratios between ~ 0.5 to 2.0, being classified as transalkaline (Fig. 5D), according to Middlemost (1997), and as high-K calc-alkaline to shoshonitic, in the SiO_2 versus K_2O diagram (Fig. 5E) of Peccerillo and Taylor (1976).

In Harker diagrams for major and trace elements (Fig. 6), the granitoids show negative correlation between SiO_2 and Al_2O_3, CaO, Fe_2O_3t, MgO, P_2O_5, TiO_2, Ba, Ce, Sr and Zr. Na_2O and K_2O do not show significant variation with increasing differentiation. A remarkable feature

of the granitoids is their high Sr and Ba contents, which can reach up to 2530 ppm and 7370 ppm respectively. These values are similar to those recorded in HiBaSr granites (Fowler et al., 2008; Lara et al., 2017; Tarney and Jones, 1994, among others). The low Rb (56 – 137 ppm), Nb (6.2 – 34.7 ppm), Th (1.6 – 15.8), Y (3.7 – 33.2 ppm) and HREE (Gd-Lu; 3.64 – 24.36 ppm) contents are also similar to those observed in HiBaSr granitoids worldwide.

Figure 5 - Geochemical characteristics of granitoids from the Teixeira Batholith. A) Alumina Saturation index diagram; B) FeOt/(FeOt+ MgO) versus SiO_2 diagram; fields of ferroan and magnesian series from Frost et al. (2001); C) SiO_2 x MALI (Modified Alkali Lime Index diagram) for granitoids of the Teixeira Batholith; D) TAS (SiO_2 versus Na_2O+K_2O) diagram with the fields after Middlemost (1997); E) SiO_2 x K_2O diagram with the fields of Peccerillo and Taylor (1976).

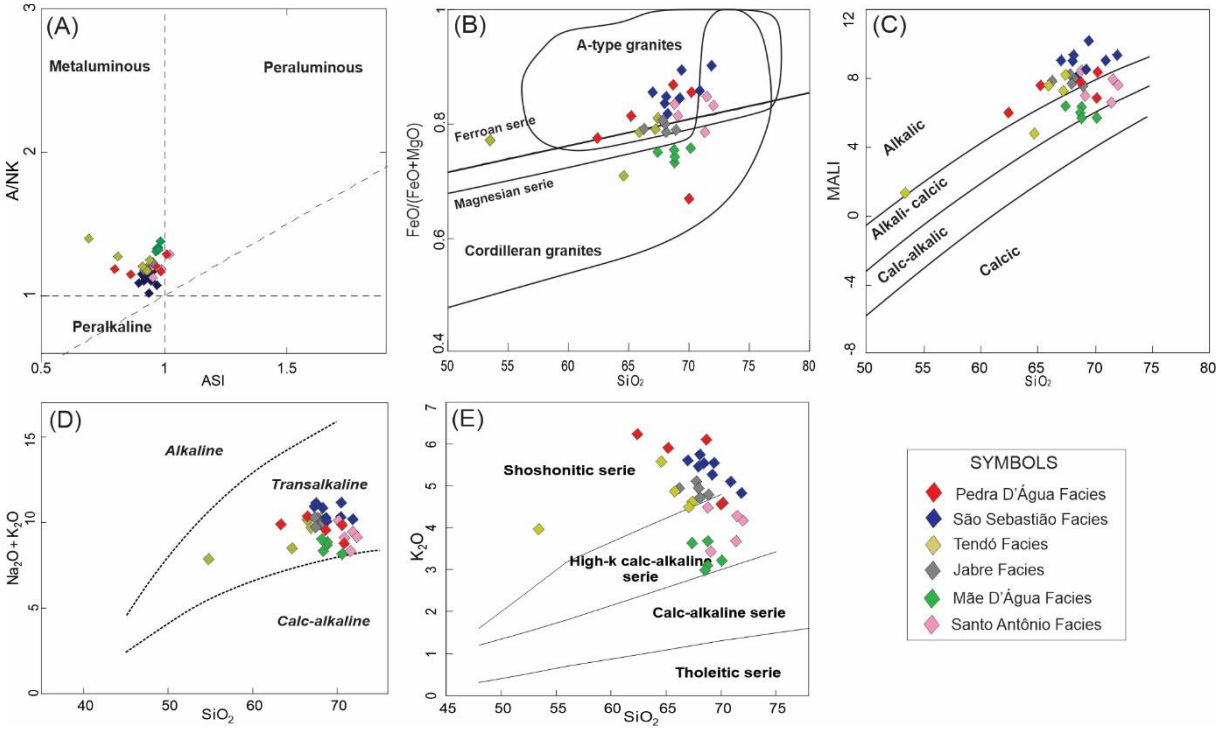

The REE patterns (Fig. 7A) of the granitoids are similar, although variations in the total REE concentrations among the different facies do occur. The patterns are characterized by high LREE/HREE ratios, with $(Ce/Yb)_N$ ratios ranging from 8.1 to 73.4 and absence of significant Eu anomalies, with Eu/Eu* ratios [Eu* =$Eu_N/(Sm_N + Gd_N)/2$] ranging from 0.84 to 1.0 (Pedra D'Água facies), 0.82 to 1.03 (São Sebastião facies), 0.93 to 1.11 (Téndo facies), 0.89 to 0.98 (Jabre facies), 1.02 to 1.15 (Mãe D'Água facies) and 0.80 to 0.95 (Santo Antônio facies). The

Pedra D'Água facies granitoids are the most fractionated, with $(Ce/Yb)_N$ ratios ranging from 8.2 to 73.4, while granitoids of the Santo Antônio facies are the less fractionated, with the $(Ce/Yb)_N$ ratios ranging from 8.08 to 11.82. The granitoids of the other facies have $(Ce/Yb)_N$ ratios intermediate between Pedra D'Água facies e Santo Antônio facies granitoids. The uniform REE patterns are similar to other HiBaSr granitoids (Fowler et al., 2008; Lara et al., 2017 and references therein).

Figure 6 – A) – L) Variation diagrams for major and trace elements of the studied granitoids. Fields in the SiO_2 versus K_2O and Na_2O diagrams for melts experimentally determined and compiled by Chen et al. (2013) from the literature: Beard and Lofgren (1991) (amphibolites; 1, 3, 6, 9 kb; 800–1000 °C), Rapp and Watson (1995) (metabasalt; 8–32 kb; 1000–1125 °C), Patiño Douce and Beard (1995) (quartz amphibolites; 3–15 kb; 850–930 °C); Patiño Douce and Beard (1995) (biotite gneiss; 3–15 kb; 850–930 °C) and Sisson et al. (2005) (medium to high K basaltic rocks; 700 Mpa; 825–975 °C).

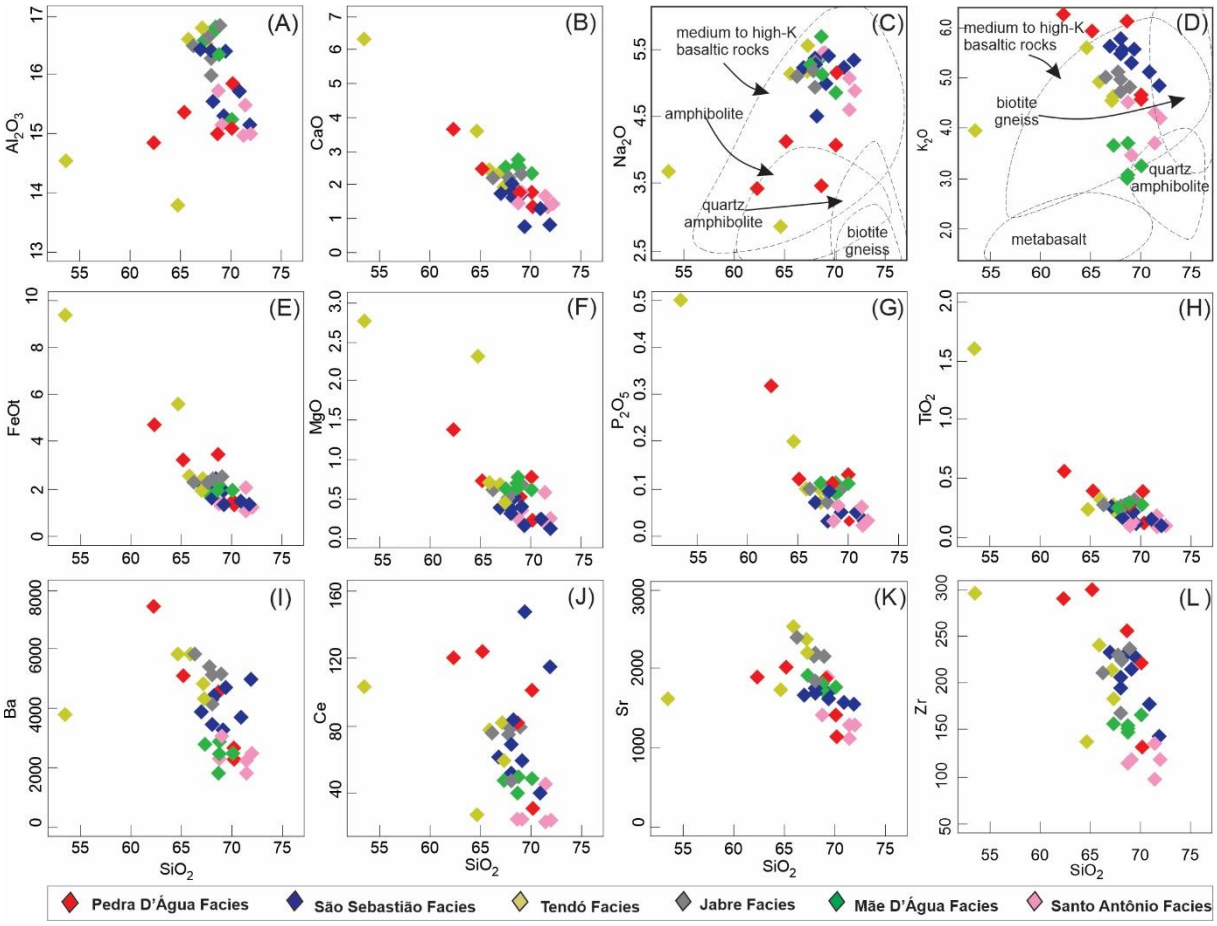

Multi-element diagrams (Fig. 7B), normalized to the values of the primitive mantle (Sun and McDonough, 1989), are characterized by modest negative anomalies of Rb and more

pronounced ones of Nb, P and Ti. Negative Nb anomaly is quite common in crustal melts or associated with crustal contamination. The P and Ti negative anomalies suggest that one or more mineral phases removed Ti and P selectively, without causing larger depletion in the other HFSE. In turn, most of the analyzed samples show positive anomalies of K, Sr and Ba, suggesting that feldspar was not a fractionated and/or residual phase.

Figure 7 – A) Chondrite-normalized REE patterns (Nakamura, 1974) of the studied granitoids; B) Primitive mantle-normalized (Sun and McDonough, 1989) trace element diagrams (spidergrams).

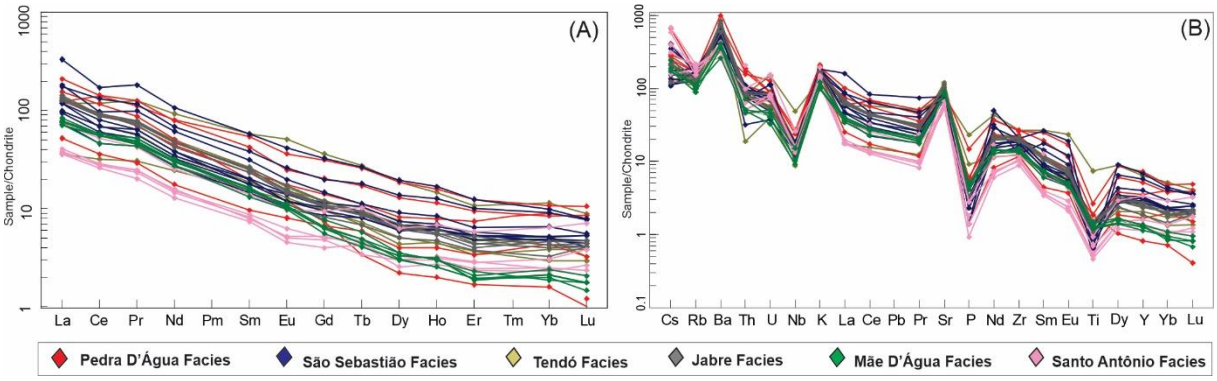

The granitoids fall in the syn-collision (Syn-COLG) + volcanic arc granites field in the Y vs Nb diagram (Pearce et al., 1984) (Fig. 8A), and plot in the post-collisional field, in intersection with the Volcanic Arc Granites (VAG) field in the (Y + Nb) vs. Rb diagram (Pearce, 1996) (Fig. 8B). In the discriminating diagrams of Whalen et al. (1987), they project, predominantly, at the intersection between the A-type granites and (I, S or M)-type fields (Fig. 9A-H), which corroborates the observed post-collisional signature.

Figure 8 - The studied granitoids plot in the tectonic discriminant diagrams: (A) and (B), fields after Pearce et al. (1984) and Pearce (1996), respectively. WPG: Within Plate granites; POG: Post-orogenic granites; ORG: Ocean Ridge Granites; VAG: Volcanic Arc Granite.

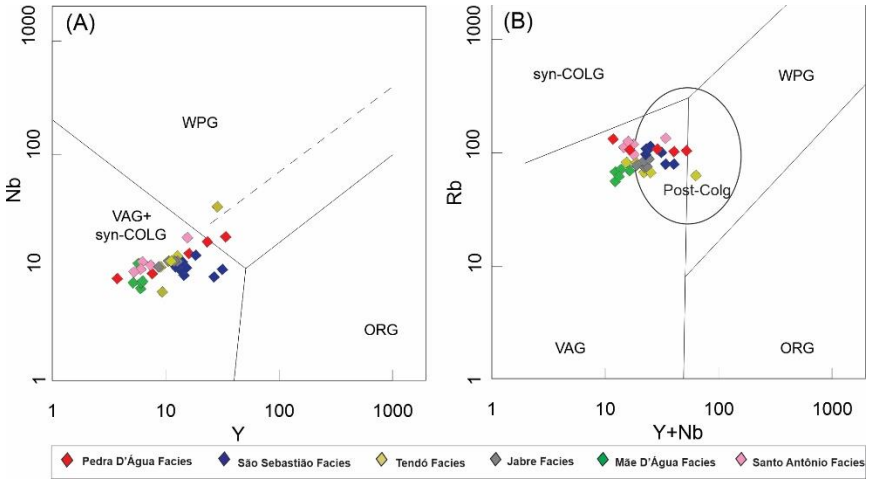

Figure 9 – Tectonic setting discrimination diagrams of Whalen et al. (1987) for granitoids of the Teixeira Batholith. FG: fractionated granite field; OTG: unfractionated granite field; A: A-type granites; I & S: I- and S-type granites.

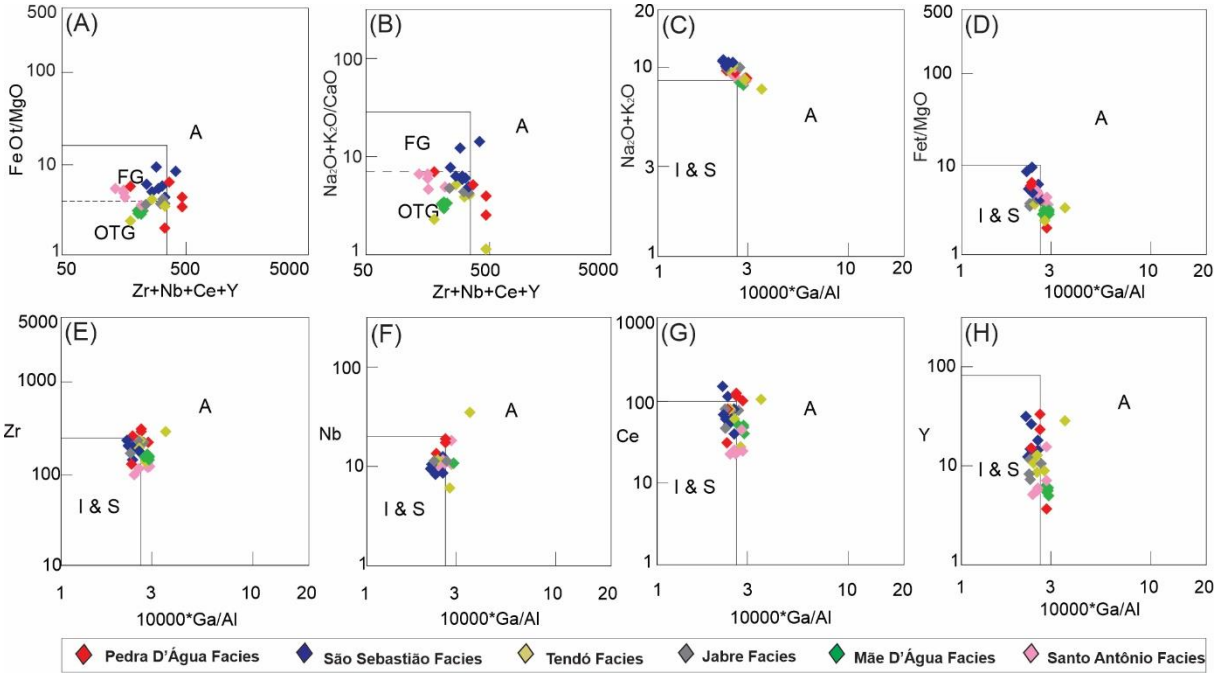

6. U-Pb zircon geocronology

6.1. Pedra D'Água facies

Nineteen zircon grains of the Pedra D'Água facies were analyzed from a sample of biotite-amphibole monzogranite (JD-28). Zircon occurs as prismatic to bipyramidal euhedral crystals, pink in color, with width/length ratios ranging from 1:3 to 1:5. Under CL

(cathodoluminescence), the zircon grains show a strong external oscillatory zoning and large number of inherited cores. Fourteen analyses were discarded due to discordance, high common Pb contents, or analytical issues. Six analyses plotted (Table 2) on the Concordia diagram (Fig. 10A) yield an age of 590.5 ± 2.24 Ma with MSWD = 0.49. The analyzed spots present Th/U ratio values from 0.1 to 0.45, which are values attributed to igneous zircons, therefore the obtained age is interpreted as crystallization age of this facies. Three analyzes on inherited cores yield $^{207}Pb/^{206}U$ ages ranging from 1824 Ma to 2136 Ma, suggesting contribution of Paleoproterozoic crust in the source of the magmas. A $^{206}Pb/^{238}U$ age of 613 Ma was defined in the rim of one zircon xenocryst.

6.2. São Sebastião facies

Twenty zircon grains were analyzed from an amphibole-pyroxene syenogranite (sample JD-30). Two zircon grains populations were identified: 1) bipyramidal crystals up to 0.111 mm and length/width ratios ranging from 1:2 to 1:3 and 2) euhedral crystals, 0.17–0.28 mm in size, with length/width ratio ranging from 1:2 to 1:4. The zircon grains of both populations are beige to pink, and the CL images show the presence of many inherited cores, surrounded by magmatic rims with strong oscillatory zoning. Thirteen analyses were discarded due to high common Pb contents. Six spots, with Th/U ratio ranging from 0.19 a 0.74 (Table 2), defined a Concordia age of 599.7 ± 2.35 Ma (MSWD = 1.2) (Fig. 10B), interpreted as the crystallization age. Three zircon grains defined one cluster with age of 555 ± 3 Ma (MSWD= 3.7), which is slightly younger than the age (566 ± 6 Ma) of the peak of high-T metamorphism, associated with the Patos Shear Zone (Viegas et al., 2014). This age is interpreted as Pb-loss associated to this high–T event. One analyzed spot located in an inherited core provided a $^{207}Pb/^{206}Pb$ age of 2132 Ma (Th/U ratio = 0.57), suggesting contribution of Rhyacian crust in the magma source. A $^{206}Pb/^{238}U$ age of 873 Ma (Th/U ratio = 0.51), obtained in one zircon grain, is similar to the ages

of detrital zircons from the São Caetano Complex (Guimarães et al., 2012) and to the crystallization age (~870Ma) of orthogneisses cropping out to the east (Neves et al., 2015).

Figure 10 – Zircon U–Pb concordia diagrams and corresponding representative zircons CL images from (a) Pedra D'Água Facies; (b) São Sebastião Facies; (c) Tendó Facies and (d) Santo Antônio Facies.

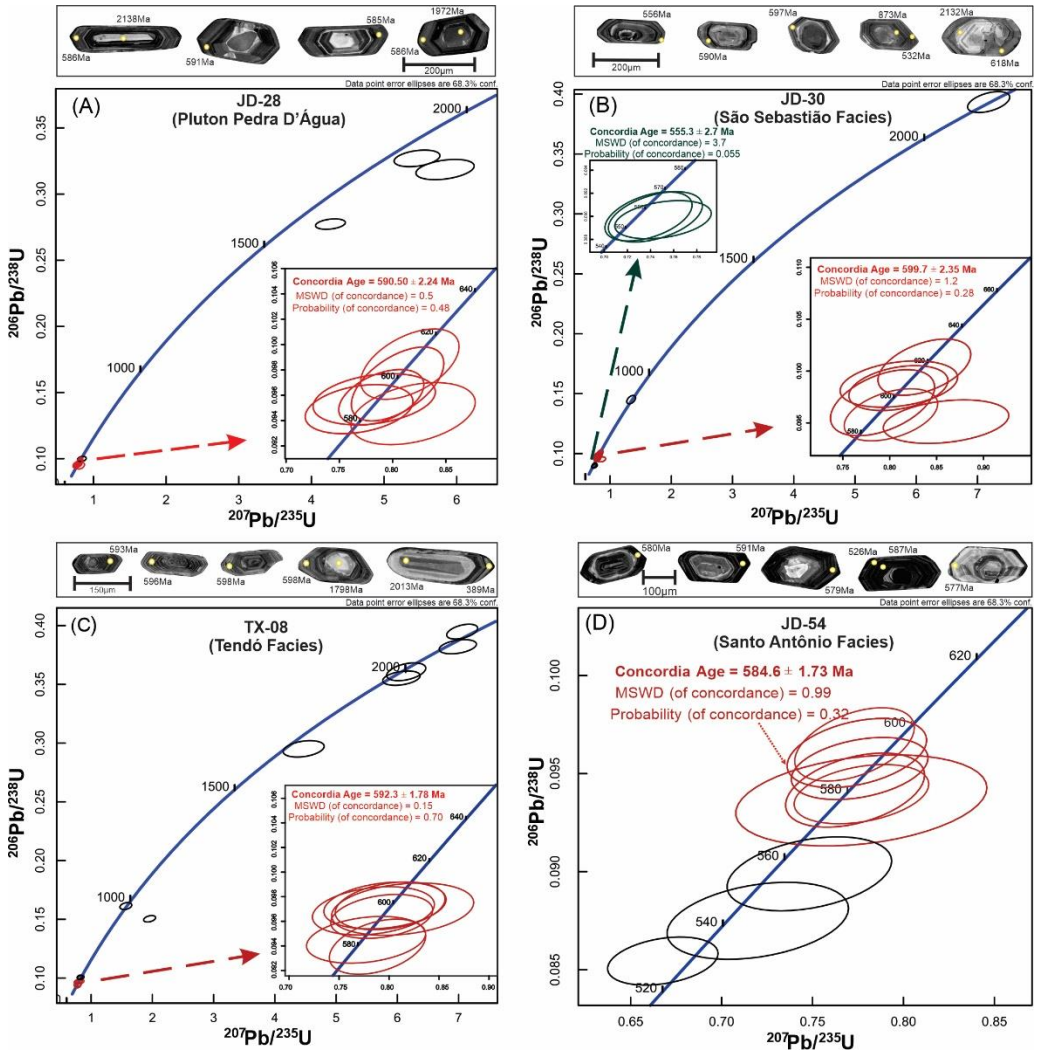

6.3. Tendó facies

A biotite-amphibole monzogranite sample (TX-08) was collected from the Tendó facies. Twenty-nine spots were analyzed in 25 zircon grains and the results are shown in Table 2. The zircon grains are beige, bipyramidal with width/length ratios ranging from 1:2 to 1:4. In the CL images the zircon grains show strong oscillatory zoning, suggesting a magmatic origin. Inherited cores are present in large quantities and narrow overgrowths are present in many grains. Thirteen analyses were discarded due to discordance or high common Pb contents.

Seven analyses plotted on the Concordia diagram (Fig. 10C), with Th/U ratios ranging from 0.25 to 0.93, yield an age of 592.3 ± 1.78 Ma (MSWD = 0.15). The zircon cores are mostly of Paleoproterozoic age (Table 2; 1800 – 2130 Ma), suggesting the contribution of Rhyacian crust to the magma source. The presence of two zircon grains with $^{206}Pb/^{238}U$ ages of 904 and 964 Ma suggest contribution of a Tonian component.

6.4. Santo Antônio facies

For dating of the Santo Antônio facies, we used twenty-four zircon grains obtained from an amphibole-biotite monzogranite sample (JD-54). Most of the crystals are euhedral and prismatic with width/length ratios of 1:2, show oscillatory zoning and large number of inherited cores. Eighteen analyses were discarded due to high common Pb contents or analytical issues. Six analyzes (Fig. 10D) yield a Concordia age of 584.6 ± 1.7 Ma (MSWD = 0.99) (Table 2).

7. Isotopic geochemistry

7.1. Lu-Hf zircon data

In situ zircon Hf isotopic data were obtained for three samples: JD-30 (São Sebastião facies – 11 spots), TX-08 (Tendó facies – 10 spots) and JD-54 (Santo Antônio facies – 10 spots). The isotopic analyses were performed on the oscillatory zoning sectors and xenocrystic cores. The results are presented in Table 3 and plotted in Figure 11A. The analyzed grains yielded $^{176}Hf/^{177}Hf$ initial ratios ranging from 0.281383 to 0.281887 (São Sebastião facies), 0.281401 to 0.282039 (Tendó facies) and 0.281448 to 0.281953 (Santo Antônio facies). The uneven values for the $^{176}Hf/^{177}Hf(t)$ ratios are associated with different portions of the analyzed zircon grains (magmatic edges/inherited cores), directly influencing the varied values of εHf. The spots made in inherited cores yield, for t = 2.1 Ga, values of εHf varying from -2.53 to +6.03 and Siderian to Neoarchean Hf T_{DM} model ages (2.31 to 2.78 Ga), while two Tonian zircon crystals (U-Pb Age = 904 and 964 Ma) show Rhyacian Hf T_{DM} model ages (2.05 and 2.1 Ga)

and negative $\varepsilon Hf_{(t)}$ values (–6.23 and -6.24). The analyzes carried out on the same magmatic grains that defined the crystallization age of the three studied petrographic facies provided $\varepsilon Hf_{(t)}$ values between -16.27 and -20.80 and Siderian to Neoarchean Hf T_{DM} model ages (2.35 to 2.59 Ga).

7.2. Whole rock Sm-Nd data

Sm–Nd data were obtained for five granitoid samples from the Teixeira Batholith and one sample of the host orthogneiss. The results are presented in Table 4 and Figure 11B. Sm-Nd data from the Tendó facies (VS11) were reported by Van Schmus et al. (2011). The granitoids have Nd T_{DM} model ages in the 1.75 – 2.23 Ga range, and $\varepsilon Nd_{(590Ma)}$ ranging from -6.08 to -16.04. The host orthogneiss sample shows Mesoproterozoic Nd model ages (T_{DM} = 1.37 Ga) and εNd value of -2.58, suggesting that they belong to the Cariris Velhos metagranitoids suite (Guimarães et al., 2016).

Figure 11 – Isotope evolution diagram for Teixeira Batholith granitoids. A) Diagram of zircon εHf(t) vs. Age (Ma). Vertical lines represent the age range recorded for the main geological events in the Borborema Province (Caxito et al., 2021); B) Diagram of εNd(t) vs. Age (Ma) studied granitoids and a sample of orthogneiss from the host rocks. The gray and yellow bands represent Cariris Velhos orthogneisses and basement rocks of the Transversal Subprovince from Van Schmus et al. (2011).

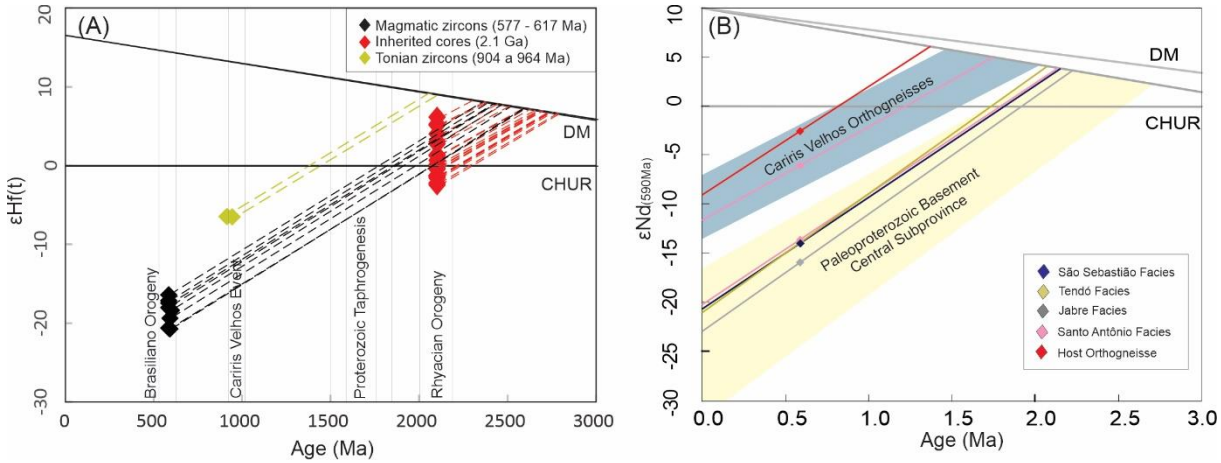

8. Discussion

8.1. Tectonic setting

The Teixeira Batholith constitutes one the largest granitic intrusions of the Borborema Province. It comprises predominantly metaluminous, magnesian to ferroan and high-K calc-alkaline to shoshonitic granitoids. The affinity of the granitoids with I-type granites of the magnetite series is indicated by their mineralogy, where the main mafic mineral is amphibole, oxides are essentially represented by primary magnetite, and titanite and epidote occur as primary phases (Chappell and White, 1974; Ishihara, 1977). The dominant weak magnetic susceptibility of the Teixeira Batholith (Lima et al., 2000; Archanjo et al., 2008) can be explained by Fe^{+3} entering the epidote structure rather than in Fe-oxide minerals, leading to magnetic susceptibility values lower than expected, as has been proposed for magnetite-series calk-alkaline granitoids with magmatic epidote in the Piancó-Alto Brígida domain, west of the Alto Pajeú domain (Sial and Ferreira, 2016).

As illustrated in the Sr-Rb-Ba ternary diagram (Fig. 12), the Teixeira Batholith has geochemical features typical of HiBaSr granitoids (Fowler et al., 2008; Lara et al., 2017; Tarney and Jones, 1994, among others): high Ba (1825 – 7370 ppm) and Sr (1110 – 2530 ppm), and low Rb (56 – 137 ppm), Nb (6.2 – 34.7 ppm), Th (1.6 – 15.8 ppm), Y (3.7 – 33.2 ppm) and HREE contents (Gd-Lu: 3.64 – 24.36 ppm), in addition to negative Nb anomaly. HiBaSr granites are mainly described in arc settings (Fowler et al., 2001, 2008; Tarney and Jones, 1994) or associated with post-collisional settings (Lara et al., 2017), involving slab break-off and/or delamination of subcontinental lithospheric mantle (Atherton and Ghani, 2002; Choi et al., 2009, among others).

The Y, Yb, Nb and Ta values of the granitoids are like volcanic arc and syn-collisional granites (Pearce et al., 1984), but plot predominantly in the field of post-collision granites (Pearce, 1996) (Fig. 8). As the isotopic data point to predominantly Paleoproterozoic sources (Fig. 11), it is likely that the arc signature was mainly inherited from the source. In the discriminating diagrams of Whalen et al., (1987), the granitoids plot in the I-type field, close to

or even within the A-type field, also consistent with a post-collisional geochemical signature (Fig. 9).

Figure 12 – Granitoids of the Teixeira Batholith plotted on the Ba-Rb-Sr ternary diagram (Tarney and Jones, 1994).

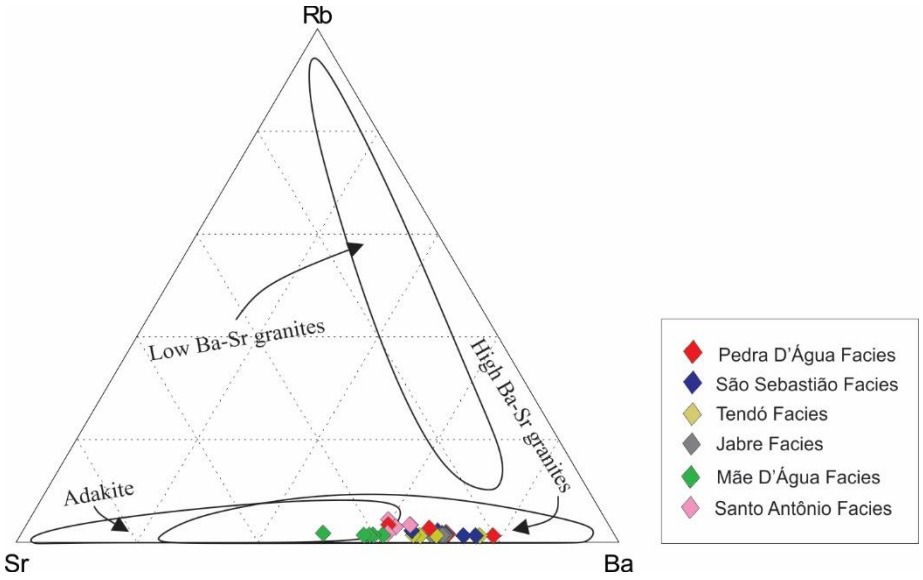

Post-collisional granites are largely associated with mechanisms that start after a major collision, following regional metamorphism, and with complex geological events, which may involve transcurrent movements along shear zones, small scale collisions and/or generation of rifts (Bonin et al., 1998; Harris et al., 1986; Pearce, 1996). According to Harris et al. (1986), the geochemical signatures of magmas generated in post-collisional environments vary according to different stages of the post-collisional context and depend on the composition of the crust and mantle from which they were derived, so post-collisional granites may show a wide compositional spectrum (Harris et al., 1986; Liégeois, 1998). For instance, post-collisional magmatism within the Himalayan-Tibet Orogen include Mg-rich ultrapotassic rocks related to melting of metasomatized upper mantle (Guo et al., 2013; Zhao et al., 2009 and references therein), and leucogranites associated with anatexis of metasedimentary protoliths coeval with post-collisional exhumation (Scharer et al., 1990; Sylvester, 1998) or resulting from partial fusion with the involvement of metaigneous crustal sources (Mahar et al., 2014). The Southern Brazilian Shear Belt also stands as a remarkable example of long and varied post-collisional

magmatism (Peruchi et al., 2021 and references therein). This magmatism evolves from a high-K subalkaline signature in the early stages to A-type signature in later stages, including granitoids of peraluminous and shoshonitic affinity between these two extremes (Bitencourt and Nardi, 2000; Chemale Jr. et al., 2012; Florisbal et al., 2012; Nardi and Bitencourt, 2007).

Post-collisional magmatism in the Central subprovince is mainly characterized by plutons with crystallization ages within the 595 to 555 Ma interval (Guimarães et al., 2004; Neves, 2015; Van Schmus et al., 2011 and references therein), comprising mainly high-K calc-alkaline to shoshonitic rocks in the early stages, and granitoids of more alkaline character in the late stages. The crystallization ages of the Teixeira Batholith granitoids are not compatible with an arc tectonic context in the studied region, since the literature data show early orogenic magmatism before the age of the Teixeira Batholith (Guimarães et al., 2004; Van Schmus et al., 2011), moreover in the Alto Pajeú Domain there is no juvenile material of Brasiliano age, nor are there rocks with typical calc-alkaline signature of magmatic arcs such as occurs to the west in the Piancó Alto-Brígida Domain (Sial and Ferreira, 2016 and references therein). Instead, the chemical characteristics and ages of the granitoids are consistent with magmatism associated with an early post-collisional tectonic setting that coincides with the transition between the flat-lying event and the transcurrent event. Thus, the mineralogical and geochemical features reflect a post-collisional tectonic setting, as is the case of most high Ba-Sr granitoids worldwide.

8.2. Sources

Several petrogenetic models have been proposed to explain the origin of HiBaSr granitoids. Most involve the interaction between crustal felsic melts and mantle mafic melts (Fowler et al., 2001, 2008; Tarney and Jones, 1994), or melting of mafic lower continental crust, with little involvement of mantle-derived magmas (Choi et al., 2009; Lara et al., 2017; Tarney and Jones, 1994, among others).

The granitoids of the Teixeira Batholith have geochemical and isotopic features compatible with crustal melts, such as high contents of silica (up to 72.0 wt.%), enrichment in large ion lithophile elements (LILE) and light rare earth elements (LREE), depletion in HFSE, and strongly negative εNd and εHf values (Fig. 11). Moreover, only the Tendó and Santo Antônio facies has a few mafic enclaves, which are generally considered the main evidence of involvement of mantle-derived melts (Roberts and Clemens, 1993). Additionally, zircon crystals from all facies have many inherited nuclei, mostly of Paleoproterozoic age, indicating that crustal reworking was the main process associated with the magma origin. The crustal signature of the granitoids is also corroborated by the chondrite-normalized trace element patterns, which show troughs at Nb, P, Ti and peaks at Sr and K, like those observed in middle and lower continental crust averages (Rudnick and Fountain, 1995).

The high-K calc-alkaline to shoshonitic affinity of the rocks can be explained by partial melting of hydrous, transitional to high-K calc-alkaline, mafic to intermediate metaigneous rocks in the middle/lower crust (Patiño-Douce, 1999; Roberts and Clemens, 1993). Figure 13A compares the composition of the studied granitoids with those of experimentally determined crustal melts. The mean values of Mg# ($MgO/(MgO+FeO_t)$ of ~ 0.20 (Fig. 13A), are like melts derived from amphibolitic/metabasaltic lower continental crust (< 0.40) without important contribution of mantle melts, since the involvement of mantle components should generate granitoids with higher Mg# values (Rapp and Watson, 1995). On the $Al_2O_3/(FeO_t+MgO)$ x $3CaO$ x $5(K_2O/Na_2O)$ ternary plot (Fig. 13B), with fields after Laurent et al. (2014), most samples share similarities with granitoids derived from partial melting of tonalites and high-K mafic rocks. The comparison of the granitoids with experimental melts from Patiño-Douce (1999) (Fig. 13C) also supports a mafic source (amphibolite), with some contribution of metagreywacke, suggesting that assimilation may have occurred during the transport of the magma to shallower crustal levels. Finally, the Na_2O and K_2O values of the granitoids, together

with their high silica contents (Figs. 6C and D), are similar to those reported for experimental melts derived from medium- to high-K basaltic rocks/amphibolites (Beard and Lofgren, 1991; Sisson et al., 2005).

Figure 13 – Discriminant diagrams for source of the studied granitoids. A) SiO_2 vs. Mg# [MgO/(FeOt + MgO)]. Fields for crustal partial melts determined in experimental studies and compiled by Jiang et al (2013) from the literature: low-K basaltic rocks at 8–16 kbar and 1000–1050 °C (Rapp and Watson,1995), moderately hydrous, medium- to high-K basaltic rocks at 7 kbar and 825–950 °C (Sisson et al., 2005), and pelitic rocks at 7–13 kbar and 825–950°C (Patiño Douce and Johnston, 1991); B) $Al_2O_3/(FeO_t+MgO)$ x 3CaO x $5(K_2O/Na_2O)$ ternary plot from Laurent et al. (2014); C) $CaO+FeO_t+MgO+TiO_2$ vs. $CaO/(FeO+MgO+TiO_2)$ binary diagrams of Patiño-Douce (1999) with fields representing composition of experimental melts generated by dehydration melting of a wide range of bulk compositions.

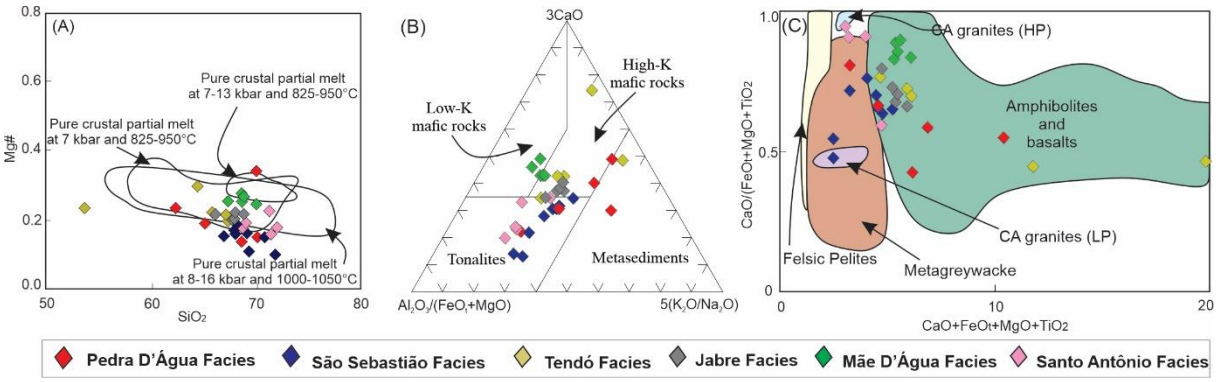

Zhang et al. (2006) proposed a relation between chemistry and depth of granitic magma generation, based mainly on Sr and Yb contents. The high Sr (1110 - 2530 ppm) and low Yb (0.35 - 2.25 ppm; mean = 1.06 ppm) contents in the Teixeira Batholith are like those of granites formed at high pressure, with residual garnet. More recently, Chapman et al. (2015) proposed that the Sr/Y ratio of orogenic granites is related to crustal thickness. This ratio is usually above 60 in the Teixeira Batholith, suggesting partial melting at depths exceeding 60 km. Sr tends to be retained in plagioclase at low pressures (<10 kbar), while at high pressures, outside the plagioclase stability field, Sr is incompatible and tends to migrate to the melt (Kay and Mpodozis, 2001). Lack of europium anomalies in the REE patterns (Fig. 7) indicates that plagioclase was not retained in the source, suggesting high degrees of partial melting that generated a plagioclase-free residue and Sr-rich melts (Martin et al., 2005). Several other

studies have shown that melts with high Sr/Y and $(La/Yb)_N$ signatures were generated at high-pressure condition (He et al., 2011; Zhang et al., 2010, among others). In synthesis, the high Sr/Y and fractioned REE patterns lacking Eu anomalies in the granitoids are compatible with their genesis through partial melting of mafic infracrustal sources, leaving garnet and/or amphibole in the residue (Cullers and Graf, 1984; Kay and Mpodozis, 2001).

The granitoids from the São Sebastião facies differ from those of the other facies for presenting aegirine-augite as one of the main mafic minerals and by having a higher average value for total alkalis ($Na_2O + K_2O$) (10.6 wt.% versus 9.3 wt%). The low MgO contents of this facies (mean ~ 0.31 wt%) is incompatible with a direct contribution of juvenile material. Most likely, during the magmatic evolution, the precursor magma interacted, in small proportions, with differentiated mantle-derived alkaline magma, as suggested by field features indicative of interaction between two different felsic magmas (Fig. 3C).

Inherited zircon cores and isotopic data allow to constrain the age(s) of the source(s) of the granitoids: (a) zircon cores revealed U-Pb ages ranging from 1.8 to 2.1 Ga (Fig. 10), with Hf model ages ranging from 2.3 to 2.8 Ga and $\varepsilon_{Hf:}$ values from -2.5 to +6.0 (Fig. 11A); (b) the Hf isotopic signatures of the 600-585 Ma zircon grains are characterized by negative ε_{Hf} values (-16.27 to -20.80) and Paleoproterozoic to Neoarchean model ages (2.3 to 2.6 Ga); (c) the granites have negative εNd values (-13.68 to -16.04) and Paleoproterozoic Nd model ages (2.08 – 2.23 Ga). These ages are similar to the ages of basement rocks from the Central subprovince, which mainly comprises 2.2-2.0 Ga-old orthogneisses with a small contribution of Archean materials (Brito Neves et al., 2020; Neves et al., 2006, 2015; Santos et al., 2017; Van Schmus et al., 2011). These results attest that the main source of the granitoids was the preexisting Paleoproterozoic basement of the Central subprovince. Other granites with similar age and chemical composition in the Central subprovince also had their origin linked to partial fusion

of tectonically thickened Paleoproterozoic crust (Guimarães et al., 2004; Van Schmus et al., 2011).

Tonian zircon xenocrysts that occur in the granitoids of the Tendó facies and in a sample from Santo Antônio facies provided a Nd model age of 1.75 Ga, which is similar to those reported for Cariris Velhos orthogneisses (Kozuch, 2003; Van Schmus et al., 2011) (Fig. 11B). Since these facies are intruded in Cariris Velhos metagranitoids, the source of the granitoids from the westernmost portion of the Teixeira Batholith may have had a contribution of Tonian rocks in addition to Paleoproterozoic ones.

8.3. Magmatic evolution

The negative correlation between SiO_2 and CaO, Fe_2O_3t, MgO, P_2O_5, TiO_2, Al_2O_3, Ba, Ce, Sr and Zr (Fig. 6) is compatible with fractionation of mineral phases such as amphibole, titanite, epidote, apatite, Fe-Ti oxides, zircon and pyroxene. Trace element diagrams showing positive anomaly of K, Ba and Sr indicate that feldspars were not fractionated during the magmatic crystallization. The non-fractionation of plagioclase throughout the magmatic differentiation of the Teixeira Batholith is corroborated by the SiO_2 versus Na_2O plot (Fig. 6C), which does not show negative correlation and by the absence of negative Eu anomaly in the Chondrite-normalized REE patterns (Fig. 7A). As plagioclase fractionation seems not to have been important, the negative CaO trend (Fig. 6B) is most likely reflecting amphibole, epidote and/or apatite fractionation. Strong negative anomalies of Ti and P (Fig. 7) are consistent with fractionation of titanite and apatite, that removed these elements selectively, without causing larger depletion in the other HFSE.

8.4. Magma genesis

Despite its proximity to the Patos Shear Zone and the ENE-WSW elongation, like most syn-transcurrent plutons of the Borborema Province, intrusion of the Teixeira Batholith predated deformation associated with this shear zone. Archanjo et al. (2008) pointed out that

the internal fabric of the batholith, as determined by AMS and shape preferred orientation, is incompatible with syn-transcurrent emplacement. Instead, the dominant NW orientation of magnetic lineations is consistent with emplacement during the waning stages of regional contraction characterized by development of flat-lying foliations related to NW-directed tectonic transport. This conclusion is corroborated by the age of the batholith (600-585 Ma), which contrasts with the 566-558 Ma interval determined for the high-grade dynamic metamorphism related to the Patos Shear Zone (Viegas et al., 2014).

The Teixeira Batholith was emplaced at the end of a long period of contractional tectonics resulting from the convergence of the São Francisco/Congo and São Luís-West African Cratons during the Brasiliano/Pan-African Orogeny. In the Central subprovince, this stage lasted from ca. 635 to 600 Ma (Fig. 14A) and is characterized by development of shallow dipping foliation associated with dominantly high-temperature (500°C-750°C), medium-pressure (500-900 MPa) metamorphism, W- to NW-directed tectonic transport, and intrusion of syn-orogenic plutons bearing a flat-lying magmatic to solid-state foliation (Guimarães et al., 2004, 2011; Medeiros, 2004; Neves et al., 2006, 2017; Sial and Ferreira, 2016; Silva and Neves, 2021). The main mechanisms proposed to explain the origin of magmatism in such a post-collisional context are delamination and/or convective removal of the lithosphere (Black and Liégeois, 1993; Zhang et al., 2017), and slab breakoff (Atherton and Ghani, 2002; Liégeois and Black, 1987).

Considering the geochemical and isotopic data, and the regional tectonic context, a possibility for the generation of the HiBaSr granites from the Teixeira Batholith is partial melting of the base of tectonically thickened crust induced by delamination of the lithospheric mantle. Where delamination has taken place, the presence of mantle-derived magmas is also expected. In the Teixeira Batholith there is no strong evidence of interaction with mantle mafic magmas, but several igneous intrusions of the Alto Pajeú Domain, in the 600 - 580 Ma time

interval, record the participation of melt with lithospheric mantle signature (Guimarães et al., 2004; Neves and Mariano, 2004; Sial and Ferreira, 2016; Van Schmus et al., 2011 and references therein). However, the absence of the expected effects of lithospheric delamination, such as rapid uplift and subsequent extension (Kay and Mahlburg-Kay, 1991; Kay and Kay, 1993), are not record in the study region and nowhere in the Central subprovince. Slab break-off is also unlikely since it occurs shortly after collision. Other possibility is foundering of densified deep-crustal fragments (Chapman et al., 2017). Ganade de Araújo et al. (2014) suggest that the Brasiliano tectonotermal evolution of the Borborema Province is marked by an initial collisional context (620 to 600 Ma) and generalized crustal thickening with development of eclogites and high-T thrusting foliation. Indeed, the great thickness of the orogenic crust, suggested by the high Sr/Y ratios of the studied granitoids, are compatible with existence of large tracts of eclogite in the lower crust (Chapman et al., 2017), as proposed by Ganade de Araujo et al., (2014). Crustal foundering would result in replacement of local portions of the lower crust by the mantle, leading to high enough temperatures to promote partial melting of mafic protoliths.

The mechanism that led the partial melting of deep mafic crust to produce the Teixeira Batholith magmatism remains unclear, however, the regional tectonic context and chemical characteristics of the studied rocks, point out the importance of processes associated with partial melting of tectonically thickened crust.

8.5. Regional implications

Metavolcanosedimentary rocks and Tonian orthogneisses correspond to the host rocks of the Teixeira Batholith and are the main constituents of the Alto Pajeú domain, which has only a small exposure of basement rocks. Despite this fact, inherited zircon grains and isotopic data reported in this work show a predominantly Paleoproterozoic crustal source for the voluminous granitic magmatism represented by the Teixeira Batholith, suggesting the presence

of a widespread Paleoproterozoic lower crust under the Alto Pajéu domain. A Paleoproterozoic basement is well documented in the Rio Capibaribe and Alto Moxotó domains that occur southeastward of the Alto Pajeú domain (Neves et al., 2006, 2015; Santos et al., 2017; Van Schmus et al., 2011), and recently, Brito Neves and Passarelli (2020) also reported Paleoproterozoic U-Pb zircon ages (2.0 – 2.2 Ga) for migmatized orthogneisses in the Piancó-Alto Brígida domain, northwestward of the Alto Pajeú domain. These findings favor the existence a continuous Paleoproterozoic basement under all domains of the Central subprovince, casting in doubt propositions that these domains are independent tectonostratigraphic terranes amalgamated during the Brasiliano Orogeny (Santos et al., 2021 and references therein). Rather, orogenic deformation in a dominantly intracontinental setting seems to be the most likely explanation for the evolution of the Central subprovince.

9. Conclusions

The Teixeira Batholith comprises metaluminous, oxidized I-type granites with shoshonitic to high-K calc-alkaline affinities. The high Ba and Sr contents, and low Rb, Nb, Th, Y and HREE contents, in addition to negative Nb anomalies are like geochemical characteristics of the so-called HiBaSr granitoids worldwide. Geochemical data and the isotope signature, characterized by negative ℇNd(590 Ma) and ℇHf(t) values and Paleoproterozoic Hf and Nd T_{DM} model ages (mostly 2.5 to 2.0 Ga), suggest generation by partial melting of intermediate to mafic rocks of the Paleoproterozoic basement, leaving a plagioclase-free residue containing amphibole and/or garnet. The batholith was intruded at 600-585 Ma after a long period of contractional tectonics (ca. 635-600 Ma) related to the Brasiliano (= Pan African) Orogeny, during the evolution of the west margin of the Gondwana supercontinent. Despite the elongate shape and location close to the major Patos shear zone, the Teixeira Batholith is ca. 20 Ma older than shear zone development. Geochronological data then allow to classify the

Teixeira Batholith as a post-collisional but pre-transcurrent intrusion, marking the transition between contractional and transcurrent tectonic regimes. Geochronological and isotopic data also point to the existence of widespread Paleoproterozoic crust beneath the exposed crustal level, whose age and isotopic signature is similar to that of the adjacent domains, suggesting a continuous basement across the central portion of the Borborema Province.

Acknowledgements

We acknowledge the Dr. Elton Dantas (University of Brasilia) for the zircon mounts. The authors are grateful to Dr. Roberto Weinberg and an anonymous reviewer for constructive comments that help to improve the manuscript. This work was supported by the Brazilian National Research Council (CNPq), Proc. 421353/2018-0. JVL thanks CAPES for the doctoral scholarship.

References

Archanjo, C.J., Hollanda, M. H. B. M., Rodrigues, S. W. O, Brito Neves, B. B., Armstong, R., 2008. Fabrics of pre- and syntectonic granite plutons and chronology of shear zones in the Eastern Borborema Province, NE Brazil. Journal of Structural Geology 30, 310-336.

Atherton, M.P., Ghani, A.A., 2002. Slab-breakoff: a model for Caledonian, Late granite syn-collisional magmatism in the orthotectonic (metamorphic) zone of Scotland and Donegal, Ireland. Lithos 62, 65-85.

Barbarin, B., 1999. A review of the relationships between granitoids types, their origins and their geodynamic environments. Lithos 46, 605-626.

Beard, J.S., Lofgren, G.E., 1991. Dehydration melting and water-saturated melting of basaltic and andesitic greenstones and amphibolites at 1, 3, and 6.9 kb. Journal of Petrology 32, 365-401.

Bitencourt, M.F., Nardi, L.V.S., 2000. Tectonic setting and sources of magmatism related to the Southern Brazilian Shear Belt. Revista Brasileira de Geociências 30, 186–189.

Bittar, S.M.B., 1998. Faixa Piancó – Alto Brígida: Terrenos tectonoestratigráficos sob regimes metamórficos e deformacionais contrastantes. PhD Thesis. Instituto de Geociências, Universidade de São Paulo.

Black, R., Liégeois, J.P., 1993. Cratons, mobile belts, alkaline rocks and continental lithospheric mantle: the Pan-African testimony. Journal of the Geological Society of London 150, 89-98.

Bonin B., Azzouni-Sekkal A., Bussy F., Ferrag S., 1998. Alkali-calcic and alkaline post-orogenic (PO) granite magmatism: petrologic constraints and geodynamic settings. Lithos 45 (1), 45-70.

Brito Neves, B.B., Passarelli, C., 2020. Terrenos tectonoestratigráficos dispersos do embasamento pré-Brasiliano (São José do Caiana, Açude Coremas, Icaiçara) na porção centro-oeste da Zona Transversal (Paraiba, Ceará e Pernambuco). Geologia USP. Série Científica 20 (3), 81–105.

Brito Neves, B.B., Van Schmus, W.R., Santos, L.C.M.L., 2020. Alto Moxotó Terrane, a fragment of Columbia supercontinent in the Transversal Zone interior: Borborema Province, Northeast Brazil. Brazilian Journal of Geology 50, e20190077.

Caxito, F.A., Santos, L.C.M.L., Ganade, C.E., Bendaoud, A., Fettous, E.H., Bouyo, M.H., 2020. Toward an integrated model of geological evolution for NE Brazil–NW Africa: The Borborema Province and its connections to the Trans-Saharan (Benino-Nigerian and Tuareg shields) and Central African orogens. Brazilian Journal of Geology 50, e20190122.

Chapman, J.B., Ducea, M.N., DeCelles, P.G., Profeta, L., 2015. Tracking changes in crustal thickness during orogenic evolution with Sr/Y: An example from the North American Cordillera. Geology 43 (10), 919–922.

Chapman, T., Clarke, G.L., Piazolo, S., Daczko, N. R., 2017. Evaluating the importance of metamorphism in the foundering of continental crust. Scientific Reports 7, 13039.

Chappell, B.W., White, A.J.R., 1974. Two contrasting granite types. Pacific Geology 8, 173-174.

Chappell, B.W., White, A.J.R., 1992. I- and S- type granites in Lachlan Fold Belt. Transactions Royal Society Edinburgh 83, 1-26.

Chemale Jr., F., Mallmann, G., Bitencourt, M.F., Kawashita, K., 2012. Time constraints on magmatism along the Major Gercino Shear Zone, southern Brazil: implications for West Gondwana reconstruction. Gondwana Research 22 (1), 184–199.

Chen, J-Y, Yang, J-H, Zhang, J-H, Sun, J.F., Wilde, S.A., 2013. Petrogenesis of the Cretaceous Zhangzhou batholith in southeastern China: Zircon U–Pb age and Sr–Nd–Hf–O isotopic evidence. Lithos 162-163,140-156.

Choi, S., Rajesh, V.J., Seo, J., Park, J.W., Oh, C.W., Pak, S.J., Kim, S.W., 2009. Petrology, geochronology and tectonic implications of Mesozoic high Ba–Sr granites in the Haemi area, Hongseong Belt, South Korea. Island Arc 18, 266–281.

Cullers, R.L., Graf, J.L., 1984. Rare earth elements in igneous rocks of the continental crust: intermediate and silicic rocks, in: Henderson, P. (Ed.), Rare Earth Elements in Igneous Rocks of the Continental Crust: Intermediate and Silicic Rocks – Ore Petrogenesis. Elsevier, New York, pp. 237-274.

Dantas, E.L., Van Schmus, W.R., Hackspacher, P.C., Fetter, A.H., Brito Neves, B.B., Cordani, U., Nutman, A.P. & Williams, I.S., 2004. The 3.4 e 3.5 Ga São José do Campestre massif, NE Brazil: remnants of the oldest crust in South America. Precambrian Research 130, 113-137.

Ferreira, C.A., Santos, E.J., 2000. Jaguaribe SE - Folha SB. 24-Z, Estados do Ceará, Rio Grande do Norte, Paraíba e Pernambuco, single ed. Programa Levantamentos Geológicos Básicos do Brasil-CPRM, Recife.

Ferreira, V.P., Sial, A.N., Jardim de Sá, E.F., 1998. Geochemical and isotopic signatures of Proterozoic granitoids in terranes of Borborema structural province, northeast Brazil. Journal of South American Earth Sciences 11, 439–455.

Florisbal, L.M., Bitencourt, M.F., Janasi, V.A., Nardi, L.V.S., Heaman, L.M., 2012. Petrogenesis of syntectonic granites emplaced at the transition from thrusting to transcurrent tectonics in post-collisional setting: whole-rock and Sr–Nd–Pb isotope geochemistry in the Neoproterozoic Quatro Ilhas and Mariscal granites, southern Brazil. Lithos 153, 53–71.

Fowler, M.B., Henney, P.J., Darbyshire, D.P.F., Greenwood, P.B., 2001. Petrogenesis of high Ba–Sr granites: the Rogart pluton, Sutherland. Journal of the Geological Society of London 158, 521-534.

Fowler, M.B., Kocks, H., Darbyshire, D.P.F., Greenwood, P.B., 2008. Petrogenesis of high Ba–Sr plutons from the Northern Highlands Terrane of the British Caledonian Province. Lithos 105, 129-148.

Frost, R.B., Barnes, C.G., Collins, W.J., Arculus, R.J., David, J.E., Frost, C.D., 2001. A geochemical classification for granitic rocks. Journal of Petrology 42 (11), 2033-2048.

Ganade de Araújo, C.E., Cordani, E., Weinberg, R., Basei, M.A.S., 2014. Extruding the Borborema Province (NE-Brazil): a two-stage Neoproterozoic collision process. Terra Nova 26 (2), 157-168.

Guimarães, I. P., Brito, M. F. L., Lages, G. A., Da Silva Filho, A. F., Santos, L., Brasilino, R. G., 2016. Tonian granitic magmatism of the Borborema Province, NE Brazil: A review. Journal of South American Earth Sciences 68, 97-112.

Guimarães, I. P., Da Silva Filho, A. F., Almeida, C. N., Van Schmus, W. R., Araujo, J. M. M., Melo, S. C., Melo, E. B., 2004. Brasiliano (Pan-African) granitic magmatism in the Pajeú-Paraíba belt, northeast Brazil: an isotopic and geochronological approach. Precambrian Research 135, 23-53.

Guimarães, I. P., Schmus, W. R. V., Neves, B. B. B., Bittar, S. M. B., Da Silva Filho, A, Armstrong, R. A., 2012. U-Pb zircon ages of orthogneisses and supracrustal rocks of the Cariris Velhos belt: Onset of Neoproterozoic rifting in the Borborema Province, NE Brazil. Precambrian Research 192, 52-57.

Guimarães, I.P., Da Silva Filho, A.F., Almeida, C.N., Macambira, M., Armstrong, R.A., 2011. U-Pb SHRIMP data constraints on calc-alkaline granitoids with 1.3-1.6 Ga Nd TDM model ages from the central domain of the Borborema province. Journal of South American Earth Sciences 31 (4), 383-396.

Guo, Z.F., Wilson, M., Zhang, M.L., Cheng, Z.H., Zhang, L.H., 2013, Post-collisional, Krich mafic magmatism in south Tibet: constraints on Indian slab-to-wedge transport processes and plateau uplift. Contribution to Mineralogy and Petrology 165, 1311–1340.

Harris, N.B.W., Pearce, J.A., Tindle, A.G., 1986. Geochemical characteristics of collision zone magmatism. In: Coward, M.P., Ries, A.C. (Eds.), Collision Tectonics. Journal of Geological Society Special Publication, London vol. 19, pp. 67–81.

He, Y., Li, S., Hoefs, J., Huang, F., Liu, S.-A., Hou, Z., 2011. Post-collisional granitoids from the Dabie orogen: New evidence for partial melting of a thickened continental crust. Geochimica et Cosmochimica Acta 75, 3815-3838.

Ishihara, S., 1977. Magnetite-series and ilmenite-series granitic rocks. Mining Geology, 27, 293–305.

Jiang, Y-H, Jia, R-Y, Liu, Z., Liao, S-Y, Zhao, P., Xhou, Q., 2013. Origin of Middle Triassic high-K calc-alkaline granitoids and their potassic microgranular enclaves from the western

Kunlun orogeny, northwest China: a record of the closure of Paleo-Tethys. Lithos 156-159, 13-30.

Kay, R.W. and Kay, S.M., 1993. Delamination and delamination magmatism. Tectonophysics, 219: 177-189.

Kay, R.W., Mahlburg-Kay, S., 1991. Creation and destruction of lower continental crust. Geologische Rundschau 80, 259-278.

Kay, S.M., Mpodozis, C., 2001, Central Andean ore deposits linked to evolving shallow subduction systems and thickening crust: GSA Today 11 (3), 4-9.

Kozuch, M., 2003. Isotopic and Trace Element Geochemistry of Early Neoproterozoic Gneissic and Metavolcanic rocks in the Cariris Velhos orogen of the Borborema Province, Brazil and their Bearing Tectonic Setting. PhD Thesis. Kansas University.

Lara, P., Oyhantçabal, P., Dadd, K., 2017. Post-collisional, Late Neoproterozoic, high-Ba-Sr granitic magmatism from the Dom Feliciano Belt and its cratonic foreland, Uruguay: Petrography, geochemistry, geochronology, and tectonic implications. Lithos 277, 178-198.

Laurent, O., Martina, H., Moyena, J.F., Doucelance, R., 2014. The diversity and evolution of late-Archean granitoids: Evidence for the onset of "modern-style" plate tectonics between 3.0 and 2.5 Ga. Lithos 205, 208-235.

Liégeois, J.P., 1998. Some words on the post-collisional magmatism. Preface to special edition on post-collisional magmatism. Lithos 45, 15–17.

Liégeois, J.P., Black, L.P., 1987. Alkaline magmatism subsequent to collision in the Pan-African belt of the Adrar des Iforas (Mali). In: Fitton, J.G., Upton, B.J.G. (Eds.), Alkaline Igneous Rocks. Geological Society Special Publication, London vol. 30, pp. 381–401.

Lima, R.G., Archanjo, C.J., Macedo, J.W.P., Melo Jr., G., 2000. Anomalias de suscetibilidade magnética no batólito granıtico de Teixeira (Província da Borborema, Nordeste do Brasil)

e sua relação com a zona de cisalhamento de Itapetim. Revista Brasileira de Geociências 30 (4), 685–692.

Loiselle, M.C., Wones, D.R., 1979. Characteristics and origin of anorogenic granites. Geological Society of America-Abstracts with Programs 11, 468.

Mahar, M.A., Mahéo, G., Goodell, P.C., Pavlis, T.L., 2014. Age and origin of post collision Baltoro granites, south Karakoram, North Pakistan: Insights from in-situ U–Pb, Hf and oxygen isotopic record of zircons. Lithos 205, 341–358

Martin, H., Smithies, R.H., Rapp, R., Moyen, J.F., Champion, D., 2005. An overview of adakite, tonalite–trondhjemite–granodiorite (TTG), and sanukitoid: relationships and some implications for crustal evolution. Lithos 79, 1–24.

Medeiros, V.C., 2004. Evolução geodinâmica e condicionamento estrutural dos terrenos Piancó-Alto Brígida e Alto Pajeú, Domínio da Zona Transversal. PhD thesis. Universidade Federal do Rio Grande do Norte.

Middlemost, E.A.K., 1997. Magmas, Rocks, and Planetary Development, First ed. Longman, Harlow.

Nakamura, N., 1974. Determination of REE, Ba, Fe, Mg, Na, and K in carbonaceous and ordinary chondrites. Geochimica et Cosmochimica Acta 38, 757-775.

Neves, S.P., Mariano, G., 2004. The lithospheric mantle as a source of magmas during orogenic processes: insights from high-K diorites in the Borborema Province and implications for continental dynamics. Journal of the Virtual Explorer 17, 3.

Nardi, L.V.S., Bitencourt, M.F., 2007. Magmatismo granítico e evolução crustal do sul do Brasil. In: Iannuzzi, R., Frantz, J.C. (Eds.), 50 anos de geologia. Instituto de Geociências, Porto Alegre, pp. 125–141.

Neves, S.P., 2003. Proterozoic history of the Borborema Province (NE Brazil): correlations with neighboring cratons and Pan-African belts, and implications for the evolution of western Gondwana. Tectonics 22 (4), 1031-1044.

Neves, S.P., Bruguier, O., Vauchez, A., Bosch, D., Silva, J. M. R., Mariano, G., 2006. Timing of crust formation, deposition of supracrustal sequences, and Transamazonian and Brasiliano metamorphism in the East Pernambuco belt (Borborema Province, NE Brazil): implications for western Gondwana assembly. Precambrian Research 149, 197-216.

Neves, S.P., 2015. Constrains from zircon geochronology on the tectonic evolution of the Borborema Province: Widespread intracontinental Neoproterozoic reworking of a Paleoproterozoic accretionary orogen. Journal of Source American Earth Science 58, 150-164.

Neves, S.P., 2021. Comparative geological evolution of the Borborema Province and São Francisco Craton (eastern Brazil): Decratonization and crustal reworking during West Gondwana assembly and implications for paleogeographic reconstructions. Precambrian Research 355, 106119.

Neves, S.P., Bezerra, J.P.S., Bruguier, O., França, R.H.M., 2020. Evidence for Early Tonian (Ca. 1000–940 Ma) continental rifting in southern Borborema Province (NE Brazil): tectonic inheritance and shear zone nucleation during assembly of West Gondwana. International Geology Review 63, 851-865.

Neves, S.P., Lages, G.A., Brasilino, R.G., Miranda, A.W.A., 2015. Paleoproterozoic accretionary and collisional processes and the build-up of the Borborema Province (NE Brazil): Geochronological and geochemical evidence from the Central Domain. Journal of South American Earth Sciences 58, 165-187.

Neves, S.P., Silva, J.M.R., Bruguier, O., 2017. Geometry, kinematics and geochronology of the Sertânia Complex (central Borborema Province, NE Brazil): Assessing the role of

accretionary versus intraplate processes during West Gondwana assembly. Precambrian Research 298, 552-571.

Patiño Douce, A.E., Johnston, A.D., 1991. Phase equilibria and melt productivity in the pelitic system: implications for the origin of peraluminous granitoids and aluminous granulites. Contributions to Mineralogy and Petrology 107, 202–218.

Patiño-Douce, A.E., 1999. What do experiments tell us about the origin of granitic magmas? In: Castro, A., Fernandez, C., Vigneresse, J.L. (Eds.), Understanding Granites: Integrating New and Classical Techniques. Special Publication vol. 158. Geologicas Society of London, London, pp. 55–75

Patiño Douce, A.E., Beard, J.S., 1995. Dehydration-melting of biotite gneiss and quartz amphibolite from 3 to 15 kbar. Journal of Petrology 36, 707–738.

Pearce, J., 1996. Sources and setting of granitic rocks. Episodes 4, 120-125.

Pearce, J.A., Harris, N.B.W., Tindle, A.G., 1984. Trace element discrimination diagrams for the tectonic interpretation of granitic rocks. Journal of Petrology 25, 956-983.

Peccerillo, A., Taylor, S. R., 1976. Plio-Quaternary Magmatism in Italy: Roman, Ernici-Roccamonfina, Intra-Apennine and Vulture Provinces. Contributions to Mineralogy and Petrology 58, 63–81.

Peruchi, F.M., Florisbal, L.M., Bitencourt, M.F., Padilha, D.F., Nardi, L.V.S., 2021. Ediacaran post-collisional K-rich granitic magmatism within the Major Gercino Shear Zone, Southern Brazil: An example of prolonged magmatism and differentiation under active transcurrent tectonism. Lithos, 106341.

Rapp, R.P., Watson, E.B., 1995. Dehydration melting of metabasalt at 8-32 kbar: implications for continental growth and crust-mantle recycling. Journal of Petrology 36, 891-931.

Roberts, M.P., Clemens, J.D., 1993. Origin of high-potassium, calc-alkaline, I-type granitoids. Geology 21, 825–828.

Rudnick, R., Fountain, D., 1995. Nature and composition of the continental crust: a lower crustal perspective. Reviews of Geophysics 33 (3), 267-309.

Santos, E. J., Medeiros, V.C., 1999. Constraints from granitic plutonism on Proterozoic crustal growth of the Transverse Zone, Borborema Province, NE Brazil. Revista Brasileira de Geociências 29, 73-84.

Santos, E.J., Van Schmus, W.R., Kozuch, M., and Brito Neves, B. B., 2010. The Cariris Velhos Tectonic event in Northeast Brazil: Journal of South American Earth Sciences 29, 61-76.

Santos, L.C.M.L., Dantas, E.L., Cawood, P.A., Santos, E.J., Fuck, R.A., 2017. Neoarchean crustal growth and Paleoproterozoic reworking in the Borborema Province, NE Brazil: Insights from geochemical and isotopic data of TTG and metagranitic rocks of the Alto Moxotó Terrane. Journal of South American Earth Sciences 79, 342-363.

Santos, L.C.M.L., Dantas, E.L., Santos, E.J., Santos, R.V., Lima, H.M., 2015. Early to late Paleoproterozoic magmatism in NE Brazil: The Alto Moxotó Terrane and its tectonic implications for the pre-West Gondwana assembly. Journal of Source American Earth Science 58, 188-209.

Santos, L.C.M.L., Olivieria, R.G., Dantas, E.L., Lages, G.A., Caxito, F., Cawood, P.A., Fuck, R.A., Lima, H.M., Santos, G.L., Araújo Neto, J.F., 2021. Evidence for Neoproterozoic terrane accretion in the central Borborema Province, West Gondwana deduced by isotopic and geophysical data compilation. International Geology Review, https://doi.org/10.1080/00206814.2021.1944332.

Santos, T.J.S., Fetter, A.H., Hackspacher, P.C., Van Schmus, W.R., and Nogueira Neto, J.A., 2008. Neoproterozoic tectonic and magmatic episodes in the NW sector of Borborema Province, NE Brazil, during assembly of Western Gondwana: Journal of South American Earth Sciences 25, 271-284.

Scharer, U., Copeland, P., Harrison, T. M. & Searle, M. P., 1990. Age, cooling history, and origin of post-collisional leucogranites in the Karakoram batholith: a multi-system isotope study. Journal of Geology, 98, 233-251.

Sial, A.N., Ferreira, V.P., 2016. Magma associations in Ediacaran granitoids of the Cachoeirinha-Salgueiro and Alto Pajeú terranes, northeastern Brazil: Forty years of studies. Journal of South American Earth Sciences 68, 113-133.

Silva, V.L., Neves, S.P., 2021. Transition from contractional to transpressive tectonics: evidence from the Feira Nova Region, Rio Capibaribe Domain, Borborema Province, NE Brazil. Brazilian Journal of Geology 51, e20200049.

Sisson, T., Ratajeski, K., Hankins, W., Glazner, A., 2005. Voluminous granitic magmas from common basaltic sources. Contributions to Mineralogy and Petrology 148, 635-661.

Sun, S.S., McDonough, W.F., 1989. Chemical and isotopic systematics of oceanic basalts: Implication for mantle composition and processes. Geological Society of London, Special Publications 42 (1), 313-345.

Sylvester, P.J., 1998. Post-collisional strongly peraluminous granites. Lithos 45, 29–44.

Tarney, J., Jones, C.E., 1994. Trace element geochemistry of orogenic igneous rocks and crustal growth models. Journal of the Geological Society of London 151, 855-868.

Trompette, R.R., 1997. Neoproterozoic (~600 Ma) aggregation of Western Gondwana: a tentative scenario. Precambrian Research 82 (1-2), 101-112.

Van Schmus, W. R., Kozuch, M., Brito Neves, B. B., 2011. Precambrian history of the Zona Transversal of the Borborema Province, NE Brazil: Insights from SmeNd and UePb geochronology. Journal of South American Earth Sciences 31, 227-252.

Van Schmus, W. R., Oliveira, E. P., Silva Filho, A. F., Toteu, S. F., Penaye, J., Guimarães, I. P., 2008. Proterozoic links between the Borborema province, NE Brazil, and the Central African Fold Belt. Geological Society of London, Special Publication 294, 69-99.

Vauchez, A., Neves, S.P., Caby, R., Corsini, M., Egydio-Silva, M., Arthaud, M.H., Amaro, V., 1995. The Borborema shear zone system, NE Brazil. Journal of South American Earth Sciences 8, 247-266.

Viegas, L.G.F., Archanjo, C.J., Hollanda, M.H.B.M., Vauchea, A., 2014. Microfabrics and zircon U-Pb (SHRIMP) chronology of mylonites from the Patos shear zone (Borborema Province, NE Brazil). Precambrian Research 243, 1-17.

Whalen, J.B., Currie, K.L., Chappell, B.W., 1987 A-types granites: geochemical characteristics, discrimination and petrogenesis. Contributions to Mineralogy and Petrology 95, 407-419.

White, A.J.R., 1979. Sources of granite magmas. Geological Society of America Abstracts with Programs 11 (7), 539.

Zhang, H., Harris, N., Guo, L., Xu, W., 2010. The significance of Cenozoic magmatism from the western margin of the eastern syntaxis, southeast Tibet. Contributions to Mineralogy and Petrology 160, 83-98.

Zhang, L.Q., Zhang, H.F., Zhang, S., Xiong, Z., Luo, B.J., Yang, H., Pan, F., Zhou, X., Xu, W., and Guo, L., 2017. Lithospheric delamination in post-collisional setting: Evidence from intrusive magmatism from the North Qilian orogen to southern margin of the Alxa block, NW China. Lithos 288-289, 20-34.

Zhang, Q., Wang, C.Y.W., Li, C.D., Wang, Y.L., Jin, W.J., Jia, X.Q., 2006. Granite classification on the basis of Sr and Yb contents and its implications. Acta Petrologica Sinica 22 (9), 2249-2269.

Zhao, Z.D., Mo, X.X., Dilek, Y, Niu, Y.L., DePaolo, D.J., Robinson P., Zhu, D.C., Sun, C.G., Dong, G.C., Zhou, S., Luo, Z.H., Hou, Z.Q., 2009. Geochemical and Sr-Nd-Pb-O isotopic compositions of the post-collisional ultrapotassic magmatism in SW Tibet: petrogenesis and implications for India-continental subduction beneath southern Tibet. Lithos 113, 190–212.

Table 1 Representative whole-rock compositions of the Teixeira Batholith granitoids.

	Pedra D'Água Facies			São Sebatião Facies			Tendó Facies			Jabre Facies			Mãe D'Água Facies			Santo Antônio Facies		
Samples	JD11	JD140	JD09	JD149	TX06	JD30	JD01C	JD48	TX08	JD45	JD67	JD45	JD72	JD73	JD75	IM02	JD54	JD56
Major oxides (wt. %)																		
SiO_2	70.2	62.4	67.4	71.9	67	68.2	53.5	67.4	65.9	68.1	66.2	68.1	70.1	67.4	68.8	68.8	71.5	72
Al_2O_3	15.85	14.85	15.1	15.15	16.45	15.55	14.55	16.55	16.6	16.3	16.5	16.3	15.25	16.6	16.35	15.75	15.5	15
Fe_2O_3	1.5	5.28	1.71	1.43	2.47	2.58	10.4	2.12	2.82	2.06	2.54	2.06	2.16	2.13	2.18	1.4	1.16	1.32
CaO	1.38	3.69	1.8	0.83	1.81	2.02	6.35	1.98	2.47	2.05	2.23	2.05	2.36	2.5	2.48	1.47	1.39	1.46
MgO	0.23	1.38	0.77	0.14	0.38	0.52	2.77	0.45	0.7	0.51	0.61	0.51	0.62	0.64	0.68	0.25	0.19	0.24
Na_2O	5.14	3.43	4.07	5.32	5.21	4.49	3.7	5.55	5.12	5.26	5.09	5.26	4.85	5.24	5.12	5.42	5.07	4.88
K_2O	4.62	6.27	4.58	4.85	5.64	5.56	3.95	4.63	4.92	4.73	4.97	4.73	3.22	3.64	3.69	4.5	4.29	4.19
TiO_2	0.14	0.57	0.4	0.11	0.27	0.29	1.6	0.23	0.33	0.23	0.29	0.23	0.28	0.27	0.27	0.12	0.1	0.11
MnO	0.05	0.12	0.02	0.04	0.07	0.08	0.29	0.06	0.09	0.05	0.08	0.05	0.05	0.05	0.05	0.04	0.03	0.03
P_2O_5	0.03	0.32	0.13	0.03	0.07	0.09	0.5	0.07	0.1	0.07	0.1	0.07	0.11	0.11	0.1	0.03	0.02	0.03
Total	100.03	100.51	99.80	101.28	101.06	101.03	99.09	100.31	100.84	100.46	100.14	100.46	100.78	100.58	100.89	98.82	100.21	100.37
Trace elements (ppm)																		
Ba	2540	7370	5090	5010	3910	4430	3800	4310	5850	4130	5850	4130	2500	2780	2890	2440	2220	2490
Ce	30.9	120.5	124	114.5	60.5	83.9	103	59.6	77.2	48	75.7	48	48.2	47.5	49.9	25.1	22.6	23.8
Cr	120	180	170	220	220	270	110	140	190	140	160	140	240	200	190	220	160	210
Cs	0.99	2.19	1.97	0.89	1.38	3.12	2.14	1.71	1.08	0.96	1.63	0.96	1.9	1.47	1.5	2.45	1.24	3.13
Dy	1.36	6.41	4.46	4.74	2.33	3.15	6.44	1.75	2.57	1.73	2.16	1.73	1.13	1.05	1.21	1.03	0.88	1.02
Er	0.76	2.78	2.12	2.25	1.3	1.45	2.43	0.83	1.07	0.84	0.99	0.84	0.42	0.44	0.47	0.65	0.53	0.55
Eu	0.62	2.79	1.9	2.01	0.91	1.52	3.91	1	1.26	0.77	1.33	0.77	0.79	0.8	0.82	0.4	0.35	0.39
Ga	19.4	20.4	21.1	19	21.4	20.8	27.1	22	22.4	19.9	21.8	19.9	22.5	25.2	25	21.1	19.6	20
Gd	1.86	8.69	5.6	5.43	2.86	4.02	10	2.59	3.21	2.25	3.26	2.25	1.74	1.75	1.81	1.44	1.1	1.34
Hf	3.9	6.9	7.1	3.8	5.5	5.7	8.6	4.9	5.9	4.5	5	4.5	4.6	4.2	4.1	3.8	3.5	4
Ho	0.28	1.11	0.8	0.89	0.46	0.59	1.03	0.31	0.44	0.33	0.44	0.33	0.22	0.18	0.21	0.23	0.19	0.21
La	17.2	41.1	69	57.7	32.6	59.8	38.8	32.5	41.8	25.2	41.9	25.2	23.2	25.2	27.6	13.4	11.9	12.6
Lu	0.11	0.36	0.29	0.26	0.18	0.19	0.3	0.1	0.16	0.14	0.14	0.14	0.06	0.05	0.07	0.07	0.09	0.08
Nb	9	19	16.9	8.4	11.3	13	34.7	10.3	12.7	10.2	11.3	10.2	7.2	10.8	7.5	11.3	9.3	10
Nd	11.1	50.1	49.7	43.1	21.9	38.7	58.4	21.9	31.6	17.3	29.5	17.3	18.7	19.1	20.2	9.9	8.1	9.2
Pr	3.28	12.45	14.05	13	6.38	11.15	14	6.42	8.63	5.1	8.28	5.1	5.16	5.33	5.82	2.72	2.25	2.6
Rb	108	105	104	81.2	118	103	63.9	81.6	67.7	79.3	76.7	79.3	62.4	69.7	71.8	121	112.5	127.5
Sm	1.96	11.05	8.55	7.82	4.07	6.38	11.8	3.77	5.4	3.14	5.29	3.14	3.27	3.33	3.3	1.61	1.5	1.66
Sr	1135	1905	2020	1545	1665	1820	1625	2220	2530	1855	2400	1855	1770	1910	1855	1415	1290	1290
Ta	0.7	1.4	1.1	1.2	0.6	1.5	1.8	0.4	1.1	0.4	0.6	0.4	14.5	0.7	0.5	0.5	0.5	0.7
Tb	0.28	1.21	0.81	0.85	0.42	0.53	1.29	0.34	0.48	0.32	0.43	0.32	0.21	0.23	0.23	0.2	0.2	0.16
Th	5.86	15.85	14.3	8.11	7.75	9.33	6.99	6.73	7.48	6.59	7.1	6.59	4.38	4.33	6.04	4.29	3.82	5.4
U	1.43	1.89	1.81	1.76	1.47	1.52	3.1	1.2	1.1	1.45	1.73	1.45	0.86	0.96	0.85	1.53	1.04	1.64
Y	7.5	33.2	23.2	26.2	14	18.3	28.5	8.5	12.7	8.4	12.3	8.4	5.9	5.7	6.2	6.2	5.2	5.9
Yb	0.96	2.36	1.86	2	1.13	1.44	2.52	0.65	1.05	0.71	0.88	0.71	0.47	0.44	0.53	0.54	0.51	0.55
Zr	132	290	300	143	233	227	296	184	241	168	211	168	166	157	151	114	98	118

Table 2 LA-ICP-MS U–Pb zircon data from some high Ba-Sr granitoid of the Batholith Teixeira. * Used analyzes in calculating Concordia age.

				Isotope Ratios									Isotope Ages (Ma)						
Samples	Spot	Pb_C	Th/U	$^{207}Pb/^{235}U$	±1σ	$^{206}Pb/^{238}U$	±1σ	coef. corr	$^{238}U/^{206}PB$	±1σ	$^{207}Pb/^{206}Pb$	±1σ	$^{206}Pb/^{238}U$	±1σ	$^{207}Pb/^{235}U$	±1σ	$^{207}Pb/^{206}Pb$	±1σ	Conc.
JD-28	7.1*	5.81	0.45	0.820	0.02	0.095	0.001	0.99	10.565	0.11	0.063	0.00	583	6	608	12	702	59	95
	16.1*	9.79	0.11	0.768	0.02	0.095	0.001	0.54	10.526	0.09	0.059	0.00	585	5	579	11	554	55	101
	9.1*	7.73	-	0.783	0.02	0.096	0.001	0.74	10.441	0.09	0.059	0.00	590	5	587	13	577	62	100
	17.1*	7.61	0.14	0.790	0.01	0.096	0.001	0.65	10.423	0.10	0.060	0.00	591	5	591	8	594	40	99
	22.1*	1.24	-	0.805	0.01	0.097	0.001	0.58	10.311	0.13	0.060	0.00	597	7	600	7	612	38	99
	18.1*	3.98	0.10	0.817	0.01	0.099	0.001	0.72	10.145	0.12	0.060	0.00	606	7	606	8	608	43	99
	5.1	0.89	0.25	4.264	0.08	0.277	0.002	0.98	3.606	0.02	0.112	0.00	1578	8	1686	14	1824	34	93
	12.1	1.79	0.30	5.843	0.15	0.319	0.003	0.96	3.139	0.03	0.133	0.00	1783	15	1953	23	2138	46	91
	14.1	0	-	5.457	0.13	0.327	0.003	0.97	3.058	0.02	0.121	0.00	1824	12	1894	19	1972	39	96
	1.1	1.02	0.02	0.840	0.02	0.100	0.001	0.75	10.018	0.08	0.061	0.00	613	5	619	11	641	58	99
JD-30	20.1*	7.42	0.37	0.802	0.02	0.096	0.001	0.93	10.440	0.11	0.061	0.00	590	6	598	10	629	48	98
	18.1*	0	0.31	0.793	0.02	0.097	0.001	0.99	10.315	0.14	0.059	0.00	597	8	593	9	580	45	100
	10.1*	0.28	0.45	0.810	0.02	0.098	0.001	0.91	10.167	0.09	0.060	0.00	605	5	603	10	594	56	100
	8.1*	0.37	0.19	0.810	0.02	0.099	0.001	0.76	10.127	0.09	0.060	0.00	607	5	603	12	586	64	100
	4.1*	7.29	0.19	0.837	0.02	0.100	0.001	0.82	9.962	0.11	0.061	0.00	617	6	617	10	620	46	99
	9.1*	0	0.74	0.861	0.02	0.095	0.001	0.96	10.512	0.09	0.066	0.00	586	5	630	12	794	63	92
	14.1	5.14	0.48	0.752	0.01	0.090	0.001	0.96	11.145	0.08	0.061	0.00	554	4	569	8	630	45	97
	1.1	2.15	0.40	0.745	0.02	0.090	0.001	0.9	11.114	0.11	0.060	0.00	555	5	565	10	605	44	98
	5.1	0	-	0.738	0.01	0.090	0.001	0.94	11.110	0.11	0.060	0.00	556	5	561	8	584	38	99
TX-08	1.1*	1.71	0.40	0.793	0.02	0.096	0.001	0.7	10.374	0.08	0.060	0.00	593	4	593	11	592	54	100
	5.1*	0.12	0.48	0.785	0.02	0.097	0.001	0.54	10.326	0.09	0.059	0.00	596	5	589	13	561	66	101
	8.1*	0.65	0.42	0.802	0.02	0.097	0.001	0.95	10.283	0.08	0.060	0.00	598	5	598	12	596	60	100
	14.2*	2.89	0.25	0.796	0.02	0.097	0.001	0.01	10.280	0.08	0.059	0.00	598	5	595	12	581	63	100
	16.1*	9.85	0.93	0.778	0.02	0.095	0.001	0.98	10.583	0.09	0.060	0.00	582	5	585	12	594	64	99
	20.1*	11.01	0.75	0.814	0.02	0.097	0.001	0.01	10.311	0.09	0.061	0.00	597	5	605	14	635	73	98
	3.1*	9.95	0.63	0.790	0.02	0.094	0.001	0.67	10.655	0.10	0.061	0.00	578	5	591	9	640	48	97
	1.11	0.85	1.09	6.148	0.12	0.361	0.003	0.99	2.772	0.02	0.124	0.00	1986	15	1997	17	2009	36	99
	2.1	5.07	0.5	7.060	0.08	0.395	0.003	0.99	2.532	0.02	0.130	0.00	2145	12	2119	12	2094	25	101
	12.1	2.33	0.28	0.833	0.02	0.101	0.001	0.84	9.949	0.07	0.060	0.00	617	4	615	11	607	55	100
	7.1	1.26	0.38	0.815	0.02	0.101	0.001	0.59	9.912	0.07	0.059	0.00	620	4	605	9	553	46	102
	18.1	1.79	0.37	1.955	0.04	0.150	0.001	1	6.647	0.05	0.094	0.00	904	6	1100	12	1513	35	82
	19.1	3.97	0.49	1.568	0.04	0.161	0.001	0.94	6.201	0.05	0.071	0.00	964	7	958	14	943	49	100
	14.1	0.67	0.34	4.473	0.11	0.295	0.003	0.97	3.389	0.03	0.110	0.00	1667	14	1726	21	1798	54	96
	2.1	0.76	1.10	6.067	0.11	0.355	0.003	0.99	2.815	0.02	0.124	0.00	1960	12	1986	16	2013	34	98
	6.1	0.54	0.46	6.989	0.12	0.382	0.003	0.96	2.618	0.02	0.133	0.00	2086	11	2110	15	2134	29	98
JD-54	10.1*	4.42	0.28	0.777	0.01	0.094	0.001	0.52	10.644	0.07	0.060	0.00	579	4	584	8	603	41	99
	16.1*	1.99	0.67	0.773	0.01	0.094	0.001	0.88	10.621	0.09	0.060	0.00	580	5	582	8	588	40	99
	15.1*	5.53	0.27	0.775	0.01	0.096	0.001	0.95	10.412	0.08	0.059	0.00	591	4	582	8	548	40	101
	4.1*	2.004	0.42	0.773	0.01	0.097	0.001	0.94	10.361	0.08	0.058	0.00	594	5	581	6	532	36	102
	8.1*	13.13	0.46	0.777	0.01	0.095	0.001	0.85	10.498	0.07	0.059	0.00	587	4	584	8	572	39	100
	11.1*	11.67	0.52	0.778	0.02	0.094	0.001	0.68	10.680	0.11	0.060	0.00	577	6	584	14	612	74	98

Table 3 Lu-Hf isotopic data of the granites from the Teixeira Batholith

Sample	Spot	$^{176}Lu/^{177}Hf$	±2σ	$^{176}Hf/^{177}Hf$	±2σ	$^{176}Hf/^{177}Hf_{(t)}$	εHf(t)	±2σ	T_{DM}	t (Ma)
TX08	seq215	0.00075	5	0.282012	24	0.281999	-6.24	1.19	2.10	964
	seq220	0.00032	2	0.282043	25	0.282037	-6.23	1.27	2.05	904
	seq213	0.00048	4	0.281869	20	0.281864	-19.18	1.01	2.52	602
	seq219	0.00089	6	0.281836	27	0.281826	-20.65	1.37	2.59	596
	seq212	0.00006	0	0.281407	22	0.281404	-1.32	1.09	2.72	2100
	seq214	0.00051	4	0.281545	22	0.281524	2.94	1.12	2.49	2100
	seq216	0.00020	1	0.281403	26	0.281395	-1.65	1.30	2.74	2100
	seq217	0.00040	3	0.281490	21	0.281474	1.17	1.04	2.59	2100
	seq218	0.00043	3	0.281420	25	0.281402	-1.39	1.24	2.73	2100
	seq221	0.00018	1	0.281558	30	0.281551	3.88	1.49	2.44	2100
JD54	seq222	0.00062	5	0.281840	18	0.281834	-20.81	0.91	2.58	577
	seq224	0.00100	7	0.281934	16	0.281923	-17.60	0.79	2.41	579
	seq225	0.00065	5	0.281914	25	0.281907	-17.66	1.23	2.43	602
	seq227	0.00109	9	0.281965	18	0.281953	-16.28	0.89	2.35	591
	seq229	0.00079	6	0.281941	13	0.281932	-17.10	0.67	2.39	587
	seq223	0.00065	4	0.281455	23	0.281429	-0.43	1.14	2.67	2100
	seq226	0.00066	4	0.281609	22	0.281583	5.02	1.10	2.37	2100
	seq228	0.00077	5	0.281456	17	0.281426	-0.56	0.85	2.68	2100
	seq230	0.00007	0	0.281480	22	0.281477	1.26	1.12	2.58	2100
	seq231	0.00031	2	0.281624	21	0.281611	6.03	1.05	2.32	2100
JD30	seq232	0.00112	7	0.281900	29	0.281887	-18.02	1.43	2.47	617
	seq233	0.00012	1	0.281406	22	0.281401	-1.44	1.11	2.73	2100
	seq234	0.00059	4	0.281540	22	0.281517	2.67	1.12	2.50	2100
	seq235	0.00114	7	0.281481	20	0.281435	-0.21	1.02	2.66	2100
	seq236	0.00037	2	0.281602	24	0.281587	5.17	1.21	2.37	2100
	seq237	0.00009	1	0.281406	19	0.281402	-1.40	0.96	2.73	2100
	seq255	0.00055	4	0.281392	26	0.281370	-2.54	1.28	2.79	2100
	seq256	0.00005	0	0.281446	21	0.281444	0.09	1.03	2.65	2100
	seq257	0.00050	3	0.281478	25	0.281458	0.59	1.25	2.62	2100
	seq258	0.00020	2	0.281385	19	0.281377	-2.28	0.94	2.78	2100
	seq259	0.00002	0	0.281438	23	0.281437	-0.17	1.17	2.66	2100

Table 4 Sm-Nd isotopic data for the studied granitoids and a sample of orthogneiss from the host rocks.

Sample	Litology	Sm	Nd	$^{147}Sm/^{144}Nd$	$^{143}Nd/^{144}Nd$	$^{143}Nd/^{144}Ndi$	εNd(t)	T_{DM}	t (Ma)
IM02	Monzogranite	1.64	9.16	0.10862	0.511597	0.511177	-13.68	2.138	590
TX02	Orthogneiss	5.3	29	0.11035	0.512172	0.511745	-2.58	1.372	590
TX05	Syenogranite	3.3	18.53	0.1078	0.511573	0.511156	-14.09	2.155	590
IM01	Monzogranite	8.94	44.17	0.12246	0.51204	0.511567	-6.08	1.750	590
TX01	Monzogranite	2.41	12.97	0.10354	0.511457	0.511057	-16.04	2.227	590
VS11	Syenite	4.7	27.78	0.10235	0.511555	0.511159	-14.03	2.078	590

5 ARTIGO 3 - MULTIPLE SOURCES AND MULTI-STAGE EMPLACEMENT OF THE ESPERANÇA GRANITIC COMPLEX AND ITS RELATIONSHIP WITH THE PATOS – CAMPINA GRANDE SHEAR ZONE SYSTEM, BORBOREMA PROVINCE - NE BRAZIL

Jefferson Valdemiro de Lima [a, *], Ignez de Pinho Guimarães [a], Sérgio Pacheco Neves [a, b], Carlos José Archanjo[c], José Victor Antunes de Amorim[d], Douglas José Silva Farias[a], José Vinicius Martins[e]

[a] Geosciences Post-graduation Program, Pernambuco Federal University, Av. da Arquitetura, s/n, 50740-550, Recife-PE, Brazil. E-mails: *jefferson1901@hotmail.com; ignez@ufpe.br; douglas.farias@ufpe.br

[b] CNPq (Brazilian Research Council) Researcher, Department of Geology, Technologic and Geosciences Center, Pernambuco Federal University, Av. da Arquitetura, s/n, 50740-550, Recife-PE, Brazil. E-mail: sergio.neves@ufpe.br

[c] CNPq (Brazilian Research Council) Researcher, Department of Mineralogy and Petrology, Institute of Geosciences, University of São Paulo, Rua do Lago, 562, Cidade Universitária, 05508-080, Sao Paulo-SP, Brasil. E-mail: archanjo@usp.br

[d] School of Earth Sciences, University of Western Australia, 35 Stirling Highway, Perth WA 6009 Austrália. E-mail: josevictor.antunesdeamorim@research.uwa.edu.au

[e] Department of Mineralogy and Petrology, Institute of Geosciences, University of São Paulo, Rua do Lago, 562, Cidade Universitária, 05508-080, Sao Paulo-SP, Brasil. E-mail: viniciusmartins@usp.br

* Corresponding Author

Abstract

Expressive granitic magmatism and a complex system of transcurrent shear zones are the main features associated with the Ediacaran evolution of the Borborema Province (northeastern Brazil). Their petrogenesis and relationships with tectonic structures can provide important insights into lithospheric processes during the collisional to post-collisional stages of the Brasiliano Orogeny. The Esperança Complex is a NE-trending elongated granitic batholith with ca. 650 km^2 comprising five plutons emplaced between the Patos and Campina Grande dextral shear zones in the central–eastern part of the Borborema Province. An integrated study of the complex was carried out using U-Pb zircon SHRIMP and LA-ICPMS geochronology, mineral and whole-rock geochemistry, and Nd–Hf isotope geochemistry (whole-rock and zircon). The plutons are metaluminous to slightly peraluminous with geochemical and isotopic signature reflecting different sources. The Remigio and Areial plutons have Paleoproterozoic to Neoarchean Nd and Hf T_{DM} model ages and strong negative εNd(t) (-15.29 to -16.71) and εHf (-12.20 to -21.03) values. Their geochemistry is compatible with derivation through partial melting of mafic to intermediate metaigneous sources like the Paleoproterozoic basement (Areial pluton) and metasedimentary sources (Remígio pluton). The Puxinanã, Serrote da Cobra and Pocinhos plutons show higher εNd (-5.90 to -7.35) and εHf (-2.83 to -6.91) values, and Statherian to Calymmian Nd and Hf T_{DM} model ages, ranging from 1.4 to 1.7 Ga and from 1.6 to 1.8 Ga, respectively. They have geochemical affinity with A-type ferroan granites. The geochemical and isotopic signature are similar to those of Tonian orthogneiss that constitute part of the plutons' host rocks, suggesting derivation from Tonian crustal sources. Evidence of magma mixing and the presence of inherited zircon grains with ages like those of metasedimentary host rocks suggest contribution of the lithospheric mantle and sedimentary sources in different proportions in their petrogenesis. The reported data are compatible with building of the Esperança Complex by multiple intrusive events. The Pocinhos and Serrote da Cobra plutons are the oldest (~600 Ma) and their genesis is probably associated with heat input

resulting from crustal thickening at the end of a long contractional period (ca. 630-600 Ma). The genesis of the Puxinanã and Areial plutons (~585 to 565 Ma) involved interactions of crustal and mantle mafic melts, with magma transport and emplacement controlled by the Campina Grande shear zone at the beginning of the transcurrent regime. The Remígio pluton is the youngest intrusion (~565 Ma) and its genesis can be related to a high geothermal gradient resulting from emplacement of the older plutons, possibly enhanced by strain heating related to displacement along the Patos shear zone.

Keywords: Syn-transcurrent granitoids; Petrogenesis; Ediacaran magmatism; Magma sources; Borborema Province; Post-collisional

1. Introduction

Granites are the most abundant igneous rock-types in the upper crust, and granitic magmatism is the leading cause for the geochemical differentiation of the continental crust (Wedepohl, 1991). They are generated in variable geodynamics environments, from plate margins to intraplate settings, by the heat and/or mass transfer from the mantle to the crust, by partial melting of infracrustal sources due to radioactive heating during orogenesis, or by differentiation (fractional crystallization and/or assimilation) of mantle-derived magmas (Barbarin, 1999).

The petrographic and geochemical variety of granites is commonly interpreted as associated with partial melting of crustal and mantle sources of varied compositions. Several studies suggest that the source exerts primary control on the diversity of granitic melts, as reflected in the genetic alphabetical scheme (Chappell and White, 1974; Gao et al., 2016; Loiselle and Wones, 1979), with I-, S- and M granite types derived, respectively, from metaigneous, metasedimentary and mantle sources. However, granites are usually derived from mixed sources, involving variable proportions of crustal and/or mantle-derived components.

Major and trace elements signatures have been proposed to discriminate tectonic setting (Harris et al., 1986; Maniar and Piccolli, 1989; Pearce et al., 1984, among others) or the relationship between source and tectonic setting (Pearce, 1996). Although major and trace element signature may be strongly associated with the magma source, crystal-melt equilibrium and mechanisms involved in the magmatic differentiation also play a role (Barbarin, 1999; Roberts and Clemens, 1993; Rollinson, 1993). Therefore, to interpret the genesis of granitic rocks it is necessary to combine detailed geochemical and isotopic data with field data, not only to discriminate sources and related processes (peritectic assemblage entrainment, restite unmixing, among others) (Clemens and Stevens, 2012), but also the mechanism involved in the magmatic evolution (fractional crystallization, assimilation, magma mixing).

During the late Neoproterozoic, the Borborema Province, northeastern Brazil (Figs. 1A and B), was intensely affected by the Brasiliano/Pan-African Orogeny (0.65 - 0.55 Ga), which resulted from the amalgamation processes leading to the assembly of West Gondwana (e.g., Brito Neves et al., 2000). Widespread granitic magmatism is one of the main expressions of this orogeny and more than 100 Ma of late Neoproterozoic (Cryogenian/Ediacaran) magmatism related to different tectonic stages of the Brasiliano/Pan African Orogeny were recognized in the Central subprovince (Guimarães et al., 2004; Van Schmus et al., 2011). In many cases, pluton emplacement correlates with high-grade metamorphism and shear zone development (Neves et al., 2020; Van Schmus et al., 2011; Vauchez el al 1995; Viegas et al., 2014, among others).

This work reports petrological studies carried out in the Ediacaran Esperança Granitic Complex, one of the largest batholiths of the Central subprovince, with ca. 650 km^2. The complex was intruded between the Patos and Campina Grande dextral shear zones and is characterized by granitoids with variable petrographic, geochemical, and isotopic signatures.

Figure 1 – A) Pre-drit reconstruction of the western portion of Gondwana from Van Schmus et al. (2008). Legend: BR/PA, Brasiliano/Pan-African belts; PaleoPr, Paleoproterozoic crust; NS, North Subprovince; TS, Transversal Subprovince; SS, South Subprovince; PEAL, Pernambuco-Alagoas domain; MK, Mayo Kebi terrane; NWCD, NW Cameroon domain; AYD, Adamawa-Yadé domain; YD, Yaoundé domain; OU, Oubanguides fold belt; PaSZ, Patos shear zone; PeSZ, Pernambuco shear zone; TBL, Transbrasiliano Lineament; TBF, Tcholliré-Banyo fault; AF, Adamawa Fault; SF, Sanaga fault. Cities: N, Natal; R, Recife; S, Salvador; D, Douala; G, Garoua; K, Kaduna area of Nigeria; B) Major domains and shear zones of the Borborema Province (modified from Van Schmus et al., 2011). Legend: Northern Subprovince (MC: Médio Coreaú Domain; CC: Ceará Central Domain; RGN: Rio Grande do Norte Domain); Southern Subprovince (RP: Riacho do Pontal Domain; SD: Sergipano Domain; PEAL: Pernambuco-Alagoas Domain); PaSZ: Patos Shear Zone; WPSZ and EPSZ: West and East Pernambuco Shear Zones; SSZ: Sobral Shear Zone; SPSZ: Senador Pompeu Shear Zone; JSZ: Jaguaribe Shear Zone; JCSZ: João Câmara Shear Zone; PASZ: Portoalegre Shear Zone; RSZ: Riachão Shear Zone; TSZ: Tauá Shear Zone; c: Phanerozoic cover. C) Transversal Subprovince of the Borborema Province with Ediacaran plutons highlighted in red (modified from Guimarães et al., 2016). Legend: RC: Rio Capibaribe Domain; AM: Alto Moxotó Domain; AP: Alto Pajeú Domain; PABD: Piancó-Alto Brigida Domain; CoSZ: Coxixola Shear Zone; CSZ: Congo Shear Zone; AISZ: Afogados da Ingazeira Shear Zone; SCSZ: Serra do Caboclo Shear Zone; EGC: Esperança Complex.

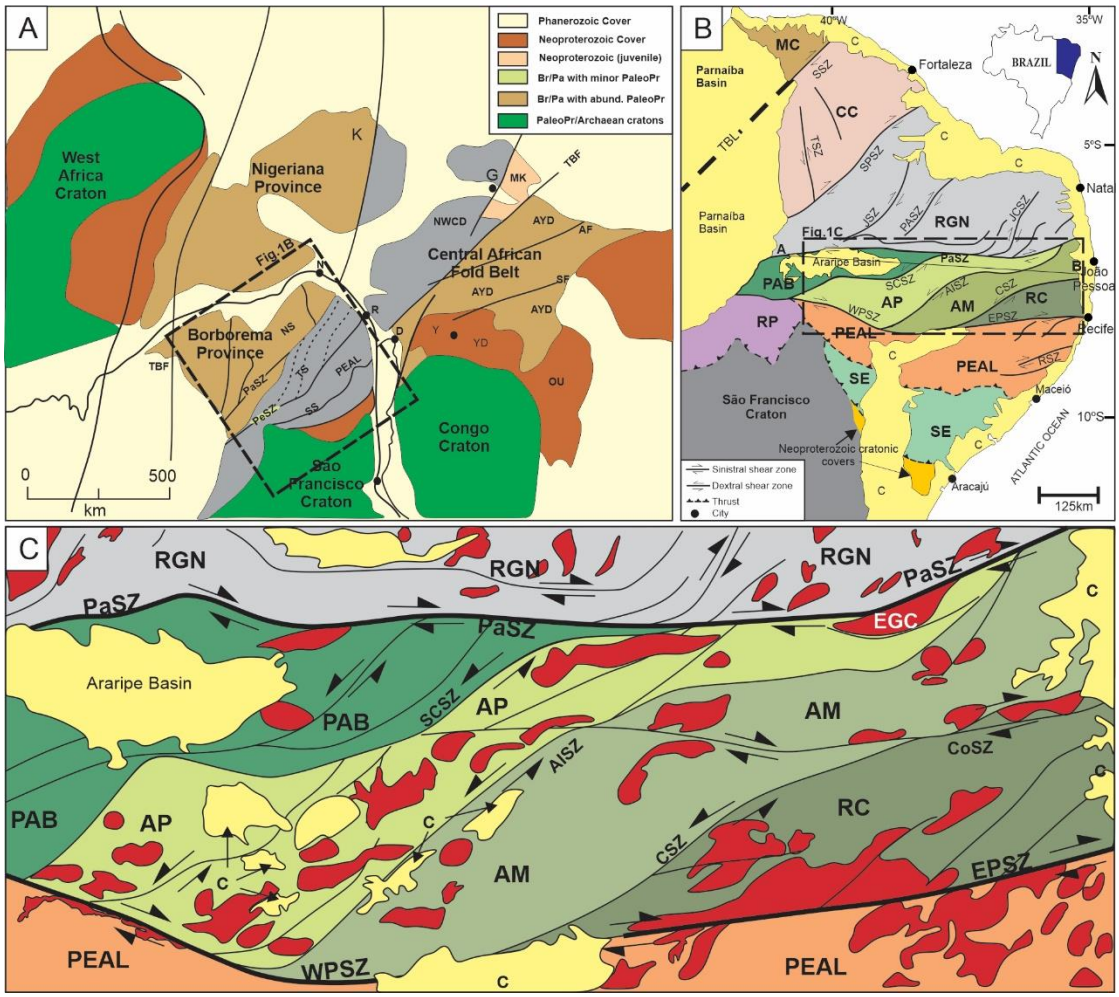

This complex was previously studied during the doctoral thesis of Sampaio (2005), who divided it into five plutons, and provided mineral chemistry, whole-rock geochemistry, some Sm-Nd data, and age for one pluton (Puxinanã; conventional U-Pb zircon age of 581 ± 7 Ma). To better constrain the magmatic evolution of the Esperança Complex, we use geochemical data from Sampaio (2005) and report new geochemical, geochronological, and isotopic data obtained in this work. These data constitute an important contribution to elucidate issues such as sources, petrogenic evolution and crystallization conditions during magma emplacement, and are essential for understanding the relationship between the granitic magmatism and development of the shear zones. We highlight the critical link between the sources and the chemical signature of granites, emphasizing that the use of discriminant tectonic diagrams should be done with caution.

2. Regional geological setting

The Borborema Province comprises a Paleoproterozoic basement of migmatite orthogneisses with TTG affinity, and small Archean nuclei (Dantas et al., 2004; Neves et al., 2006, 2015; Santos et al., 2015, among others) formed mainly during the Transamazonian Orogeny (2.2 Ga to 2.0 Ga). Metamorphic supracrustal sequences overly the basement units and are intruded by granitic bodies of Tonian (Guimarães et al., 2012, 2016; Neves et al., 2020; Santos et al., 2010) and Cryogenian to Cambrian (Archanjo et al., 2012; Ferreira et al., 2015; Guimarães et al., 2004; Sial and Ferreira, 2016; Silva Filho et al., 2016; Van Schmus et al., 2011, among others) ages.

Extensive Brasiliano E-W and NE-SW striking transcurrent shear zones constitute a major feature of the Borborema Province. Some of these are of continental scale and can be correlated with shear zones in the African continent (Ganade de Araújo et al., 2016, among others). The Patos shear zone, one of these continental-scale shear zones, in pre-drift

reconstruction (Fig. 1A) is shown as continuing in Africa, bordering the Benino-Nigerian Shield to the south (Caxito et al., 2020; Van Schmus et al., 2008, among others). Based on the Patos and Pernambuco shear zones, the Borborema Province is divided into three major subprovinces (Van Schmus et al., 2008, 2011) (Fig. 1B): i) Northern, north of the Patos shear zone; ii) Southern, south of the Pernambuco shear zone and iii) Central (Fig. 1C), between the Patos and Pernambuco shear zones.

The Esperança Complex (Fig. 2) is in the northeastern part of the Central subprovince (Alto Pajeú domain), between the dextral Remígio – Pocinhos (Eastern branch of the Patos shear zone) and Campina Grande shear zones. The Alto Pajeú domain is bounded eastward and westward, respectively, by the sinistral Afogados da Ingazeira and Serra do Caboclo shear zones (Fig. 1C), which separate it from the Alto Moxotó and Piancó Alto-Brígida domains. The Alto Pajeú domain comprises a Paleoproterozoic basement, metasedimentary sequences (e.g., muscovite-biotite gneisses, garnet-biotite schists), a belt of Tonian orthogneisses of granitic composition and bimodal metavolcanic rocks, with the predominance of meta-rhyolite, small volumes of metabasic (greenschist facies) rocks and local occurrence of metapyroclastic rocks (Bittar, 1998; Brito Neves et al., 2001; Guimarães et al., 2012, 2016), and Ediacaran granitoids. The Brasiliano/Pan African Orogeny promoted an extensive reworking of the basement and deformation of the supracrustal rocks, with the development of a planar fabric, with WNW transport direction (Medeiros et al., 2004), metamorphism under greenschist facies conditions in the west to amphibolite facies conditions in the east, followed by strike-slip deformation and local extensional conditions (Bittar, 1998; Brito Neves et al., 2001; Leite et al., 2000).

The Remígio-Pocinhos shear zone constitutes the east boundary between the Alto Pajeú and Rio Grande do Norte domains. High-temperature metamorphism and widespread syn-kinematic anatexis have been dated at 560 to 565 Ma in the central part of the Patos shear zone (Viegas et al., 2014). In the Remígio-Pocinhos shear zone and its ramifications, the

metamorphic conditions vary from low amphibolite facies in the northwest, in the sectors farthest from the shear zone to upper amphibolite to granulite facies in the central mylonitic corridor (Souza et al., 2006). The Campina Grande shear zone is characterized as a SE-trending mylonitic belt of around 50 km long and 2 km width and dextral kinematic (Rodrigues and Archanjo, 2008). The Campina Grande shear zone connects westward with the sinistral NE-SW Afogados da Ingazeira shear zone, and splits eastward into a horse-tail termination, forming branches with ENE-WSW orientation (Vauchez et al., 1995). It is responsible for shear strain along the entire southern edge of the Esperança Complex, and especially in the southeastern portion where the granites are mylontized and acquire an augen texture.

Figure 2 - Simplified geological map of the Esperança Complex.

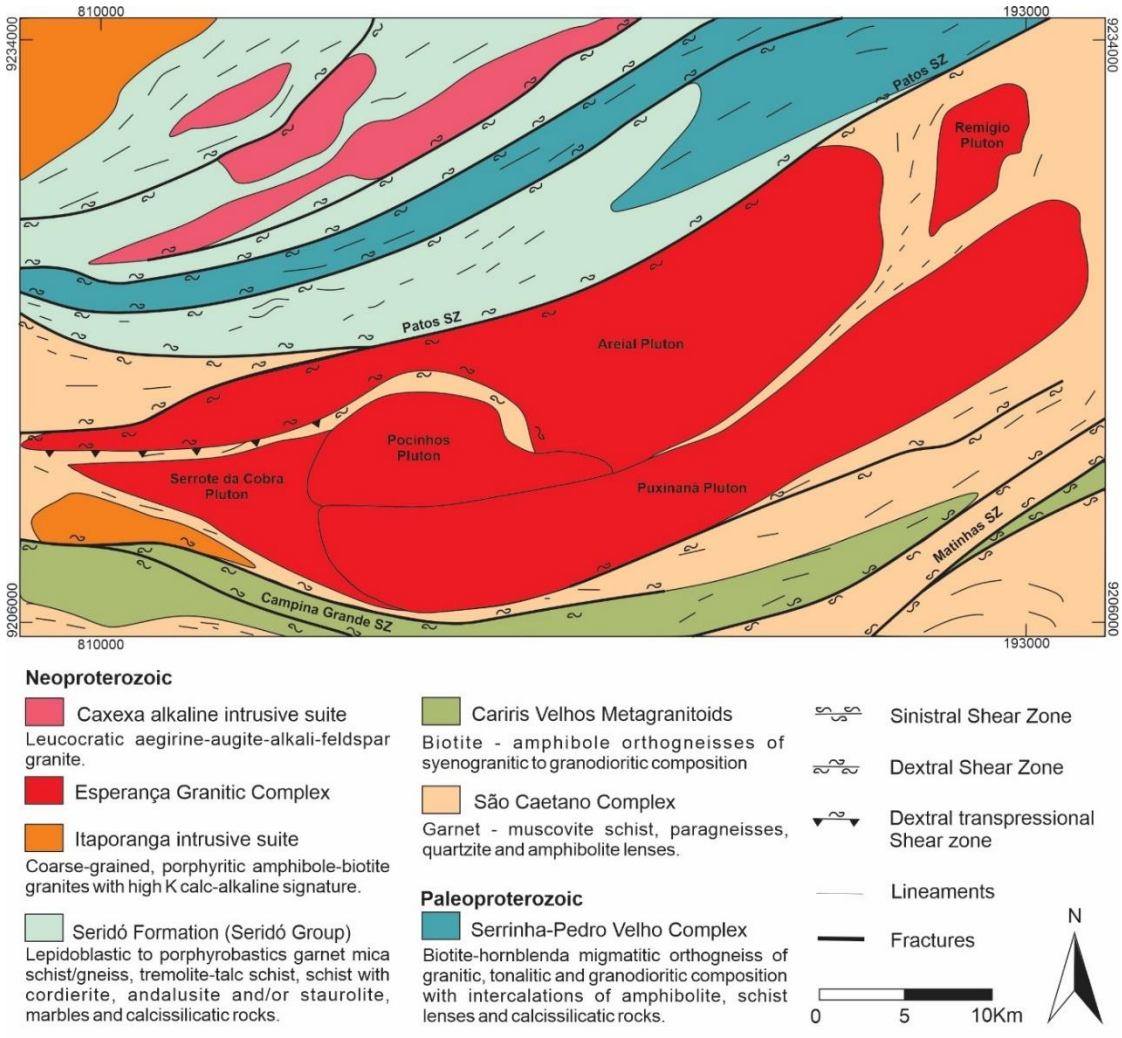

3. Geological context

The Esperança Complex, c. 650 km^2, comprises a sigmoidal-shaped batholith, elongated in the NE-SW direction (Fig. 2). It intrudes Tonian metagranitoids and Neoproterozoic metavolcanosedimentary sequences. Guimarães et al., (2012) dated a metasedimentary sample, collected 25 km to the east of the Esperança Complex. It yielded a large population of zircon grains with ages within 612–670 Ma interval, and few ages in the 700–900 Ma range. An age of 612 ± 8 Ma, recorded in the core of a zoned subhedral grain, showing $^{232}Th/^{238}U$ ratio = 0.43, was used to constraint the maximum deposition age of this sequence.

The Esperança Complex comprises five plutons with compositions ranging from syenogranite to monzogranite and minor granodiorite/tonalite (Archanjo and Fetter, 2004; Sampaio, 2005):

1) The Serrote da Cobra Pluton, in the western part, comprises medium to coarse-grained porphyritic leucocratic tonalite to granodiorite. Plagioclase occurs as megacrysts up to 4 cm, defining with biotite a magmatic fabric with WNW-ESE direction (Fig. 3A). Shear zone-related deformation occurs at the SW-edge of the pluton, with NW-SE stretched biotite. Mafic microgranular enclaves have ovoid-shape and are parallel to the pluton elongation direction. Surmicaceous enclaves occur in small amounts. Quartz occurs as anhedral crystals showing undulose extinction and recrystallization by grain boundary migration (Fig. 3B), which are typical features of high-temperature deformation. Plagioclase crystals show preserved igneous zoning, and K-feldspar crystals are replaced by myrmekite at the grain edges.

2) The Pocinhos Pluton constitutes a round-shaped intrusion in the central part of the complex, comprising mesocratic, coarse-grained to porphyritic amphibole-biotite syenogranites. To the north, the pluton is in contact with sheared and migmatized gneisses and schists, showing well-defined magmatic foliation with ENE-WSW and locally NW-SE directions (Fig. 3C) given by the shape preferred orientation of K-feldspar megacrysts, biotite,

and mafic enclaves. Small, elongate, fine-grained monzodioritic enclaves occur locally. Quartz shows grain boundary migration and local chessboard-type extinction (Fig. 3D), indicating high-temperature deformation. Plagioclase crystals in the matrix usually show twinning parallel to the foliation, suggesting magmatic foliation.

Figure 3 – Field and petrographic aspects of Esperança Complex. A) Magmatic fabric in tonalite rock, with elongated parallel enclave; B) Quartz crystal showing recrystallization by grain boundary migration and myrmekite at the grain edges; C) Syenogranite showing well-preserved magmatic foliation; D) Chessboard-type extinction in quartz; E) Granite with typical solid-state fabric and elongated parallel enclave; F) Pegmatite dykes cutting the Areial granitoids; G) Foliated Puxinanã granitoids due to shearing deformation; H) Magmatic fabric in the Puxinanã granitoids characterized by orientation of K-feldspar tabular phenocrysts and biotite; I) Grain boundary migration in quartz; J) Myrmekite at grain boundaries of K-feldspar crystals; K) Microgranular enclave in straight contact with host granite; L) Recrystallization by grain boundary migration in quartz. Qz: quartz, Kfs: K-feldspar.

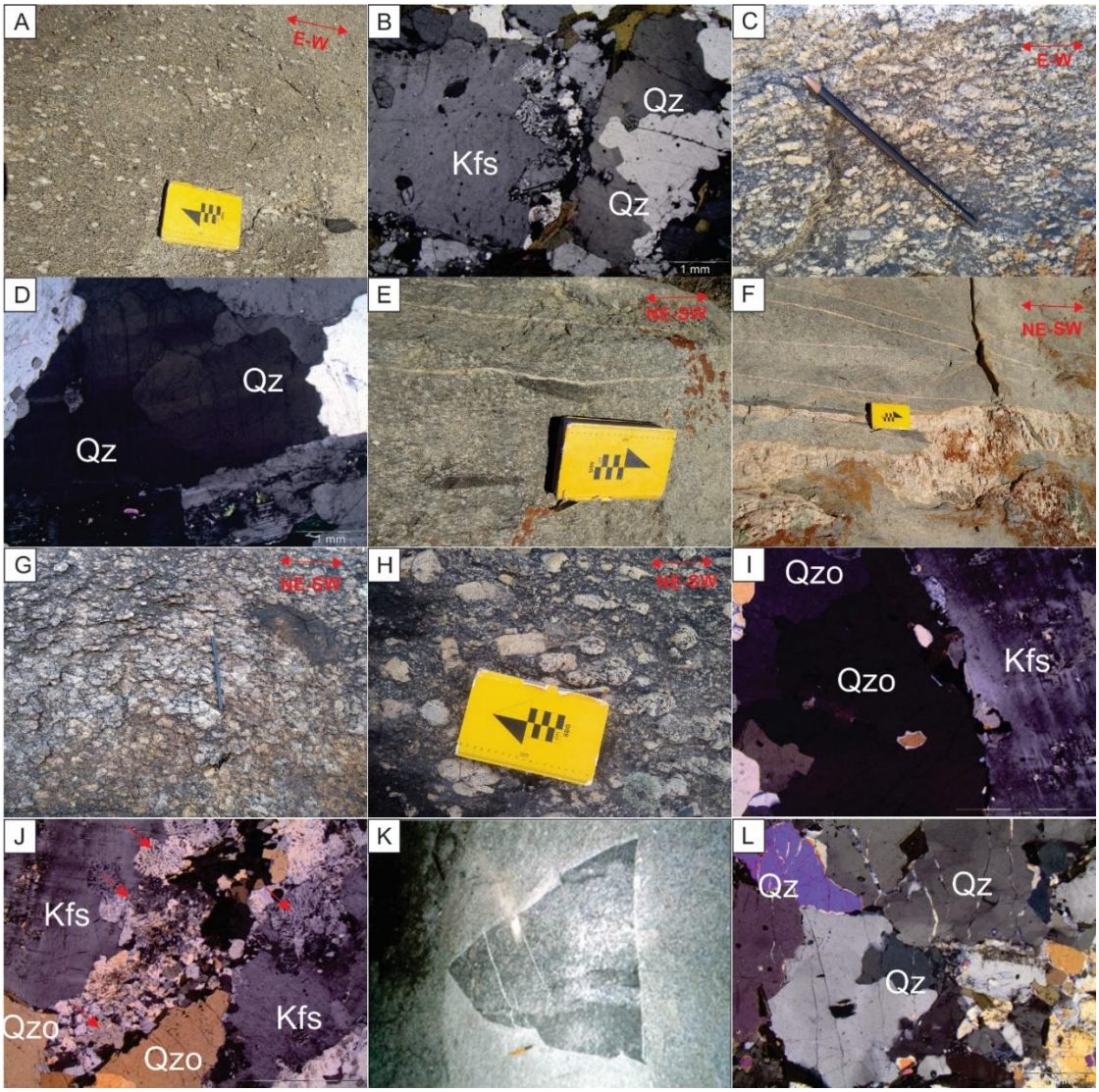

3) The Areial Pluton is a NE-trending elongated intrusion, c. 200 km^2, that is separated from the other plutons by continuous stripes of metasedimentary rocks. It is composed of gray, fine to medium-grained biotite monzogranite to leucocratic, equigranular to slightly porphyritic syenogranite. These granitoids show weak foliation characterized by the shape preferred orientation of tabular crystals of feldspar, mafic minerals, and enclaves, oriented mainly in the ENE-WSW direction. Oval-shaped microgranular enclaves of dioritic composition are common and oriented parallel to the foliation in the host granite (Fig. 3E) and amphibolite xenoliths are present locally. A typical solid-state fabric, characterized by sheared rocks, occurs mainly at the edges of the intrusion. There, stretched quartz crystals show strong undulose extinction and K-feldspar crystals show recrystallization by subgrain rotation. The pluton is cut by numerous NE-SW to NW-SE trending sets of fractures, quartz-feldspathic veins, and pegmatite dykes (Fig. 3F), indicating post-magmatic process associated with fluids, corroborated by presence of plagioclase crystals affected by saussuritization and deformated mafic phases. Dioritic dykes are present locally.

4) The Puxinanã Pluton is an elongated intrusion, c. 250 km^2, parallel to the NE-SW trending of the Remígio Pocinhos and branches of the Campina Grande shear zone. It consists mainly of mesocratic, porphyritic amphibole-biotite syenogranite to monzogranite, with K-feldspar megacrysts up to 10 cm long surrounded by a coarse-grained matrix composed of quartz, feldspars, and mafic minerals. Overall, the granitoids are strongly foliated due to shearing deformation (Fig. 3G), showing a NE-SW preferential orientation, which coincides with the magmatic fabric, characterized by oriented K-feldspar tabular megacrysts and mafic minerals (Fig. 3H). Locally, where the magmatic fabric has not been entirely overprinted, features of both deformation stages can be observed. Microgranular enclaves occur in greater amounts than in the other plutons, having granodiorite to diorite composition. They are elongated, most parallel to the foliation of the host granite and, locally, are associated with

dismembered sin-plutonic dykes. Sinuous and irregular contacts between enclaves and host granite is indicative of coexistence and mixture of magmas. Under the microscope, quartz shows strong undulose extinction, exhibiting high temperature deformation features such as chessboard extinction and recrystallization by grain boundary migration (Fig. 3I), but there are also places where quartz ribbons comprise finely recrystallized grains, suggesting deformation at lower temperatures. Large amounts of myrmekite and recrystallized K-feldspars crystals also suggest deformation under high temperature (Fig. 3J).

5) The Remígio Pluton is intruded in the northeast portion of the Esperança Complex, immediately south of the Remígio-Pocinhos shear zone and east of the Areial Pluton. It comprises a 40 km^2 sigmoidal-shaped intrusion emplaced into sheared and migmatized gneisses. It comprises three petrographic facies with monzogranite to syenogranite composition. The predominant facies is porphyritic, medium-grained, showing NE-trending oriented enclaves and flow structures. Fine-grained, slightly oriented equigranular granitic rocks form another facies, often found as enclaves in the medium-grained granite. In general, solid-state deformation is weak, with NE-trending aligned crystals of feldspar and biotite defining a magmatic foliation. Microgranular enclaves and numerous amphibolitic and gneissic xenoliths of varying sizes generally occur as angular fragments (Fig. 3K). Pegmatite dykes are also present but are less common. Microscopically high-temperature deformation features in quartz, such as recrystallization by grain boundary migration (Fig. 3L), are locally observed.

All plutons of the Esperança Complex have similar mineral assemblage. The mafic minerals assemblage includes biotite and amphibole, except the Remígio granites where amphibole is absent. Biotite crystals usually exhibit inclusions of titanite, apatite, zircon, and opaque minerals. Titanite is the main accessory mineral phase. It forms brown diamond-shaped euhedral crystals, often associated with biotite and amphibole. Subhedral to anhedral grains of titanite also occur as clusters around opaque minerals, indicating a late fluid activity. Euhedral

crystals of epidote are present in the Areial and Serrote da Cobra granitoids. Apatite occurs as acicular to euhedral crystals, while zircon forms bipyramidal euhedral crystals most included in ferromagnesian minerals. Opaque minerals consist of euhedral to subhedral strongly anisotropic pinkish-gray ilmenite (Puxinanã, Pocinhos e Remígios plutons), small subhedral grains of magnetite (Areial Pluton), yellow anhedral pyrite crystals, and minor chalcopyrite crystals. Opaque minerals are rare in the Serrote da Cobra granitoids.

4. Analytical techniques

This work presents unpublished data (mineral and whole-rock chemistry, zircon U-Pb geochronology, zircon trace element chemistry and zircon Lu-Hf isotope chemistry) together with chemical (mineral and whole-rock chemistry) and isotopic (Nd isotope geochemistry) data compiled from the literature (Archanjo and Fetter, 2004; Brito Neves et al. 2001; Sampaio, 2005). The analytical procedures used include: 1) EMPA (Electron Microprobe Analyzer) for mineral chemistry analyses; 2) ICP-AES (Inductively Coupled Plasma Emission Spectrometry) and ICP-MS (Inductively Coupled Plasma Mass Spectrometry) for major-and trace-element analyses; 3) LA-ICP-MS (Laser Ablation Inductively Coupled Plasma Mass Spectrometry) and SHRIMP (Sensitive High-Resolution Ion Microprobe) for zircon dating; 4) LA-Q-ICPMS (Quadrupole Inductively Coupled Plasma Mass Spectrometry) for zircon trace elements composition, and 5) LA-MC-ICPMS (Laser Ablation Multi-collector Inductively Coupled Plasma Mass Spectrometer) for zircon Hf isotope analysis. Detailed analytical procedures are available in Electronic Appendix 1A.

5. Results

5.1. Mineral chemistry

5.1.1. Biotite

Analyses were performed in all plutons and representative results are shown in Table 1 (Electronic Appendix 2A). Biotite compositions from the Serrote da Cobra, Pocinhos, Puxinanã and Remígio plutons have TiO_2 contents (mean value = 2.6 wt%) like those of primary biotite (Nachit et al., 2005). In contrast, biotite compositions from the Areial Pluton have lower TiO_2 contents (mean value: 1.4 wt%) and are classified as rebalanced primary biotite, suggesting late magmatic rebalancing. The analyzed biotite grains form an evolutionary trend in the Fe# [Fe/ (Fe + Mg)] versus Solidification Index (SI) diagram (Fig. 4A). The SI is calculated from [SI = 100 MgO / (MgO + FeO + Fe_2O_3 + Na_2O + K_2O)] and the value is directly associated with the evolutionary character of biotite-bearing granites: biotite with high SI values indicates less evolved rocks and with lower SI values are characteristics of more evolved rocks. The biotite crystals of the Pocinhos Pluton show the lowest SI values (4.18 to 19.71), while those of the Areial Pluton have higher SI values (25.58 to 42.04), suggesting that the granites of these plutons are the most evolved and least evolved, respectively.

According to the classification of Speer (1984), based on Al^{IV} versus Fe#, the biotites from the Areial Pluton are classified as eastonite (Fig. 4B), while biotite from the others studied granitoids are siderophyllite-rich. The Al^{T} content (2.24 to 3.05) of the analyzed biotite crystals from the different plutons of the Esperança Complex (Fig. 4C) are like biotite from subalkaline granites (Nachit et al., 1985). The chemical signature of the magma from which biotite crystallizes can be inferred from FeO_t, MgO and Al_2O_3 contents (Abdel Rahman, 1994). Analyses from the Areial and Serrote da Cobra plutons plot in calc-alkaline granite field, those from the Puxinanã Pluton plot between the fields of calc-alkaline and alkaline granites, and those from the Pocinhos and Remígio plutons plot in the calc-alkaline to peraluminous granites fields (Figs. 4D, E, F).

Figure 4 – Chemical classification of the biotite from the Esperança Complex. A) S.I. [100MgO/(MgO+FeO+Fe_2O_3+Na_2O+K_2O)] versus Fe/(Fe + Mg) diagram; B) Fe# x Al^{IV} diagram; C) Mg x Al^{T} diagram after Nachit et al. (1985); D), E), F) Discriminant diagrams after Abdel-Rahman (1994). Legend: A: alkaline anorogenic; C: calc-alkaline; P: peraluminous. I – This study; II – Data from Sampaio (2005).

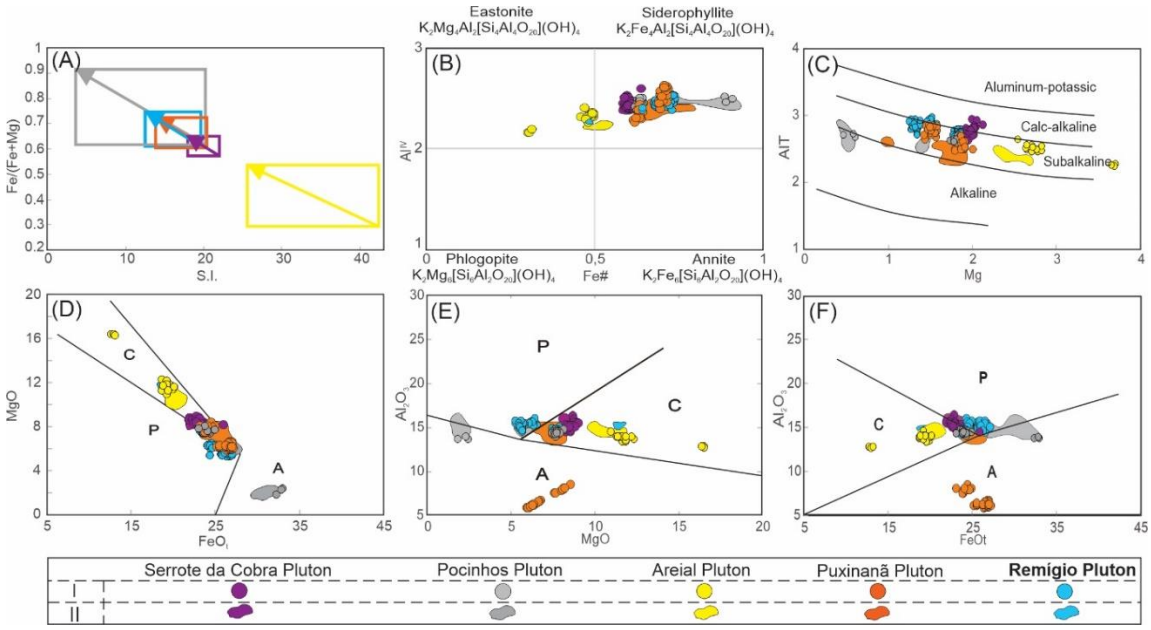

5.1.2. Amphibole

One hundred five amphibole crystals were analyzed, and representative data are shown in Table 2 (Electronic Appendix 2A). The studied amphiboles show alkali contents like calcic magmatic amphiboles (Fig. 5A and B) (Czamanske and Wones, 1973; Leake et al., 1997). According to the Leake et al. (1997) amphibole classification (Fig. 5C and D), the Areial Pluton amphiboles range from Mg-hornblende to edenite, in the less evolved granitoids, and Fe-hornblende to Fe-edenite, in the more evolved granitoids. The amphiboles of the other plutons have higher iron content. The Serrote da Cobra and Puxinanã plutons amphiboles range from Fe-edenite to Fe-pargasite, and Fe-hornblende to Fe-tschermakite. The amphiboles of the Pocinhos granites range from Fe-hornblende in the least evolved facies to hastingsite in the most evolved facies.

5.1.3. Feldspars

The feldspars characterization was made using 130 feldspar analyses, from all studied plutons. Representative data are shown in Table 3 (Electronic Appendix 2A). The plagioclase crystals range in composition from albite to labradorite (Fig. 6A), with anorthite content varying between $An_{21-43\%}$ (Serrote da Cobra granitoids), An_{17-30} (Pocinhos granitoids), $An_{17-27\%}$ (Areial granitoids), $An_{21-30\%}$ (Puxinanã granitoids), $An_{28-51\%}$ (Remígio granitoids). Some plagioclase crystals show compositional zoning with decreasing calcium towards the rim. Plagioclase crystals surrounded by alkali feldspar, characterizing an anti-rapakivi texture, were recorded in the Serrote da Cobra granitoids.

Alkali feldspar of the Areial and Puxinanã granitoids are orthoclase (Puxinanã - $Or_{90-93\%}$; Areial - $Or_{84-96\%}$). BaO contents are higher for the K-feldspars of the Areial granitoids (BaO: 0.90 to 1.20 wt%), when compared to those of Puxinanã granitoids (BaO: 0.57 - 0.80 wt%).

Figure 5 – Classification diagram for amphiboles of the studied granitoids. A) Composition of amphibole crystals plotted in the Si^{IV} x (Na + K + Ca) diagram, with fields after Czamanske e Wones (1973); B), C) and D) Classification of the studied amphiboles according to Leake et al. (1997). I – This study; II – Data from Sampaio (2005).

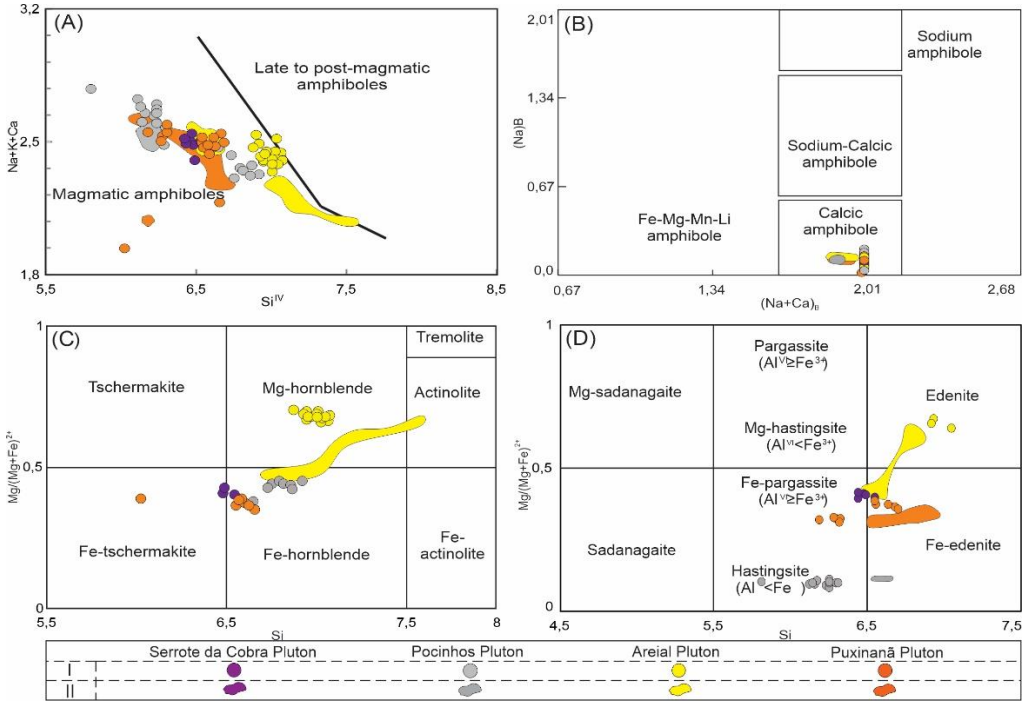

Figure 6 - Chemical characteristics of the studied feldspars and oxydes. A) An-Ab-Or ternary diagram for the classification of the plagioclase and K-feldspar (modified from Deer et al., 1992); B) Fe_2O_3 x TiO_2 x FeO ternary diagram for the studied oxides according to the classification by Buddington and Lindsley, (1964). I – This study; II – Data from Sampaio (2005).

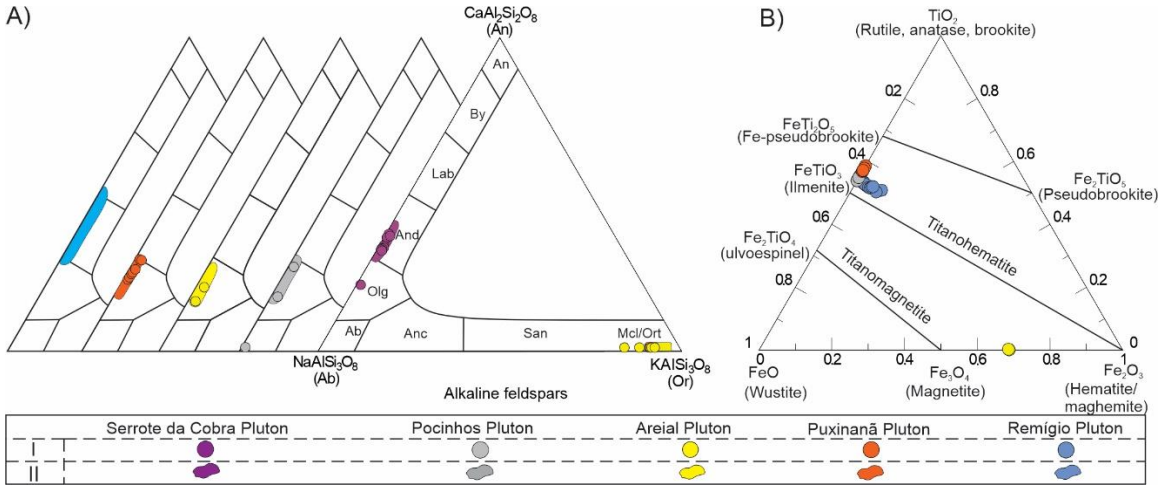

5.1.4. Titanite

Titanite constitutes the main accessory phase of the Esperança Complex, occurring in granitoids of all five plutons. Thirty-seven crystals were analyzed, and representative analyses are shown in Table 4 (Electronic Appendix 2A). They are characterized by TiO_2 ranging from 32.5 to 38 wt%, FeO = 0.4 to 2.0 wt% and CaO from 26.6 to 29 wt%. Furthermore, the Al_2O_3 concentrations are consistent with primary titanite (Enami et al., 1993; Tulloch, 1979) i.e., Remígio Pluton - 1.5 to 3.8 wt%; Serrote da Cobra Pluton -2.1 to 2.8 wt%; Pocinhos Pluton - 3.3 wt%; Areial Pluton - 1.3 to 3.4 wt%; and Puxinanã Pluton - 1.3 to 2.2 wt%.

5.1.5. Oxides

Oxide mineral compositions (33) were obtained from granitoids of the Pocinhos, Remígio, Puxinanã, and Areial plutons. Representative analyses are shown in Table 5 (Electronic Appendix 2A). They are subhedral to euhedral crystals, usually showing flat faces, and locally, occur as anhedral crystals surrounded titanite. The oxides from Remígio, Puxinanã and Pocinhos granitoids are ilmenite, with FeO content ranging between 39 and 46 wt% and of TiO_2 between 48 and 57 wt%, and ilmenite molecule varying between 81 and 95 % (Fig. 6B).

The Areial granitoids have lower modal proportions of oxides. They are most small subhedral grains classified as magnetite (magnetite molecule is c. 99%) and characterized by FeO and Fe_2O_3 content of ~ 31 wt% and 68 wt%, respectively, and of TiO_2 ranging from 0.05 to 0.24 wt%.

5.2. Whole-rock chemistry

Analyses of representative samples are shown in Table 1. The granitoids of the Remígio and Pocinhos plutons display the highest SiO_2 contents (66.71 to 73.9 wt%), while the Serrote da Cobra tonalites show intermediate SiO_2 contents (62.6 to 67.53 wt.%). The Puxinanã and Areial granitoids show a considerable variation in silica content, with the more evolved granites showing 72.35 wt.% and 71.01 wt.% of SiO_2, respectively. The diorite to granodiorite enclaves of the Puxinanã and Areial plutons display silica contents ranging from 57.35 to 63.79 wt.%. The Remígio granitoids are slightly peraluminous with Alumina Saturation Index (ASI) values ranging from 0.99 to 1.09, while the granitoids of the other plutons are predominantly metaluminous (ASI = 0.83 – 1.07) (Fig. 7A). The studied granitoids show FeOt/ (FeOt + MgO) ratios from 0.52 to 0.94, which according to Frost et al. (2001) classification range from ferroan (Pocinhos granitoids) to magnesian (Areial granitoids) (Fig. 7B). The granitoids of the other plutons have intermediate FeOt/ (FeOt + MgO) ratios.

In the SiO_2 versus [(Na_2O + K_2O) – CaO] diagram with fields after Frost et al. (2001), the studied granitoids plot mainly within the alkali-calcic fields (Fig. 7C). The high total alkalis (K_2O + Na_2O) contents, ranging from 6.25 to 10.03 wt% in the most evolved granitoids and between 6.65 and 8.51 wt% in the dioritic rocks (Fig. 7D), are consistent with rocks of the subalkaline series (Cox et al., 1979). In the K_2O x SiO_2 plot (Fig. 7E) with fields after Peccerillo and Taylor (1976), the Esperança Complex granitoids, with mean values for the K_2O/Na_2O ratio of 1.41, plot in the high-K calc-alkaline and shoshonitic series fields (Fig. 7E). In contrast, the Areial granitoids plot predominantly in the shoshonitic series field. Furthermore, the diorite

samples of the Areial Pluton display K_2O/Na_2O ratios (1.03 to 2.34) higher than the diorites/granodiorites of the Puxinanã Pluton (0.62 – 0.71).

Figure 7 - Geochemical characteristics of granitoids of the Esperança Complex. A) Studied granitoids in the Alumina Saturation index diagram; B) $FeO_{tot}/(FeO_{tot} + MgO)$ versus SiO_2 diagram; fields of ferroan and magnesian series from Frost et al. (2001); C) SiO_2 x Mali (Modified Alkali Lime Index) diagram for granitoids of the Esperança Complex; D) SiO_2 x K_2O diagram with the fields of Peccerillo and Taylor (1976).

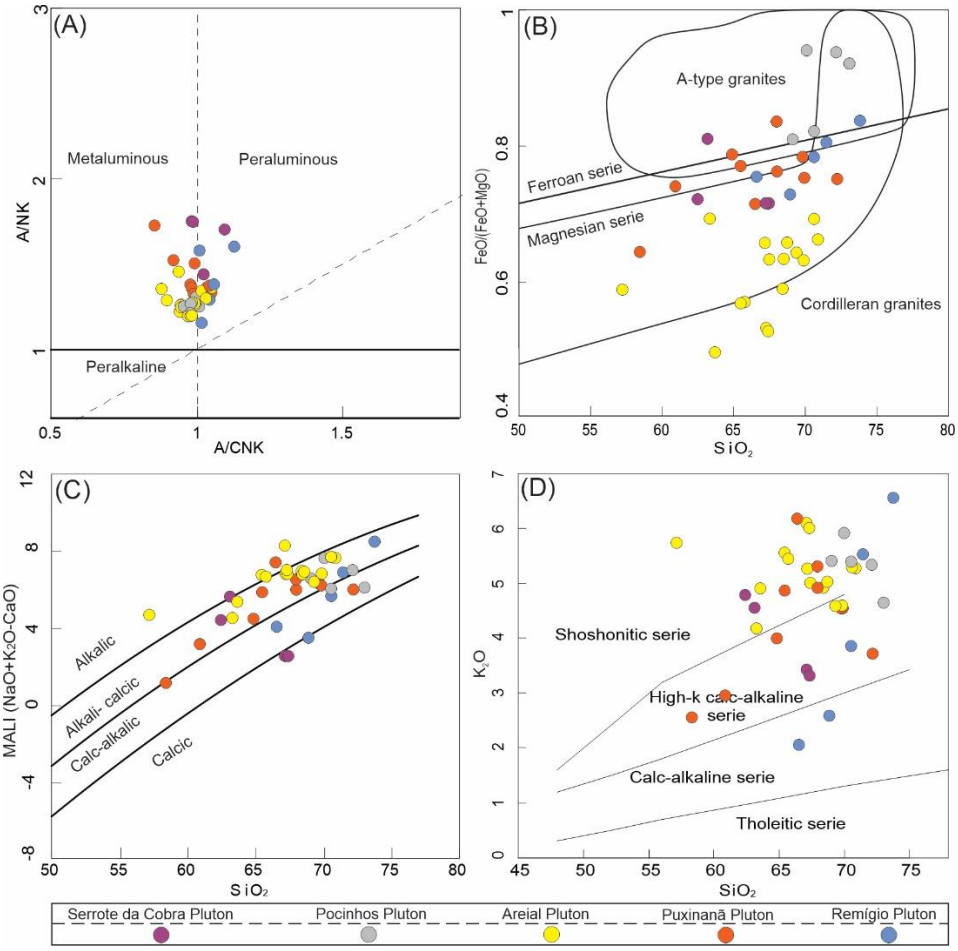

In the Harker-type diagrams for major elements (Figs. 8A-L), the granitoids show negative correlations for Al_2O_3, CaO, P_2O_5, FeO, MgO and TiO_2, suggesting fractionation of plagioclase, amphibole, Fe-Ti oxides, apatite and titanite during the magmatic evolution. The diorite trends for the Areial Pluton differ with the negative trends of the monzogranites and syenogranites for Al_2O_3, CaO, TiO_2, Ba, Sr and Zr, and suggest the diorites and granites are not comagmatic. Most trace element variations show dispersion, except the Serrote da Cobra

Pluton, which exhibits negative trends for BaO and Rb, which associated with the negative trend of K_2O, suggest K-feldspar and/or biotite fractionation. The other plutons show a discreet negative trend for Sr, suggesting plagioclase and/or apatite fractionation. The Areial granitoids have high Ba (1817 – 3208 ppm) and Sr (809 – 1505 ppm) (Figs. 8I, K), and low Rb (mean = 167 ppm), Th (mean = 18.17 ppm), Nb (mean = 11.72 ppm), Zr (mean = 213 ppm) and Y (mean = 11 ppm), akin to shoshonitic rocks (Nardi, 1986) and high barium-strontium (HiBaSr) granitoids (Fowler et al., 2008).

Figure 8 - A) – L) Variation diagrams for major and trace elements of the Esperança Complex granitoids.

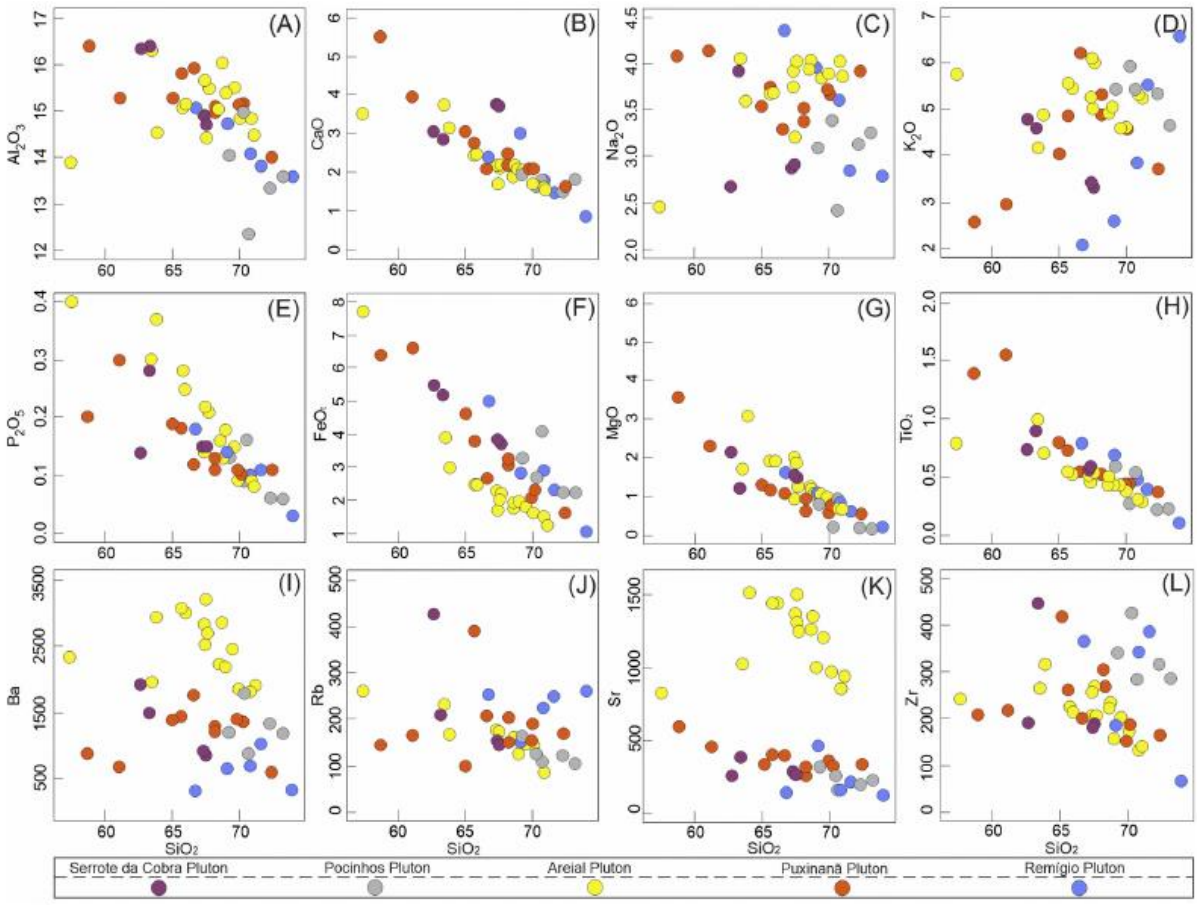

The granitoids have chondrite-normalized (Nakamura, 1974) fractionated REE patterns, with negative Eu anomalies, with Eu/Eu* ratios ranging from 0.62 to 0.85 (Pocinhos Pluton), 0.47 to 0.97 (Puxinanã Pluton), 0.32 to 0.97 (Remígio Pluton), and 0.66 to 0.74 (Serrote da Cobra Pluton) (Fig. 9A). The Areial granitoids show the most fractionated patterns, with

$(Ce/Yb)_N$ ratios ranging from 20.35 to 67.91, and weakly positive to negative Eu anomalies, with Eu/Eu* ranging from 0.67 to 1.09.

The trace element patterns normalized to the values of Sun and McDonough (1989) of all granitoids are similar, excepting for the Areial Pluton (Fig. 9B), being characterized by negative anomalies of Ba, Nb, Sr, P and Ti. These negative anomalies are more pronounced in the Pocinhos and Remígio plutons, compared with the Serrote da Cobra and Puxinanã plutons. The Areial Pluton, in turn, has a pronounced negative Nb anomaly, commonly associated with crustal melts or crustal contamination, and minor in Ti and P.

Figure 9 – Trace elements geochemical characteristics for the studied granitoids. A) Chondrite-normalized REE patterns (Nakamura, 1974); B) Primitive mantle-normalized (Sun and McDonough, 1989) trace element diagrams (spidergrams).

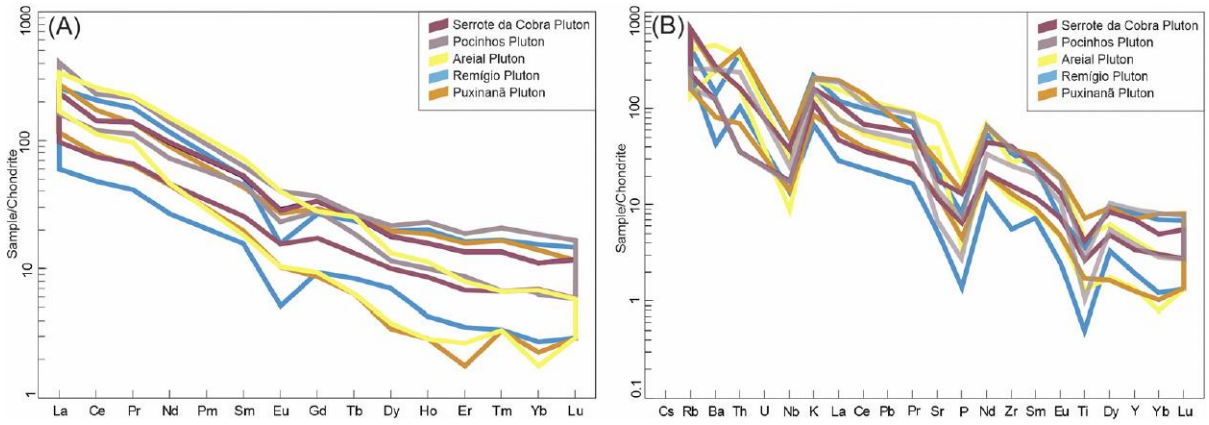

In trace element discrimination diagrams (Pearce et al., 1984) (Fig. 10A), the studied granitoids plot across the within-plate (WPG) and syn-collision (Syn-COLG) + volcanic arc (VAG) granites fields, with most analyses falling within the field of post-collisional granitoids (Post-COLG) of Pearce (1996) (Fig. 10B). The exception are the granitoids of the Areial Pluton, which plot predominantly within the VAG + Syn-COLG field. The studied granitoids have high 1000*Ga/Al ratios (> 2.6) and HSFE contents, with [Zr + Nb + Ce + Y] > 371 ppm, which make most analyses to plot in the A-type granites field of Whalen et al. (1987) (Fig. 10C-H).

Figure 10 – Tectonic setting discrimination diagrams for granitoids of the Esperança Complex. A) and B) Fields after Pearce et al. (1984) and Pearce (1996), respectively. WPG: Within Plate granites; POG: Post-orogenic granites; ORG: Ocean Ridge Granites; VAG: Volcanic Arc Granite; C) – H) Diagrams from the Whalen et al. (1987). FG: fractionated granite field; OTG: unfractionated granite field; A: A-type granites; I & S: I- and S-type granites.

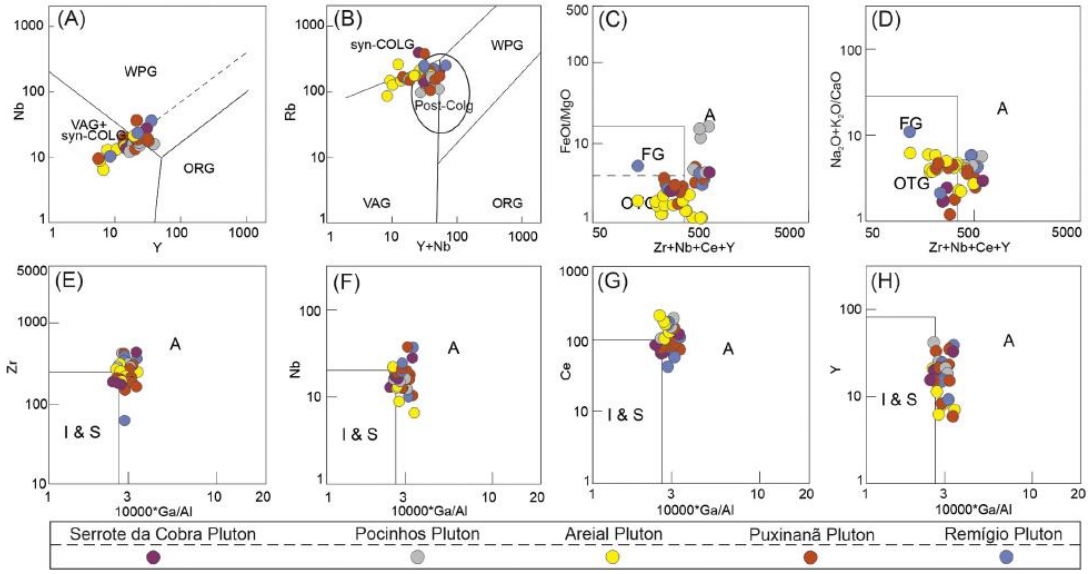

5.3. Chemical and isotopic systematics of zircon

5.3.1. Zircon U-Pb geochronology

5.3.1.1 Remígio Pluton

Twenty-four zircon grains were analyzed from a biotite-monzogranite sample (ESP-25C) from the Remígio Pluton. The analyses are shown in Table 2. Zircon crystals (Fig. 11A) are most euhedral, pink to colorless, prismatic to bipyramidal, with width/length ratios ranging from 1:5 to 1:6, with few grains with width/length ratios from 1:2 to 1:3 and show slight oscillatory zoning. Four analyses were discarded due to discordance, high common Pb contents, or analytical issues. Seven spots yielded a Concordia age of 564.7 ± 1.5 Ma (Th/U = 0.11 to 1.51; MSWD = 1.4), five others defined an age of 539 ± 1.54 Ma (Th/U = 0, 19 to 1.07; MSWD = 0.32) and five others an age of 525.5 ± 1.6 Ma (Th/U = 0.41 to 1.75; MSWD = 0.24) (Fig. 11B). The 564.7 ± 1.5 Ma age has the best MSWD and fits more coherently with the regional

and local context, so we consider it as the Remigío Pluton crystallization age. Xenocrystic core analyzed from one zircon grain yielded a $^{207}Pb/^{206}Pb$ age of 2.15 Ga, suggesting contribution of Rhyacian crust in the magma source.

Figure 11 – Geochronological characteristics of the studied granitoids. A) Representative zircons CL images; B) – F) Zircon U–Pb concordia diagram for the different plutons of the Esperança Complex.

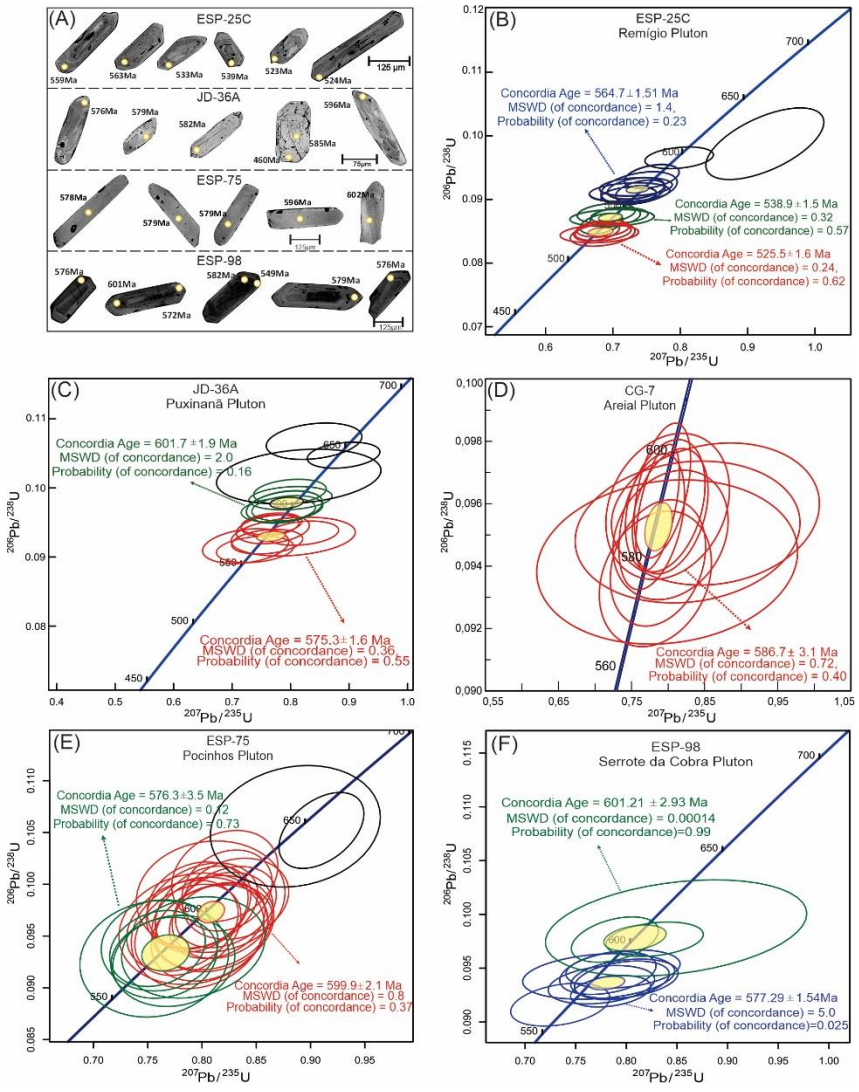

5.3.1.2. Puxinanã Pluton

A granodiorite sample (ESP-36A) was collected from the Puxinanã Pluton. Twenty-four spots were analyzed in 23 zircon grains and the results are shown in Table 2. The zircon crystals are subhedral, with rounded edges and width/length ratios ranging from 1:3 to 1:4 (Fig. 11A).

Th/U ratios range from 0.21 to 2.31, which are values of igneous zircons. Eight grains yielded a Concordia age of 575.3 ± 1.6 Ma, with MSWD = 0.36 (Fig. 11C). Considering errors, this age is marginally like the U-Pb zircon TIMS age reported by Sampaio (2005) (581 ± 7 Ma). Hence, it is considered the best estimate for the crystallization age. Another five analyses with Th/U ranging from 0.87 to 2.17 provided a concordant age of 601.7 ± 1.9 Ma (MSWD = 2.0), which reflects the incorporation of older materials belonging to the other plutons (Pocinhos and Serrote da Cobra plutons) or from the host rocks. Three analyses provided $^{206}Pb/^{238}U$ ages between 620 and 645 Ma. Detrital zircon grains with similar ages were reported by Guimarães et al. (2012) in the metasedimentary host rocks of the Esperança Complex. The other analyzed spots were not used to calculate the age, due to analytical problems or high contents of common Pb.

5.3.1.3. Areial Pluton

A total of twelve analyses were conducted on zircon grains extracted from a sample of granite (CG-7) collected in the southwest portion of the Areial Pluton. Results are shown in Table 2. The analyzed spots, with Th/U ratios ranging from 0.15 to 1.71, yielded an age of 586.7 ± 3.1 Ma (MSWD = 0.72 and probability of concordance = 0.40) (Fig. 11D), interpreted as the crystallization age of this pluton.

5.3.1.4. Pocinhos Pluton

Thirty zircon grains extracted from a sample of biotite syenogranite (ESP-75) were analyzed and the results are shown in Table 2. Most zircon grains are euhedral to subhedral, prismatic (width/length ratios from 1:2 to 1:4) and exhibit light to pinkish brown colors; overgrowths are rare and occur as narrow layers in the edge. Under CL, zircon grains typically show oscillatory zoning (Fig. 11A), suggesting a magmatic origin, reinforced by the values of the Th/U ratio (0.30 to 0.71). The analyzes were carried out mainly at spots in the center of the zircon grains and form in the Concordia diagram (Fig. 11E), a scattering of ages between ca.

600 and 570 Ma, which can be separated into two groups. Six analyzes, with discordance < 2% yielded Concordia age of 576.3 ± 3.6 Ma (MSWD = 0.46), similar to the age of the Puxinanã Pluton. Seventeen spots yielded an age of 599.9 ± 2.1 (MSWD = 0.8 and probability of concordance = 0.37) Ma like that reported by Archanjo and Fetter (2004) using U-Pb zircon TIMS data (592 ± 5 Ma). Thus, we suggest that the age of 599 Ma is the best estimate for crystallization of the Pocinhos Pluton. Two analyses provided $^{206}Pb/^{238}U$ ages ~ 645 Ma, may reflecting assimilation of older materials during the magmatic evolution.

5.3.1.5. Serrote da Cobra Pluton

Twenty-two zircon grains were picked from a tonalite (ESP-98) sample. They can be group into two morphological populations: 1) elongated, euhedral, bipyramidal crystals (width/length from 1:5 to 1:6), and 2) euhedral shorter crystals, with a length/width ratio ~1:3. Some grains show narrow overgrowths with high common Pb contents and were excluded from the age calculation. Crystals from both populations show weak oscillatory zoning and rare inherited cores (Fig. 11A). Eight spots with Th/U ratios between 0.02 and 0.71 plotted in the Concordia diagram yielded a Concordia age of 577.29 ± 1.54 Ma (MSWD = 5) (Table 2; Fig. 11F). Three other analyzes yielded a Concordia age of 601.21 ± 2.95 Ma (MSWD = 0.00014), which is similar to mean age (601.21 ± 2.93 Ma; MSWD = 0.2). Since the Th/U ratios (0.10 to 0.64) are typical values of igneous zircons, we consider this age as the best estimate for the crystallization age. The low Th/U ratio values associated to the younger Concordia age suggests a disturbance in the U-Pb isotopic system possibly related to emplacement of the ca. 575 Ma-old Puxinanã Pluton.

5.4. Zircon trace elements

The trace elements composition of the studied zircon grains is presented in the Tables 1 – 5 of Electronic Appendix 2B. The chondrite normalized REE patterns (Taylor and McLennan, 1985) of the syenogranitic facies of the Pocinhos and Puxinanã plutons are uniform and do not

present systematic core to rim variations (Figs. 12A and B). Zircon crystals of the Pocinhos granitoids, with $^{206}Pb/^{238}U$ age varying from 570 to 606 Ma, have REE patterns characterized by expressive positive Ce anomalies (Ce/Ce*= 4.68 – 16.71) and negative Eu anomalies (Eu/Eu*= 0.15 – 0.31), while zircon crystals of the Puxinanã granitoids, with similar $^{206}Pb/^{238}U$ ages (562 to 597 Ma), have REE patterns with lower positive Ce anomalies (Ce/Ce*= 1.09 – 3.11) and negative Eu anomalies (Eu/Eu*= 0.21 – 0.46). The same zircon grains used to Concordia ages calculation (565, 539 and 525 Ma) of the Remígio granitoids have REE patterns characterized by slight positive Ce anomalies (Ce/Ce*= 0.98 – 2.16) and very pronounced negative Eu anomaly (Eu/Eu*=0.03 – 0.23) (Fig. 12C). A zircon xenocryst ($^{207}Pb/^{206}Pb$ age of 2.15 Ga) with overgrowth of $^{206}Pb/^{238}U$ age of 607 Ma, shows patterns characterized by low REE contents and weak negative Eu anomalies, with Eu/Eu* varying from 0.36 (core) to 0.31 (rim). The REE patterns of the zircon grains from the Pocinhos, Puxinanã and Remígio granitoids with enrichment in HREE, negative Eu and positive Ce anomalies, and Th/U ratios ranging from 0.17 to 1.29 are typical of igneous zircon

The granitoids of the Serrote da Cobra and Areial plutons were more affected by post-magmatic processes, reflected in their zircon grains REE patterns. The chondrite normalized REE patterns for zircon grains of the Serrote da Cobra granitoids, with $^{206}Pb/^{238}U$ age varying from 584 to 601 Ma (Th/U= 0.14 – 0.44), are characterized by moderate positive Ce anomalies (Ce/Ce*= 6.15 – 12.17) and slight negative Eu anomalies (Eu/Eu*= 0.21 – 0.73) (Fig. 12D). However, younger zircon grains ($^{206}Pb/^{238}U$ ages of 559 – 576 Ma) with Th/U ratios varying from 0.06 to 0.35, show an increase in LREE concentration and have slighter positive Ce anomalies (Ce/Ce*= 1.40 – 5.19). Most of the analyses performed on zircon grains of the syenogranite sample (JD-06A) of the Areial Pluton (Fig. 12E) show enrichment in LREE and approximately horizontal REE patterns, without clear Ce and Eu anomalies. Part of these zircon grains have higher Ta, Li, Sc, Ti, Sr, and Ba (Table 5 of Electronic Appendix 2B) values than

those reported for unaltered igneous crystals (Hoskin and Schaltegger, 2003), but some of them still preserve magmatic character. The magmatic zircon grain cores have REE patterns characterized by strong positive Ce anomalies (Ce/Ce*= 5.04 – 46.16), consistent with crystallization under high fO_2 values, negative Eu anomalies (Eu/Eu*=0.38 – 0.59) and HREE/LREE ratios >1.

Figure 12 – A) – E) Chondrite-normalized REE patterns (Taylor e McLennan, 1985) for the zircon crystals of the studied plutons.

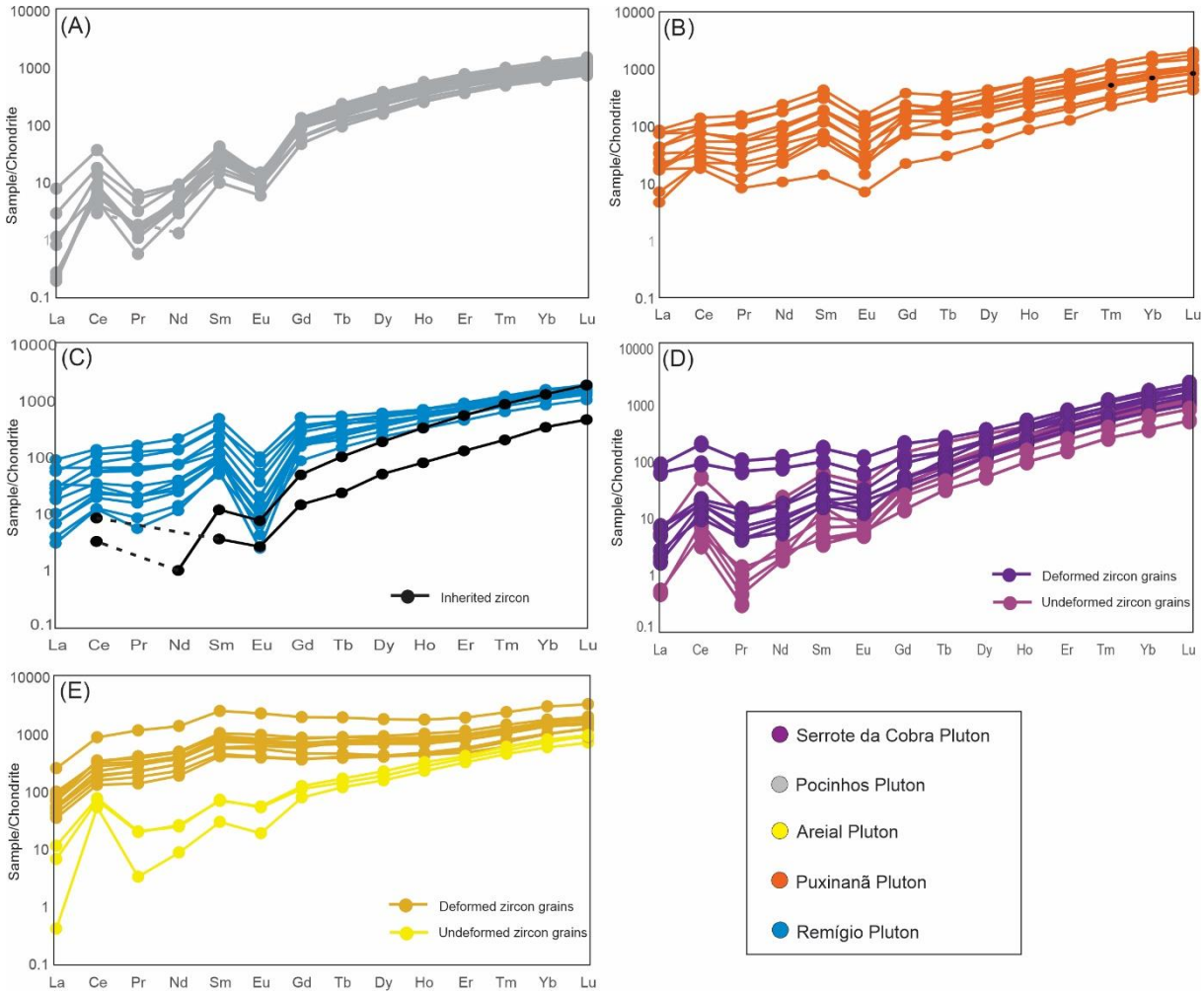

5.5. Lu-Hf zircon isotope geochemistry

5.5.1. Remígio Pluton

Sixteen spots analyzed in twelve zircon grains from the ESP-25C sample (Table 3) show Paleoproterozoic to Neoarchean Hf T_{DM} model ages (2.23-2.58 Ga) and negative εHf (t = 565 Ma) values (-14.46 to -21.03) (Fig. 13A). Rim and core analyses were performed in two zircon

grains, without significant variation in Hf isotopic composition, except for one analyzed spot from a xenocrystic core with a $^{207}Pb/^{206}Pb$ age of 2.1 Ga, that display εHf = +5.56 and T_{DM} model age = 2.34 Ga.

5.5.2. Puxinanã Pluton

Twelve spots analyzed in ten zircon grains from sample ESP-72 yielded εHf (t = 575 Ma) values of -3.66 to -5.92 and Hf T_{DM} model ages ranging between 1.65 and 1.77 Ga (Table 3; Fig. 13A). Rim and core analyses of two zircon grains show no significant variation in Hf isotopic composition.

5.5.3. Areial Pluton

The Hf isotopic data for Areial Pluton were obtained in eleven zircon grains from one sample of syenogranite (JD-06A) and nine zircon grains from one sample of a monzodiorite enclave (JD-06B). The results are shown in Table 3. Because granitoids of this pluton were intensely affected by late- to post-magmatic processes, the Hf isotope analyses were preferably conducted in the zircon cores. Eleven analyzed spots of the JD-06A sample show negative εHf (t = 590 Ma) values ranging from -17.14 to -19.80 and Siderian to Neoarchean Hf T_{DM} model ages, ranging from 2.39 to 2.54 Ga (Fig. 13A). Nine analyzed spots from zircon grains of the monzodiorite enclave (JD-06B), have Hf isotopic composition like the host granitoid (JD-06A), with εHf (590 Ma) values ranging from -18.61 to -19.64 and Hf T_{DM} model ages of 2.47 to 2.53 Ga. Only one analyzed grain displays higher εHf = -12.20 and Rhyacian Hf T_{DM} model age (2.13 Ga).

5.5.4. Serrote da Cobra Pluton

Ten zircon grains comprising twelve spots (Table 3) analyzed preferably in the crystal cores from a tonalite (sample ESP-98), showed εHf (600 Ma) values ranging from -4.87 to -6.91 and Paleoproterozoic (1.74 to 1.85 Ga) Hf T_{DM} model ages (Fig. 13A).

5.5.5. Pocinhos Pluton

Thirteen spots analyzed in thirteen zircon grains from ESP-75 sample displayed εHf values (t = 600 Ma) ranging from -2.83 to -5.14 and Hf T_{DM} model ages ranging between 1.63 and 1.75 Ga (Table 3; Fig. 13A).

Figure 13 – Chemical and isotopic diagrams for the studied granitoids. A) Diagram of εHf(t) vs. Age (Ma). Vertical lines represent the age range recorded for the main geological events in the Borborema Province (Caxito et al., 2021); B) Diagram of εNd(t) vs. Age (Ma) for the studied granitoids and host rocks. Data from Brito Neves et al. (2001), Archanjo and Fetter (2003) and Sampaio (2005); C) Al_2O_3/(FeOt+MgO) x 3CaO x 5(K_2O/Na_2O) ternary plot from Laurent et al. (2014).

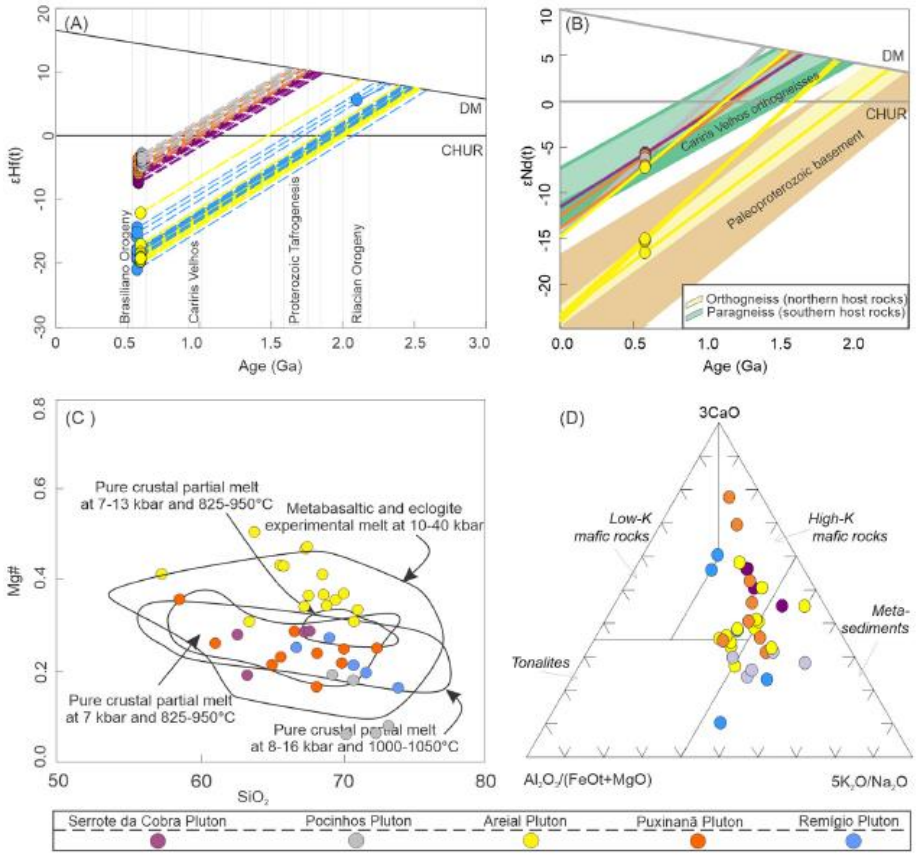

6. Discussion

6.1. Geochemical affinity and geotectonic environments

The ca. 587 Ma Areial Pluton comprises metaluminous, magnesian (Frost et al. 2001) granitoids, and contains mineral assemblage (calcic-amphibole + biotite + titanite + magnetite + epidote) like I-type granitoids of the magnetite series (Ishihara, 1977). The Areial granitoids

potassic character [$K_2O > (Na_2O - 2)$], trace element signature characterized by high Ba and Sr, and low Nb, Zr and Y contents, enrichment in LILE relative to HFSE, and fractionated REE pattern with lack of significant Eu anomalies, are similar to high-Ba-Sr (e.g., Fowler et al., 2008; Lara et al., 2017) or shoshonitic (Nardi, 1986; Nardi, 2016) granitoids. The Areial granitoids have lower MgO, Cr and Ni contents, and lack comagmatic diorites in comparison with other shoshonitic granitoids described in the Central subprovince (Guimarães et al., 1993**;** Guimarães and Silva Filho, 1998). Hence, although the Areial granitoids share some characteristics with granitoids of shoshonitic affinities, the lack of comagmatic mafic rocks does not allow defining them as typical shoshonites (Morrison, 1980). The crystallization age and geochemical signature of the Areial granitoids correspond to those observed in post-collisional high-K calc-alkaline granitoids of the Central subprovince (Almeida et al., 2002; Guimarães et al., 2004; Brito Neves et al., 1995; Van Schmus et al., 2011) and Uruguayan HiBaSr granites, which are "shoshonitic-like" rocks but formed by predominantly crustal melts (Lara et al., 2017).

In contrast with the Areial Pluton, granitoids of the Pocinhos Pluton belong to the ilmenite-series and are essentially ferroan, whereas those from the other plutons are slightly ferroan. The granitoids show fractionated REE patterns with pronounced negative Eu anomalies, also observed in zircon REE patterns, and have trace element patterns characterized by troughs at Nb, Ta, Sr, P and Ti. These characteristics are like that of post-collisional granites (Pearce, 1996; Fig. 10B) and like others ca. 570 Ma age plutons from the Central subprovince (Guimarães et al., 2004; Van Schmus et al., 2011).

The Puxinanã, Remígio, Pocinhos and Serrote da Cobra granitoids have HFSE (high field strength elements) contents like A-type granites (Whalen et al., 1987), with mean values of (Ce + Y + Nb + Zr) of 380 ppm, 401 ppm, 530 ppm and 371 ppm respectively, and a mean value of Ga/Al of ~ 2.86. Their Fe-rich mafic mineralogy, with amphiboles varying in

composition from Fe-edenite to Fe-tschermakite and siderophyllite-rich biotite, is also characteristic of A-type granites. A-type granites are commonly associated with anorogenic and/or extensional settings. However, the tectonic context of intrusion, the structural characteristics, and the ages of the granitoids show that they are syn-orogenic. Their ages are also like post-collisional (595 and 555 Ma) plutons from the Central subprovince (Amorim et al., 2019; Guimarães et al., 2017a; Neves et al., 2006; Van Schmus et al., 2011). Granites associated with a post-collisional context may involve different components in the magma source, as they depend on the composition and crustal thickening during orogenesis (Liégeois, 1998). The trace element signature of granitoids is primarily controlled by source composition and crystal-melt equilibrium throughout magma evolution (Rollinson, 1993), with the tectonic environment playing secondary control (Roberts and Clemens, 1993), so it is likely that the A-type affinity reflects source rock composition rather than the tectonic setting.

6.2. Magma source(s) and evolution

Lu-Hf zircon (this work) and Sm-Nd whole-rock (Table 4; Archanjo and Fetter, 2004; Brito Neves et al. 2001; Sampaio, 2005) isotopic data (Figs. 13A and B) allow to distinguish the granitoids of the Esperança Complex into two groups: 1) Areial and Remigio plutons with strongly negative ε_{Nd} (-15.29 to -16.71) and ε_{Hf} (-12.20 to -21.03) values, and Paleoproterozoic Nd T_{DM} model ages and Paleoproterozoic to Neoarchean Hf T_{DM} model ages, and 2) Pocinhos, Puxinanã and Serrote da Cobra plutons with Statherian–Calymmian Hf and Nd T_{DM} model ages and negative values for the ε_{Nd} (-5.90 to -7.35) and ε_{Hf} (-2.83 to -6.91).

Group 1

The isotopic signature (Figs. 13A and B) of the Areial pluton, i.e., strong negative $\varepsilon_{Nd}(t)$ (-15.29 to -16.71) and εHf (-17.14 to -19.80) values, suggest magma derivation mainly from melting of Paleoproterozoic to Neoarchean crustal sources. A single analysis yielded a younger Nd T_{DM} model age (1.56 Ga; Fig. 13B), suggesting some contribution of Tonian age materials,

likely the host paragneiss. The mean values of Mg# (MgO/(MgO+FeOt) = 0.39 for the granitoids of Areial Pluton reinforces genesis from predominantly crustal material, since mantle components should generate granitoids with higher Mg# values (Rapp and Watson, 1995). The comparison between the studied granitoids and experimental melts (Fig. 13C) supports a metabasaltic/eclogitic source under infracrustal conditions. Chemical analyses plot mainly in the field of melts derived from partial melting of high-K mafic rocks in the $Al_2O_3/(FeO_t+MgO)$ x $3CaO$ x $5(K_2O/Na_2O)$ ternary plot (Laurent et al., 2014; Fig. 13D). High Sr and low Y (mean Sr/Y ratio of 120), and low HREE contents (mean = 5.2 ppm), are compatible with partial melting at high pressures of mafic infracrustal sources (Kay and Mpodozis, 2001; Zhang et al., 2006, among others). Such conditions allow for the presence of garnet in the residue, accounting for low HREE contents and the absence of plagioclase, justifying the high contents of Sr and the lack of negative Eu anomalies in REE patterns. Experimental data from Sisson et al. (2005) showed that metaluminous to slightly peraluminous, high-K calc-alkaline, including the high Ba-Sr granites, can be generated by partial melting of potassium amphibolite.

The high - K signature of the coeval dioritic enclaves suggest that the diorite magma was generated by melting of Paleoproterozoic enriched lithospheric mantle. This is a feature shared by many high-K calc-alkaline and shoshonitic granitoids from the Central subprovince (Guimarães et al., 2004; Neves et al., 2000). Interactions between crustal felsic magmas and diorite magmas explain the higher Mg# values of the Areial granitoids than in other plutons of the Esperança Complex (Fig. 13C).

The absence of negative Eu anomalies (Fig. 9A) and spidergrams showing peaks at Sr (Fig. 9B) suggest that fractionation of plagioclase was not important during the magmatic evolution of the Areial Pluton. On the other hand, negative correlations of Rb and Ba versus SiO_2 (Figs. 8I and J) and negative trends of Sr versus Rb/Sr and Ba (Fig. 14A and B) suggest fractionation of K-feldspar and/or biotite, whereas positive trends of Ce/Yb versus Hf/Ta, Ta

versus Ta/Nb and La versus $(La/Yb)_N$ (Figs. 14 C, D and E) and negative anomalies of Ti (Fig. 9B) suggest fractionation of accessory mineral phases such as titanite and ilmenite.

The Remígio Pluton has the youngest crystallization age (565 Ma) and shows the most negative ƐHf values (-14.46 to -21.03) and the oldest Hf T_{DM} model age (2.23 to 2.58 Ga) amongst the Esperança Complex plutons. The isotopic data indicate Paleoproterozoic to Neoarchean crustal sources, without the contribution of juvenile material, which is corroborated by the presence of a zircon grain with inherited core with $^{207}Pb/^{206}Pb$ age of 2.15 Ga, $ƐHf_{(2.15\ Ga)}$ = +5.56 and T_{DM} model age = 2.34 Ga. Other features are also distinct, i.e.: biotite is the only mafic phase; enclaves show straight contacts, without features of hybridization processes; and (MgO + CaO) contents are lower (mean 2.8 wt% versus 3.8 wt% in the other plutons). These characteristics suggest that the Remigio granitoids have crystallized essentially from crustal magmas, without the contribution of mafic magmas, probably resulting from partial melting of predominantly metasedimentary sources (Fig. 13D). Geochronological data is not available to the Remigio Pluton metasedimentary country rocks. However, a metasedimentary sequence, composed of plagioclase-rich biotite paragneiss (metagraywacke), intercalated with quartzite and amphibolite, was dated by U-Pb zircon LA-ICP-MS (Guimarães et al., 2017b), 35 km to the east. All analyzed detrital zircon grains show concordant $^{207}Pb/^{206}Pb$ ages within the 2.3 – 1.9 Ga interval, suggesting that this sequence is a potential source for the Remigio granitoids magma. Low Sr contents and pronounced negative Eu anomalies (Figs. 9A and 14F) indicate plagioclase fractionation or its retention in the sources. Plagioclase fractionation is further supported by strong negative correlations between Al_2O_3, CaO, NaO and Sr with SiO_2 (Fig. 8)

Group 2

Zircon grains from the Pocinhos, Puxinanã and Serrote da Cobra granitoids share similar zircon Hf isotopic signatures (Fig. 13A), suggesting magmas derived from similar sources. Syn-

plutonic dykes and enclaves of diorite to granodiorite composition showing evidence of magma mixing/mingling processes, and the presence of inherited zircon grains with ages like those recorded in the host Tonian orthogneisses and metasedimentary rocks (Guimarães et al., 2012), suggest that the precursor magmas had contribution of lithospheric mantle sources and of orthogneisses and metasedimentary country rocks. Their Nd isotopic signatures are like those of the Tonian orthogneisses of the Alto Pajeú domain (Fig. 13B), which are slightly magnesian to typical ferrroan metagranitoids with extension-related geochemical signature (Guimarães et al., 2016). Melting of such crustal materials, could generate magmas with A-type signature, as recorded in these plutons.

The Pocinhos granitoids have the lowest CaO (mean = 1.74 wt%) and Mg# (mean = 0.11) values, being the most ferrous, with FeO/FeO+MgO ratios ranging from 0.82 and 0.95 (Fig. 7B) and show the strongest A-type signature among the studied granitoids. Their geochemical signature, associated to the scarcity of mafic enclaves, suggest generation by partial melting of Tonian crust, with small contribution of mantle component. A hybrid source for these granitoids magma is also supported by their projection in the Al_2O_3/(FeOt+MgO) x 3CaO x 5(K_2O/Na_2O) ternary diagram (Fig. 13D).

Many occurrences of Tonian orthogneisses are reported in the studied region (Brito Neves et al., 2001; Guimarães et al., 2012, 2016) but zircon Hf isotope data are quite scarce. In the Southern subprovince, Caxito et al. (2020) reported Hf-in-zircon isotopic data for the A-type Afeição augen-gneisses suite (975 Ma) i.e., εHf(t) ranging between -1.51 and +2.41, and Hf T_{DM} model ages between 1.6 - 1.4 Ga, which are like the Hf isotopic signatures of the Puxinanã, Serrote da Cobra, Pocinhos granitoids, corroborating the importance of a component like the Afeição augen-gneiss in their source.

Partial melting of Statherian–Calymmian crustal sources could also generate magmas with Hf isotopic signatures like those recorded in the Serrote da Cobra, Pocinhos and Puxinanã

granitoids. Rocks of these ages are rare in the Borborema Province, but several ca. 1.7-1.5 Ga orthogneiss bodies and a large metanorthosite complex occur southwards of the Esperança Complex (Accioly, 2000; Lages et al., 2019; Santos et al., 2015). These rocks have a strong intraplate geochemical signature, interpreted as resulting from failed attempt to break-up a large, previously agglutinated landmass (Neves et al., 2015; Santos et al., 2015). However, a Tonian source is more likely given the widespread occurrence of Tonian orthogneisses in the Alto Pajeú domain, even constituting part of the host rocks of the Esperança Complex.

Decreasing of major (Al_2O_3, CaO, P_2O_5, FeO, MgO e TiO_2) and trace elements (Sr, Ba and Rb) contents with increasing SiO_2 for the Serrote da Cobra, Pocinhos, and Puxinanã granitoids (Fig. 8) suggest that their magmas evolved through fractionation of plagioclase, biotite, amphibole, Fe-Ti oxides, apatite and titanite at different proportions. The remarkable negative Eu anomalies (Figs. 9A and 14F) and negative trends for Sr versus Rb/Sr (Figs. 14 A) corroborate plagioclase fractionation during the magmatic evolution or its retention in the source.

6.3. Estimation of crystallization parameters

6.3.1. Temperature

Crystallization temperature of granitic magmas is obtained mainly from the plagioclase - amphibole equilibrium (Blundy and Holland, 1990, among others) or element partitioning between amphibole and silicate melt (Purtika, 2016; Ridolfi and Renzulli, 2012 and references therein). Due to the scarcity of plagioclase and Ca-amphibole crystals in equilibrium, in the studied granitoids, we used the amphibole - liquid thermometers of Putirka (2016). This thermometer was built up using natural and experimental calcic amphibole data from Ridolfi and Renzulli, (2012), with precisions of ± 30ºC. The crystallization temperatures obtained are: 746 to 763 °C (Serrote da Cobra Pluton); 698 to 742 °C (Pocinhos Pluton); 709 to 787 °C (Puxinanã Pluton) and 723 to 803º C (Areial Pluton) (Table 5).

Figure 14 - Trace element variation binary diagrams indicative of mineral fractionation. A) Sr vs. Rb/Sr; B) Sr vs. Ba; C) Ce/Yb vs. Hf/Ta; D) Ta vs. Ta/Nb; E) La vs. $(La/Yb)_N$; F) Sr vs. Eu/Eu*. Bt, Kfs, Pl, Hb, Aln, Ttn, Zrc, Ilm and Ap corresponds the mineral phases biotite, K-feldspar, plagioclase, hornblende, allanite, titanite, zircon and apatite respectively.

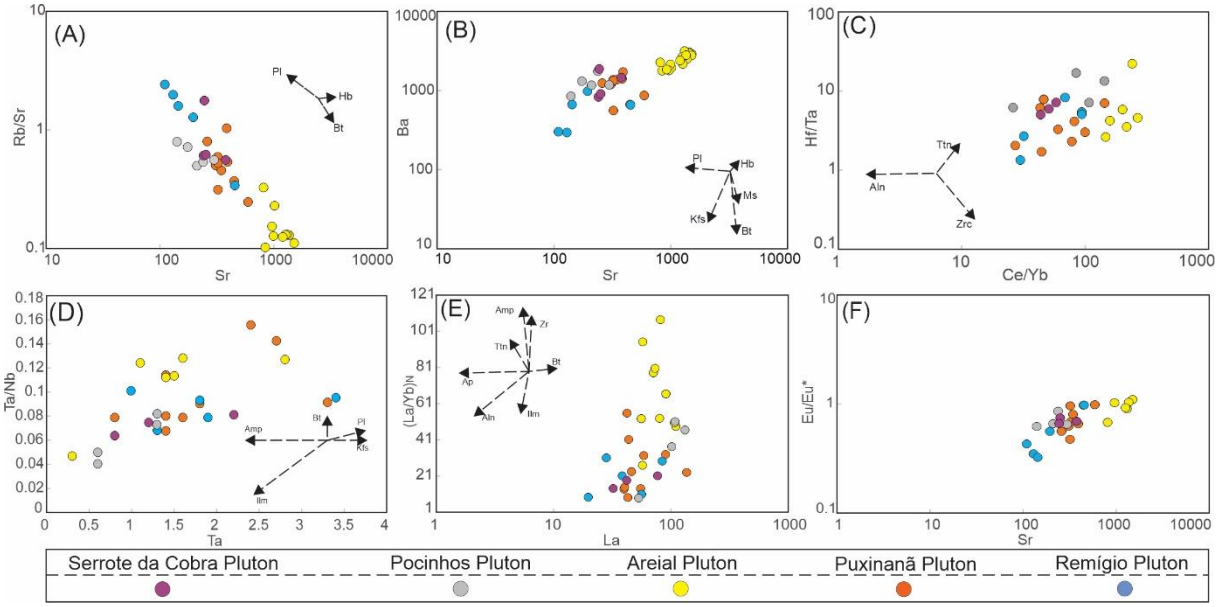

Zircon saturation temperatures were estimated from the equation of Watson and Harrison (1983) that is based on Zr contents of whole rock. The zircon solubility in crustal melts is associated with melt composition and temperature (Watson and Harrison, 1983), so the concentration of Zr in rock can be used to estimate the liquidus temperature when zircon is an early crystallized phase. Samples with M {(M [(Na + K + 2Ca) / (Si*Al)]} values outside the desired range (0.9 and 1.7) were discarded. The temperatures obtained are: 787 to 866 ºC (Remígio Pluton); 755 to 807 °C (Areial Pluton); 752 to 854 °C (Puxinanã Pluton); 824 to 867 °C (Pocinhos Pluton) and 778 to 857 °C (Serrote da Cobra Pluton) (Table 5), which are considered the liquidus temperatures.

The high near-liquidus temperatures obtained for the Esperança Complex magmas correlate to those of high-temperature granites proposed by Chappell and White (2001), which require significant heat input in the crust or the participation of mantle-derived magmas (Chappell and White, 2001; Miller et al., 2003), supporting the mantle source to the diorites.

6.3.2. Pressure and depth of emplacement

Al_t content in hornblende of calc-alkaline granites is directly proportional to pressure, when buffered by the assemblage quartz + hornblende + plagioclase + K-feldspar + biotite + titanite + magnetite or ilmenite (Anderson and Smith, 1995; Hollister et al., 1987). The calibration proposed by Schmidt (1992) has a wider pressure range (2.5 to 13.0 kbar) and a lower error (0.6 kbar) compared to other calibration equations (Blundy and Holland, 1990; Hollister et al., 1987).

The crystallization pressure, based on the calibration proposed by Schmidt (1992), are as follow: 5.94 to 7.11 kbar (Serrote da Cobra Pluton) and 5.56 to 6.18 kbar (Areial Pluton) (Table 5). Amphibole of the Pocinhos and Puxinanã granitoids has Fe# values higher than the values recommended (0.40 to 0.65) by Anderson and Smith (1995), so the calibration proposed by these authors was used (Table 5) and range from 5.48 to 7.93 kbar and from 3.51 to 6.16 kbar for the Pocinhos and Puxinanã respectively. The calculated pressures suggest that the granitoids of the Esperança Complex were emplaced at ca. 16.5 to 24.2 km depth.

6.3.3. Oxygen fugacity

The oxygen fugacity (fO_2) is a parameter that depends on the source, pressure, and temperature conditions during the magmatic evolution (Loiselle & Wones, 1979). It plays an important role in controlling the mineral assembly in various igneous rocks. Biotite of the Esperança Complex granitoids have variable values of Fe#. Most analyzed biotite from the Pocinhos granitoids, and some from the Remígio and Puxinanã granitoids, have Fe# > 0.65 like those reported by Anderson et al. (2008) for biotite of granites originated from magmas crystallized under low fO_2, the so-called granites of the ilmenite series. Biotite of the Serrote da Cobra, and of the less evolved facies of the Remígio, Pocinhos and Puxinanã granitoids, have Fe# ranging from 0.58 to 0.61 and were possibly originated from magmas crystallizing under intermediate fO_2 conditions. On the other hand, biotite from the Areial granites, have Fe# ranging from 0.30 to 0.53, composition like that of magnetite-series granites i.e., crystallized

from magmas under high fO_2 (Anderson et al., 2008). Amphiboles have characteristics like the studied biotite, i.e., amphiboles of the less evolved Pocinhos granitoids have Fe# ranging from 0.91 to 0.92, that suggest crystallization under low fO_2 conditions, while amphiboles of the Areial granitoids have Fe# ranging from 0.30 to 0.61 like those crystallized from the oxidized magma. Amphiboles from the other plutons has composition compatible with crystallization under fO_2 intermediate conditions i.e., have Fe# ranging from 0.58 to 0.75. The oxides of the Pocinhos, Remígio and Puxinanã granitoids are characterized by primary crystals of ilmenite, corroborating crystallization under low fO_2 conditions. Locally, ilmenite crystals were observed surrounded by a thin edge of titanite, suggesting late percolation of oxidizing fluids. Sampaio (2005) reported epidote crystals with petrographic features and pistacite molecule content consistent with magmatic epidote in the Areial and Serrote da Cobra granitoids. The presence of a mineral assembly containing magmatic epidote + magnetite + titanite + quartz in the Areial and Serrote da Cobra granitoids indicate magmas evolved under high fO_2 conditions (Schmidt and Thompson, 1996), which is corroborated by strong Ce anomalies observed in zircon crystals of the Areial granitoids.

6.4. Evolution of the Esperança Complex

The ages obtained in this work for the Serrote da Cobra and Pocinhos plutons (~600 Ma) are slightly older than that reported for the Pocinhos Pluton by Archanjo and Fetter (2004) using U–Pb zircon TIMS (592 ± 5 Ma). This discrepancy may be explained by the presence of younger zircon crystals dated at ca. 575 Ma in these plutons. Recent studies show that mushes (solids with interstitial melt) are long-term reservoirs of magma (Weinberg et al., 2021) and we propose that these younger zircon grains crystallized from the interstitial melt contemporaneously with intrusion of the nearby c. 575 Ma-old Puxinanã Pluton. Anisotropy of Magnetic Susceptibility (ASM) data reported by Archanjo and Fetter (2004) show that the Serrote da Cobra and Pocinhos plutons are characterized by dominantly moderately southeast

dipping magnetic foliations, concordant with the host rock foliation away from the Campina Grande shear zone, and southeast-plunging magnetic lineations. This finding is compatible with intrusion of the Serrote da Cobra and Pocinhos plutons coeval with the end of a long period of contractional tectonics in the Central subprovince responsible for development of shallow dipping foliation, W- to NW-directed tectonic transport, dominantly high-temperature (500°C-750°C), medium-pressure (500-900 MPa) metamorphism, and intrusion of syn-orogenic plutons (Guimarães et al., 2004; Medeiros, 2004; Neves et al., 2006, 2017; Sial and Ferreira, 2016; Silva and Neves, 2021). The heat required for the genesis of crustal melts can be provided by underplating/intraplating of mantle-derived basaltic melts (Thybo and Artemieva, 2013) or by internal heat production driven by radioactivity and/or strain heating (Brown, 2007). In the Alto Pajeú domain, the peak of the Ediacaran metamorphism reached amphibolite facies conditions (Bittar, 1998; Leite et al., 2000). Therefore, it is possible that in deep regions of the crust, the temperature was higher than that indicated as the liquidus of the Serrote da Cobra and Pocinhos granitoids (778 - 867 °C). If partial melting took place at the base of the crust, it is also likely that the lithospheric mantle immediately below participated in the process, providing mafic melts that originated the dioritic enclaves that are present in great quantity in the Serrote da Cobra Pluton.

The Areial and Puxinanã granitoids have crystallization ages of ca. 585 Ma and 575 Ma, respectively, and features suggestive of emplacement controlled by the Campina Grande shear zone. These granitoids show magmatic fabric partly superimposed by a solid-state foliation, both with predominantly NE-SW strike and parallel to the elongation of the intrusion, and kinematic criteria indicating dextral shear (C-S fabrics and shear bands) and to. The magnetic fabric of these plutons (Archanjo and Fetter, 2004) is characterized by foliations dipping systematically to the SE, towards the Campina Grande shear zone, and by gently-plunging NE–SW magnetic lineations. The presence of magmatic to submagmatic microstructures (migration

of grain boundaries in quartz, zoning, and curving of twinning in plagioclase crystals, and large amount of myrmekite) together with typical solid-state features, such as quartz ribbons and recrystallized feldspars, suggest a deformational continuum during the crystallization of the Puxinanã and Areial magmas. The data are consistent with syn-transcurrent emplacement, placing the beginning of the transcurrent regime in the region at ca. 585 Ma. Similar age has been proposed for the beginning of the transcurrent stage of the Brasiliano Orogeny in the Central subprovince (Guimarães et al., 2004; Neves et al., 2006). The large volume of mafic enclaves in both plutons suggests contribution from a mantle component. Roberts and Clemens (1993) suggested that mantle upwelling and underplating of the lower crust by mafic magmas is quite effective in explaining the origin of high-K, I-type rocks in post-collisional settings, especially when associated with extension following crustal thickening.

Decompression of the lithospheric mantle in response to mantle upwelling during relaxation, after the long period of contractional tectonics, seems to be a reasonable to explain interactions of mantle mafic melts with the crustal melts of different composition, generated by partial melting due to the increase in temperature. Vaughan and Scarrow (2003) postulated that metasomatized portions of the lithospheric mantle may control the localization and initiation of strike-slip faulting. Once generated, transcurrent shear zones subvertical foliation favor the transport of magmas through penetrative flow mechanism (Brown and Solar, 1998), allowing interaction of mantle melts with crustal melts of different compositions. We propose that these processes generated the progenitor magmas of the Puxinanã and Areial plutons, which had their composition slightly modified by fractional crystallization during the ascent and emplacement.

The Remígio Pluton, located immediately south of the Remígio - Pocinhos shear zone, is the youngest pluton (565 Ma) of the Esperança Complex, coeval with a high temperature metamorphic event along the Patos shear zone (Viegas et al., 2014). The increase in the geothermal gradient resulting from emplacement of the older plutons, possibly also aided by

strain heating, may explain partial melting of metasedimentary protoliths, inferred to be the main source of the Remígio granitoids (section 6.2), during the advanced stages of strike-slip shearing.

6.5. General Implications

This work reports an example of how an apparent simple case of a syn-transcurrent granitic batholith intrusion, with monotonous field and mineralogical features, can reveal its complexity once more detailed studies are conducted. The Esperança Complex had a long construction time (35 Ma), which started during the final stages of a contractional regime and continued in a dominantly transcurrent regime, as registered in their magmatic, sub-solidus and magnetic fabrics. The different chemical and isotopic signatures of granitoids from the plutons is mainly controlled by the composition of their sources since all where emplaced in the same tectonic setting. Therefore, the trace elements composition of the granites do not reflect the tectonic regime in which they were generated. On the contrary, it is probably related to the tectonic setting of their sources, as inferred from isotopic data, i.e., arc signature inherited from components of the Paleoproterozoic crust and lithospheric mantle, and extensional signature associated with predominantly Tonian or Statherian–Calymmian contributions and/or sources. The studied case can represent a situation more common than normally recognized, suggesting that the use of discriminant diagrams to infer tectonic setting, should be used with caution.

7. Conclusions

Based on geochronological, geochemical and Nd and Hf isotopic data, the following conclusions can be drawn, regarding the origin, evolution and tectonic setting of the Esperança magmatism:

1 – The isotopic and chemical signature point to an origin from distinct sources, i.e., mafic to intermediate Paleoproterozoic crust for the Areial pluton; Tonian sources such as the Cariris

Velhos orthogneisses for the Serrote da Cobra, Puxinanã and Pocinhos plutons; and metasedimentary sources for the Remigio granitoids. The interaction, in different proportions, with mafic melts from the lithospheric mantle and/or crustal assimilates also contributed to the variable geochemical trends of the granites from the magnesian to the ferrous series, from metaluminous to slightly peraluminous, from high Ba-Sr to low Ba -Sr I-type.

2 – U-Pb zircon data integrated with the regional context are compatible with a building by multiple intrusive events, involving from the end of a long contractional tectonics and metamorphic peak (Pocinhos and Serrote da Cobra ~600 Ma plutons) with heat input by crustal thickening, until the dominantly transcurrent regime (Puxinanã, Areial and Remígio plutons - 585 to 565 Ma), with the first two associated with interactions of crustal and mantle mafic melts, generated during mantle upwelling, and the Remígio granitoids generated possibly by a high geothermal gradient resulting from emplacement of the older plutons, possibly enhanced by strain heating. The age of the plutons associated with the magnetic and microstructural fabrics support penetrative flow as a transport process for syn-transcurrent plutons.

3 – The thermobarometric conditions of the magma crystallization are compatible with crystallization between the middle and upper crust.

4 – Our data corroborate previous works that support various thermotectonic processes in the Borborema Province, during the Ediacaran, generating a great diversity of magmas from interactions of a heterogeneous Paleoproterozoic crust and an enriched lithospheric mantle, and call attention to an important control of the transcurrent shear zones at different crustal levels, from genesis to the accommodation of intrusive bodies.

Acknowledgements

We acknowledge Dr Valdecir Janasi (University of Sao Paulo) and Dr Elson Paiva (Campinas State University) for the chemical analyses and zircon dating, and Dr Elton Dantas (University of Brasilia) for the zircon mounts. We also appreciate the two anonymous reviewers of Lithos for their constructive comments and suggestions, which helped improve the manuscript. This work was supported by the Brazilian National Research Council (CNPq), Proc. 421353/2018-0. JVL is grateful to CAPES for the doctoral scholarship.

References

Abdel-Rahman, A.F.M., 1994. Nature of biotites from alkaline, calc-alkaline and peraluminous magmas. Journal of Petrology 35, 525-541.

Accioly, A.C.A., 2000. Geologia, geoquímica e significado tectônico do Complexo Metanortosítico de Passira, Província Borborema, Nordeste Brasileiro. PhD Thesis. Universidade de São Paulo.

Almeida, C.N., Guimaraes, I.P., Da Silva Filho, A.F., 2002. Petrogênese de rochas plutônicas félsicas e máficas na Província Borborema, NE do Brasil: O Complexo Cálcio-Alcalino de Alto-K de Campina Grande. Revista Brasileira De Geociências, Brasilia 32 (2), 205-216.

Amorim, J.V.A., Guimarães, I.P., Farias, D.J.S., Lima, J.V., Santos, L., Ribeiro, V.B., Brainer, C., 2019. Late-Neoproterozoic ferroan granitoids of the Transversal subprovince, Borborema Province, NE Brazil: petrogenesis and geodynamic implications. International Geology Review 61, 1745 – 1767.

Anderson, J.L., Barth, A.P., Wooden, J.L., Mazdab, F., 2008. Thermometry and Thermobarometers in Granitic Systems. Reviews in Mineralogy and Geochemistry 69(1), 121-142.

Anderson, J.L., Smith, D.R., 1995. The Effects of temperature and fO_2 on the Al-in-hornblende barometer. American Mineralogist 80, 549-559.

Archanjo, C.J., Fetter, A.H., 2004. Emplacement setting of the granite sheeted pluton of Esperança (Brasilian Orogen, Northeastern Brazil). Precambrian Research 135, 193-215.

Archanjo, C.J., Viegas, L.G.F., Hollanda, M.H.B.M., Souza, L.C., Liu, D., 2012. Timing of the HT/LP transpression in the Neoproterozoic Seridó Belt (Borborema Province, Brazil): Constraints from UPb (SHRIMP) geochronology and implications for the connections between NE Brazil and West Africa. Gondwana Research 23 (2), 701-714.

Barbarin, B., 1999. A review of the relationships between granitoids types, their origins and their geodynamic environments. Lithos 46, 605-626.

Bittar, S.M.B., 1998. Faixa Piancó – Alto Brígida: Terrenos tectonoestratigráficos sob regimes metamórficos e deformacionais contrastantes. PhD Thesis. Instituto de Geociências, Universidade de São Paulo.

Blundy, J., Holland, T., 1990. Calcic amphibole equilibria and a new amphibole-plagioclase geothermometer. Contributions to Mineralogy and Petrology 104, 208-224.

Brito Neves, B. B., Van Schmus, W. R., Santos, E. J., Campos Neto, M. C., Kozuch, M., 1995. O evento Cariris Velhos na Província Borborema: Integração de dados, implicações e perspectivas. Revista Brasileira de Geociências 25, 279–296.

Brito Neves, B.B., Campos Neto, M.C., Van Schmus, W.R., Santos, E.J., 2001. O “Sistema” Pajeu-Paraiba e o “Maciço” São José do Campestre no leste da Borborema. Revista Brasileira de Geociências 31, 173–184.

Brito Neves, B.B., Santos, E.J., Van Schmus, W.R., 2000. Tectonic history of the Borborema province. In: Cordani, U.G., Milani, E.J., Thomaz Filho, A., Campos, D.A. (Eds.), Tectonic Evolution of South America. 31º International Geological Congress, Rio de Janeiro, pp. 151–182.

Brown, M., 2007. Crustal melting and melt extraction, ascent and emplacement in orogens: mechanisms and consequences. Journal of the Geological Society 164, 709-730.

Brown, M., Solar, G.S., 1998. Shear-zone systems and melts: feedback relations and self-organization in orogenic belts. Journal of Structural Geology 20 (2–3), 211-227.

Buddington, A.F., Lindsley, H.D., 1964. Iron-Titanium oxides minerals and synthetic equivalents. Journal of Petrology 5(2), 310-357.

Caxito, F.A., Basto, C.F., Santos, L.C.M.L., Dantas, E.L., Medeiros, V.C., Dias, T.G., Barrote, V., Hagemann, S., Alkmim, A.R., Lana, C.C., 2021. Neoproterozoic magmatic arc volcanism in the Borborema Province, NE Brazil: possible flare-ups and lulls and implications for western Gondwana assembly. Gondwana Research 92, 1–25

Caxito, F.A., Santos, L.C.M.L., Ganade, C.E., Bendaoud, A., Fettous, E.H., Bouyo, M.H., 2020. Toward an integrated model of geological evolution for NE Brazil–NW Africa: The Borborema Province and its connections to the Trans-Saharan (Benino-Nigerian and Tuareg shields) and Central African orogens. Brazilian Journal of Geology 50, e20190122.

Chappell, B. W., White, A. J. R., 2001. Two contrasting granite types: 25 years later. Australian Journal of Earth Science 48(4), 489-499.

Chappell, B.W., White, A.J.R., 1974. Two contrasting granite types. Pacific Geology 8, 173-174.

Clemens, J.D., Stevens, G., 2012. What controls chemical variation in granitic magmas? Lithos 134–135, 317–329.

Cox, K.G., Bell, J.D., Pankhurst, R.J., 1979. The Interpretation of Igneous Rocks, first ed. Allen & Unwin, London.

Czamanske, G. K., Wones, D. R., 1973. Oxidation during magmatic differentiation, Finnmarka Complex, Oslo area, Norway; part 2, the mafic silicates. Journal of Petrology 14(3), 349-380.

Dantas, E.L., Van Schmus, W.R., Hackspacher, P.C., Fetter, A.H., Brito Neves, B.B., Cordani, U., Nutman, A.P., Williams, I.S., 2004. The 3.4 e 3.5 Ga São José do Campestre massif,

NE Brazil: remnants of the oldest crust in South America. Precambrian Research 130, 113-137.

Enami, M., Suzuki, K., Liou, J.G., Bird, D.K., 1993. Al-Fe3+ anf F-OH substitution in titanite and constraints on their P-T dependence. Eur. J. Mineral., 5, 219-231.

Ferreira, V. P., Sial, A. N., Pimentel, M. M., Armstrong, Richard., Guimarães, I. P., Silva Filho, A. F., De Lima, M. M. C., Da Silva, T. R., 2015. Reworked old crust-derived shoshonitic magma: The Guarany pluton, Northeastern Brazil. Lithos 6, 20-29.

Fowler, M.B., Kocks, H., Darbyshire, D.P.F., Greenwood, P.B., 2008. Petrogenesis of high Ba–Sr plutons from the Northern Highlands Terrane of the British Caledonian Province. Lithos 105, 129-148.

Frost, R.B., Barnes, C.G., Collins, W.J., Arculus, R.J., David, J.E., Frost, C.D., 2001. A geochemical classification for granitic rocks. Journal of Petrology 42 (11), 2033-2048.

Ganade de Araújo, C. E., Cordani, U. G., Agbossoumounde, Y., Caby, R., Basei, M. A., Weinberg, R. F., Sato, K., 2016. Tightening-up NE Brazil and NW Africa connections: New U–Pb/Lu–Hf zircon data of a complete plate tectonic cycle in the Dahomey belt of the West Gondwana Orogen in Togo and Benin. Precambrian Research 276, 24-42.

Gao, P., Zheng, Y.-F., Zhao, Z.-F., 2016. Experimental melts from crustal rocks: a lithochemical constraint on granite petrogenesis. Lithos 266–267, 133–157.

Guimarães, I. P., Brito, M. F. L., Lages, G. A., Da Silva Filho, A. F., Santos, L., Brasilino, R. G., 2016. Tonian granitic magmatism of the Borborema Province, NE Brazil: A review. Journal of South American Earth Sciences 68, 97-112.

Guimarães, I. P., Da Silva Filho, A. F., Almeida, C. N., Van Schmus, W. R., Araujo, J. M. M., Melo, S. C., Melo, E. B., 2004. Brasiliano (Pan-African) granitic magmatism in the Pajeú-Paraíba belt, northeast Brazil: an isotopic and geochronological approach. Precambrian Research 135, 23-53.

Guimarães, I. P., Van Schmus, W. R., Brito Neves, B. B., Bittar, S. M. B., Silva Filho, A. F., Armstrong, R., 2012. U-Pb zircon ages of orthogneisses and supracrustal rocks of the Cariris Velhos belt: Onset of Neoproterozoic rifting in the Borborema Province, NE Brazil. Precambrian Research 192-195, 52-57.

Guimarães, I.P., Bittar, S.M.B., Farias, D.J.S., Yadav, R., Almeid, a, C.N., 2017b. Geologia e recursos minerais da Folha Sapé SB.25-Y-C-II Escala 1:100.000. Estado da Paraíba, single ed. Programa Geologia do Brasil, CPRM, Recife.

Guimarães, I.P., Da Silva Filho, A.F., 1998. Nd- and Sr-isotopic and U-Pb geochronologic constraints for the evolution of the shoshonitic Brasiliano Bom Jardim and Toritama complexes: evidence for a Transamazonian enriched mantle under Borborema tectonic province, Brazil. International Geology Review 40(6), 500-527.

Guimarães, I.P., Silva Filho A.F., Armstrong R., 2017a. Origin and age of coeval gabbros and leucogranites in the northern subprovince of the Borborema Province, NE-Brazil. Journal of South American Earth Sciences 76, 71-93.

Guimarães, I.P., Silva Filho, A.F., Nolan, J., Williams, T., 1993. The mineral chemistry of the Brasiliano age Bom Jardim and Toritama shoshonitic complexes, State of Pernambuco, Northeast Brazil. Anais da Academia Brasileira de Ciências 65, 83-106.

Harris, N.B.W., Pearce, J.A., Tindle, A.G., 1986. Geochemical characteristics of collision zone magmatism, in: Coward, M.P., Ries, A.C. (Eds.), Collision Tectonics. Journal of Geological Society Special Publication 19, London, pp. 67–81.

Hollister, L.S., Grisson, G.C., Peters, E.K., Stowell, H.H., Sisson, V.B., 1987. Confirmation of the empirical correlation of Al in hornblende with pressure of solidification of calc-alkaline plutons. American Mineralogist 72, 231-239.

Hoskin, P.W., Schaltegger, U., 2003. The composition of zircon and igneous and metamorphic petrogenesis. Reviews in Mineralogy and Geochemistry 53(1): 27-62.

Ishihara, S., 1977. The magnetite-series and Ilmenite-series granitic rocks. Mining Geology 27, 293–305.

Kay, S.M., Mpodozis, C., 2001, Central Andean ore deposits linked to evolving shallow subduction systems and thickening crust: GSA Today 11 (3), 4-9.

Lages. G.A., Santos. L.C.M.L., Brasilino, R.G., Rodrigues, J.B., Dantas, E.L., 2019. Statherian-Calymmian (ca. 1.6 Ga) magmatism in the Alto Moxotó Terreno, Borborema Province, Northeast Brazil: Implications for within-plate and coeval collisional tectonics in West Gondwana. Journal of South American Earth Sciences 91, 116-130.

Lara, P., Oyhantçabal, P., Dadd, K., 2017. Post-collisional, late Neoproterozoic, high-Ba-Sr granitic magmatism from the Dom Feliciano Belt and its cratonic foreland, Uruguay: Petrography, geochemistry, geochronology, and tectonic implications. Lithos 277, 178–198.

Laurent, O., Martina, H., Moyena, J.F., Doucelance, R., 2014. The diversity and evolution of late-Archean granitoids: Evidence for the onset of “modern-style” plate tectonics between 3.0 and 2.5 Ga. Lithos 205, 208-235.

Leake, B.E., Woolley, A.R., Arps, C.E.S., Birch, W.D., Gilbert, M.C., Grice, J.D., Hawthorne, C., Kato, A. Kisch, H.J., Krivovichev, V.G., Linthout, K., Laird, J., Mandarino, J., Maresch, W.V., Nickel, E.H., Rock, N.M.S., Schumacher, J.C., Smith, D.C., Stephenson, N.C.N., Ungaretti, L., Whittaker, E.J.W., Youzhi, G., 1997. Nomenclature of amphiboles: Report of the Subcommittee on Amphiboles of the International Mineralogical Association, Commission on New Minerals and Mineral Names. Mineralogical Magazine 61(405), 295-310.

Leite, P.R.L.B., Bertrand, J.M., Lima, E.S., Leterrier, J., 2000. Timing of granitic magmatismin the northern Borborema Province, Brazil: A U-BP study of granitoids from the Alto Pajeu Terrain. Journal of South American Earth Sciences 13, 549–559.

Liégeois, J.P., 1998. Some words on the post-collisional magmatism. Preface to special edition on post-collisional magmatism. Lithos 45, 15–17.

Loiselle, M.C., Wones, D.R., 1979. Characteristics and origin of anorogenic granites. Geological Society of America-Abstracts with Programs 11, 468.

Maniar, P.D., Piccoli, P.M., 1989. Tectonic discrimination of granitoids. Geological Society of America Bulletin 101, 635-643.

Medeiros, V.C., 2004. Evolução geodinâmica e condicionamento estrutural dos terrenos Piancó-Alto Brígida e Alto Pajeú, Domínio da Zona Transversal. PhD Thesis. Universidade Federal do Rio Grande do Norte.

Miller, C.F., McDowell, S.M., Mapes, R.W., 2003. Hot and cold granites? Implications of zircon saturation temperatures and preservation of inheritance. Geology 31, 529-532.

Morrison, G.W., 1980. Characteristics and tectonic settings of the shoshonite rocks association. Lithos 13, 97–108.

Nachit, H., IbhI, A., Abia, E.H., Ohoud, M.B., 2005. Discrimination between primary magmatic biotites, reequilibrated and neoformed biotites. Comptes Rendus Geoscience 337, 1415-1420.

Nachit, H., Razafimahefa, N., Stussi, J.M., Carron, J.P., 1985. Composition chimique des biotites et typologie magmatique des granitos. Comptes Rendus de l'Académie des sciences Paris 301(11), 813–818.

Nakamura, N., 1974. Determination of REE, Ba, Fe, Mg, Na, and K in carbonaceous and ordinary chondrites. Geochimica et Cosmochimica Acta 38, 757-775.

Nardi, L.V.S., 1986. As rochas granitoides da série shoshonitica. Revista Brasileira de Geociências 16, 3–10.

Nardi, L.V.S., 2016. Granitoides e séries magmáticas: o estudo contextualizado dos granitoides. Pesquisa em Geociências 43(1), 85-99.

Neves S.P., Silva J.M.R., Bruguier O., 2017. Geometry, kinematics and geochronology of the Sertânia Complex (central Borborema Province, NE Brazil): Assessing the role of accretionary versus intraplate processes during West Gondwana assembly. Precambrian Research 298, 552-571.

Neves, S.P., 2015. Constrains from zircon geochronology on the tectonic evolution of the Borborema Province: widespread intracontinental Neoproterozoic reworking of a Paleoproterozoic accretionary orogen. Journal of South American Earth Science 58, 150–164.

Neves, S.P., Bezerra, J.P.S., Bruguier, O., França, R.H.M., 2020. Evidence for Early Tonian (Ca. 1000–940 Ma) continental rifting in southern Borborema Province (NE Brazil): tectonic inheritance and shear zone nucleation during assembly of West Gondwana. International Geology Review 63(7), 851-865.

Neves, S.P., Lages, G.A., Brasilino, R.G., Miranda, A.W.A., 2015. Paleoproterozoic accretionary and collisional processes and the build-up of the Borborema Province (NE Brazil): Geochronological and geochemical evidence from the Central Domain. Journal of South American Earth Sciences 58, 165-187.

Neves, S.P., Mariano, G., Correia, P.B., Silva, J.M.R., 2006. 70 m.y. of synorogenic plutonism in eastern Borborema Province (NE Brazil): temporal and kinematic constraints on the Brasiliano Orogeny. Geodinamica Acta 19(3-4), 213-236.

Patiño Douce, A.E., Johnston, A.D., 1991. Phase equilibria and melt productivity in the pelitic system: implications for the origin of peraluminous granitoids and aluminous granulites. Contribution to Mineralogy and Petrology 107, 202–218.

Pearce, J., 1996. Sources and setting of granitic rocks. Episodes 4, 120-125.

Pearce, J.A., Harris, N.B.W., Tindle, A.G., 1984. Trace element discrimination diagrams for the tectonic interpretation of granitic rocks. Journal of Petrology 25, 956-983.

Peccerillo, A., Taylor, S. R., 1976. Plio-Quaternary Magmatism in Italy: Roman, Ernici-Roccamonfina, Intra-Apennine and Vulture Provinces. Contributions to Mineralogy and Petrology 58, 63–81.

Putirka, K., 2016. Amphibole thermometers and barometers for igneous systems and some implications for eruption mechanisms of felsic magmas at arc volcanoes. American Mineralogist 101 (4), 841–858.

Rapp, R.P., Shimizu, N., Norman, M.D., Applegate, G.S., 1999. Reaction between slab derived melts and peridotite in the mantle wedge: experimental constraints at 3.8 GPa. Chemical Geology 160, 335–356.

Rapp, R.P., Watson, E.B., 1995. Dehydration melting of metabasalt at 8-32 kbar: implications for continental growth and crust-mantle recycling. Journal of Petrology 36, 891-931.

Ridolfi, F., Renzulli, A., 2012. Calcic amphiboles in calc-alkaline and alkaline magmas: thermobarometric and chemometric empirical equations valid up to 1,130 °C and 22 GPa. Contribution to Mineralogy and Petrology 163, 877–895

Roberts, M.P., Clemens, J.D., 1993. Origin of high-potassium, calc-alkaline, I-type granitoids. Geology 21, 825–828.

Rodrigues, S.W.O., Archanjo, C.J., 2008. Microestruturas e tramas de eixo C de quartzo em milonitos do Sistema de Cisalhamento Campina Grande (PB), Província Borborema. Revista Brasileira de Geociências 38 (2), 392-405.

Rollinson, 1993. Using geochemical data: evaluation, presentation, interpretation, first ed. Longman Group Limited, London.

Sampaio, M. A. F., 2005. Petrologia, Geoquímica E Evolução Crustal Do Complexo Granítico Esperança, Terreno Alto Pajeú, Domínio Da Zona Transversal, Província Borborema, Nordeste Brasil. PhD Thesis. Universidade Federal de Pernambuco.

Santos, E.J., Van Schmus, W.R., Kozuch, M., Brito Neves, B. B., 2010. The Cariris Velhos Tectonic event in Northeast Brazil: Journal of South American Earth Sciences 29, 61-76.

Santos, L.C.M.L., Dantas, E.L., Santos, E.J., Santos, R.V., Lima, H.M., 2015. Early to late Paleoproterozoic magmatism in NE Brazil: The Alto Moxotó Terrane and its tectonic implications for the pre-West Gondwana assembly. Journal of Source American Earth Science 58, 188-209.

Schmidt, M.W., 1992. Amphibole composition in tonalite as a function of pressure: an experimental calibration of the Al-in-hornblende barometer. Contributions to Mineralogy and Petrology 110, 304-310.

Schmidt, M.W., Thompson, A.B., 1996. Epidote in calc-alkaline magmas: an experimental study of stability, phase relationships, and the role of epidote in magmatic evolution. American Mineralogist 81, 424-474.

Sial, A.N., Ferreira, V.P., 2016. Magma associations in ediacaran granitoids of the Cachoeirinha-Salgueiro and Alto Pajeú terranes, northeastern Brazil: Forty years of studies: Journal of South American Earth Sciences, Special Issue: Granite Magmatism in Brazil 68, 113–133.

Silva Filho, A.F., Guimarães, I.P., Santos, L., Armstrong, R., Van Schmus, W.R., 2016. Geochemistry, U-Pb geochronology, Sm-Nd and O isotopes of ca. 50my long Ediacaran High-K Syn-Collisional magmatism in the Pernambuco-Alagoas domain, Borborema Province, NE Brazil. Journal of South America Earth Sciences 68, 134-154.

Silva, V.L., Neves, S.P., 2021. Transition from contractional to transpressive tectonics: evidence from the Feira Nova Region, Rio Capibaribe Domain, Borborema Province, NE Brazil. Brazilian Journal of Geology 51, e20200049.

Sisson, T.W., Ratajeski, K., Hankins, W.B., Glazner, A.F., 2005. Voluminous granitic magmas from common basaltic sources. Contribution to Mineralogy and Petrology 148, 635–661.

Souza, Z.S., Montel, J-M., Gioia, S.M.L.C., Hollanda, M.H.B.M., Nascimento, M.A.L., Sá, E.F.J., Amaro, V.E., Pimentel, M.M., Lardeaux, J-M., Veschambre, M., 2006. Electron microprobe dating of monazite from high-T shear zones in the São José do Campestre Massif, NE Brazil. Gondwana Research 9, 441-455.

Speer, J. A., 1984. Micas in igneous rocks. Reviews in Mineralogy and Geochemistry 13, 299-356.

Sun, S.S., McDonough, W.F., 1989. Chemical and isotopic systematics of oceanic basalts: Implication for mantle composition and processes. Geological Society of London, Special Publications 42 (1), 313-345.

Taylor S.R., McLennan S.H., 1985. The Continental Crust: Its Composition and Evolution, first ed. Blackwell Scientific Publishing, United States.

Thybo, H., Artemieva, I.M., 2013. Moho and magmatic underplating in continental lithosphere. Tectonophysics 609, 605–619.

Tulloch, A.J., 1979. Secondary Ca-Al silicates as low-grade alteration products of granitoid biotite. Contribution to Mineralogy and Petrology 69, 105-117.

Van Schmus, W. R., Kozuch, M., Brito Neves, B. B., 2011. Precambrian history of the Zona Transversal of the Borborema Province, NE Brazil: Insights from SmeNd and UePb geochronology. Journal of South American Earth Sciences 31, 227-252.

Van Schmus, W.R., Oliveira, E.P., Silva Filho, A.F., Toteu, S.F., Penaye, J., Guimarães, I.P., 2008. Proterozoic links between the Borborema province, NE Brazil, and the Central African Fold Belt. Geological Society of London, Special Publication 294, 69–99.

Vauchez, A., Neves, S.P., Caby, R., Corsini, M., Egydio-Silva, M., Arthaud, M.H., Amaro, V., 1995. The Borborema shear zone system, NE Brazil. Journal of South American Earth Sciences 8, 247-266.

Vaughan, A.P.M., Scarrow, J.H., 2003. K-rich mantle metasomatism control of localization and initiation of lithospheric strike-slip faulting. Terra Nova 15 (3), 163-169.

Viegas, L.G.F., Archanjo, C.J., Hollanda, M.H.B.M., Vauchea, A., 2014. Microfabrics and zircon U-Pb (SHRIMP) chronology of mylonites from the Patos shear zone (Borborema Province, NE Brazil). Precambrian Research 243, 1-17.

Watson, E.B., Harrison, T.M., 1983. Zircon saturation revisited: temperature and composition effects in a variety of crustal magma types. Earth and Planetary Science Letters 64, 295 – 304.

Wedepohl, K. H., 1991. Chemical composition and fractionation of the continental crust. Geologische Rundschau 80, 207-223.

Weinberg, R.F., Vernon, R.H., Schmeling, H., 2021. Processes in mushes and their role in the differentiation of granitic rocks. Earth-Science Reviews 220, 103665.

Whalen, J.B., Currie, K.L., Chappell, B.W., 1987 A-types granites: geochemical characteristics, discrimination and petrogenesis. Contributions to Mineralogy and Petrology 95, 407-419.

Zhang, Q., Wang, C.Y.W., Li, C.D., Wang, Y.L., Jin, W.J., Jia, X.Q., 2006. Granite classification on the basis of Sr and Yb contents and its implications. Acta Petrologica Sinica 22 (9), 2249-2269.

Table 1 Representative whole-rock compositions of the Esperança Complex granitoids.

	Serrote da Cobra Pluton			Pocinhos Pluton			Areial Pluton			Puxinanã Pluton			Remígio Pluton		
Samples	ESP82*	ESP91*	JD05**	ESP111*	ESP33*	ESP108**	ESP52E*	ESP31*	ESP14*	ESP41B*	ESP36B*	ESP36C*	ESP25E*	ESP25B*	ESP25D*
Major oxides (wt.%)															
SiO2	63.29	67.3	62.6	73.16	69.21	70.2	57.35	68.55	71.01	58.55	68.13	72.35	66.71	70.73	73.9
TiO2	0.89	0.58	0.74	0.23	0.59	0.28	0.79	0.43	0.29	1.38	0.53	0.37	0.79	0.48	0.11
Al2O3	16.43	14.84	16.35	13.6	14.01	15	13.9	15.05	14.47	16.41	14.97	14.01	15.08	14.08	13.55
Fe2O3	5.78	4.29	6.08	2.47	3.63	3	8.58	1.97	1.41	7.08	3.67	1.84	5.55	3.25	1.14
MnO	0.07	0.06	0.08	0.03	0.04	0.03	0.12	0.03	0.02	0.1	0.04	0.02	0.1	0.04	0.01
MgO	1.22	1.54	2.12	0.19	0.77	0.17	5.43	1.24	0.65	3.54	0.65	0.55	1.63	0.81	0.2
CaO	2.87	3.75	3.07	1.82	1.93	1.67	3.52	1.93	1.51	5.52	2.17	1.66	2.37	1.83	0.88
Na2O	3.92	2.89	2.68	3.26	3.1	3.38	2.45	3.95	3.86	4.09	3.38	3.93	4.36	3.62	2.8
K2O	4.57	3.43	4.79	4.65	5.41	5.92	5.74	4.93	5.28	2.56	5.31	3.72	2.06	3.86	6.56
P2O5	0.28	0.15	0.14	0.06	0.13	0.09	0.4	0.16	0.08	0.2	0.11	0.11	0.18	0.1	0.03
Total	99.65	99.3	100.28	99.64	99.55	100.2	99.81	99.49	99.33	99.74	99.81	99.83	100.07	99.28	99.61
Trace elements (ppm)															
Ba	1485	924	1905	1185	1201	1785	2310	2204	1883	882	1265	569	300	677	306
Rb	208	153	426	103.5	164.3	126	260.9	162.7	NA	144.2	204.7	167.3	252.2	225.7	261.7
Sr	376	251	244	210	297	238	809.1	1259.5	918	590.4	258.8	322.5	129.3	143.4	109.6
Y	31	18.5	15.3	17.4	24.4	24.6	6.9	7.9	NA	14.7	23.1	5.8	36.7	23.3	14
Zr	446	173.5	186	284	337.7	424	248.5	218.3	136	205.8	269.1	160.1	362.4	341.9	62.2
Nb	27	16	12.5	12	17.8	14.9	6.4	12.4	NA	20.2	19.5	10.1	35.5	24	19.2
Th	11	11	13.75	14	20.1	8.64	14	16.8	NA	14.6	28.1	28.3	26	31.9	14.2
Ga	30	22	21.8	23	0	22.7	25.9	23.8	NA	23	25.1	25.7	27.7	22.2	21.2
Hf	13	6	5.7	8	9.2	10.1	6.6	5.6	NA	5.2	7.4	5.6	9.1	9.6	2.4
Ta	2.2	1.2	0.8	0.6	1.3	0.6	0.3	1.6	NA	1.6	1.8	0.8	3.4	1.9	1.8
La	76.3	32	41.7	107.5	100.7	130.5	80.7	70.4	NA	45.8	89.2	41.9	55.8	83.6	19.6
Ce	122	65.5	86.7	201	193.6	158	120.4	130.1	NA	78.4	147.2	72	108.1	178.6	41.8
Pr	15.5	7.3	9.17	21.1	20.1	24.1	11.5	13.7	NA	8.3	15.3	7.8	15.6	20	4.6
Nd	59.5	28.4	33.4	74.5	72.9	86.1	42.2	47.1	NA	31.9	56.4	30.7	59.7	73.1	16.8
Sm	10.5	5.2	6.2	10.1	11.7	12.75	4.2	6.9	NA	4.9	8.1	4.9	10.8	10.6	3.2
Eu	2.2	1.2	1.19	2	2	3.14	0.8	1.4	NA	1.4	1.3	0.8	1	0.9	0.4
Gd	9.2	4.8	5.01	8.8	7.8	10.15	3.2	3.2	NA	4	6.4	2.7	7.3	7	2.6
Tb	1.2	0.7	0.62	0.9	1.1	1.12	0.3	0.4	NA	0.6	0.9	0.3	1.1	1.9	0.4
Dy	6.1	3.6	3.45	4	5.3	5.39	1.3	1.9	NA	2.8	4.4	1.2	6.8	5.1	2.7
Ho	1.1	0.6	0.6	0.7	1	0.94	0.2	0.3	NA	0.5	0.8	0.2	1.4	0.9	0.5
Er	3	1.8	1.53	2	2.3	2.37	0.6	0.7	NA	1.3	1.9	0.4	3.7	2.4	1.5
Tm	0.4	0.2	0.25	0.2	0.3	0.34	0.1	0.1	NA	0.2	0.3	0.1	0.5	0.3	0.2
Yb	2.4	1.5	1.49	1.4	1.8	1.87	0.5	0.6	NA	1.3	1.8	0.5	3.4	1.9	1.4
Lu	0.4	0.2	0.23	0.2	0.3	0.26	0.1	0.1	NA	0.2	0.2	0.1	0.5	0.3	0.2

* Data from Sampaio (2005); ** This study

NA - Not analyzed.

Table 2 U–Pb zircon data from the Esperança Complex granitoids.

			Isotope Ratios									Isotope Ages (Ma)						
Spot	Pb_C	Th/U	$^{207}Pb/^{235}U$	±1σ	$^{206}Pb/^{238}U$	±1σ	c. corr	$^{238}U/^{206}PB$	±1σ	$^{207}Pb/^{206}Pb$	±1σ	$^{206}Pb/^{238}U$	±1σ	$^{207}Pb/^{235}U$	±1σ	$^{207}Pb/^{206}Pb$	±1σ	Conc.
ESP-25C (Remígio Pluton)																		
1,1*	9.84	0.45	0.685	0.02	0.085	0.001	0.93	11.835	0.11	0.059	0.002	523	4	530	11	560	58	98
2,1*	2.73	1.09	0.680	0.02	0.085	0.001	0.98	11.818	0.08	0.058	0.002	524	3	527	13	540	74	99
22,1*	2.81	0.41	0.686	0.02	0.085	0.001	0.7	11.784	0.08	0.059	0.001	525	3	531	9	554	53	98
6,1*	4.76	0.61	0.676	0.01	0.085	0.001	0.98	11.765	0.09	0.058	0.001	526	4	525	8	519	41	100
16,1*	0.12	1.75	0.686	0.02	0.085	0.001	0.94	11.707	0.07	0.058	0.001	528	3	530	9	539	47	99
5,1*	2.80	0.19	0.684	0.01	0.086	0.001	0.87	11.601	0.09	0.058	0.001	533	4	529	7	512	39	100
12,1*	0.00	1.05	0.699	0.03	0.087	0.001	0.69	11.480	0.07	0.058	0.002	538	3	538	15	536	80	100
10,1*	3.35	0.88	0.704	0.02	0.087	0.001	0.76	11.460	0.08	0.059	0.001	539	4	541	9	550	47	99
15,1*	4.12	1.07	0.711	0.02	0.087	0.001	0.98	11.435	0.07	0.059	0.001	540	3	545	11	565	54	99
13,1*	4.49	0.04	0.690	0.02	0.088	0.001	0.89	11.382	0.08	0.057	0.001	543	4	533	10	490	53	101
18,1*	0.57	1.39	0.724	0.02	0.091	0.001	0.89	11.030	0.07	0.058	0.001	559	3	553	10	526	48	101
20,1*	1.48	1.26	0.725	0.02	0.091	0.001	0.75	10.976	0.07	0.058	0.002	562	4	554	13	520	69	101
3,1*	2.03	0.11	0.741	0.01	0.091	0.001	0.78	10.960	0.09	0.059	0.001	563	4	563	8	563	41	99
17,1*	0.40	1.51	0.735	0.02	0.092	0.001	0.67	10.906	0.08	0.058	0.001	566	4	560	9	535	47	101
9,1*	3.48	0.83	0.740	0.02	0.092	0.001	0.94	10.895	0.13	0.058	0.002	566	6	562	12	546	63	100
19,1*	1.83	1.54	0.735	0.02	0.092	0.001	0.67	10.872	0.07	0.058	0.002	567	4	559	12	527	66	101
14,1*	0.17	1.05	0.758	0.02	0.094	0.001	0.68	10.682	0.09	0.059	0.001	577	5	573	9	558	47	100
21,1	0.59	2.56	0.799	0.02	0.097	0.001	0.98	10.357	0.07	0.060	0.002	594	4	596	9	605	54	99
8,1	5.62	0.42	0.927	0.06	0.099	0.002	0.99	10.125	0.24	0.068	0.002	607	12	666	15	870	35	91
7,1	-0.05	2.75	7.344	0.14	0.398	0.004	0.88	2.515	0.02	0.134	0.002	2158	17	2154	17	2151	29	100
ESP-36A (Puxinanã Pluton)																		
2,1*	1.03	2.00	0.739	0.03	0.091	0.001	0.83	10.979	0.09	0.059	0.002	562	5	562	17	562	78	99
16,1*	2.34	2.19	0.723	0.03	0.092	0.001	0.82	10.920	0.12	0.057	0.002	565	6	553	17	502	88	102
19,1*	6.86	1.02	0.761	0.02	0.092	0.001	0.94	10.845	0.09	0.060	0.002	569	4	574	14	598	68	98
9,1*	6.29	0.21	0.805	0.04	0.093	0.001	0.73	10.758	0.13	0.063	0.003	573	7	600	21	702	116	95
21,1*	0.00	0.84	0.821	0.02	0.093	0.001	0.96	10.701	0.08	0.064	0.002	576	4	608	13	732	68	94
17,1*	1.37	2.31	0.769	0.02	0.094	0.001	0.89	10.638	0.10	0.059	0.002	579	5	579	14	580	68	99
5,1*	2.49	0.32	0.766	0.02	0.095	0.001	0.87	10.575	0.07	0.059	0.002	582	4	577	11	556	58	100
11,1*	4.22	0.28	0.770	0.02	0.095	0.001	0.87	10.535	0.07	0.059	0.002	585	4	580	12	560	60	100
7,1*	1.25	-	0.780	0.03	0.097	0.001	0.5	10.330	0.08	0.058	0.002	596	4	585	15	545	70	101
1,1*	6.93	2.07	0.795	0.02	0.097	0.001	0.96	10.304	0.08	0.059	0.002	597	4	594	13	581	64	100
4,1*	0.29	0.88	0.790	0.02	0.097	0.001	0.73	10.283	0.10	0.059	0.002	598	6	591	14	564	68	101
8,1*	1.12	1.86	0.800	0.03	0.099	0.001	0.5	10.151	0.07	0.059	0.002	606	4	597	16	562	74	101
18,1*	2.50	2.18	0.800	0.03	0.099	0.001	0.95	10.057	0.08	0.058	0.002	611	4	597	15	543	68	102
13,1	2.66	1.95	0.891	0.02	0.105	0.001	0.01	9.548	0.07	0.062	0.002	642	5	647	11	665	61	99
22,1	4.36	1.36	0.840	0.03	0.107	0.001	0.54	9.367	0.09	0.057	0.002	654	6	619	18	494	81	105
14,1	9.63	3.48	0.814	0.08	0.102	0.002	0.1	9.838	0.16	0.058	0.004	624	9	605	34	533	95	103

Table 2 Continued

				Isotopic Ages (Ma)												Isotope Ratios			
Spot	$\%^{206}Pb_C$	Th/U	$^{206}Pb^*_{ppm}$	$^{206}Pb/^{238}U$ (1)	±1σ	$^{206}Pb/^{238}U$ (2)	±1σ	$^{206}Pb/^{238}U$ (3)	±1σ	$^{207}Pb/^{206}Pb$ (1)	±1σ	$^{208}Pb/^{232}Th$ (1)	±1σ	% Disc	$^{238}U/^{206}PB$	±1σ	$^{207}Pb/^{206}Pb$	±1σ
CG-7 (Areial Pluton)																			
1.1*	0.85	0.60	37.2	580	5	579	5	582	5	625	70	558	12	7.5	10.552	0.87	0.066	2.50
2.1*	0.70	0.15	47.5	590	5	589	5	590	5	632	54	576	31	7.1	10.385	0.85	0.065	1.92
5.1*	0.56	0.74	31.2	591	5	590	5	592	6	610	57	578	24	3.4	10.372	0.90	0.064	2.08
7.1*	1.49	0.68	20.6	590	6	590	5	592	7	620	91	580	27	4.9	10.281	0.96	0.072	1.97
8.1*	1.61	0.30	26.1	577	5	576	5	577	5	627	84	576	34	8.3	10.531	0.92	0.072	2.14
9.1*	0.90	0.67	34.5	585	5	584	5	586	6	651	84	576	13	10.6	10.456	0.88	0.067	3.23
10.1*	0.63	0.58	26.0	588	5	588	5	587	6	571	47	589	22	-3.1	10.408	0.92	0.065	1.05
11.1*	0.33	0.73	43.7	590	5	590	5	591	5	583	28	586	9	-1.3	10.393	0.86	0.062	0.74
12.1*	0.41	0.60	28.5	593	5	593	5	592	6	589	38	603	11	-0.8	10.327	0.91	0.063	1.02
13.1*	1.14	0.18	20.2	580	6	578	6	581	6	658	194	543	134	12.4	10.530	0.97	0.069	3.82
14.1*	5.67	0.59	31.0	586	5	583	6	582	6	710	160	620	31	18.3	9.964	0.90	0.106	3.25
15.1*	1.79	1.71	22.3	589	5	585	6	592	8	792	139	579	12	26.8	10.343	0.95	0.074	5.30

			Isotope Ratios										Isotope Ages (Ma)				
Spot	$\%^{206}Pb_C$	Th/U	$^{207}Pb/^{235}U$	±1σ	$^{206}Pb/^{238}U$	±1σ	c. corr	$^{238}U/^{206}PB$	±1σ	$^{207}Pb/^{206}Pb$	±1σ	$^{206}Pb/^{238}U$	±1σ	$^{207}Pb/^{235}U$	±1σ	$^{207}Pb/^{206}Pb$	±1σ	Conc.
ESP-75 (Pocinhos Pluton)																		
258	0.32	0.60	0.886	0.03	0.106	0.002	0.15	9.470	0.22	0.062	0.00	646	14	637	17	825	39	101
259*	0.10	0.53	0.801	0.02	0.098	0.002	0.34	10.246	0.18	0.059	0.00	600	9.7	597	10	610	27	100
261*	0.16	0.63	0.782	0.02	0.096	0.002	0.27	10.417	0.20	0.059	0.00	592	10	586	12	697	32	101
262*	0.58	0.58	0.753	0.04	0.096	0.003	0.09	10.428	0.29	0.061	0.00	588	16	562	20	936	54	104
263*	0.31	0.57	0.792	0.03	0.094	0.002	0.19	10.650	0.23	0.060	0.00	578	12	588	15	784	41	98
264*	0.21	0.56	0.81	0.02	0.096	0.002	0.17	10.395	0.21	0.061	0.00	591	11	601	13	741	35	98
266*	0.11	0.39	0.814	0.02	0.097	0.002	0.26	10.363	0.16	0.061	0.00	594	8.9	604	10	691	26	98
267*	0.16	0.57	0.787	0.02	0.096	0.002	0.31	10.460	0.20	0.059	0.00	588	10	589	11	649	31	100
268*	0.36	0.57	0.756	0.03	0.093	0.002	0.10	10.776	0.27	0.060	0.00	573	13	564	16	837	43	102
271*	0.33	0.45	0.808	0.03	0.099	0.002	0.08	10.121	0.23	0.059	0.00	608	13	600	16	830	41	101
272*	0.34	0.54	0.792	0.03	0.096	0.002	0.14	10.449	0.24	0.060	0.00	590	13	587	16	814	42	101
273*	0.22	0.30	0.761	0.02	0.094	0.002	0.09	10.627	0.20	0.059	0.00	579	11	570	13	742	38	102
278*	0.33	0.65	0.768	0.03	0.097	0.002	0.11	10.309	0.23	0.062	0.00	597	13	576	16	787	45	104
279*	0.14	0.72	0.831	0.02	0.099	0.002	0.18	10.142	0.16	0.061	0.00	606	9.3	615	11	717	31	98
280*	0.15	0.67	0.796	0.02	0.098	0.002	0.18	10.204	0.18	0.058	0.00	603	10	593	11	621	29	102
281*	0.13	0.39	0.823	0.02	0.099	0.002	0.21	10.060	0.16	0.060	0.00	610	9.2	606	9.6	641	27	101
282	0.03	0.34	0.91	0.02	0.105	0.002	0.44	9.506	0.14	0.062	0.00	645	8.8	656	8.1	694	22	98
283*	0.12	0.62	0.807	0.02	0.095	0.002	0.26	10.493	0.21	0.060	0.00	586	11	594	12	680	31	99
287*	0.18	0.46	0.765	0.02	0.093	0.002	0.18	10.764	0.19	0.059	0.00	573	9.6	577	11	653	34	99
288*	0.29	0.71	0.796	0.03	0.095	0.002	0.17	10.493	0.24	0.061	0.00	586	13	586	14	752	37	100
289*	0.14	0.63	0.8	0.02	0.098	0.002	0.29	10.215	0.18	0.059	0.00	602	10	596	11	667	30	101
290*	0.23	0.49	0.774	0.02	0.093	0.002	0.12	10.799	0.21	0.060	0.00	571	11	578	13	734	36	99
291*	0.14	0.68	0.822	0.02	0.098	0.002	0.31	10.225	0.17	0.060	0.00	601	9.5	608	10	641	27	99
294*	0.07	0.56	0.759	0.02	0.094	0.002	0.21	10.661	0.17	0.058	0.00	577	8.7	575	10	617	27	100
295*	0.13	0.41	0.821	0.02	0.101	0.002	0.23	9.921	0.18	0.058	0.00	620	10	605	11	643	28	102

Table 2 Continued

			Isotope Ratios									Isotope Ages (Ma)						
Spot	Pb_c	Th/U	$^{207}Pb/^{235}U$	±1σ	$^{206}Pb/^{238}U$	±1σ	c. corr	$^{238}U/^{206}PB$	±1σ	$^{207}Pb/^{206}Pb$	±1σ	$^{206}Pb/^{238}U$	±1σ	$^{207}Pb/^{235}U$	±1σ	$^{207}Pb/^{206}Pb$	±1σ	Conc.
ESP-98 (Serrote da Cobra Pluton)																		
3.1*	4.25	0.02	0.735	0.017	0.092	0.001	0.50	10.916	0.10	0.058	0.002	565	5	559	10	536	56	101
12.1*	1.38	0.15	0.785	0.016	0.093	0.001	0.90	10.770	0.07	0.061	0.001	572	4	588	9	650	43	97
24.1*	1.03	0.41	0.776	0.020	0.094	0.001	0.94	10.700	0.08	0.060	0.002	576	4	583	11	611	57	98
8.1*	0.50	0.02	0.796	0.019	0.094	0.001	0.85	10.653	0.08	0.062	0.001	578	4	595	10	658	50	97
13.1*	2.71	-	0.799	0.020	0.094	0.001	0.91	10.637	0.08	0.062	0.002	579	4	596	11	660	55	97
22.1*	1.23	0.09	0.772	0.028	0.094	0.001	0.87	10.612	0.10	0.060	0.002	581	5	581	16	584	82	99
19.1*	5.89	0.71	0.782	0.016	0.095	0.001	0.94	10.577	0.09	0.060	0.001	582	5	586	9	602	51	99
23.1*	2.83	0.05	0.798	0.020	0.095	0.001	0.98	10.535	0.08	0.061	0.002	585	4	595	11	637	59	98
2.1*	1.10	0.10	0.789	0.015	0.098	0.001	0.91	10.240	0.09	0.059	0.001	601	5	591	8	553	46	101
14.1*	0.28	0.07	0.828	0.019	0.098	0.001	0.58	10.237	0.07	0.062	0.001	601	4	612	10	656	47	98
18.1*	0.29	0.64	0.849	0.041	0.099	0.002	0.37	10.128	0.19	0.062	0.004	607	11	624	22	687	122	97

* Used analyzes in calculating Concordia age.

Pbc and Pb* indicate the common and radiogenic portions, respectively

(1) Common Pb corrected using measured ^{204}Pb

(2) Common Pb corrected by assuming $^{206}Pb/^{238}U$–$^{207}Pb/^{235}U$ age-concordance

(3) Common Pb corrected by assuming $^{206}Pb/^{238}U$–$^{208}Pb/^{232}Th$ age-concordance

Table 3 Lu-Hf isotopic data of the granites from the Esperança Complex.

Spot	$^{176}Lu/^{177}Hf$	±2σ	$^{176}Hf/^{177}Hf$	±2σ	$^{176}Hf/^{177}Hf_{(t)}$	εHf(t)	±2σ	T_{DM}	t (Ma)
ESP-25C (Remígio Pluton)									
Seq061	0.00078	5	0.28190	26	0.28189	-19.16	1.27	2.49	565
Seq062	0.00068	4	0.28184	67	0.28183	-21.03	3.34	2.59	565
Seq063	0.00072	5	0.28199	24	0.28198	-15.95	1.22	2.31	565
Seq064	0.00068	6	0.28189	28	0.28188	-19.38	1.41	2.50	565
Seq065	0.00080	8	0.28192	25	0.28191	-18.22	1.26	2.43	565
Seq066	0.00079	6	0.28193	28	0.28192	-17.86	1.38	2.42	565
Seq067	0.00072	5	0.28191	23	0.28191	-18.51	1.13	2.45	565
Seq068	0.00076	5	0.28190	27	0.28189	-18.92	1.33	2.47	565
Seq069	0.00077	6	0.28192	26	0.28191	-18.36	1.31	2.44	565
Seq070	0.00079	6	0.28192	24	0.28191	-18.34	1.20	2.44	565
Seq071	0.00086	5	0.28192	44	0.28191	-18.24	2.17	2.44	565
Seq072	0.00078	5	0.28190	26	0.28189	-19.13	1.32	2.48	565
Seq073	0.00167	10	0.28204	22	0.28202	-14.47	1.11	2.23	565
Seq074	0.00091	6	0.28201	22	0.28200	-15.24	1.12	2.27	565
Seq075	0.00084	5	0.28193	22	0.28192	-18.08	1.12	2.43	565
Seq076	0.00049	3	0.28162	32	0.28160	5.56	1.58	2.34	2100
ESP-72 (Puxinanã Pluton)									
Seq045	0.00059	4	0.28229	27	0.28229	-4.76	1.37	1.71	575
Seq048	0.00038	9	0.28231	18	0.28231	-4.04	0.92	1.67	575
Seq050	0.00039	2	0.28229	29	0.28228	-4.98	1.44	1.72	575
Seq051	0.00083	16	0.28233	37	0.28232	-3.66	1.83	1.65	575
Seq053	0.00040	2	0.28226	36	0.28226	-5.73	1.78	1.77	575
Seq054	0.00041	2	0.28229	26	0.28228	-5.01	1.32	1.73	575
Seq055	0.00063	4	0.28227	38	0.28226	-5.70	1.88	1.76	575
Seq056	0.00064	6	0.28229	30	0.28228	-4.92	1.52	1.72	575
Seq057	0.00056	4	0.28226	23	0.28226	-5.92	1.14	1.78	575
Seq058	0.00044	3	0.28227	30	0.28226	-5.59	1.50	1.76	575
Seq059	0.00055	3	0.28229	27	0.28228	-5.02	1.33	1.73	575
Seq060	0.00037	3	0.28229	25	0.28229	-4.69	1.27	1.71	575
JD-06 A (Areial Pluton)									
Seq019	0.00045	3	0.28186	25	0.28185	-19.80	1.24	2.54	590
Seq020	0.00036	3	0.28187	24	0.28186	-19.40	1.19	2.52	590
Seq021	0.00048	3	0.28186	24	0.28185	-19.76	1.21	2.54	590
Seq022	0.00065	5	0.28188	35	0.28187	-19.13	1.73	2.50	590
Seq023	0.00051	4	0.28189	29	0.28189	-18.61	1.44	2.48	590
Seq024	0.00124	9	0.28194	27	0.28193	-17.14	1.37	2.40	590
Seq025	0.00136	9	0.28191	22	0.28189	-18.36	1.10	2.46	590
Seq026	0.00085	5	0.28189	40	0.28188	-18.98	1.99	2.50	590
Seq027	0.00064	4	0.28189	26	0.28188	-18.76	1.32	2.48	590
Seq028	0.00024	1	0.28189	23	0.28188	-18.69	1.16	2.48	590
Seq029	0.00055	4	0.28187	24	0.28186	-19.57	1.19	2.53	590
JD-06B (Areial Pluton)									
Seq010	0.00041	3	0.28186	28	0.28186	-19.58	1.38	2.53	590
Seq011	0.00041	3	0.28189	27	0.28188	-18.76	1.37	2.48	590
Seq012	0.00097	6	0.28208	28	0.28207	-12.20	1.41	2.13	590
Seq013	0.00039	2	0.28186	24	0.28186	-19.64	1.18	2.53	590
Seq014	0.00056	4	0.28189	24	0.28189	-18.62	1.21	2.48	590
Seq015	0.00072	4	0.28188	31	0.28187	-19.08	1.57	2.50	590
Seq016	0.00045	3	0.28188	30	0.28187	-19.19	1.48	2.51	590
Seq017	0.00024	1	0.28187	23	0.28186	-19.43	1.13	2.52	590
Seq018	0.00057	4	0.28187	44	0.28187	-19.29	2.21	2.51	590
ESP-98 (Serrote da Cobra Pluton)									
Seq030	0.00057	5	0.28226	29	0.28225	-5.55	1.44	1.78	600
Seq031	0.00073	7	0.28222	30	0.28221	-6.91	1.52	1.85	600
Seq032	0.00034	2	0.28224	22	0.28223	-6.10	1.12	1.81	600
Seq033	0.00056	4	0.28226	31	0.28226	-5.30	1.57	1.76	600
Seq034	0.00063	4	0.28227	20	0.28226	-5.23	1.02	1.76	600
Seq035	0.00062	4	0.28225	25	0.28224	-5.76	1.25	1.79	600
Seq036	0.00049	4	0.28227	27	0.28227	-4.87	1.36	1.74	600
Seq037	0.00031	2	0.28223	31	0.28223	-6.41	1.54	1.82	600
Seq039	0.00069	4	0.28227	23	0.28226	-5.12	1.14	1.75	600
Seq041	0.00046	3	0.28225	34	0.28224	-5.88	1.68	1.79	600
Seq043	0.00067	4	0.28223	35	0.28222	-6.68	1.76	1.84	600
Seq044	0.00057	4	0.28225	25	0.28224	-5.85	1.24	1.79	600

Table 3 Continued

Spot	$^{176}Lu/^{177}Hf$	±2σ	$^{176}Hf/^{177}Hf$	±2σ	$^{176}Hf/^{177}Hf_{(t)}$	εHf(t)	±2σ	T_{DM}	t (Ma)
ESP-75 (Pocinhos Pluton)									
Seq098	0.00080	5	0.28229	38	0.28228	-4.45	1.91	1.72	600
Seq099	0.00063	5	0.28232	24	0.28231	-3.27	1.19	1.65	600
Seq100	0.00036	3	0.28232	23	0.28232	-3.11	1.17	1.64	600
Seq101	0.00055	4	0.2823	20	0.28229	-4.05	0.99	1.69	600
Seq102	0.00066	4	0.28229	22	0.28228	-4.45	1.12	1.72	600
Seq103	0.00090	6	0.28227	28	0.28226	-5.15	1.41	1.75	600
Seq104	0.00053	4	0.2823	27	0.28229	-4.11	1.36	1.70	600
Seq105	0.00129	8	0.2823	26	0.28229	-4.24	1.29	1.70	600
Seq106	0.00048	3	0.2823	22	0.28229	-4.10	1.09	1.70	600
Seq107	0.00079	7	0.28231	25	0.28230	-3.88	1.24	1.68	600
Seq120	0.00025	2	0.28233	25	0.28233	-2.84	1.25	1.63	600
Seq121	0.00024	2	0.28232	33	0.28232	-3.08	1.63	1.64	600
Seq122	0.00026	2	0.28231	35	0.28231	-3.46	1.74	1.66	600

Table 4 Sm-Nd isotopic data for the studied granitoids and host rocks.

Sample	Litology	Sm	Nd	$^{147}Sm/^{144}Nd$	$^{143}Nd/^{144}Nd$	$^{143}Nd/^{144}Ndi$	εNdi	T_{DM}	t (Ma)	Ref
Northern host rock										
ESFER1	Augen gneiss	5.20	27.68	0.1136	0.511497	0.511076	-16.28	2.381	565	1
ESTeo	Biotite gneiss	8.29	53.56	0.0936	0.511397	0.511050	-16.79	2.124	565	1
Es134E	Biotite gneiss	6.60	43.90	0.0909	0.511382	0.511045	-16.88	2.097	565	1
Southern host rock										
SPP-GR-LR	Muscovite gneiss	11.36	52.87	0.1299	0.512127	0.511646	-5.15	1.747	565	2
SCB-AGN-59	Augen gneiss	15.82	73.02	0.131	0.512079	0.511594	-6.17	1.851	565	2
SCB-MGV-AG	Muscovite gneiss	6.00	28.26	0.1283	0.512252	0.511777	-2.59	1.508	565	2
Areial Pluton										
ESP03A	Monzogranite	5.96	45.55	0.07914	0.511401	0.511108	-15.66	1.901	565	3
ESP08A	Syenogranite	4.34	31.33	0.08371	0.511437	0.511127	-15.29	1.925	565	3
ESP12A	Monzogranite	4.68	27.20	0.10409	0.51144	0.511055	-16.71	2.260	565	3
SCB-GP-ESP	Leucogranite	4.94	31.46	0.0949	0.51188	0.511529	-7.45	1.558	565	2
ESP-12	Granite	3.47	26.33	0.0798	0.511409	0.511114	-15.55	1.902	565	2
Puxinanã Pluton										
ESP01	Monzogranite	6.91	39.04	0.10708	0.51193	0.511534	-7.35	1.659	565	3
PX01	Syenogranite	8.15	45.22	0.10897	0.511997	0.511594	-6.18	1.595	565	3
Pocinhos Pluton										
Es01	Syenogranite	10.63	77.38	0.083	0.511891	0.511584	-6.37	1.410	565	1
Serrote da Cobra Pluton										
Es130	Tonalite	6.89	35.08	0.1187	0.512047	0.511608	-5.90	1.674	565	1

1- Archanjo et al., (2004); 2- Brito Neves et al., (2001); 3- Sampaio et al., (2005)

Table 5 Estimation of temperature and pressure for the Esperança Complex granitoids

Pluton	Serrote da Cobra		Pocinhos		Areial		Puxinanã		Remígio	
Temperature (°C)	Min	Max	Min	Max	Min	Max	Min	Max	Min	Max
Putirka (2016)	746	763	698	743	723	803	709	787	-	-
Watson & Harrison (1983)	778	857	824	867	755	807	752	854	787	866
Pressure (kbar)	Min	Max	Min	Max	Min	Max	Min	Max	Min	Max
Schmidt et al. (1992)	5.94	7.11	-	-	5.56	6.18	-	-	-	-
Anderson & Smith (1995)	-	-	5.48	7.93	-	-	3.51	6.16	-	-

SUPPLEMENTARY MATERIAL/APPENDIX

ELETRONIC APPENDIX 1A – ANALYTICAL TECHNIQUES

Mineral chemistry analyses were carried out using an electron probe microanalyzer (EPMA) JEOL JXA-8230 superprobe at Brasília University. The samples were carbon-coated in a vacuum chamber. The analyses were carried out using a beam size of 5 μm for plagioclase and 1 μm for other minerals, an acceleration voltage of 15 kV and a probe current of 10 nA for silicates and oxides. The crystals used for the analysis were TAP for Na, F, Mg, Si, Al, and P; PETJ for K, Ca and Cl; LIF for Ti, Cr, Mn, Ni, V and Fe; and LIFH for Fe. Calibration standards used were albite (Na), fluorite (F), forsterite (Mg), microcline (Si, Al and K), apatite (P), vanadinite (V and Cl), MnTiO3 (Ti and Mn), Cr2O3 (Cr), NiO (Ni), andradite and Fe2O3 (Fe). Cationic proportions and structural formulae calculation used the following oxygen bases: (23) amphiboles, (24) biotites, (24) feldspars, (5) titanite, (32) magnetite and (24) ilmenite.

For whole-rock chemical analyses, representative whole fresh rocks of the Pocinhos e Serrote da Cobra plutons were crushed in a stainless-steel jaw crusher and then sprayed in a chromium steel ring mill at NEG-LABISE (Center for Granite Studies and Stable Isotope Laboratory) at Pernambuco Federal University. The samples were analyzed at ALS Laboratories in Canada from the LiBO2 alkaline fusion ICP-AES (Inductively Coupled Plasma Emission Spectrometry) for major elements and by LiBO2 alkaline fusion ICP-MS (Inductively Coupled Plasma Mass Spectrometry) for trace elements. Detection limits are available online in the ALS Laboratories brochure.

For in situ zircon isotopic (U-Pb, Lu-Hf) and chemical analysis, zircon grains were separated at NEG-LABISE Laboratory of the Pernambuco Federal University using conventional crushing, sieving, and heavy liquid techniques. The non-magnetic zircon grains were hand-picked and mounted along with chips of the Temora 2 (206Pb/238U age = 416.8 ± 0.3 Ma; Black et al., 2004) and FC1 zircon standards onto double-sided tape. Zircon grains and the standards were enclosed by epoxy resin and polished. Back-scattered electron (BSE) and cathodoluminescence (CL) imaging were performed to identify internal structures and inclusions. The U-Pb isotopic analyses of zircon grains were performed using a Thermo Scientific NEPTUNE LA-ICP-MS coupled with a Photon-machines® - Analyzer G2 – 193 nm – Excimer Laser Ablation System and following the procedures described by Sato et al. (2012). The laser was configured to operate with 6 mJ and 6 Hz, producing spots with diameters up to 20 μm, and each analysis lasted about 40s. The zircon grains from ESP-75 sample (Pocinhos

Pluton) were analyzed by LA-ICP-MS at Campinas University - Brazil, using a sector field ICP-MS Element XR (Thermo Scientific), coupled with an Excite 193 (Photon Machines) laser ablation system, equipped with a two-volume HelEx ablation cell. The analytical conditions were 25 μm-diameter spots, 10 Hz laser frequency and 60 s ablation time. The CG-7 sample was prepared using standard crushing and separating procedures at the Geochronology Research Center at University of São Paulo, Brazil. Before analysis, zircon grains were hand-picked under a binocular microscope, mounted in epoxy resin and sectioned approximately in half and polished. The analyses of CG-7 sample were conducted using the SHRIMP II at the Beijing SHRIMP Centre (China) in sets of five scans throughout the masses. The measured U, Th and Pb abundances as well as Pb isotope ratios were normalized using the SL13 zircon standard (U = 238 ppm). The data reduction was performed using the SQUID/Excel macro (Ludwig, 2000) and the statistical assessments (at the 95% confidence level) were calculated using the geochronological ISOPLOT/Excel 3.0 software of Ludwig (2003). All Concordia age errors were calculated at the 1σ level.

Analysis of trace and rare earth elements of zircon crystals were carried out at the Chemistry Laboratory of the Institute of Geosciences of the University of São Paulo - using plasma quadrupole mass spectrometer (LA-Q-ICPMS; iCAP Q – Thermo Scientific) inductively coupled to a New Wave 213 A/F laser ablation system and controlled by the Qtegra software. Sampling was carried out in 60 μm raster mode, producing holes in the zircons of up to 30 μm and 1 μm/s pitch. Glitter® (GEMOC Laser ICP-MS Total Trace Element Reduction) was used to data reduction software

Lu-Hf isotopic analysis were carried out at UFOP using a Thermo-Scientific Neptune MC-ICPMS coupled to a Photon Machines 193 (λ=193 nm) ArF Excimer laser ablation system. The correction for isobaric interferences between 176Lu and 176Yb was applied (Gerdes and Zeh, 2009). Three standards were analyzed before and during runs: GJ, BB and TEMORA. The analyses of GJ yielded an average 176Hf/177Hf = 0.282003 ± 32, whereas the analyses in the BB standard yielded 176Hf/177Hf = 0.281672 ± 29. The average 176Hf/177Hf for TEMORA was 0.282691 ± 23. These values agree within error with the recommended values (Morel et al., 2008; Santos et al., 2017; Woodhead et al., 2005). The εHf(t) was calculated using chondritic values of 176Lu/177Hf and 176Hf/177Hf ratios, 0.0336 and 0.282785 respectively (Bouvier et al., 2008). The Depleted Hf model age was calculated relative to the depleted mantle with present-day 176Lu/177Hf and 176Hf/177Hf ratios of 0.03933 and 0.283294 (Blichert-Toft and Puchtel, 2010). Hf isotope data were obtained mainly in zircon grain spots with REE

patterns typical of alteration-free magmatic crystals and/or with well-defined magmatic crystallization age.

References

Black, L.P., Kamo, S.L., Allen, C.M., Davis, D.W., Aleinikoff, J.N., Valley, J.W., Mundil, R., Campbell, I.H., Korsch, R.J., Williams, I.S., Foudoulis, C., 2004. Improved 206Pb/238U microprobe geochronology by the monitoring of a trace-element-related matrix effect; SHRIMP, ID–TIMS, ELA–ICP–MS and oxygen isotope documentation for a series of zircon standards. Chemical Geology 205, 115–140.

Blichert-Toft, J., Puchtel, I.S., 2010. Depleted mantle sources through time: evidence from Lu–Hf and Sm–Nd isotope systematics of Archean komatiites. Earth Planetary Science Letters 297, 598–606.

Bouvier A., Vervoort J.D., Patchett P.J., 2008. The Lu–Hf and Sm-Nd isotopic composition of CHUR: constraints from unequilibrated chondrites and implications for the bulk composition of terrestrial planets. Earth and Planetary Science Letters 273 (1-2), 48-57.

Gerdes, A., Zeh, A., 2009. Zircon formation versus zircon alteration – new insights from combined U-Pb and Lu-Hf in situ LA-ICP-MS analyses and consequences for the interpretation of Archean zircon from the Central Zone of the Limpopo Belt. Chemical Geology 261, 230–243.

Ludwig, K.R., 2000. SQUID 1.00. A User Manual. Berkeley Geochronology Center, Special Publication, vol. 2. Berkeley, CA, 17 pp.

Ludwig, K.R., 2003. Isoplot 3.00: A Geochronological Toolkit for Microsoft Excel® (revised version) Berkeley Geochronological Center, Special Publication, vol. 4. Berkeley, CA, 70 pp.

Morel, M.L.A., Nebel, O., Nebel-Jacobsen, Y.J., Miller, J.S., Vroon, P.Z., 2008. Hafnium isotope characterization of the GJ-1 zircon reference material by solution and laser-ablation MC-ICPMS. Chem. Geol. 255, 231–235.

Santos, M.M., Lana, C., Scholz, R., Buick, I., Schmitz, M.D., Kamo, S.L., Gerdes, A., Corfu, F., Tapster, S., Lancaster, P., Storey, C.D., Basei, M.A.S., Tohver, E., Alkmim, A., Nalini, H., Krambrock, K., Fantini, C., Wiedenbeck, M., 2017. A new appraisal of Sri Lankan BB zircon as a reference material for LA-ICP-MS U-Pb geochronology and Lu-Hf isotope tracing. Geostandards and Geoanalytical Research 41, 335-358.

Sato, K., Basei, M.A.S., Sproesser, W.M., Siga Jr., O., 2012. The application of U–Pb geochronology to zircon and titanite by laser ablation—ICP-MS. The 8th International Conference on the Analysis of Geological and Environmental Materials, Annals, Búzios.

Woodhead J.D., Hergt J.M., 2005. A preliminary appraisal of seven natural zircon reference materials for in situ Hf isotope determination. Geostandards and Geoanalytical Research 29 (2), 183-195.

ELETRONIC APPENDIX 2A – MINERAL CHEMISTRY

Table 1 Representative electron microprobe analyses of biotite of the Esperança Complex. * Data from Sampaio (2005)

Pluton	Serrote da Cobra			Pocinhos			Areial			Puxinanã			Remígio		
Sample	ESP104	ESP104	ESP93	ESP75	ESP136	ESP136	JD07A	JD06	ESP08B*	ESP36A	ESP35	ESP35	ESP25C	ESP25B	ESP25E*
Spot	C2BT3	C5BT1	C9BT1	C1BT2	C2BT2	C7BT2	C5BT2	C3BT1	2/D1	C4BT01	C1BT02	C6BT01	C6BT1	C5BT3	7
wt.%															
SiO_2	35.76	33.80	36.04	32.79	35.45	35.41	36.27	38.87	37.27	36.59	35.57	33.71	35.06	33.92	36.62
TiO_2	2.31	2.66	2.15	3.55	3.85	3.04	1.66	0.55	1.92	2.45	3.09	3.27	2.43	2.69	0.95
Al_2O_3	15.61	14.60	14.79	13.75	14.28	14.39	13.99	12.85	14.92	13.65	14.71	15.10	15.83	15.52	14.89
FeO	21.74	25.87	23.09	32.31	24.19	23.01	19.44	12.70	20.39	23.06	26.62	26.81	24.85	26.64	18.81
MnO	0.40	0.20	0.27	0.25	0.45	0.34	0.28	0.13	0.28	0.36	0.23	0.36	0.16	0.29	0.33
MgO	8.68	8.27	8.56	1.86	7.60	7.94	11.38	16.52	1.01	8.14	6.74	6.01	6.28	5.29	11.45
CaO	0.00	0.03	0.00	0.03	0.01	0.04	0.03	0.00	0.00	0.05	0.01	0.01	0.04	0.02	0.11
Na_2O	0.12	0.16	0.09	0.00	0.09	0.07	0.08	0.09	0.07	0.18	0.11	0.06	0.05	0.06	0.12
K_2O	9.69	8.88	9.63	9.02	9.51	9.26	9.51	10.03	9.71	9.55	9.29	9.45	9.51	9.59	9.42
BaO	0.13	0.07	0.01	0.17	0.13	0.03	0.16	0.07	0.14	-	-	-	0.06	0.36	0.18
F	0.17	0.21	0.39	0.29	0.16	0.21	1.38	1.34	0.81	0.40	0.12	0.42	1.51	0.82	1.47
Cl	0.01	0.07	0.00	0.06	0.04	0.04	0.06	0.02	0.03	0.21	0.06	0.05	0.14	0.11	0.06
Cr_2O_3	0.05	0.00	0.03	0.03	0.00	0.01	0.01	0.03	0.02	0.01	0.13	0.10	0.10	0.03	0.00
NiO	0.00	0.00	0.01	0.00	0.07	0.05	0.06	0.04	-	0.00	0.03	0.06	0.00	0.00	NA
Li_2O*	0.71	0.15	0.79	0.00	0.62	0.61	0.86	1.60	1.14	0.95	0.66	0.12	0.51	0.18	0.96
H_2O*	3.79	3.64	3.67	3.42	3.77	3.69	3.18	3.35	3.19	3.60	3.79	3.53	3.05	3.30	3.17
SubTotal	99.17	98.60	99.52	97.52	100.21	98.14	98.35	98.20	90.90	99.19	101.16	99.06	99.55	98.83	98.53
O=F,Cl	0.07	0.10	0.16	0.13	0.07	0.10	0.59	0.57	0.35	0.22	0.07	0.19	0.67	0.37	0.63
Total	99.09	98.50	99.36	97.39	100.13	98.04	97.76	97.63	90.55	98.98	101.09	98.87	98.89	98.46	97.90
Structural formulae															
Si	5.54	5.40	5.60	5.50	5.52	5.58	5.65	5.84	6.25	5.71	5.52	5.40	5.53	5.47	5.66
Al ^{iv}	2.46	2.60	2.40	2.50	2.48	2.42	2.35	2.16	1.75	2.29	2.48	2.60	2.47	2.53	2.34
Alt	2.85	2.75	2.71	2.72	2.62	2.68	2.57	2.28	2.95	2.51	2.69	2.85	2.95	2.95	2.71
Al ^{vi}	0.40	0.15	0.31	0.22	0.13	0.26	0.22	0.11	1.20	0.22	0.21	0.26	0.48	0.42	0.37
Ti	0.27	0.32	0.25	0.45	0.45	0.36	0.19	0.06	0.24	0.29	0.36	0.39	0.29	0.33	0.11
Cr	0.01	0.00	0.00	0.00	0.00	0.00	0.00	0.00	0.00	0.00	0.02	0.01	0.01	0.00	0.00
Fe	2.82	3.46	3.00	4.53	3.15	3.03	2.53	1.60	2.86	3.01	3.45	3.59	3.28	3.59	2.43
Mn	0.05	0.03	0.04	0.04	0.06	0.05	0.04	0.02	0.04	0.05	0.03	0.05	0.02	0.04	0.04
Mg	2.01	1.97	1.98	0.46	1.76	1.87	2.64	3.70	0.25	1.89	1.56	1.44	1.48	1.27	2.64
Ni	0.00	0.00	0.00	0.00	0.01	0.01	0.01	0.00	NA	0.00	0.00	0.01	0.00	0.00	NA
Li*	0.44	0.10	0.49	0.00	0.39	0.39	0.54	0.97	0.77	0.60	0.41	0.08	0.32	0.12	0.60
Ca	0.00	0.01	0.00	0.01	0.00	0.01	0.00	0.00	0.00	0.01	0.00	0.00	0.01	0.00	0.02
Na	0.04	0.05	0.03	0.00	0.03	0.02	0.02	0.03	0.02	0.06	0.03	0.02	0.01	0.02	0.04
K	1.92	1.81	1.91	1.93	1.89	1.86	1.89	1.92	2.08	1.90	1.84	1.93	1.92	1.97	1.86
Ba	0.01	0.00	0.00	0.01	0.01	0.00	0.01	0.00	0.01	0.00	0.00	0.00	0.00	0.02	0.01
OH*	3.92	3.88	3.81	3.83	3.91	3.89	3.30	3.36	3.56	3.75	3.92	3.78	3.21	3.55	3.27
F	0.08	0.10	0.19	0.15	0.08	0.10	0.68	0.64	0.43	0.20	0.06	0.21	0.76	0.42	0.72
Cl	0.00	0.02	0.00	0.02	0.01	0.01	0.01	0.00	0.01	0.05	0.02	0.01	0.04	0.03	0.02
Fe/Fe+Mg	0.58	0.64	0.60	0.91	0.64	0.62	0.49	0.30	0.92	0.61	0.69	0.71	0.69	0.74	0.48

Table 2 Representative electron microprobe analyses of amphibole of the Esperança Complex. * Data from Sampaio (2005)

Pluton	Serrote da Cobra			Pocinhos			Areial			Puxinanã		
Sample	ESP93	ESP93	ESP93	ESP75	JD136	JD136	JD06	ESP17 *	ESP8B *	ESP36 A	ESP35	ESP27 *
Spot	C4anf 1	C8anf 1	C10anf 1	C2Anf 2	C5Anf 1	C6Anf 1	C8anf 1	3BD2	F1NDB	C9anf0 2	C5anf0 2	4/Bd
wt.%												
SiO_2	41.61	42.02	42.17	37.73	45.46	42.73	47.31	51.67	41.79	42.46	40.41	38.75
TiO_2	0.89	0.60	0.79	0.81	0.41	1.19	0.10	0.08	0.83	1.37	1.93	0.41
Al_2O_3	11.36	11.81	11.04	11.25	8.10	9.52	6.91	3.34	10.55	9.39	9.55	12.24
Cr_2O_3	0.04	0.09	0.00	0.01	0.07	0.03	0.16	0.00	0.01	0.01	0.03	0.00
Fe_2O_3	3.91	3.96	2.73	4.01	3.10	2.21	4.51	3.46	3.76	2.35	6.33	7.44
FeO	18.24	17.59	18.52	25.95	17.85	19.74	10.66	9.24	17.68	20.03	20.17	19.08
MnO	0.35	0.57	0.53	0.34	0.46	0.46	0.36	0.31	0.32	0.44	0.58	0.48
MgO	6.70	6.97	6.83	1.33	8.30	6.78	13.14	15.53	7.65	6.65	5.38	4.85
NiO	0.00	0.05	0.00	0.00	0.07	0.04	0.00	0.00	0.00	0.05	0.02	NA
CaO	11.52	11.57	11.48	10.80	11.74	11.60	11.73	12.03	11.69	11.43	11.19	11.38
Na_2O	1.02	1.21	1.11	1.36	0.94	1.04	1.19	0.71	1.26	1.22	1.40	1.34
K_2O	1.47	1.41	1.41	1.70	0.78	1.18	1.01	0.31	1.46	1.29	1.33	1.62
F	0.15	0.21	0.08	0.26	0.18	0.06	1.04	NA	NA	0.28	0.00	NA
Cl	0.00	0.02	0.05	0.08	0.02	0.02	0.03	NA	NA	0.09	0.05	NA
H_2O*	1.87	1.86	1.89	1.67	1.88	1.89	1.53	2.06	1.94	1.77	1.91	1.91
Subtotal	99.20	99.95	98.63	97.30	99.35	98.53	99.66	98.74	98.94	98.83	100.29	99.49
O=F,Cl	0.06	0.09	0.05	0.13	0.08	0.03	0.44	0.00	0.00	0.14	0.01	0.00
Total	99.13	99.86	98.59	97.18	99.27	98.50	99.22	98.74	98.94	98.69	100.28	99.49
Structural formulae												
Si	6.43	6.42	6.53	6.24	6.92	6.65	7.00	7.51	6.46	6.62	6.31	6.09
Al ^{iv}	1.57	1.58	1.47	1.76	1.08	1.35	1.00	0.49	1.54	1.38	1.69	1.91
Al ^{vi}	0.49	0.55	0.54	0.43	0.37	0.39	0.21	0.09	0.38	0.34	0.06	0.36
Ti	0.10	0.07	0.09	0.10	0.05	0.14	0.01	0.01	0.10	0.16	0.23	0.05
Cr	0.01	0.01	0.00	0.00	0.01	0.00	0.02	0.00	0.00	0.00	0.00	0.00
Fe^{3+}	0.45	0.45	0.32	0.50	0.36	0.26	0.50	0.38	0.44	0.28	0.74	0.88
Fe^{2+}	2.36	2.25	2.40	3.59	2.27	2.57	1.32	1.12	2.28	2.61	2.63	2.51
Mn	0.05	0.07	0.07	0.05	0.06	0.06	0.04	0.04	0.04	0.06	0.08	0.06
Mg	1.54	1.59	1.58	0.33	1.88	1.57	2.90	3.37	1.76	1.55	1.25	1.14
Ni	0.00	0.01	0.00	0.00	0.01	0.01	0.00	0.00	0.00	0.01	0.00	NA
Ca	1.91	1.89	1.90	1.91	1.91	1.93	1.86	1.87	1.94	1.91	1.87	1.92
Na	0.30	0.36	0.33	0.44	0.28	0.31	0.34	0.20	0.38	0.37	0.42	0.41
K	0.29	0.27	0.28	0.36	0.15	0.23	0.19	0.06	0.29	0.26	0.26	0.32
F	0.07	0.10	0.04	0.13	0.09	0.03	0.48	NA	NA	0.14	0.00	NA
Cl	0.00	0.01	0.01	0.02	0.00	0.00	0.01	NA	NA	0.02	0.01	NA
OH*	1.93	1.89	1.95	1.84	1.91	1.96	1.51	2.00	2.00	1.84	1.99	2.00
Total	17.50	17.53	17.52	17.71	17.34	17.48	17.39	17.13	17.60	17.53	17.56	17.65
Na $_{(B)}$	0.09	0.11	0.10	0.09	0.09	0.07	0.14	0.13	0.06	0.09	0.13	0.08
(Na+K) $_{(A)}$	0.50	0.53	0.52	0.71	0.34	0.48	0.39	0.13	0.60	0.53	0.56	0.65
Mg/(Mg+Fe^{2+})	0.40	0.41	0.40	0.08	0.45	0.38	0.69	0.75	0.44	0.37	0.32	0.31
Fe/(Fe+Mg)	0.65	0.63	0.63	0.93	0.58	0.64	0.39	0.31	0.61	0.65	0.73	0.75

Table 3 Representative electron microprobe analyses of feldspars (Pl: plagioclase; Kf: K-feldspar) of the Esperança Complex. * Data from Sampaio (2005)

Pluton	Serrote da Cobra			Pocinhos			Areial				Puxinanã				Remígio		
Sample	ESP104	ESP104	ESP100*	ESP75	ESP33*	ESP75*	ESP8B*	ESP17*	JD07A	JD07A	ESP35*	ESP35	ESP36A	ESP27*	ESP25E*	ESP25E*	ESP25E*
Spot	C2pl1	C3pl1	617N	C4Pl 1	1BD	2.6B	FD1BFII	5Bd	C4pl1	C3kf1.5	1Bd3	C6pl01	C3pl01	1Bd	1Nc	2Bd	2Nc
Mineral	Pl	Pl	Pl	Pl	Pl	Pl	Pl	Pl	Pl	Kf	Pl	Pl	Pl	Kf	Pl	Pl	Pl
wt.%																	
SiO_2	59.99	59.77	57.73	63.03	60.55	67.82	60.89	65.00	62.43	61.44	62.55	57.64	61.79	64.05	61.00	56.63	54.75
TiO_2	0.04	0.00	0.00	0.06	0.00	0.02	0.00	0.04	0.00	0.00	0.03	0.00	0.03	0.00	0.04	0.07	0.00
Al_2O_3	25.98	25.63	26.75	21.49	24.80	19.53	22.71	22.33	22.30	17.58	22.63	24.89	24.35	18.33	24.05	27.00	28.23
FeO	0.04	0.07	0.04	0.04	0.04	0.03	0.01	0.16	0.10	0.05	0.12	0.03	0.05	0.13	0.05	0.01	0.12
MnO	0.04	0.00	0.00	0.07	0.02	0.00	0.00	0.00	0.03	0.03	0.00	0.00	0.00	0.00	0.04	0.00	0.01
MgO	0.00	0.00	0.00	0.00	0.01	0.00	0.00	0.03	0.01	0.00	0.00	0.01	0.00	0.00	0.01	0.00	0.00
CaO	7.79	7.61	9.07	3.58	6.31	0.40	5.10	3.36	4.07	0.03	4.16	6.21	4.99	0.00	5.72	8.78	10.44
BaO	0.01	0.00	0.00	0.04	0.00	0.00	0.00	0.13	0.07	0.80	0.04	0.00	0.00	0.57	0.00	0.00	0.00
Na_2O	7.18	7.34	6.60	9.19	7.89	11.43	7.57	8.87	8.58	0.95	8.85	7.99	8.07	0.78	7.87	6.24	5.44
K_2O	0.31	0.18	0.11	0.33	0.24	0.01	0.18	0.38	0.40	14.83	0.19	0.15	0.21	15.40	0.14	0.07	0.07
Total	101.37	100.59	100.30	97.82	99.86	99.24	96.46	100.30	97.97	95.72	98.57	96.92	99.50	99.26	98.92	98.80	99.06
Structural formulae																	
Si	2.22	2.23	2.17	2.38	2.27	2.51	2.33	2.40	2.36	2.47	2.35	2.22	2.31	2.49	2.29	2.15	2.08
Ti	0.00	0.00	0.00	0.00	0.00	0.00	0.00	0.01	0.00	0.00	0.00	0.00	0.00	0.00	0.00	0.00	0.00
Al	1.14	1.13	1.18	0.96	1.09	0.85	1.02	0.97	0.99	0.83	1.00	1.13	1.07	0.84	1.07	1.21	1.27
Mn	0.00	0.00	0.00	0.00	0.00	0.00	0.00	0.00	0.00	0.00	0.00	0.00	0.00	0.00	0.00	0.00	0.00
Mg	0.00	0.00	0.00	0.00	0.00	0.00	0.00	0.00	0.00	0.00	0.00	0.00	0.00	0.00	0.00	0.00	0.00
Ca	0.31	0.30	0.37	0.14	0.25	0.02	0.21	0.13	0.16	0.00	0.17	0.26	0.20	0.00	0.23	0.36	0.43
Ba	0.00	0.00	0.00	0.00	0.00	0.00	0.00	0.00	0.00	0.01	0.00	0.00	0.00	0.01	0.00	0.00	0.00
Na	0.52	0.53	0.48	0.67	0.57	0.82	0.56	0.64	0.63	0.07	0.65	0.60	0.58	0.06	0.57	0.46	0.40
K	0.01	0.01	0.01	0.02	0.01	0.00	0.09	0.02	0.02	0.76	0.01	0.01	0.01	0.76	0.01	0.00	0.00
Or	1.73	1.00	0.62	1.89	1.36	0.06	1.13	2.28	2.39	90.99	1.10	0.87	1.28	92.85	0.82	0.41	0.41
An	36.83	36.05	42.89	17.36	30.23	1.90	26.82	16.91	20.26	0.18	20.39	29.80	25.13	0.00	28.41	43.56	51.25
Ab	61.44	62.95	56.49	80.75	68.40	98.05	72.05	80.80	77.34	8.84	78.50	69.34	73.58	7.15	70.75	56.02	48.33

Table 4 Representative electron microprobe analyses of titanite of the Esperança Complex. * Data from Sampaio (2005)

Pluton	Serrote da Cobra			Pocinhos	Areial			Puxinanã			Remígio		
Sample	ESP07	JD07A	JD07A	ESP75	JD06	JD06	JD06	ESP35	ESP36A	ESP36A	JD07A	JD07A	ESP25E*
Spot	C6ttn1	C5ttn1	C6ttn1	C2Ttn1	C4ttn1	C5ttn1	C7ttn1	C7ttn01	C5ttn01	C5ttn02	C5ttn1	C6ttn1	-1
wt.%													
SiO_2	29.75	29.10	30.37	28.72	29.43	30.91	29.28	30.43	30.48	29.69	29.10	30.37	30.01
TiO_2	34.98	34.92	33.35	32.49	33.25	32.97	37.60	37.01	34.93	34.57	34.92	33.35	34.54
Al_2O_3	2.71	1.81	2.45	3.30	1.44	3.45	1.36	1.98	1.94	2.13	1.81	2.45	3.08
FeO	1.14	1.38	1.37	1.10	1.56	1.61	1.28	0.42	1.05	1.11	1.38	1.37	0.82
MnO	0.11	0.16	0.00	0.13	0.08	0.08	0.04	0.05	0.06	0.08	0.16	0.00	0.08
MgO	0.09	0.04	0.01	0.01	0.04	0.02	0.04	0.07	0.04	0.02	0.04	0.01	0.01
CaO	27.28	27.00	28.28	26.78	27.62	28.33	26.60	28.22	27.12	27.31	27.00	28.28	28.85
F	0.86	0.64	1.15	0.93	0.38	1.80	0.17	1.21	0.11	1.15	0.64	1.15	1.14
Cr_2O_3	0.00	0.00	0.00	0.14	0.06	0.29	0.00	0.00	0.01	0.00	0.00	0.00	0.00
NiO	0.00	0.00	0.01	0.00	0.04	0.00	0.00	0.00	0.00	0.00	0.00	0.01	0.00
Total	96.92	95.04	97.00	93.59	93.88	99.44	96.37	99.40	95.73	96.05	95.04	97.00	98.53
Structural formulae													
Si	1.01	1.00	1.03	1.01	1.03	1.03	0.99	1.01	1.03	1.02	1.00	1.03	1.00
Al^{iv}	0.11	0.07	0.10	0.14	0.06	0.14	0.05	0.08	0.08	0.09	0.07	0.10	0.12
Ti	0.89	0.91	0.85	0.86	0.87	0.82	0.96	0.92	0.89	0.89	0.91	0.85	0.87
Cr	0.00	0.00	0.00	0.00	0.00	0.01	0.00	0.00	0.00	0.00	0.00	0.00	0.00
Fe^{3+}	0.03	0.04	0.04	0.03	0.05	0.04	0.04	0.01	0.03	0.03	0.04	0.04	0.02
Mn	0.00	0.00	0.00	0.00	0.00	0.00	0.00	0.00	0.00	0.00	0.00	0.00	0.00
Mg	0.00	0.00	0.00	0.00	0.00	0.00	0.00	0.00	0.00	0.00	0.00	0.00	0.00
Ni	0.00	0.00	0.00	0.00	0.00	0.00	0.00	0.00	0.00	0.00	0.00	0.00	0.00
Ca	0.99	1.00	1.03	1.01	1.03	1.01	0.96	1.00	0.99	1.00	1.00	1.03	1.03

Table 5 Representative electron microprobe analyses of oxydes of the Esperança Complex**.**

Pluton	Pocinhos			Remígio			Puxinanã			Areial	
Sample	ESP75	JD136	JD136	ESP25C	ESP25B	ESP25A	JD49B	JD49B	JD49B	JD07A	JD07A
Spot	C3Ox1	C6ox1	C10ox1	C7ox1	C1ox1	C1Ox1	C2ox1	C4C1ox1	C4C1ox2	C6ox1	C6ox2
wt.%											
SiO_2	0.05	0.05	0.05	0.06	0.05	0.02	0.05	0.04	0.05	0.03	0.07
TiO_2	51.96	54.10	53.54	53.15	48.18	50.99	57.13	53.45	55.34	0.05	0.24
Al_2O_3	0.03	0.00	0.01	0.00	0.00	0.01	0.00	0.01	0.02	0.04	0.01
MnO	3.41	3.70	1.65	2.53	2.54	2.04	2.65	2.55	2.30	0.00	0.03
MgO	0.03	0.26	0.07	0.00	0.01	0.02	0.12	0.01	0.14	0.00	0.00
CaO	0.04	0.01	0.06	0.00	1.15	0.03	0.08	0.00	0.03	0.00	0.00
Na_2O	0.00	0.00	0.01	0.00	0.04	0.00	0.04	0.00	0.04	0.00	0.00
K_2O	0.00	0.02	0.02	0.03	0.01	0.00	0.01	0.00	0.00	0.00	0.01
Cr_2O_3	0.08	0.11	0.00	0.01	0.00	0.00	0.06	0.00	0.05	0.08	0.00
V_2O_3	0.45	0.39	0.60	0.39	0.40	0.40	0.00	0.03	0.00	0.17	0.05
NiO	0.00	0.00	0.05	0.39	0.40	0.40	0.00	0.00	0.00	0.01	0.05
Fe_2O_3	2.10	0.00	0.00	1.45	7.84	4.21	0.00	0.00	0.00	68.32	68.49
FeO	43.25	43.25	45.84	44.83	38.76	43.37	39.64	40.31	39.96	31.04	31.30
Total	101.37	101.87	101.88	102.84	99.36	101.48	99.77	96.39	97.93	99.73	100.24
Structural formulae											
Ti	0.97	1.01	1.00	0.98	0.92	0.96	1.09	1.06	1.08	0.00	0.01
Cr	0.00	0.00	0.00	0.00	0.00	0.00	0.00	0.00	0.00	0.00	0.00
V	0.01	0.01	0.01	0.01	0.01	0.01	0.00	0.00	0.00	0.01	0.00
Fe^{3+}	0.04	0.00	0.00	0.03	0.15	0.08	0.00	0.00	0.00	1.99	1.98
Fe^{2+}	0.90	0.89	0.95	0.92	0.82	0.90	0.84	0.89	0.86	1.00	1.00
Mn	0.07	0.08	0.03	0.05	0.05	0.04	0.06	0.06	0.05	0.00	0.00
Ni	0.00	0.00	0.00	0.01	0.01	0.01	0.00	0.00	0.00	0.00	0.00
%Ilm or Mag	90.26	89.09	94.86	92.36	83.25	90.63	80.62	86.12	83.29	99.38	98.97

ELETRONIC APPENDIX 2B – TRACE-ELEMENTS DATA OF ZIRCON

Table 1 Trace elements composition of zircon crystals from the Pocinhos Pluton granitoids (ESP-72 sample - results obtained from LA-ICPMS analyses).

Element	Pt1	Pt2	Pt3	Pt4	Pt5N	Pt5B	Pt6	Pt7	Pt8	Pt9	Pt10	Pt11	Pt12	Pt13	Pt14
Li	2.02	<0.37	1.21	1.64	<0.36	<0.40	<0.38	0.70	0.63	1.37	0.60	0.43	1.42	0.45	<0.39
Sc	188.60	198.9	194.27	205.13	202.61	200.42	207.73	208.13	197.87	203.92	198.97	199.66	217.84	210.98	205.08
Ti	<7.81	<7.12	<6.12	10.00	7.09	9.05	9.16	6.18	9.75	12.51	8.97	<5.71	<5.44	8.99	15.88
Sr	0.310	0.259	0.176	2.06	0.227	0.187	0.109	0.316	0.172	0.195	0.289	0.353	0.258	0.316	0.147
Zr	496007.16	496007.16	496007.16	496007.16	496007.16	496007.13	496007.13	496007.16	496007.16	496007.09	496007.09	496007.09	496007.06	496007.06	496007.09
Ba	<0.70	<0.66	0.63	<0.62	<0.58	<0.49	<0.59	<0.74	<0.47	0.86	<0.58	<0.76	<0.72	<0.66	<0.76
La	1.10	<0.081	0.072	<0.073	<0.085	<0.112	<0.091	<0.098	<0.097	2.99	0.083	0.433	0.312	0.103	<0.081
Ce	17.96	4.77	7.89	4.22	7.31	9.04	2.92	7.94	5.33	36.77	9.04	6.13	13.51	5.65	4.25
Pr	0.731	0.081	0.187	0.261	0.218	0.153	<0.072	0.210	<0.080	0.883	0.191	0.208	0.454	0.243	0.254
Nd	6.41	2.15	3.14	3.60	4.06	2.96	2.38	4.27	0.97	6.89	3.28	3.18	6.67	3.43	3.49
Sm	6.97	6.20	7.02	5.90	8.28	6.46	3.63	8.04	2.40	10.25	8.91	5.42	9.47	4.28	7.82
Eu	1.00	0.84	0.81	1.33	0.86	0.72	0.77	1.36	0.54	1.21	0.94	0.87	1.23	0.83	1.20
Gd	29.20	31.11	34.58	28.96	34.59	34.55	19.83	33.50	15.12	41.24	36.85	28.50	42.85	20.28	28.82
Tb	8.54	9.44	10.53	8.75	10.94	11.97	6.68	10.64	5.78	13.14	12.30	8.92	14.30	7.65	9.75
Dy	90.90	99.18	113.81	91.85	119.35	127.45	68.80	113.93	62.63	134.35	136.14	95.54	150.93	75.54	99.70
Ho	31.24	33.41	38.56	30.31	37.95	42.31	23.61	37.94	22.70	46.18	45.34	31.44	50.41	26.62	34.20
Er	132.84	136.09	153.89	124.23	154.97	172.86	94.31	153.08	95.86	181.35	184.50	129.25	203.80	106.97	133.07
Tm	25.20	25.88	28.60	23.06	29.17	31.98	18.40	28.96	19.32	32.92	33.53	25.29	37.59	20.81	25.58
Yb	221.34	217.23	245.46	207.13	253.94	277.12	158.97	247.71	169.83	295.17	290.79	221.77	331.57	188.65	222.00
Lu	40.77	41.49	46.30	37.30	47.55	51.50	29.73	47.48	33.64	53.03	54.66	41.77	60.94	35.64	41.07
Hf	10667.30	8924.25	9246.70	9191.04	9549.87	9974.45	8952.22	9048.20	10076.64	9646.97	9988.77	10017.12	10350.60	9409.98	9047.15
Th	166.21	53.92	93.77	43.05	74.16	111.22	27.31	73.05	38.54	91.74	110.24	53.28	164.37	44.83	57.81
U	463.66	110.52	189.66	133.87	142.52	232.55	64.60	135.55	106.98	170.91	221.91	116.63	331.70	95.09	102.61
Eu/Eu*	0.22	0.19	0.16	0.31	0.16	0.15	0.28	0.25	0.27	0.18	0.16	0.21	0.19	0.27	0.24
Ce/Ce*	4.69	-	15.80	-	-	-	-	-	-	5.30	16.71	4.78	8.42	8.37	-
Th/U	0.36	0.49	0.49	0.32	0.52	0.48	0.42	0.54	0.36	0.54	0.50	0.46	0.50	0.47	0.56
Zr/Hf	46.50	55.58	53.64	53.97	51.94	49.73	55.41	54.82	49.22	51.42	49.66	49.52	47.92	52.71	54.82

Table 2 Trace elements composition of zircon crystals from the Puxinanã Pluton granitoids (ESP-36A sample - results obtained from LA-ICPMS analyses).

Element	Pt1	Pt2B	Pt2N	Pt3	Pt5	Pt6	Pt7	Pt8	Pt9	Pt10	Pt11	Pt12	Pt13
Li	19.77	104.33	116.6	14.62	8.83	6.78	10.44	4.69	22.69	5.16	8.44	4.18	5.63
Sc	176.13	217.47	215.45	170.67	156.46	158.89	161.73	160.06	165.95	147.23	158.5	146.37	156.37
Ti	65.31	260.25	57.99	51.86	55.8	49.37	20.34	16.05	41.6	26.57	25.32	20.14	20.25
Sr	3	25.61	3.38	1.06	1.93	2.75	0.512	2.9	2.39	0.322	0.7	4.66	0.377
Zr	496007	496007	496007	496007	496007	496007	496007	496007	496007	496007	496007	496007	496007
Ba	3.09	9.77	1.85	1.32	1.65	1.53	<0,64	2.18	1.5	<0,65	1.08	<0,97	<0,77
La	33.74	28.99	8.75	16.97	29.6	12.88	6.95	1.76	16.81	6.85	6.52	9.61	2.69
Ce	144.36	79.81	31.82	100.49	103.64	35.92	54.95	23.39	76.52	18.24	44.19	26.37	22.89
Pr	22.54	8.01	2.82	17.98	15.89	4.64	7.69	1.77	9.24	1.17	5.41	2.72	3.27
Nd	186.28	50.5	19.34	136.94	135.98	36.98	69.83	17.19	78.91	7.86	46.19	16.76	25.63
Sm	109.48	32.94	17.33	76.33	82.93	18.53	46.07	13.04	48.04	3.41	29.05	9.33	16.79
Eu	14.71	4.12	2.08	11.6	10.42	2.91	6.48	1.87	7.8	0.64	4.47	1.29	2.04
Gd	126.61	53.77	50.52	79.02	79.44	24.7	60.78	27.57	55.1	7.13	40.62	11.11	23.23
Tb	21.72	12.72	15.68	12.91	11.95	4.31	12.6	7.97	10.03	1.84	7.65	1.87	4.33
Dy	182.07	125.31	163.4	107.2	89.49	38.04	111.5	79	86.41	19.8	69.41	18.69	37.55
Ho	55.31	44.8	56.15	32.06	26.81	12.91	36.25	27.46	27.81	7.9	22.01	6.63	14.4
Er	208.82	185.91	231.99	122.55	103.66	54.62	141.78	114.61	112.38	33.92	92.09	32.53	62.68
Tm	40.13	40.28	49.23	24.46	20.35	11.71	29.05	23.23	22.36	8.65	19.52	7.52	13.11
Yb	360.96	381.1	465.27	219.69	190.82	113.9	253.9	233.4	213.77	86.23	183.07	70.18	134.49
Lu	62.34	74.69	84.58	40.91	35.35	22.34	47.19	42.57	39.81	17.91	34.94	15.11	27.46
Hf	9777.88	12855.6	12058.7	10368	10466	11490.8	10232.2	9941.62	10038.5	12542.5	10357.9	11364.1	9821.43
Th	1467.59	563.65	649.28	713.52	573.78	251.68	752.4	460.27	677.1	98.29	424.62	74.09	293.7
U	1136.34	3268.21	3474.36	685.34	572.99	430.01	956.7	608.44	741.39	358.31	568.66	288.67	450.31
Eu/Eu*	0.38	0.30	0.21	0.46	0.39	0.42	0.37	0.30	0.46	0.40	0.40	0.39	0.32
Ce/Ce*	1.23	1.23	1.50	1.35	1.12	1.09	1.76	3.11	1.44	1.51	1.74	1.21	1.81
Th/U	1.29	0.17	0.19	1.04	1.00	0.59	0.79	0.76	0.91	0.27	0.75	0.26	0.65
Zr/Hf	50.73	38.58	41.13	47.84	47.39	43.17	48.47	49.89	49.41	39.55	47.89	43.65	50.50

Table 3 Trace elements composition of zircon crystals from the Remígio Pluton granitoids (ESP-25C sample - results obtained from LA-ICPMS analyses).

Element	Pt1	Pt2	Pt3	Pt5	Pt6	Pt7B	Pt7N	Pt8	Pt9	Pt10	Pt11	Pt12	Pt13	Pt14
Li	2.38	2.34	1.37	4.98	1.69	0.252	0	1.31	3.39	3.63	0.923	3.3	2.43	2.15
Sc	34.84	30.85	29.81	36.4	32.72	22.85	24.83	27.09	29.05	32.11	29.58	28.58	29.66	30.9
Ti	0.0388	0.083	0.0278	0.0461	8.29	0.0061	0	0.0109	0.0526	0.764	0.0086	0.0262	0.0296	0.0857
Sr	0.172	0.067	0.094	0.395	0.0703	0.0151	0.0219	0.044	0.265	0.151	0.147	0.125	0.0626	0.56
Zr	89532	89532	89532	89532	89532	89532	89532	89532	89532	89532	89532	89532	89532	89532
Ba	0.28	0	0.65	0.95	0	0	0	0	0.167	0.39	0	0.3	0	2.41
La	26.33	7.19	24.74	30.73	7.35	0	0	4.18	60.4	70.24	11.05	35.39	19.08	98.51
Ce	59.37	24.44	61.48	86.32	20.73	3.48	9.07	13.39	123.14	69.5	26.81	33.9	37.27	149.93
Pr	61.27	21.93	68.73	110.12	16.51	0	0	9.16	134.05	71.76	21.25	21.64	32.99	178.8
Nd	82.04	28.09	78.41	145.47	26.18	0	1.06	15.18	151.77	81.72	41.37	32.42	42.97	232.35
Sm	241.93	98.36	129.96	352.39	92.2	3.84	12.69	53.61	389.17	185.08	102.33	89.74	116.92	531.99
Eu	39.72	15.78	14.9	89.57	10.29	2.81	8.09	7.18	56.8	22.13	4.56	8.84	15.36	111.18
Gd	345.8	201.2	178.56	401.04	186.76	15.58	53.05	93.81	397.76	301.37	210.77	178.88	218.93	555.51
Tb	473.75	301.58	218.96	431.82	268.53	25.22	110.42	160.64	482.23	403.09	304.77	268.63	312.9	585.63
Dy	595.52	429.35	312.28	472.36	397.17	54.66	205.06	250.69	558	549.9	429.55	409.9	417.96	663.86
Ho	774.31	605.55	444.89	584.01	560.83	86.72	360.24	353.05	669.16	744.94	600.55	578.12	614	765.28
Er	987.87	821.28	605.34	796.6	765.4	140.72	598.58	489.12	846.33	1004.17	772.65	772.24	826.94	932.14
Tm	1331.31	1109.17	873.44	1153.76	1038.05	219.79	951.2	693.14	1096.35	1294.07	1016.27	1053.36	1073.25	1177.5
Yb	1739.95	1454.6	1140.82	1663.83	1330.39	370.16	1419.4	911.03	1391.53	1687.22	1260.64	1364.83	1436.32	1468.65
Lu	2014.8	1729.37	1400.31	2113.84	1630.31	503.42	2066.81	1132.29	1667.63	1953.73	1518.89	1650.22	1741.8	1747.63
Hf	61584.7	63672.6	60258.1	70519.4	63332.5	64793.2	61288.3	65774.7	67518.7	61834.3	64074.1	65426.8	64393	63662.2
Th	14421.1	8375.48	7169.92	4158.31	7765.57	376.16	1204.77	4635.61	11075.2	13985.1	10191.9	8808.85	9687.36	13195.7
U	55270.8	43258.3	30410.1	79043.2	32975.5	7771.42	11144.1	22112	69892.6	76350.1	32095.3	36613	37033.8	53091.8
Eu/Eu*	0.14	0.11	0.10	0.24	0.08	0.36	0.31	0.10	0.14	0.09	0.03	0.07	0.10	0.20
Ce/Ce*	1.48	1.95	1.49	1.48	1.88	-	-	2.16	1.37	0.98	1.75	1.22	1.49	1.13
Th/U	0.91	0.67	0.82	0.18	0.82	0.17	0.38	0.73	0.55	0.64	1.11	0.84	0.91	0.87
Zr/Hf	44.99	43.52	45.99	39.29	43.75	42.77	45.21	42.13	41.04	44.81	43.25	42.35	43.03	43.53

Table 4 Trace elements composition of zircon crystals from the Serrote da Cobra Pluton granitoids (ESP-98 sample - results obtained from LA-ICPMS analyses).

Element	Pt1	Pt2	Pt3	Pt4	Pt5	Pt6	Pt7	Pt8	Pt9	Pt10	Pt11	Pt12	Pt13	Pt14	Pt15
Li	3.79	3.90	3.36	1.95	6.28	3.14	4.81	3.33	6.76	2.98	2.31	2.87	7.90	4.15	3.09
Sc	200.34	207.53	198.65	216.34	243.40	206.20	210.44	171.25	182.16	192.53	210.72	191.91	215.39	197.72	168.68
Ti	<6.15	<6.18	<5.85	11.87	14.03	<5.70	<5.66	<5.72	28.82	<5.51	7.48	<5.62	<5.38	8.20	<5.08
Sr	0.169	0.347	0.177	0.271	1.33	0.217	0.490	0.117	2.52	0.297	0.176	0.273	0.310	0.250	0.184
Zr	496007.09	496007.09	496007.13	496007.09	496007.09	496007.06	496007.13	496007.16	496007.16	496007.16	496007.13	496007.16	496007.13	496007.16	496007.13
Ba	<0.78	<0.52	<0.57	0.90	1.81	<0.50	1.15	<0.51	3.93	<0.51	<0.57	<0.58	<0.82	<0.51	<0.52
La	<0.063	0.803	<0.064	2.05	24.29	0.178	1.89	0.197	33.44	<0.072	2.65	0.645	1.04	2.73	<0.056
Ce	4.90	17.99	5.32	52.23	91.39	8.35	18.74	5.08	204.63	7.07	17.43	12.94	9.74	21.29	3.27
Pr	<0.063	0.821	0.064	1.64	9.55	0.144	1.60	0.188	14.78	0.094	1.01	0.610	0.625	2.05	0.042
Nd	<0.52	6.85	1.37	16.63	57.29	2.50	13.05	1.77	87.77	1.53	7.94	5.59	4.13	12.47	<0.55
Sm	1.06	5.02	1.66	14.71	23.98	2.45	11.44	1.07	41.38	3.76	4.95	3.87	4.12	8.15	0.84
Eu	0.449	1.29	0.66	3.68	5.66	0.80	2.81	0.53	10.55	0.55	2.18	1.85	1.15	2.16	0.49
Gd	9.32	13.29	11.47	46.11	38.10	12.16	29.85	4.52	66.43	17.15	16.77	11.53	14.90	16.62	7.90
Tb	3.39	4.86	4.09	13.24	9.18	5.23	8.73	1.94	15.69	5.74	5.27	3.99	6.61	5.21	2.67
Dy	47.97	63.09	51.10	123.29	96.07	59.38	92.68	21.13	140.79	68.79	55.37	46.63	92.21	56.51	34.96
Ho	17.66	25.98	19.14	37.22	34.80	21.36	32.07	8.75	46.63	25.89	19.27	18.94	38.14	22.13	13.74
Er	87.36	133.10	90.08	148.89	160.57	102.30	143.17	40.44	205.93	114.53	88.33	87.61	188.81	106.43	63.39
Tm	19.62	30.43	20.32	28.32	34.49	22.89	29.46	9.68	41.78	25.48	19.15	19.69	44.46	24.21	14.59
Yb	206.95	334.44	204.70	257.91	353.53	229.41	303.77	95.53	405.87	264.35	194.56	193.24	455.60	257.92	159.57
Lu	44.48	76.21	43.10	49.30	76.23	49.17	62.14	21.19	81.96	54.88	40.59	41.03	96.59	56.12	33.82
Hf	12228.38	14578.62	11281.48	11067.62	11355.46	10663.82	11346.50	12739.93	14891.71	11810.81	10399.32	13095.56	13670.89	14119.74	11112.61
Th	60.86	47.12	92.45	189.86	99.87	89.2	129.42	26.94	90.45	132.48	71.59	42.41	61.07	59.55	42.72
U	337.44	763.8	344.92	430.92	711.57	306.05	440.84	198.43	930.24	514.16	203.8	363.78	1070.06	741.96	279.83
Eu/Eu*	0.44	0.48	0.46	0.43	0.57	0.45	0.46	0.73	0.62	0.21	0.73	0.85	0.45	0.57	0.58
Ce/Ce*	-	5.19	-	6.67	1.41	12.17	2.53	6.15	2.16	-	2.50	4.83	2.84	2.11	-
Th/U	0.18	0.06	0.27	0.44	0.14	0.29	0.29	0.14	0.10	0.26	0.35	0.12	0.06	0.08	0.15
Zr/Hf	40.56	34.02	43.97	44.82	43.68	46.51	43.71	38.93	33.31	42.00	47.70	37.88	36.28	35.13	44.63

Table 5 Trace elements composition of zircon crystals from the Areial Pluton granitoids (JD-06A sample - results obtained from LA-ICPMS analyses).

Element	Pt1	Pt2	Pt3	Pt4	Pt5	Pt6	Pt7	Pt8	Pt9	Pt11	Pt12	Pt13n	Pt13b
Li	2.41	4.56	4.88	11.41	4.02	2.72	4.52	2.03	4.94	1.60	1.89	4.37	8.03
Sc	168.61	280.02	248.18	245.22	224.08	227.98	274.42	175.02	251.43	308.74	181.13	293.18	550.25
Ti	<3.95	135.86	151.83	120.26	60.17	70.26	113.92	6.56	115.91	140.49	8.17	174.15	3122.75
Sr	0.319	12.80	39.54	9.15	5.24	5.83	12.82	2.68	13.21	7.23	3.62	22.12	54.53
Zr	496006.97	496006.97	496007.03	496007.03	496007.03	496007.03	496007.06	496007.06	496007.06	496007.06	496007.09	496007.16	496007.16
Ba	<0.47	17.27	29.66	11.77	6.38	7.55	13.72	<0.75	13.21	7.60	<0.56	21.59	65.35
La	0.157	20.94	27.04	19.66	13.43	16.31	21.47	2.59	38.46	28.51	4.40	33.90	98.68
Ce	53.82	195.21	279.71	183.47	132.72	158.55	231.40	70.38	320.97	351.06	77.12	334.55	888.48
Pr	0.472	32.50	44.11	32.69	19.92	26.02	41.72	2.83	46.83	54.74	2.92	59.49	168.43
Nd	6.50	224.36	274.81	225.90	141.67	172.27	287.00	19.41	308.91	361.91	18.32	373.63	1040.12
Sm	7.18	144.20	181.36	138.54	100.81	109.79	196.29	16.76	210.52	227.61	17.48	254.79	621.22
Eu	1.72	56.91	64.35	50.73	35.99	37.09	68.16	5.06	70.86	75.79	4.86	89.52	212.05
Gd	25.51	189.63	202.68	148.21	116.72	120.23	206.76	40.21	226.81	270.35	36.01	281.14	640.88
Tb	7.31	44.61	42.24	28.05	25.07	23.70	41.26	10.32	47.13	54.60	8.85	54.21	119.89
Dy	63.13	282.81	278.90	173.08	169.10	163.11	273.41	90.65	320.46	371.65	75.26	338.03	732.19
Ho	20.57	69.53	64.20	39.27	42.80	39.37	60.99	29.22	73.79	91.68	24.62	79.54	161.20
Er	85.02	238.20	214.29	125.33	150.89	141.64	209.89	109.14	246.47	299.58	99.44	259.09	513.15
Tm	17.06	46.21	40.99	22.85	29.70	27.46	38.66	22.74	44.47	54.92	19.51	47.36	90.91
Yb	154.92	433.28	364.99	208.01	267.88	264.10	358.07	210.93	392.15	469.40	189.35	424.88	798.77
Lu	28.68	72.02	63.46	35.97	50.41	50.21	60.41	38.61	64.19	80.72	37.49	74.14	133.99
Hf	10196.59	11850.28	10899.44	12986.55	11628.79	11917.73	10604.20	10278.43	11507.13	10986.52	10901.60	11078.30	12632.02
Th	282.26	558.92	836.42	949.77	542.93	540.93	639.21	413.57	1251.70	1160.19	356.93	736.26	1451.32
U	429.99	1304.95	1344.19	1398.85	941.24	1053.81	1071.35	651.20	1123.31	909.58	636.03	1274.27	2533.14
Eu/Eu*	0.39	1.05	1.03	1.08	1.01	0.99	1.03	0.60	0.99	0.93	0.59	1.02	1.03
Ce/Ce*	46.17	1.75	1.90	1.70	1.90	1.80	1.81	6.09	1.77	2.08	5.04	1.75	1.61
Th/U	0.66	0.43	0.62	0.68	0.58	0.51	0.60	0.64	1.11	1.28	0.56	0.58	0.57
Zr/Hf	48.64	41.86	45.51	38.19	42.65	41.62	46.77	48.26	43.10	45.15	45.50	44.77	39.27

6 CONSIDERAÇÕES FINAIS

Os três artigos que compõem esta tese, abordaram a petrologia de duas grandes intrusões ígneas (Batólito Teixeira e Complexo Esperança) localizadas nas porções central e leste, respectivamente, da Subprovíncia Central – Província Borborema. Os dados de campo e petrográficos, assim como os resultados de geoquímica de rocha total, química mineral, datação U-Pb em zircão (LA-ICP-MP e SHRIMP) e geoquímica isotópica (Lu-Hf e Sm-Nd), foram utilizados em conjunto com dados da literatura e forneceram importantes contribuições para o conhecimento do magmatismo granítico na região estudada e de forma mais abrangente contribui para o melhor entendimento do magmatismo e relações com processos tectônicos, durante a evolução Ediacarana no Domínio Alto Pajeú.

Ambas as intrusões, de dimensões batolíticas, são alojadas imediatamente a sul da Zona de Cisalhamento Patos, estrutura de grande importância para a área estudada, e para o entendimento da Província Borborema no contexto da orogênese Brasiliana e evolução de Gondwana Ocidental (Archanjo et al., 2021). A partir dos estudos microestruturais e geocronologia de migmatitos e milonitos sin-cinemáticos ao longo das porções central e oeste da Zona de Cisalhamento Patos, é sugerido que o pico metamórfico de alta temperatura com fusão parcial associada ocorreu aproximadamente há 565 Ma (Viegas et al., 2014; Archanjo et al., 2021), com taxas de resfriamento e *uplift* heterogêneos, sendo mais rápidos no ramo oeste.

O Batólito Teixeira está alojado na porção central da Zona de Cisalhamento Patos, e apesar da proximidade e de ser um corpo alongado paralelamente a esta zona de cisalhamento (ENE-WSE), sua idade (600 a 585 Ma) e trama mineral são consistentes com uma intrusão anterior a deformação associada à Zona de Cisalhamento Patos, bem como sugerido por Archanjo et al. (2008) a partir de dados de ASM (Anisotropia de Suscetibilidade Magnética). Considerando a média das idades obtidas neste trabalho nos granitoides das Fácies Pedra D'Água, São Sebastião, Tendó e Santo Antônio, o pico do magmatismo do Batólito Teixeira ocorreu há 592 Ma, semelhante à idade reportada por Archanjo et al. (2008) para a Fácies Jabre (~591 Ma). Estas idades correspondem ao regime transicional entre o fim do regime contracional e pico metamórfico, e o regime dominantemente transcorrente (Guimarães et al., 2004), onde o núcleo da Província Borborema estava parcialmente fundido (580 – 550 Ma; Archanjo et al., 2021).

Quimicamente, os granitoides do Batólito Teixeira são caracterizados como granitoides tipo-I oxidados, com assinatura metaluminosa e afinidade com rochas cálcio-alcalinas de alto-

K a shoshonítica. Além disso, eles apresentam teores de Ba, Sr e demais elementos traços característicos de granitos de alto Ba e Sr (Tarney and Jones, 1994). Outras características químicas importantes nestes granitos são os baixos valores para o Mg#, altos valores para a razão Sr/Y (média = 186 ppm), os padrões fracionados de ETR, com média para a razão La/Yb = 40, e ausência ou inexpressiva anomalia negativa de Eu. Estas características químicas, somadas a presença de núcleos herdados de zircão com idade Paleoproterozoica e assinatura isotópica caracterizada por ƐNd e ƐHf variando de -13,68 a -16,04, e de -16,27 a -20,80, respectivamente, e idades modelo TDM Nd e Hf variando entre 2,08 – 2,23, e 2,3 – 2,6 Ga, respectivamente, sugere que o magmatismo do Batólito Teixeira foi produzido principalmente por fusão parcial de fontes infracrustais Paleoproterozoicas de composição anfibolítica, com granada e/ou anfibólio no resíduo. A escassez de enclaves máficos neste granitoides também corrobora com uma fonte essencialmente crustal.

O contexto químico particular para os granitoides do Batólito Teixeira e as idades incompatíveis com os principais intervalos de tempo que registram picos de temperatura associados a eventos tectonotermais na região estudada sugere que uma fonte de calor externa pode ser necessária para a fusão parcial que gerou o expressivo magmatismo granítico em questão. Levando em consideração o contexto pós-colisional, os dados químicos e a idade destes granitoides, um cenário que se adequa bem é o da fusão parcial de crosta tectonicamente espessada após delaminação litosférica, onde alto fluxo térmico é promovido em resposta a ascensão do manto astenosférico local (Kay and Mahlburg-Kay, 1991). No entanto, algumas feições que são típicas de orógenos que sofreram delaminação, tais como o rápido *uplift* e extensão subsequente não estão presentes na região estudada, tornando mais improvável a hipótese de gênese do magmatismo estudado a partir de delaminação. Alternativamente, o afundamento de fragmentos densos da crosta profunda também pode ser um processo efetivo para a geração de magmatismo, uma vez que o afundamento crustal permite a substituição local da crosta inferior por material mantélico e promove a elevação da temperatura, que pode ser suficiente para induzir o processo de fusão parcial dos protólitos infracrustais.

O Complexo Esperança é constituído por cinco plútons com características químicas e isotópicas distintas, alojados entre as Zonas de Cisalhamento Campina Grande e Remígio-Pocinhos (ramo leste da Zona de Cisalhamento Patos), ambas orientadas na direção ENE-WSW. Os dados geocronológicos são compatíveis com um longo período de construção para este complexo granítico, se estendendo desde os estágios finais de tectônica contracional, onde os Plútons Pocinhos e Serrote da Cobra (~600Ma) foram gerados, até regime dominantemente

transcorrente, que corresponde as intrusões dos Plútons Puxinanã, Areial e Remígio, entre 585 e 565 Ma. É importante destacar que a idade, feições de campo e microestruturas evidenciadas nos granitoides do Pluton Areial e Puxinanã, juntamente com a trama magnética reportada por Archanjo e Fetter (2004), sugerem o início do regime transcorrente na região estudada há aproximadamente 585 Ma com a Zona de Cisalhamento Campina Grande exercendo importante controle no alojamento destes plutons.

A variação química dos granitoides do Complexo Esperança é algo bastante evidente. No geral, os granitoides dos Plútons Serrote da Cobra, Pocinhos, Puxinanã e Areial são classificados como granitos tipo-I com afinidade cálcio-alcalina de alto potássio a shoshonítica, no entanto apresentam trends químicos variando de ferrosos a magnesianos e de metaluminosos a levemente peraluminosos. Os granitoides do Plúton Areial apresentam assinatura química semelhante aos granitos de alto Ba-Sr, com teores de elementos traços compatíveis com magmas originados a partir de um contexto tectônico de arco (Pearce et al., 1984, 1996), enquanto os granitoides dos demais plutons contêm teores de Ba e Sr comumente observado em granitos tipo-I, com assinatura de elementos traços mais sugestiva de contexto extensional (Pearce et al., 1984, 1996; Whalen et al., 1987). No entanto, estas configurações tectônicas não são suportadas quando é levado em consideração as idades dos plutons e geologia regional. Por outro lado, os dados reportados nesta tese mostram uma forte correlação entre a assinatura química dos granitoides e suas fontes.

Para os granitoides do Pluton Areial, que apresentam principalmente idades modelo TDM Paleoproterozoicas a Neoarqueanas (Nd: 1.9 a 2.3 Ga; Hf: 2.39 to 2.54 Ga) e valores de ƐNd e ƐHf fortemente negativos, variando de -15,29 a -16,71, e -17.14 a -19.80, respectivamente, são apontadas fontes crustais Paleoproterozoicas como as do embasamento da Subprovíncia Central, com envolvimento de fundidos máficos do manto litosférico, representados pelos enclaves. Fundidos crustais a partir de fontes anfibolíticas Paleoproterozoicas se ajustam bem aos dados químicos, sendo compatíveis inclusive com a assinatura de arco, que pode ter sido herdada durante acresção crustal no Paleoproterozoico, como também sugerido por Ferreira et al. (2015) para as fontes anfibolíticas do Pluton Guarany. Destaca-se também aqui, a semelhança entre as características químicas dos granitoides dos Pluton Areial e os do Batólitos Teixeira, evidenciando a importância de fontes infracrustais intermediárias a máficas na produção do magmatismo granítico tipo-I com afinidades cálcio-alcalinas de alto-K a shoshonítica na região estudada.

Para o magmatismo granítico que originou os Plutons Puxinanã, Serrote da Cobra e Pocinhos, componentes Tonianos como os ortognaisses Cariris Velhos constituem a principal fonte, bem como apontada pelos dados isotópicos, que são caracterizados por menores valores para o ƐNd (-5.90 a -7.35) e ƐHf (-2.83 a -6.91) quando comparados aos dos granitoides do Pluton Areial, e por idades modelo TDM Calimianas a Estaterianas. Sobretudo, fundidos originados a partir desses Ortognaisses Tonianos, que são caracterizados como metagranitoides ferrosos com assinatura química relacionada a configuração extensional (Guimarães et al., 2016), são suscetíveis a gerar granitos com teores de elementos traços (Zr, Nb, Ce, Y e Ga) semelhantes aos observados em granitos tipo-A, já que a assinatura de elementos traços é controlada principalmente pela fonte dos magmas (Roberts and Clemens, 1993; Rollinson, 1993). As diferenças composicionais entre estes plutons são associadas aos diferentes níveis de interação com assimilados crustais e fundidos mantélicos, como evidenciado pelos dados químicos e aspectos de campo.

Os Plutons Serrote da Cobra e Pocinhos tem idades semelhantes (~600 Ma) e foram gerados possivelmente durante o mesmo contexto tectônico, que corresponde aos estágios finais de um longo período de tectônica contracional e pico metamórfico, sugerindo que espessamento crustal pode ter sido fundamental para fornecer o calor necessário para o processo de fusão parcial que gerou o magma destes plutons. Por outro lado, para a gênese dos granitoides dos Plutons Puxinanã e Areial é sugerida uma maior interação entre fundidos crustais e máficos mantélicos, estes últimos gerados por fusão por descompressão durante a elevação do manto litosférico.

Diferente dos demais, o Plúton Remígio compreende rochas graníticas cuja composição é marcada pela ausência de anfibólio. Além disso, os biotitas granitos do Pluton Remígio não mostram feições de forte interação com fundidos mantélicos, sugerindo fontes essencialmente crustais como apontadas pelos dados isotópicos, caracterizados por ƐHf variando de -14,46 a -21,03, e idade modelos TDM Hf variando de 2.23 a 2.58 Ga. Os granitoides do Pluton Remígio estão alojados imediatamente a sul da Zona de Cisalhamente Patos e tem idade de cristalização (~565 Ma) similar aos registros do evento metamórfico de alta temperatura ao longo desta zona de cisalhamento (Viegas et al., 2014; Archanjo et al., 2021), portanto o elevado gradiente geotérmico associado as intrusões dos demais plutons e a deformação contemporânea ao longo da Zona de Cisalhamento Patos correspondem as fontes de calor para a fusão dos metassedimentos apontados com a principal fonte destes granitoides.

REFERÊNCIAS

ALMEIDA, F. F. M. et al. Brazilian structural provinces: an introduction. **Earth-Science Reviews**, v. 17, p. 1 – 29, 1981.

ALMEIDA, F.F.M., HASUI, Y. & BRITO NEVES, B.B. The upper precambrian of South America. **Boletim IG/USP**, v. 7. p. 45-80, 1976.

ALMEIDA, F.F.M., LEONARDOS, O.H., VALENÇA, J., 1967. Review on granitic rocks of Northeast South America. In: **SYMPOSIUM ON NORTHEAST SOUTH AMERICA GRANITES**, 1967, Recife, Proc. Recife, IUGS/UNESCO, 1967, 41p.

ARCHANJO, C. J., FETTER, A. H. Emplacement setting of the granite sheeted pluton of Esperança (Brasilian Orogen, Northeastern Brazil). **Precambrian Research**, v. 135, p. 193-215, 2004.

ARCHANJO, C. J., HOLLANDA, M. H. B, VIEGAS, L. G. F. 2021. Late Ediacaran lateral-escape tectonics as recorded by the Patos shear zone (Borborema Province, NE Brazil). **Brasilian Journal of Geology**, v. 51 (2), 2021

ARCHANJO, C. J., HOLLANDA, M. H. B. M., RODRIGUES, S. W. O, BRITO NEVES, B. B., ARMSTONG, R. Fabrics of pre- and syntectonic granite plutons and chronology of shear zones in the Eastern Borborema Province, NE Brazil. **Journal of Structural Geology**, v. 30. p. 310-336, 2008.

ARCULUS, R.J. Use and Abuse of the Terms Calcalkaline and Calcalkalic. **Journal of Petrology**, 44: 929-935, 2003.

Bakelma, Rotterdam/Broofield, 350 p, 1997.

BARBARIN, B. A review of the relationships between granitoid types, their origins and their geodynamic environments. **Lithos**, v. 46. p. 605-626, 1999.

BERTRAND, J.M. & JARDIM DE SA, E.F. Where are the EburnianTransamazonian collisional belts ? **Can. Jour. Earth Sci**., v. 27. p. 1382-1393, 1990.

BEURLEN, H., DA SILVA FILHO, A.F., GUIMARÃES, I.P. E BRITO, S.B. Proterozoic C-type eclogites hosting unsual Ti±Fe±Cr±Cu in northeatern Brazil. **Precambrian Res**., v. 58. P. 1-19, 1992.

BLUNDY, J. & HOLLAND, T. Calcic amphibole equilibria and a new amphibole-plagioclase geothermometer. **Contributions to Mineralogy and Petrology**, v. 104, p. 208-224, 1990.

BONIN, B. A-type granites and related rocks: evolution of a concept, problems and prospects. **Lithos**, v. 97. p. 1-29, 2007.

BONIN, B., DUBOIS, R. & GOHAU, G. **Le métamorphisme et la formation des granites.** Évolution des idées et concepts actuels. FacSciences Nathan-Université, Paris, 317 p. 1997.

BOWEN, N.L. The evolution of the Igneous Rocks. **Princeton University Press**, Princeton. p: 333, 1928.

BRITO NEVES, B. B. & PESSOA, R.J.R. Considerações sobre as rochas graníticas do nordeste oriental. In: **XXVIII Cong. Bras. Geol**., 1974, Porto Alegre, SBG. Anais 4, 1974, p: 143 – 157.

BRITO NEVES, B. B. **O mapa geológico do Nordeste Oriental do Brasil, escala 1/1.000.000.** Tese (Livre Docência) - Universidade de São Paulo, 1983.

BRITO NEVES, B. B. **Regionalização geotectônica do precambriano nordestino.** São Paulo. 195 p. Tese (Doutorado) – Instituto de Geociências, Universidade de São Paulo, 1975.

BRITO NEVES, B. B., VAN SCHMUS, W.R., SANTOs, E.J., CAMPOS NETO, M.C. & KOZUCH, M. O. Evento Cariris Velhos na Província Borborema: integração de dados, implicações e perspectiva. **Revista Brasileira de Geociências**, v. 25. P. 279-296, 1995.

BRITO NEVES, B. B.; CORDANI, U. G. Tectonic evolution of South América during the Late Proterozoic. **Precambrian Res**, v. 53, p. 23–40, 1991.

BRITO NEVES, B. B.; VAN SCHMUS, W. R.; FETTER, A. Northwestern Africa-Northeastern Brazil. Major tectonic links and correlation problems. **J. Afr. Earth Sci**. V. 34, p. 275–278, 2002.

BRITO NEVES, B.B., SANTOS, E.J. & VAN SCHMUS, W.R. Tectonic history of the Borborema Province, Northeastern Brazil. In: Cordani, U.G. Milani, E. J., Thomaz Filho, A.; Campos, D.A.(eds). Rio de Janeiro: Tectonic evolution of South America, 31st International Geological Congress, 2000, p: 151–182.

Brito Neves, B.B., Van Schmus, W.R., Santos, E.J., Campos Neto, M.C., Kozuch, M. O evento Cariris Velhos na Província Borborema: integração de dados, implicações e perspectivas. **Rev. Bras. Geociências**. 25, 279e296, 1995

CABY, R. The Precambriam terranes of Benin-Nigeria and Northeast Brazil and the late Proterozoic south Atlantic fit. In: Dallmeyer, R.D., (Ed.), Terranes in the Circum-Atlantic Paleozoic Orogens. **Geol. Soc. Spec. Paper**, v. 23. p. 145–158, 1989.

CASTRO, A. The off-crust origin of granite batholiths. **Geoscience Frontiers**, v. 5. p. 63-75, 2014.

CAXITO, F. A.; UHLEIN, A.; DANTAS, E. L. The Afeição augen-gneiss Suite and the record of the Cariris Velhos Orogeny (1000-960 Ma) within the Riacho do Pontal fold belt, NE Brazil. **Journal of South American Earth Sciences**, n. 51, p. 12 – 27, 2014.

CHAPPELL, B.W. & WHITE, A.J.R. Two contrasting granite types. **Pacific Geology**, v. 8. p. 173-174, 1974.

COLLINS, W.J., BEAMS, S.D., WHITE, A.J.R. & CHAPPELL, B.W. Nature and origin of A-type granites with particular reference to southeasthern Australia. **Contrib. Mineral. Petrol**, v. 80. p. 189 – 200, 1982.

CPRM, 2008. Projeto Aerogeofísico Borda Leste do Planalto da Borborema. Consórcio LASA Engenharia e Prospecções S.A./ PROSPECTORS Aerolevantamentos e Sistemas Ltda.

CRUZ, R. F.; ACCIOLLY, A. C. A. Petrografia, geoquímica e idade U/Pb do Ortognaisse Rocinha, no Domínio Pernambuco-Alagoas W da Província Borborema. **Estudos Geológicos**, v. 2, n. 23, 2013.

DALL'AGNOL, R. & OLIVEIRA, D.C. Oxidized, magnetite-series, rapakivi-type granites of Carajás, Brazil: Implications for classification and petrogenesis of A-type granites. **Lithos**, v. 93. p. 215-233, 2007.

DANTAS, E. L., HACKSPACHER, P.C., VAN SCHMUS, W.R., BRITO NEVES, B.B. Archean accretion in the Sao Jose do Campestre Massif, Borborema Province, Northeast Brazil. **Revista Brasileira de Geociências**, v. 2, n. 28, p. 221 – 228, 1998.

DANTAS, E.L., SOUZA, Z.S., WERNICKE, E., HACKSPACHER, MARTIN, H., XIAODONG, L. Crustal growth in the 3.4 to 2.7 Ga S~ao Jose de Campestre Massif, Borborema Province, NE Brazil. **Precambrian Res.**, v. 227, 120e156, 2013.

DANTAS, E.L., VAN SCHMUS, W.R., HACKSPACHER, P.C., FETTER, A.H., BRITO NEVES, B.B.,CORDANI, U., NUTMAN, A.P. & WILLIAMS, I.S. The 3.4 e 3.5 Ga São José do Campestre massif, NE Brazil: remnants of the oldest crust in South America. **Precambrian Research,** v. 130. p: 113-137, 2004.

DE WIT, M. C. J. Post-Gondwana drainage and the development of diamond placers in western South Africa. **Economic Geology**, v. 94, n. 5, p. 721-740, 1999.

DEPAOLO, D. A Neodymium and Strontium Isotopic Study of the Mesozoic Calc Alkaline Granitic Batholiths of the Sierra Nevada and Penisular Ranges, California. **Journal of Geophisical Research,** v. 86. p: 10.470–10.488, 1981.

EBY, G.N. Chemical subdivision of the A-type granitoids: petrogenetic and tectonic implications. **Geology,** v. 20. p. 641-644, 1992.

EBY, G.N. Distinctions between A-type granites and petrogenetic pathways. In: Dall'Agnol, R. et al. (eds.). Symposium on Magmatism, Crustal Evolution, and Metallogenesis of the Amazonian Craton, Abstracts Volume and Field Trips Guide. Belém, PRONEX-UFPA/SBGNO, p. 48, 2006.

EBY, G.N. The A-type granitoids: a review of their occurrence and chemical characteristics and speculations on their petrogenesis. **Lithos,** v.26. p. 115-134, 1990

FERREIRA, V. P., SIAL, A. N., PIMENTEL, M. M., ARMSTRONG, Richard; GUIMARÃES, I. P., SILVA FILHO, A. F., DE LIMA, M. M. C., DA SILVA, T. R. Reworked old crust-derived shoshonitic magma: The Guarany pluton, Northeastern Brazil. **Lithos (Oslo. Print)**, v. 6, p. 20-29, 2015.

FERREIRA, V. P., SIAL, A. N., Whitney, J.A. Large-scale silicatic liquid immiscibility: a possible example from northeastern Brazil, **Lithos**, v. 33, 285 – 302, 2014.

FERREIRA, V. P.; SIAL, A. N.; JARDIM DE SÁ, E. F. Geochemical and isotopic signatures of Proterozoic granitoids in terranes of Borborema structural province, northeast Brazil. **Journal of South American Earth Sciences**, v. 11. p. 439-455, 1998.

FLORISBAL, L.M., JANASI, V., BITENCOURT, M.F., NARDI, L.V.S. & HEAMAN, L. Contrasted crustal sources as defined by whole-rock and Sr-Nd-Pb isotope geochemistry of Neoproterozoic early post-collisional granitic magmatism within the Southern Brazilian Shear Belt, Camboriú, Brazil. **Journal of South America Earth Science**, v. 39. p. 24-43, 2012.

FOLHA SB. 24-Z-B-VI - PICUÍ: Carta Geológica-Geofísica / Projeto ARIM Seridó – CPRM. Escala 1:100.000. Recife: CAVALCANTE et al., 2018.

FOLHA SB.25-Y-A-IV SOLÂNEA: Programa Geologia do Brasil – CPRM. Escala 1:100.000. Recife: GUIMARÃES et al. 2008.

FOLHA SB.25-Y-C-I CAMPINA GRANDE: Carta Geológica – Programa Geologia do Brasil- CPRM. Escala 1:100.000: RODRIGUES et al. 2011.

FOLHA SC. 24-Z - JAGUARIBE SE: Programa Levantamentos Geológicos Básicos do Brasil - CPRM. Escala 1:500.000. Recife: FERREIRA e SANTOS, 2000.

FOLHA SC.24-X-A- BELÉM DO SÃO FRANCISCO: Carta Geológica - Programa Levantamentos Geológicos Básicos do Brasil. Escala 1:250.000. Brasília, CPRM: SANTOS, E.J. 1998

FONTANA, E., NARDI, L.V.S. & BITENCOURT, M.F. Caracterização Geoquímica e Petrogenética dos Granitoides Arroio Divisa, Região de Quitéria, Rio Grande do Sul. **Geologia USP, Série Científica**, v. 12(3). p.56, 2012.

FROST, B. R. & LINDSLEY, D. H. The occurrence of Fe–Ti oxides in igneous rocks. In: Lindsley, D. H. (ed.), Oxide Minerals: Petrologic and Magnetic Significance. Mineralogical Society of America, **Reviews in Mineralogy**, v. 25, p. 433 – 486, 1991.

FROST, B. R., & FROST, C. D. A geochemical classification for feldspathic rocks. Journal of **Petrology**, v. 49 no. 11, p. 1955-1969, 2008.

FROST, B. R.; BARNES, C.; COLLINS, W.; ARCULUS, R. Ellis D. & FROST, C. A chemical classification for granitic rocks. **J. Petrol**., v. 42, p. 2033-2048, 2001.

FROST, B.R., LINDSLEY, D.H. & ANDERSEN, D.J. Fe–Ti oxide–silicate equilibria: assemblages with fayalitic olivine. **American Mineralogist,** v. 73. p. 727–740, 1988.

FROST, C.D. & FROST, B.R. Reduced rapakivi-type granites: the tholeiite connection. **Geology,** v. 25. p. 647 – 650, 1997.

FUHRMAN, M. L., FROST, B. R. & LINDSLEY, D. H. The petrology of the Sybille Monzosyenite, Laramie Anorthosite Complex, Wyoming. **Journal of Petrology,** v.29. p. 699 – 729, 1988.

GAO, Y. Y.; LI, X. H.; GRIFFIN, W. L.; O'REILLY, S. Y., WANG, Y. F. Screening criteria for reliable U–Pb geochronology and oxygen isotope analysis in uranium-rich zircons: a case study from the Suzhou A-type granites, SE China. **Lithos**, v. 192–195, p. 180–191, 2014.

GUIMARÃES, I. P.; BRITO, M. F. L.; LAGES, G. A.; DA SILVA FILHO, A. F., SANTOS, L.; BRASILINO, R. G. Tonian granitic magmatism of the Borborema Province, NE Brazil: A review. **Journal of South American Earth Sciences,** v. 68, p. 97-112, 2016.

GUIMARÃES, I. P.; DA SILVA FILHO, A. F. Evolução Petrológica e Geoquímica do Complexo Bom Jardim, Pernambuco. Revista Brasileira de Geociência. 22(1). pp.29–42, 1992.

GUIMÃRAES, I. P.; DA SILVA FILHO, A. F. Nd and Sr-Isotopic and U-Pb Geochronologic Constraints for Evolution of the Shoshonitic Brasiliano Bom Jardim and Toritama Complexes: Evidence for a Transamazonian Enriched Mantle Under Borborema Tectonic Province, Brazil. **International Geology Review**, v. 40, n. 6, p. 500-527, 1998.

GUIMARAES, I. P.; DA SILVA FILHO, A. F.; ALMEIDA, C. N.; VAN SCHMUS, W. R.; ARAUJO, J. M. M.; MELO, S. C.; MELO, E. B. Brasiliano (Pan-African) granitic magmatism in the Pajeú-Paraíba belt, northeast Brazil: an isotopic and geochronological approach. **Precambrian Res**., v. 135. P. 23-53, 2004.

GUIMARAES, I. P.; SCHMUS, W. R. V.; NEVES, B. B. B.; BITTAR, S. M. B.; DA SILVA FILHO, A; ARMSTRONG, R. A. U Pb zircon ages of orthogneisses and supracrustal rocks of

the Cariris Velhos belt: Onset of Neoproterozoic rifting in the Borborema Province, NE Brazil. **Precambrian Research**, v. 192, p. 52-57, 2012.

Guimarães, I.P., da Silva Filho, A.F., Almeida, C.N., Armstrong, R.A. U–Pb data of granitoids showing 1.4–1.5 Ga TDM model ages from the Central Domain of the Borborema Province. In: **Simpósio 45 anos de geocronologia no Brasil, São Paulo**, Extended Abstracts, p. 251–253, 2009.

GUIMARÃES, I.P., SILVA FILHO, A. F., VALDEMIRO, J., FARIAS, D., AMORIM, J.V.A., DA SILVA, F.M.J.V. Geocronologia U-Pb e Caracterização geoquímica dos granitoides do Pluton Marinho, Provínicia Borborema. In: **46º CONGRESSO BRASILEIRO DE GEOLOGIA**, 2012, Santos - São Paulo. Anais Proceedings.

HACKSPACHER, P.C., VAN SCHMUS, W.R., DANTAS, E.L. Um embasamento Transamazônico na Provincia Borborema. In: **36º Congresso Brasileiro de Geologia,** v. 6. p. 2683-2696, 1990.

HARRIS, N. B. W.; PEARCE, J. A.; TINDLE, A. G. Geochemical characteristics of collision-zone magmatism. In: Coward, M.P., Ries, A.C. Eds. Collision Tectonics. **Geol. Soc. Spec. Pub**. v. 19. p. 67-81, 1986.

HOLLANDA, M. H. B.; PIMENTEL, M. M.; SÁ, E. F. J. de. Paleoproterozoic subduction-related metasomatic signatures in the lithospheric mantle beneath NE Brazil: inferences from trace element and Sr–Nd–Pb isotopic compositions of Neoproterozoic high-K igneous rocks. **Journal of South American Earth Sciences**, n. 15, p. 885 – 900, 2003.

HOLLANDA, M.H.B.M., ARCHANJO, C.J., SOUZA, L.C., ARMSTRONG, R., VASCONCELOS, P.M. Cambrian mafic to felsic magmatism and its connections with transcurrent shear zones of the Borborema Province (NE Brazil): implications for the late assembly of the West Gondwana. **Precambrian Research**, v. 178, p. 1–14, 2010.

HOSKIN P.W.O. Minor and trace element analysis of natural zircon (ZrSiO4) by SIMS and laser ablation ICPMS: a consideration and comparison of two broadly competitive techniques. **J Trace Microprobe Tech**, v. 16. p. 301-326, 1998.

IRVINE, T.N. & BARAGAR, R.W.A. A guide to the chemical classification of the common volcanic rocks. **Canadian Journal of Earth Sciences**, v. 8. p. 523-548, 1971.

ISHIHARA, S. Magnetite-series and ilmenite-series granitic rocks. **Mining Geology**, v. 27. p. 293 – 305, 1977.

JARDIM DE SÁ E.F. **A Faixa Seridó (Província Borborema, NE do Brasil) e o seu significado geodinâmico na Cadeia Brasiliana/Pan-Africana.** Tese de Doutorado, Instituto de Geociências da Universidade de Brasília, 1994.

JARDIM DE SÁ, E. F. A evolução proterozóica da Província Borborema. In: Proceedings of the XI Geological Symposium of Northeast Brazil. **Extended Abstract**. p. 297–316, 1984.

JARDIM DE SÁ, E.F. & HACHSPACHER, P.C. **Reconhecimento estrutural na borda noroeste do Cráton de São Francisco**. Anais, Congresso Brasileiro de Geologia, 31, v. 5. p. 2719-2731, 1980.

JARDIM DE SÁ, E.F., FUCK, R.A., MACEDO, M.H.F. & KAWASHITA, K. Terrenos Proterozóicos na Província Borborema e a margem Norte do Cráton São Francisco. **Revista Brasileira de Geociências**, v. 22(4). p. 472-480, 1992.

KAY, R.W., MAHLBURG-KAY, S. Creation and destruction of lower continental crust. **Geol Rundsch,** v. 80, 259-278, 1991.

KEBEDE, T. and KOEBERL, C. Petrogenesis of A-type granitoids from the Wallagga area, western Ethiopia: constraints from mineralogy, bulk-rock chemistry, Nd and Sr isotopic compositions. **Precambrian Res**, v. 121. p. 1 – 24, 2003.

KILPATRICK, J. A. & ELLIS, D. J. C-type magmas: igneous charnockites and their extrusive equivalents. **Transactions of the Royal Society of Edinburgh: Earth Sciences,** v. 83. p. 155–164, 1992.

King, P.L., White, A.J.R., Chapell, B.W. and Allen, C.M. Characterization and origin of aluminous A-type granites from the Lachlan Fold Belt, southeastern Australia. **J. Petrol.** 38, p. 371-391, 1997.

Kozuch, M. Isotopic and Trace Element Geochemistry of Early Neoproterozoic Gneissic and Metavolcanic rocks in the Cariris Velhos orogen of the Borborema Province, Brazil and their Bearing Tectonic Setting. PhD Thesis. Kansas University, 2003.

LAMEYRE, J. & BOWDEN, P. Plutonic rock type series: discriminations of various granitoid series and related rocks. **Journal of Volcanology and Geothermal Research**, v. 14. p. 169-186, 1982.

LE BAS, M. J.; LE MAITRE, R. W.; STRECKEISEN, A. & ZANETTIN, B. A chemical classification of volcanic rocks based on the total alkali-silica diagram. **Journal of Petrology,** v. 27. p. 745-750, 1986.

LE MAITRE, R. W. A Classification of Igneous Rocks and Glossary of Terms. Oxford: Blackwell, 193 p, 1989. ISBN:9780511535581

LE MAITRE, R. W. Igneous Rocks – A classification and Glossary of Terms. Cambridge University Press, Cambridge. 236 p, 2002.

LIÉGEOIS, J. P.; NAVEZ, J.; HERTOGEN, J. & BLACK, R. Contrasting origin of postcollisional high-K calc-alkaline and shoshonitic versus alkaline and peralkaline granitoides: the use of sliding normalization. **Lithos**, v. 45. p. 1-28, 1998.

LOISELLE, M.C., & WONES, D.R. Characteristics and origin of anorogenic granites. **Geological Society of America-Abstracts with Programs**, v. 11, p. 468, 1979.

MACDONALD, G. A. & KATSURA, T. Chemical composition of Hawaiian lavas**. Journal of Petrology**, v. 5. P. 83-133, 1964.

MACEDO, M.H.F; JARDIM DE SÁ, E.F. & SÁ, J.M. Datações Rb-Sr em ortognaisses e a idade do Grupo Seridó. **Atas do Simpósio de Geologia do Nordeste**, v. 11. p. 253-262, 1984.

MARIANO, G., NEVES, S. P., SILVA FILHO, A. F., GUIMARAES, I. P. Diorites of the high-K calc-alkalic Association: Geochemistry and Sm-Nd data and implications for the Evolution of the Borborema Province, Northeast Brazil. **International Geology Review**, Estados Unidos, v. 43, n.10, p. 921-929, 2001.

MATTEINI M., DANTAS E.L., PIMENTEL M.M., BÜHN B. Combined U–Pb and Lu–Hf isotope analyses by laser ablation MC-ICP-MS: methodology and applications. **An Acad Bras Cienc**, v. 82(2). p. 479–491, 2010.

MIDDLEMOST, E. A. K. Magmas and Magmatic Rocks. Longman, London, p. 1-266, 1985.

MIYASHIRO, A. Volcanic rock series in island arcs and active continental margins. **Journal of American Science**, v. 274. p. 321 – 355, 1970.

MORRISON, G. W. Characteristics and tectonic selling of the shoshonite rock association: **Lithos**, v. 13. p. 97-108, 1980.

MUSHKIN, A., NAVON, O., HALICZ, L., HARTMANN, G. and STEIN, M. The petrogenesis of A-type magmas from the Amram Massif, Southern Israel. **J. Petrol**, v. 44. p. 815-832, 2003.

NARDI L. V. S. **Geochemistry and Petrology of the Lavras Granite Complex, RS, Brasil.** Tese (Doutorado em Geociências - Geoquímica) - University of London, 1984.

NARDI, L. V. S. As rochas granitoides da série shoshonítica. **Revista Brasileira de Geociências**, v. 16. p. 3-10, 1986.

NARDI, L. V. S. Granitoides e séries magmáticas: o estudo contextualizado dos granitoides. **Pesquisas em Geociências**, v. 43 (1). p. 85-99, 2016.

NARDI, L. V. S., BITENCOURT, M. F. Magmatismo granítico e evolução crustal do sul do Brasil. 50 Anos de Geologia. Instituto de Geociências. Contribuições. Eds. Roberto Iannuzzi & José Carlos Frantz. Editora Comunicação e Identidade, CIGO e IG-UFRGS, Porto Alegre, 2007, 125-141.

NARDI, L.V.S. & BITENCOURT, M.F. A-type granitoids in post-collisional settings from southernmost Brazil: their classification and relationship with magmatic series. **Canadian Mineralogist**, v. 47(6). p. 1493-1504, 2009.

NEVES S.P., MARIANO G. Província Borborema: orógeno acrescionário ou intracontinental? **Estudos Geológicos,** 11:26-36, 2001.

NEVES, S. P. & MARIANO G. The lithospheric mantle as a source of magmas during orogenic processes: insights from high-K diorites in the Borborema Province and implications for continental dynamics. **Journal of the Virtual Explorer, Eletronic Edition**, v. 17, p, 2004.

NEVES, S. P. Proterozoic history of the Borborema province (NE Brazil): correlations with neighboring cratons and Pan-African belts and implications for the evolution of western Gondwana. **Tectonics**, v 22(4), 2003.

NEVES, S. P.; BRUGUIER, O.; VAUCHEZ, A.; BOSCH, D.; SILVA, J. M. R. & MARIANO, G. Timing of crust formation, deposition of supracrustal sequences, and Transamazonian and Brasiliano metamorphism in the East Pernambuco belt (Borborema Province, NE Brazil): implications for western Gondwana assembly**. Precambrian Res**., 149:197-216, 2006.

NEVES, S. P.; MARIANO, G. **Segmentação lateral e transversal da porção leste do lineamento Pernambuco: implicações tectônicas.** In: XVII Simpósio de Geologia do Nordeste, 1997, Fortaleza, CE. Atas, p. 91-94, 1997.

NEVES, S. P.; MARIANO, G.; GUIMARÃES, I. P.; SILVA FILHO, A. F.; MELO, S. C.. Intralithospheric differentiation and crustal growth: Evidence from the Borborema province, northeastern Brazil. **Geology**, v. 28, n.6, p. 519-522, 2000.

NEVES, S.P. & MARIANO, G. Assessing the tectonic significance of a large-scale transcorrent shear zone system: The Pernambuco Lineament, Northeastern Brazil. **Journal of Structural Geology**, v. 21, p. 1369-1383, 1999.

NEVES, S.P. Atlantica revisited: new data and thoughts on the formation and evolution of a long-lived continente. **International Geology Review** 53, 1377e1391, 2011

NEVES, S.P. **Granitos Orogênicos: da geração dos magmas à intrusão e deformação**. 1. Ed. Recife-PE: Synergia, 2012, 148p. ISBN 978-85-61325-78-7.

NEVES, S.P., BEZERRA, J.P.S., BRUGUIER, O., FRANÇA, R.H.M. Evidence for Early Tonian (Ca. 1000–940 Ma) continental rifting in southern Borborema Province (NE Brazil): tectonic inheritance and shear zone nucleation during assembly of West Gondwana. **International Geology Review** 63(7), 851-865, 2020.

NEVES, S.P., BRUGUIER, O., SILVA, J.M.R., MARIANO, G., DA SILVA FILHO, A.F., TEIXEIRA, C.M.L. From extension to shortening: dating the onset of the Brasiliano Orogeny in eastern Borborema Province (NE Brazil). **J. South Am. Earth Sci**. 58, 238e256, 2015.

OLIVEIRA, E. P.; WINDLEY, B. F.; ARAÚJO, M. N. C. The Neoproterozoic Sergipanoorogenic belt, NE Brazil: A complete plate tectonic cycle in western Gondwana. **Precambrian Research,** v. 181. p. 64-84, 2010.

OLIVEIRA, R.G. & MEDEIROS, V.C. Contrastes geofísicos e heterogeneidade crustal do Terreno Pernambuco-Alagoas, Província Borborema, NE Brasil. In: **XVIII SIMPÓSIO DE GEOLOGIA DO NORDESTE**., 2000, Recife-PE. RESUMOS - Boletim N° 16, Sociedade Brasileira de Geologia Núcleo Nordeste, 2000, p. 176.

OLIVEIRA, R.G. & MEDEIROS, W.E. Deep crustal framework of the Borborema Province, NE Brazil, derived from gravity and magnetic data. **PRECAMBRIAM RESEARCH**, v. 315, p. 45-65, 2018.

OLIVEIRA, R.G. & SANTOS, E.J. Seção geológica-geofísica e inferências geotectônicas na porção centro-sul da Província Borborema. In: **CONGRESSO INTERNACIONAL DA SOCIEDADE BRASILEIRA DE GEOFÍSICA**, 3., 1993. Res. Expand., 1:643-747.

PAGEL, M.; LETERRIER, J. The suba1kaline potassic magmatism of the Balloons massif(southem Vosges, France): shoshonitic affinity. **Lithos**, v.13, p. l-l0, 1980.

PEACOCK, M. A. Classification of igneous rock series. **Journal of Geology**, v. 25. p. 54 – 67, 1931.

PEARCE, J. A.; HARRIS, N. B. W.; TINDLE, A. G. Trace element discrimination diagrams for the tectonic interpretation of granitic rocks. **Journal of Petrology**, v. 25. p. 956 – 983, 1984.

PEARCE, J. Sources and setting of granitic rocks. **Episodes**, v. 4. p. 120 – 125, 1996.

Roberts, M.P., Clemens, J.D. Origin of high-potassium, calc-alkaline, i-type granitoids. **Geology** 21, 825–828, 1993.

ROLLINSON, H.R. Using geochemical data: evaluation, presentation, interpretation, first ed. Longman Group Limited, London, 1993.

SAMPAIO, M. A. F. **Petrologia, Geoquímica E Evolução Crustal Do Complexo Granítico Esperança, Terreno Alto Pajeú, Domínio Da Zona Transversal, Província Borborema,**

Nordeste Brasileiro. Tese (Doutorado em Geociências) – Universidade Federal de Pernambuco. 2005.

SANTOS, E. J. **O Complexo Granítico Lagoa das Pedras: Acresção e colisão na região de Floresta (Pernambuco) Província Borborema.** São Paulo, Brasil. 220p. Tese (Doutorado) - Universidade de São Paulo, 1995.

SANTOS, E. J.; MEDEIROS, V. C. Constraints from granitic plutonism on Proterozoic crustal growth of the Transverse Zone, Borborema Province, NE Brazil. **Revista Brasileira de Geociências**, v. 29, p. 73-84, 1999.

SANTOS, E.J. & BRITO NEVES, B.B. Província Borborema. In: Almeida, F.F.M & Hasuy, Y. (coords). O Pré-Cambriano do Brasil. São Paulo, Edgar Blucher, p.123-186, 1984.

SANTOS, E.J. e MELO, C.B.M. Diversidade do plutonismo granítico granítico brasiliano no nordeste. In: **Cong. Bras. Geol.,** 30, Recife, Anais, SBG, 1978. p.2624-2634.

SANTOS, E.J. Ensaio preliminar sobre terrenos e tectônica acrescionária na Província Borborema. In: **CONGRESSO BRASILEIRO DE GEOLOGIA**, 39, 1996. Salvador, Anais, v. 6. P. 47-50.

SANTOS, E.J. O episódio magmático de 1.1-0.9 Ga do Domínio Extremo Nordeste. In: **Simpósio de Geologia do Nordeste**, 1993. Resumos expandidos, v. 15. P. 322-323

SANTOS, E.J. Programa Levantamentos Geológicos Básicos do Brasil: Carta Geológica. Escala 1:250.000 (Folha SC.24-X-A- Belém do São Francisco). Brasília, CPRM, 1998.

SANTOS, L. C. M. L., Dantas, E. L., Santo, E. J., Santos, R. V., Lima, H. M. Early to late Paleoproterozoic magmatism in NE Brazil: the Alto Moxoto Terrane and its tectonic implications for the pre-Western Gondwana assembly. **Journal of South American Earth Sciences**, n. 58, p. 188 – 209, 2015.

SATO K., BASEI M.A.S., SPROESSER W.M., SIGA Jr. O. The application of U–Pb geochronology to zircon and titanite by laser ablation—ICP–MS. In: **Geonalysis 2012: the 8th international conference on the analysis of geological and environmental materials**, abstracts, p 86, 2012.

SATO K., SIGA O. Jr, SILVA J.A., MCREATH I, LIU D, IIZUKA T, RINO S, HIRATA T, SPROESSER WM, BASEI MAS. In situ isotopic analyses of U and Pb in Zircon by remotely operated SHRIMP II, and Hf by LA-ICP-MS: an example of dating and genetic evolution of zircon by 176Hf/177Hf from the Ita Quarry in the Atuba Complex, SE Brazil. **Geol USP Sér Cient,** v. 9. P. 61–69, 2009.

SB.25-Y-A-IV: Mapa Geológico – Folha Solânea. Escala 1:100.000. GUIMARÃES, I.P., BITTAR, S.M.B. & DA SILVA, J.M.R, 2008.

SCHMIDT, M.W. Amphibole composition in tonalite as a function of pressure: an experimental calibration of the Al-in-hornblende barometer. **Contributions to Mineralogy and Petrology**, 110, 304-310, 1992.

SIAL, A.N. Granite types in Northeastern Brazil: current knowledge. **RBG**, v.16(1). p. 54-72, 1986.

Sial, A.N., Ferreira, V.P. Magma associations in Ediacaran granitoids of the Cachoeirinha-Salgueiro and Alto Pajeú terranes, northeastern Brazil: Forty years of studies. **Journal of South American Earth Sciences**, 68, 113-133, 2016.

SILVA FILHO, A. F., GUIMARÃES, I. P., FERREIRA, V. P., ARMSTRONG, R., SIAL, A. N. Ediacaran Águas Belas pluton, Northeastern Brazil: evidence on age, emplacement and magma sources during Gondwana amalgamation. **Gondwana Researcch**, v.17(4). p.676-687, 2010.

SILVA FILHO, A. F., GUIMARÃES, I. P., SANTOS, L., ARMSTRONG, R., VAN SCHMUS, W. R. Geochemistry, U-Pb geochronology, Sm-Nd and O isotopes of ca. 50 Ma long Ediacaran high-K Syn-collisional magmatism in the Pernambuco Alagoas Domain, Borborema Province, NE Brazil. **Journal of South American Earth Sciences**, v. 68, p. 134-154, 2016.

SILVA FILHO, A. F., GUIMARÃES, I. P., VAN SCHMUS, W. R., ARMSTRONG, R., RANGEL DA SILVA, J. M., OSAKO, L. S., COCENTINO, L. M. SHRIMP U-Pb zircon geochronology and Nd signatures of supracrustal sequences and orthogneisses constrain the Neoproterozoic evolution of the PernambucoAlagoas domain, southern part of Borborema\Province, NE Brazil. **International. Journal Earth Sciences (Geol. Rundsc),** v. 103(8), p. 2155-2190, 2014.

SILVA FILHO, A. F.; GUIMARÃES, I. P.; VAN SCHMUS, W. R.; DANTAS, E.; ARMSTRONG, R.; CONCENTINO, L.; LIMA, D. Long-lived Neoproterozoic high-K magmatism in the Pernambuco-Alagoas Domain, Borborema Province, northeast Brazil. International **Geology Review**, v. 55 (10). p. 1280-1299, 2013.

SILVA, J.M.R. & MARIANO, G. Geometry and kinematics of the Afogados da Ingazeira shear zone, northeast Brazil. **International Geology Review**, v. 42, p. 86 – 95, 2000.

SPEER, J. A. Micas in igneous rocks. **Reviews in Mineralogy and Geochemistry**, v. 13, 299-356, 1984.

STRECKEISEN, A.L. Classification and nomenclature of igneous rocks. **Earth-Science Reviews,** v. 12. p. 1-35, 1976.

TARNEY, J., JONES, C.E.Trace element geochemistry of orogenic igneous rocks and crustal growth models. **Journal of the Geological Society of London,** v. 151, 855-868, 1994.

TAUSON, L. V. Geochemistry and metallogeny of the latitic series. **International Geology Review**, 25. p. 125-135, 1983.

TROMPETTE R. Geology of Western Gondwana (2000-500 Ma): Pan-African-Brasiliano Aggregation of South América and Africa. A.A. Balkema, Rotterdam, Brookfield, 350p, 1994.

TROMPETTE, R. Geology of Western Gondwana (200–500 Ma) Pan-African Aggregation of South America and Africa. Bakelma, Rotterdam/Broofield, 350 p, 1997.

VAN SCHMUS, W. R.; BRITO NEVES, B. B; HARCKSPACHER, P. & BABINSKY, M. U/BP and Sm/Nd geochronologic studies of the eastern Borborema province, northeastern Brazil: initial conclusions. **J. South Amer. Earth Sci**., v. 8. p. 267-288, 1995.

VAN SCHMUS, W. R.; KOZUCH, M. & BRITO NEVES, B. B. Precambrian history of the Zona Transversal of the Borborema Province, NE Brazil: Insights from SmeNd and UePb geochronology. **Journal of South American Earth Sciences** 31, p: 227 – 252, 2011.

VAN SCHMUS, W. R.; OLIVEIRA, E. P.; SILVA FILHO, A. F.; TOTEU, S. F.; PENAYE, J.; & GUIMARÃES, I. P. Proterozoic links between the Borborema province, NE Brazil, and

the Central African Fold Belt. **Geological Society of London, Special Publication**, v. 294, p. 69–99, 2008.

VAN SCHMUS, W.R., BRITO NEVES, B.B., HACKSPACHER, P., BABINSKI, M.; FETTER, A.H.; DANTAS E.L. Application of U-Pb in Sm-Nd geochronology to understanding the geotectonic history of the Borborema Province, NE Brazil, in the its implications for the evolution of West Gondwana. In: **South Americam Symposium on Isotope Geology, 1997. Campos do Jordão-SP**, Resumo Expandido, p. 27-29.

VAUCHEZ, A. & EGYDIO-SILVA, M. Termination of a continental-scale strike-slip fault in partially melted crust: The West-Pernambuco shear zone, northeast Brazil. **Geology**, v. 20. P. 1007 – 1010, 1992.

VIEGAS, L.G.F., ARCHANJO, C.J., HOLLANDA, M.H.B.M., VAUCHEZ, A. Microfabrics and zircon U–Pb (SHRIMP) chronology of mylonites fromthe Patos shear zone (Borborema Province, NE Brazil). **Precambriam Research**, v.243. p.1-17, 2014.

WATSON, E.B. & HARRISON, T.M. Zircon saturation revisited: temperature and composition effects in a variety of crustal magma types. **Earth and Planetary Science Letters,** v. 64, p. 295 – 304, 1983.

WATSON, E.B. The hole of accessory minerals in granitoids geochemistry. In: Hutton Conference Of The Origin Of Granites, 4, Edinburgh, Anais. p. 209-211, 1987.

WEDEPOHL, K. H. Chemical composition and fractionation of the continental crust. **Geologische Rundschau**, v. 80. p. 207-223, 1991.

Wernick, E. Rochas magmáticas: conceitos fundamentais e classificação modal, química, termodinâmica e tectônica. Editora Unesp, 655 p, 2004.

WHALEN, J.B., CURRIE, K.L. & CHAPPELL, B.W. A-types granites: geochemical characteristics, discrimination and petrogenesis. **Contributions to Mineralogy and Petrology**, v. 95. P. 407-419, 1987.

WHITE, A. J. R. Sources of Granitic Magma. In: Annual meetings of the geological society of america and associated societies, San Diego. Abstracts. San Diego, v. 11. p. 539, 1979.

WILSON, M. Igneous Petrogenesis. London: Unwin Hyman, 1989, 466p. ISBN 978-0-412-75080-9.

WONES, D. R. Significance of the assemblage titanite + magnetite + quartz in granitic rocks* **Am. Mineral**, v. 74. p. 744-749, 1989.

WU, F.Y., Sun, D.Y., Li, H., Jahn, B.M. and Wilde, S. A-type granites in northeastern China: age and geochemical constraints on their petrogenesis. **Chemical Geol**, v. 187. p. 143-173, 2002.